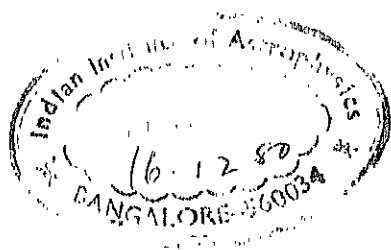




# KODAIKANAL OBSERVATORY BULLETINS

SERIES A  
VOLUME 1.



INDIAN INSTITUTE OF ASTROPHYSICS  
BANGALORE-5600 34, INDIA

13767



# KODAIKANAL OBSERVATORY BULLETINS

Series A - Volume I

## CONTENTS

No.		Page
178.	THE SPECTRUM OF COMET IKEYA-SEKI (1965f). M.K.V. Bappu and K.R. Sivaraman	1
179.	THE COSMIC RAY FLARE OF MARCH 7, 1942, K.R. Sivaraman and L.M. Punetha	7
180.	THE EVERSHED EFFECT AND LINE ASYMMETRY IN SUNSPOT PENUMBRAE. A. Bhatnagar	13
181.	PHOTOELECTRIC LIGHT CURVE OF YY ERIDANI. J.C. Bhattacharyya	52
182.	TWO COLOUR PHOTOELECTRIC OBSERVATIONS OF THE ECLIPSING VARIABLE UW CANIS MAJORIS. A.T. Doss	68
183.	THE WOLF-RAYET BINARY HD 68273. K.S. Ganesh and M.K.V. Bappu	77
184.	THE WOLF-RAYET ECLIPSING BINARY HD 193576. K.S. Ganesh, M.K.V. Bappu and V. Natarajan	93
185.	THREE WOLF-RAYET BINARIES. K.S. Ganesh and M.K.V. Bappu	104
186.	LINE PROFILE ANALYSIS OF CARBON MOLECULES IN THE SUN. Nirupama Raghavan	120
187.	COMET IKEYA-SEKI (1965f) AND THE NATURE OF THE INTERPLANETARY MEDIUM DURING ITS APPARITION. M.K.V. Bappu and K.R. Sivaraman	149
188.	SOLAR LIMB GRADIENT FROM ECLIPSE SPECTRA OF FEBRUARY 15, 1961. Aleksander Kubicela	155
189.	A DOPPLER COMPARATOR FOR SOLAR SPECTRA. Aleksander Kubicela and K.R. Sivaraman	164
190.	THE SOLAR CORONA OF JULY 20, 1963. M.K.V. Bappu and A. Bhatnagar	169
191.	NARROW BAND PHOTOMETRY OF RHO PUPPIS. A. Thulasi Doss	179
204.	ON THE POLAR CORONAL RAYS OF THE SUN. A. Bhatnagar and K.C.A. Raheem	189
205.	THE SOLAR MAGNETOMETER OF KODAIKANAL OBSERVATORY. J.C. Bhattacharyya	203
208.	APSIDAL MOTION IN THE BINARY DELTA ORIONIS. V. Natarajan and R. Rajamohan	219
209.	PHOTOELECTRIC AND SPECTROGRAPHIC STUDIES OF NOVA DELPHINI (1967). A. Thulasi Doss, A. Bhatnagar and V. Natarajan	231



# AUTHOR INDEX TO KOB SER.A - VOL.1

	<u>Page</u>
Bappu, M.K.V. and Bhatnagar, A. The Solar Corona of July 20, 1963, No.190	169
Bappu, M.K.V. and Sivaraman, K.R. The Spectrum of Comet Ikeya-Seki (1965f), No.178	1
Bappu, M.K.V. and Sivaraman, K.R. Comet Ikeya-Seki (1965f) and the nature of interplanetary medium during its apparition, No.187	149
Bappu, M.K.V. See Ganesh and Bappu	
_____ See Ganesh, Bappu and Natarajan	
Bhatnagar, A. The Evershed Effect and line asymmetry in sunspot penumbrae, No.180	13
_____ See Bappu and Bhatnagar	
_____ See Doss, Bhatnagar and Natarajan	
Bhatnagar, A. and Raheem, K.C.A. On the polar coronal rays of the sun. No.204	189
Bhattacharyya, J.C. Photoelectric light curve of YY Eridani. No.181.	52
_____ The Solar magnetometer of Kodaikanal Observatory. No.205	203
Doss, A.T. Two colour photoelectric observations of the eclipsing variable UW Canis Majoris. No.182	68
_____ Narrow band photometry of RHO Puppis. No.191.	179
Doss, A.T., Bhatnagar, A. and Natarajan, V. Photoelectric and spectrographic studies of Nova Delphini (1967). No.209	231
Ganesh, K.S., and Bappu, M.K.V. The Wolf-Rayet Binary HD 68273. No.183	77
_____ Three Wolf-Rayet Binaries. No.185	104
Ganesh, K.S., Bappu, M.K.V. and Natarajan, V. The Wolf-Rayet eclipsing binary HD 193576. No.184	93
Kubicela, A. Solar limb gradient from eclipse spectra of February 15, 1961. No.188	155
Kubicela, A., and Sivaraman, K.R. A Doppler comparator for solar spectra. No.189	164
Natarajan, V., and Rajamohan, R. Apsidal Motion in the Binary Delta Orionis. No.208	219
Natarajan, V. See Doss, Bhatnagar and Natarajan	
_____ See Ganesh, Bappu and Natarajan	
Punetha, L.M. See Sivaraman and Punetha	

# AUTHOR INDEX TO KOB SER.A - VOL.1

	<u>Page</u>
Raghavan, Nirupama. Line Profile analysis of Carbon Molecules in the sun. No.186	120
Raheem, K.C.A. See Bhatnagar and Raheem	
Rajamohan, R. See Natarajan and Rajamohan	
Sivaraman, K.R. and Punetha, L.M. The Cosmic Ray Flare of March 7, 1942. No.179	7
Sivaraman, K.R. See Bappu and Sivaraman	
_____. See Kubicela and Sivaraman	

# KODAIKANAL OBSERVATORY

BULLETIN Number 178

## The Spectrum of Comet Ikeya-Seki (1965f)

M.K.V. Bappu and K.R. Sivaraman

### Abstract

Spectroscopic observations of Comet Ikeya-Seki (1965f) with slit and slitless instruments are described. Sodium emission in the coma is seen from October 9 to November 1. A sodium tail extending upto  $2^\circ$  from the nucleus has been seen.

Spectroscopic observations of Comet Ikeya-Seki were commenced on October 9, 1965 and carried through beyond perihelion until November 4, when the Comet was 0.63 A.U. from the Sun. The spectra were obtained both with slit and slitless instruments. The cassegrain grating spectrograph on the 50 cm. reflector was used in the first order with a dispersion of 250 Å/mm. Two slit spectra were obtained on October 30.985 ( $r=0.497$  A.U.) and November 3.975 ( $r=0.626$  A.U.), using Eastman Kodak 103a-F emulsion with exposure times of 30 and 45 minutes respectively. The nucleus was guided on the slit. On other days, particularly prior to perihelion passage and on a few days after perihelion passage, until October 31, the same spectrograph was used in the slitless mode. A field lens was used in place of the slit and the whole spectrograph functioned essentially as a Meinel camera with a grating for dispersing the light. The scale in the focal plane of the 50 cm. telescope is  $10''/\text{mm}$ . The ratio of collimator to camera focal lengths is 7.5. The spectra were obtained in the first order covering the range 4700Å to 6800Å and in the second order from 3800Å to 4800Å. Exposures were of the order of 1 to 2 minutes for both the blue and red regions of the spectrum on Eastman 103a-F emulsion, during which period the comet was guided with the aid of the finder telescope.

Two other slitless instruments functioned simultaneously on the 50 cm. mounting for obtaining prismatic spectra of the cometary head and the cometary tail. Both used  $60^\circ$  glass prisms and the cameras were of focal lengths 5 cm. and 28 cm. with aperture ratios of  $f/2$  and  $f/5.6$ . The emulsion used was Kodak Linagraph Shellburst film, and while a certain degree of reciprocity failure exists with this emulsion, its primary advantage was the extensive wavelength coverage possible combined with speed, since the emulsion is sensitive to about 7100Å. The dispersions at  $H\gamma$  are 360Å/mm for the 5 cm. camera and 65Å/mm for the 28 cm. camera. Exposure times on nights free of moonlight rarely exceeded 20 minutes. The longer focal length prismatic camera had a field of about  $4.5^\circ$  by  $6.5^\circ$  and showed details of the tail spectrum out to  $3^\circ$  from the nucleus. The shorter focal length prismatic camera could follow the tail spectrum to  $12^\circ$ .



The close approach of Comet Ikeya-Seki to the Sun coincided with the peak of the spell of very bad weather due to the North-east monsoon that we have at Kodaikanal. This prevented us particularly from exploiting the solar spectrographic instrumentation available at Kodaikanal, especially on October 21 when the comet was closest to the Sun. Also, until November 1, moonlight prevented long exposures with the slitless instruments. In Table I, we give details of the spectra obtained at Kodaikanal of this comet.

TABLE I

Instrument	Date	Time U.T. h. m.	Helio- centric distance A.U.	Exposure	Emulsion	Wavelength Region	Remarks
50cm. Cassegrain slit spectrograph.	October, 30	23 40	0.497	30 min.	103a-F	3800—6700A	Well-exposed spectrum. D lines strongest feature.
	November, 3	23 24	0.626	50 min.	103a-F	3800—6700A	Swan bands and CN (0,0) well-exposed, NH <sub>2</sub> bands in visual region seen.
50cm. Cassegrain slit- less spectrograph.	October, 11	23 36	0.509	3 min.	103a-F	3800—4800A (second order).	CN moderate strength; C <sub>2</sub> weak. Dispersion 125A/mm.
		23 45		10 min.	103a-F	3800—4800A	Well-exposed.
		23 56		3 min.	103a-F	3800—4800A	Sky fog present.
	October, 12	23 38	0.474	2 min.	103a-F	3800—4800A	Well-exposed.
		23 42		4 min.	103a-F	3800—4800A	Well-exposed. C <sub>2</sub> stronger than on October 11.
		23 51		8 min.	103a-F	3800—6700A (first order).	Over-exposed.
		23 58		3 min.	103a-F	3800—6700A	Over exposed for photometry — Na emission strong.
	October, 29	23 40	0.426	1 min.	103a-F	3800—4800A (Second order).	Under exposed.
		23 37		2 min.	103a-F	3800—4800A	Well-exposed.
		23 33		25 secs.	103a-F	3800—6700A (first order).	Very well-exposed.
		23 32		60 secs.	103a-F	3800—6700A	Over-exposed for photometry.
		23 54		20 secs.	103a-F	3800—6700A	Well-exposed for photometry. Intense Na emission.
		23 55		30 secs.	103a-F	3800—6700A	Poor.
		23 56		1 min.	103a-F	3800—6700A	Well-exposed.
		23 59		2 min.	103a-F	3800—6700A	Over-exposed.
28cm. Prismatic camera.	October, 8	23 46		32 min.	Kodak Linagraph Shellburst.	3850—7100A	Over-exposed.
					Do.		
	October, 16	00 00		3 min.	Do.	3850—7100A	Fogged by twilight.
	October, 28	23 37		19 min.	Do.	3850—7100A	Well-exposed.
		23 50		4 min.	Do.	3850—7100A	Good.
	October, 29	23 40		10 min.	Kodak Linagraph Shellburst	3850—7100A	Well-exposed.
	October, 30	23 28		27 min.	Do.	3850—7100A	Very well-exposed.
		23 42		2 min.	Do.	3850—7100A	Good.
	October, 31	23 13		15 min.	103a-F	3800—6700A	Through clouds — slightly under-exposed.

TABLE I---Contd.

Instrument	Date	Time U.T. h. m.	Helio- centric distance A.U.	Exposure	Emulsion	Wavelength Region	Remarks
5 cm. Prismatic Camera	November, 2	23 12		16 min.	Kodak Linagraph Shellburst.	3850—7100A	Good.
	November, 3	23 18		45 min.	Do.	3850—7100A	Very good.
	November, 4	23 29		13 min.	Baked Ha-o	3800—4800A	Good.
	October, 28	23 37		19 min.	Kodak Linagraph Shellburst.	3850—7100A	Slightly fogged.
	November, 3	23 07		25 min.	Do.	3850—7100A	Very good.
		23 30		20 min.	Do.	3850—7100A	Very good.

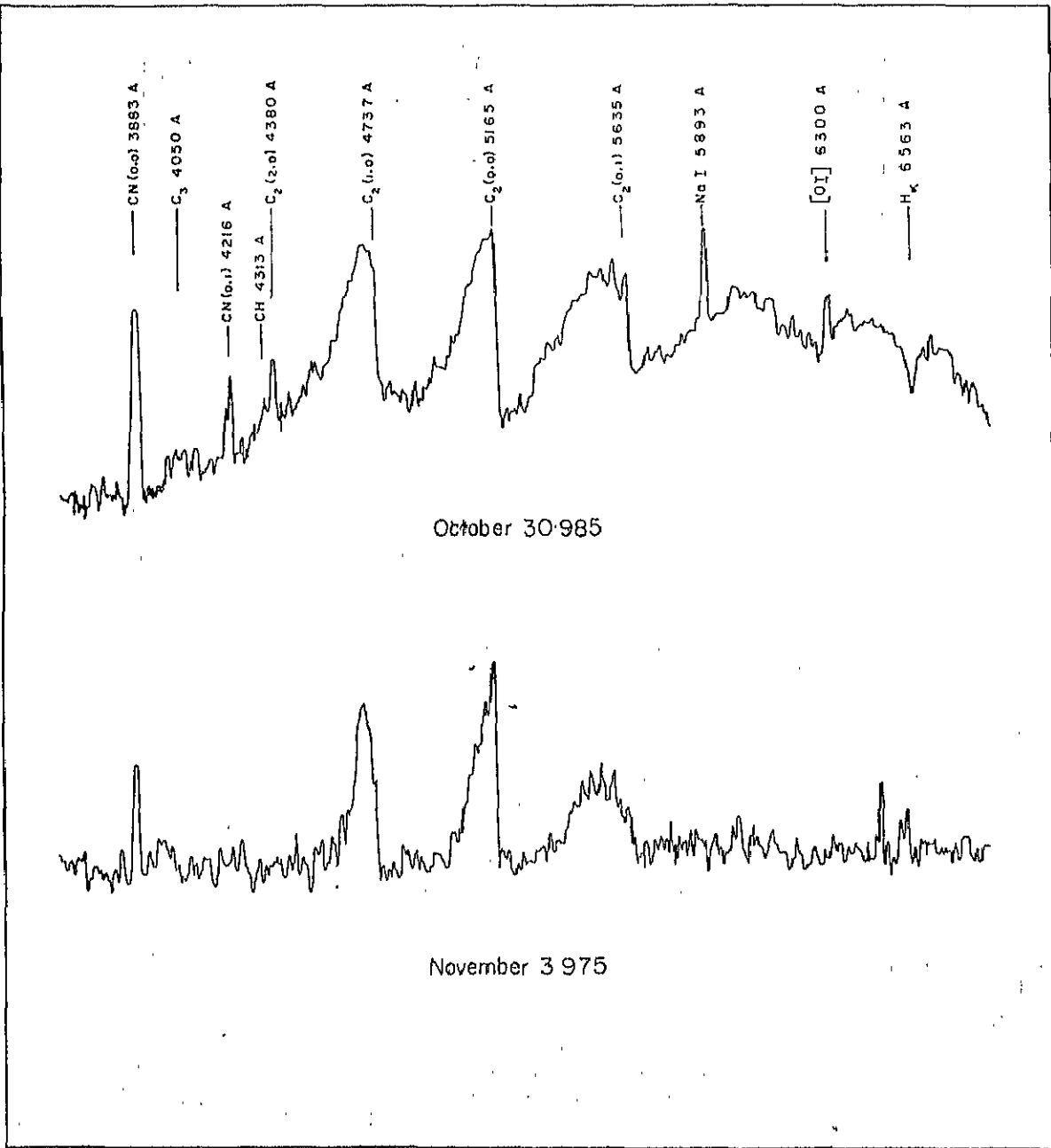


Figure 1. Microphotometric tracings of slit spectrum of Comet Ikeya-Seki (1965f) obtained on October 30.985 and November 3.975.

Figure 1 shows microphotometer tracings of the slit spectrograms obtained on October 30.985 and November 3.975. The swan bands of  $C_2$ , the CN bands, and the D line of sodium are the dominant features of the spectrum. The brightest lines in the spectrum on that day were the D lines of sodium. The cometary head displayed a fairly strong continuous spectrum. Particularly noteworthy is the very strong  $H\alpha$  absorption line that can be seen in the spectrum of the nucleus. Also easily seen is the  $H\beta$  absorption line. The other features in the spectrum are the bands of  $NH_2$  particularly near 5976A, and an emission feature at 6299A which we identify as the forbidden oxygen line at 6300A.

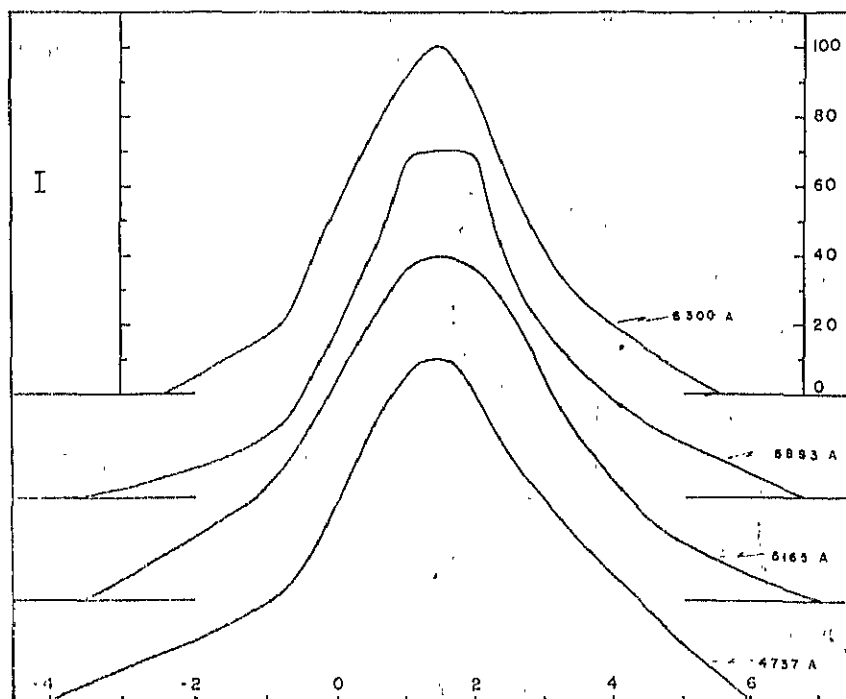


Figure 2 Intensity distributions perpendicular to the dispersion in the monochromatic images of the coma. These scans are of the slit-spectrum of October 30.985.

The intensity distributions across the coma in the light of the  $C_2$  bands and Na-emission can be seen in figure 2 where we also include the intensity distributions of 6300A of OI. An easily noticeable feature is the steep intensity gradient in the direction of the sun. This aspect is most striking in the case of Na-emission, possibly by virtue of the high 'f' value of the D lines.

The spectra obtained with the prismatic cameras as well as with the slitless cassegrain spectrograph have a fair coverage on either side of the time of perihelion passage. The D line in emission was seen to be weak on the first prismatic spectrum obtained on October 8.99. Subsequently on all spectra obtained until November 1, the Na-emission in the cometary head was easily detectable.

Soon after perihelion passage we had a spell of bad weather, that prevented us from obtaining spectra for over a week. Our first slitless spectrum obtained after perihelion was on October 29, and this showed very bright Na-emission in the coma. The 28 cm. prismatic camera spectra show the Na-emission extending into the tail to about  $2^\circ$ . This feature is seen on our prismatic spectra until November 1. In figure 3, we give a succession of scans at different distances from the cometary head to show the intensity of Na-emission in the tail. The sodium tail is relatively narrow, with little spread. This tail seems to possess a slight inclination to the dust tail of the comet. We have tried to reconstruct the position of the sodium tail against the sky background on a picture obtained at Kodaikanal with a Schmidt camera at the same time. While the

proceed  
the so

procedure we have adopted is of low accuracy in defining position, it indicates, that the sodium tail was approximately along the direction of the radius vector from the

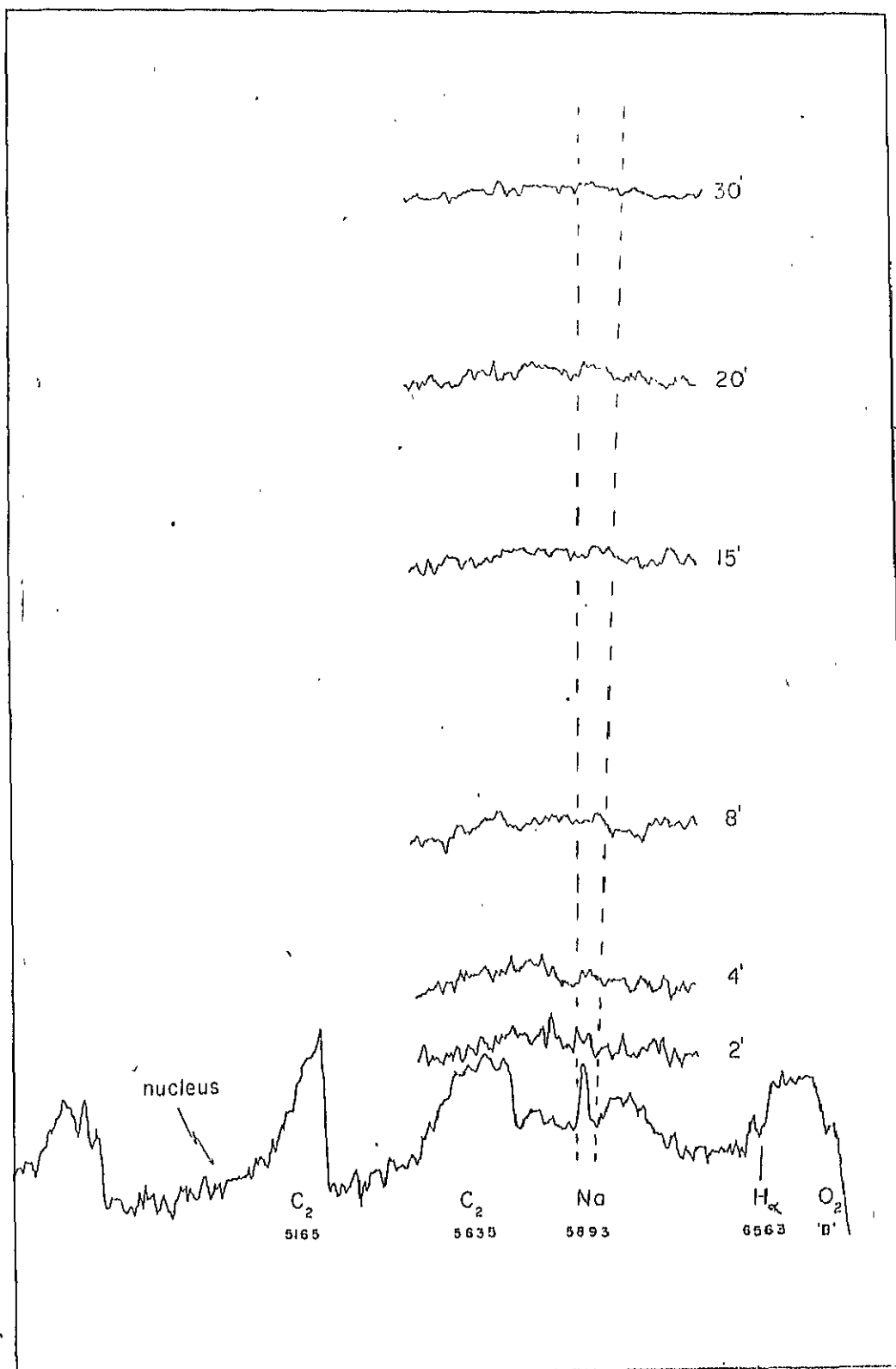


Figure 3, Successive scans at distances 2', 4', 8', 15', 20' and 30', from the cometary head. The Na-tail is seen easily. The dotted lines indicate the boundaries of the spread of the tail. The scans are of the prismatic spectrum obtained with the 28cm. prismatic camera on October 30, 1985.

Sun. The tail spectra obtained on both prismatic cameras show a predominantly continuous spectrum which we interpret as due to scattering by the abundant dust in the tail that was present after the comet's encounter with the Sun. The tail bands of  $\text{CO}^+$  can be seen very weakly on the 28cm. prismatic spectrum obtained on October 30.985. Hence, we conclude that while the tail spectrum has been dominantly a continuous one, it nevertheless showed the tail bands of  $\text{CO}^+$  weakly and showed up well a sodium tail extending a little beyond  $2^\circ$ .

We last saw the Na-emission in the coma on October 31.967. This is on the basis of a prismatic spectrum. On November 2.967 we could detect no Na-emission in the coma on a normal 16 minute exposure. On November 3.971, well-exposed pictures have been obtained with both prismatic cameras and these fail to show any trace of Na-emission. This was also confirmed on a slit spectrogram obtained of the comet, which, though a little underexposed, shows up all the strong emission bands in the comet and should have shown the D lines in emission, if they were of weak to moderate intensity. We thus consider, that, the Na-emission ceased to exist sometime from November 3 onwards, when the comet was at a heliocentric distance of 0.593 A. U. This conclusion seems surprising in view of the fact that Na-emission is generally supposed to occur in comets, when their heliocentric distances are less than 0.8 A.U. However, our observations of November 3 and 4, from different spectra obtained with two different instruments, show clearly beyond doubt, that the Na-emission ceased to exist on these dates.

The cassegrain slitless spectra have been obtained with a telescope scale of  $10''/\text{mm}$ . We have well-exposed spectra, both before and after perihelion passage and these will be used for the derivation of isophotes of the  $\text{C}_2$  (1,0) band as well as the CN (0,0) band. The results will be published later. Since the effective scale in the spectrograph focal plane is  $75''/\text{mm}$ , the dispersion of  $250\text{\AA}/\text{mm}$  is low enough to show the CN (0,0) band as a single blob of emission. In contrast to this situation we have the 28 cm. prismatic spectra show up the coma, resolved in the P and R branches by virtue of the much greater dispersion used in combination with the small telescopic scale.

Kodaikanal Observatory,  
December, 1966.

# KODAIKANAL OBSERVATORY

BULLETIN No. 179

## The Cosmic Ray Flare of March 7, 1942

K. R. Sivaraman and L. M. Punetha

### Abstract

The variation of the dynamic characteristics of the cosmic ray limb flare of March 7, 1942 based on the  $K_{232}$  spectroheliograms and H-alpha spectrohelioscope observations of Kodaikanal is presented. Although the flare had high flare ribbon velocities of the order of 17 km/sec. during the flash phase, with subsequent changes in its configuration, its effect on the nearby prominence was trivial. The loop prominence with typical condensations and knots formed at a height of 30,000 km. above the limb and connected to the chromosphere by thin curved threads was noticed, about  $1\frac{1}{2}$  hours after the flash phase.

---

Observations on limb flares are of great interest, as they give information about the vertical aspects of flares in the chromosphere. Observations of these flares are important, as the dynamic characteristics of the flares and of the loop prominences associated with these flares, during their evolution can be studied conveniently, free from the background of photospheric light.

The flare of March 7, 1942, is one of the 10 great solar flares observed so far which have generated cosmic rays recorded at ground level (Ellison *et al* 1961). Apparently the only sequence of spectroheliograms obtained of this solar event was those taken at the Kodaikanal Observatory. This flare occurred over the sunspot group (Greenwich 14015). Examination of the solar disc sketchings shows no other active region. The only other spot group present on March 7 and March 8 (Greenwich 14021) was not active. According to Greenwich, the spot group (Greenwich 14015) was first seen approaching the West limb by February 7, returned to the east limb on February 22 and passed the west limb on March 7, during its second rotation. It returned to traverse the disc during the next two rotations (Greenwich photoheliographic results 1942). The group during the second rotation, gave rise to three flares of importance 3\*. The first one, on February 21, when on the east limb was recorded at Meudon, Newton (1947) the second flare on February 28, was described by Ellison *et al* (1961) and the third flare was on March 7, when the spot was on the west limb. From the sunspot drawing of Ellison 1961 it was seen that the group during its

A-8

present passage across the solar disc was of complex magnetic type and the two main umbrae of the principal spot had field strengths of 5100 gauss (south) and 3900 gauss (north). The spot was of the potsdam  $\delta$ -configuration, thus satisfying an almost

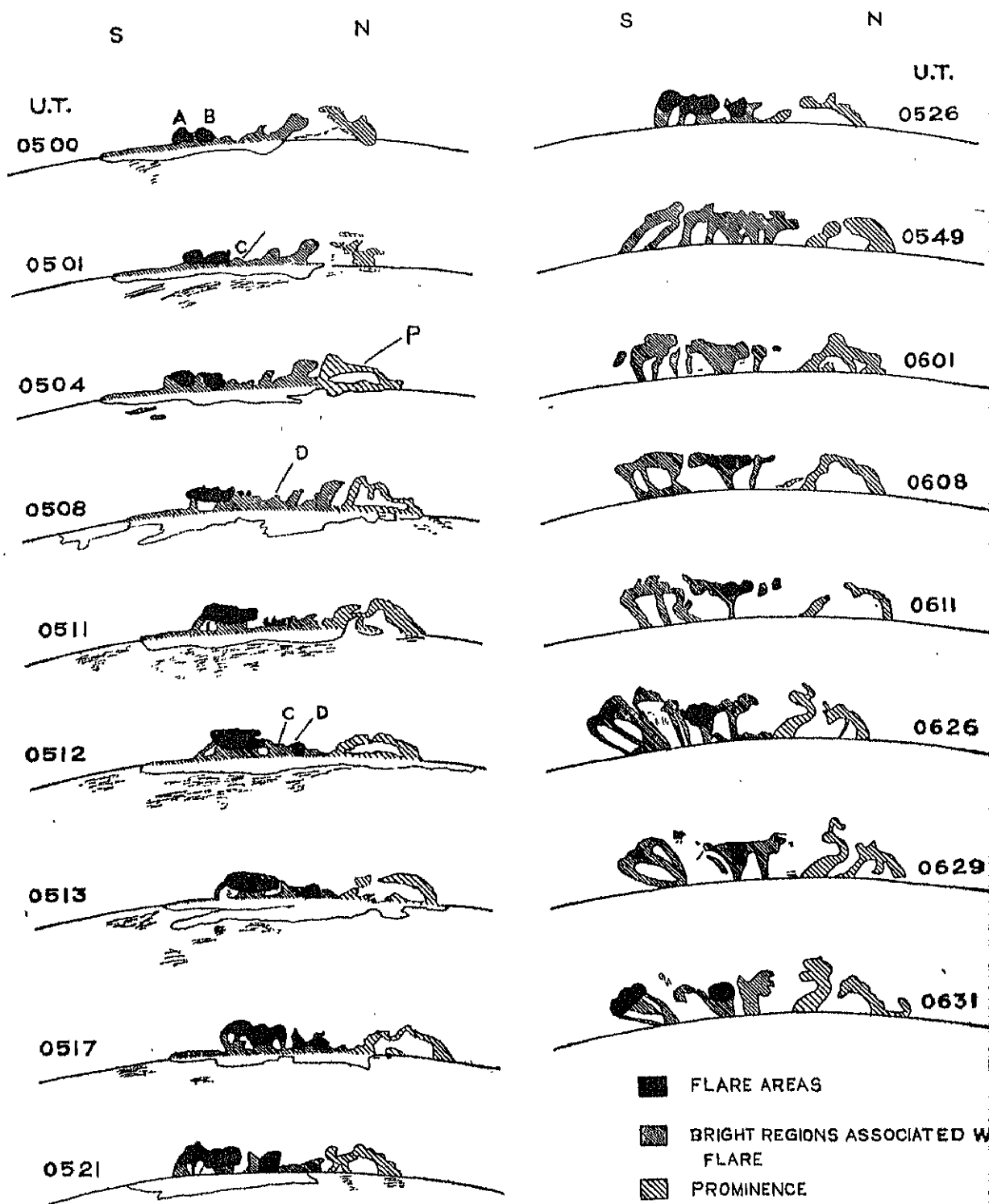


Figure 1: The Cosmic Ray Flare of March 7, 1942

necessary condition for generating a proton flare according to Warwick (1966). reached maximum area of 2048 millionths of the hemisphere on February 25. The ar

progressively decreased during the following days and on March 6 was only 907 millionths and on the day of the flare, 383 millionths. The spot group was at longitude  $85^\circ$  W and heliographic latitude  $7^\circ$  N at the time of the flare.

The Kodaikanal records on the March 7 flare, consist of a series of 50 spectroheliograms in  $K_{232}$ , H-alpha spectrohelioscope observations and original sketchings. The flash phase according to spectrohelioscope observations, is at 0445 U.T. and the time of maximum brightness at 0450 U.T. The times of the flash phase and the peak intensity based on ten best magnetic crochet records, Ellison *et al* (1961) are  $0442 \pm 1$  m U.T. and  $0450 \pm 2$  m U.T. respectively.

In the spectroheliograms taken at 0424 U.T. and 0428 U.T. two thin loops of prominences originating from  $1^\circ$  South of the flare eruption region could be seen. They were not present in the morning spectroheliograms taken at 0258 U.T. These were also absent in the flare sequence spectroheliograms starting 0500 U.T. One of the loops, extended towards the SW direction, whereas the other, curved over the

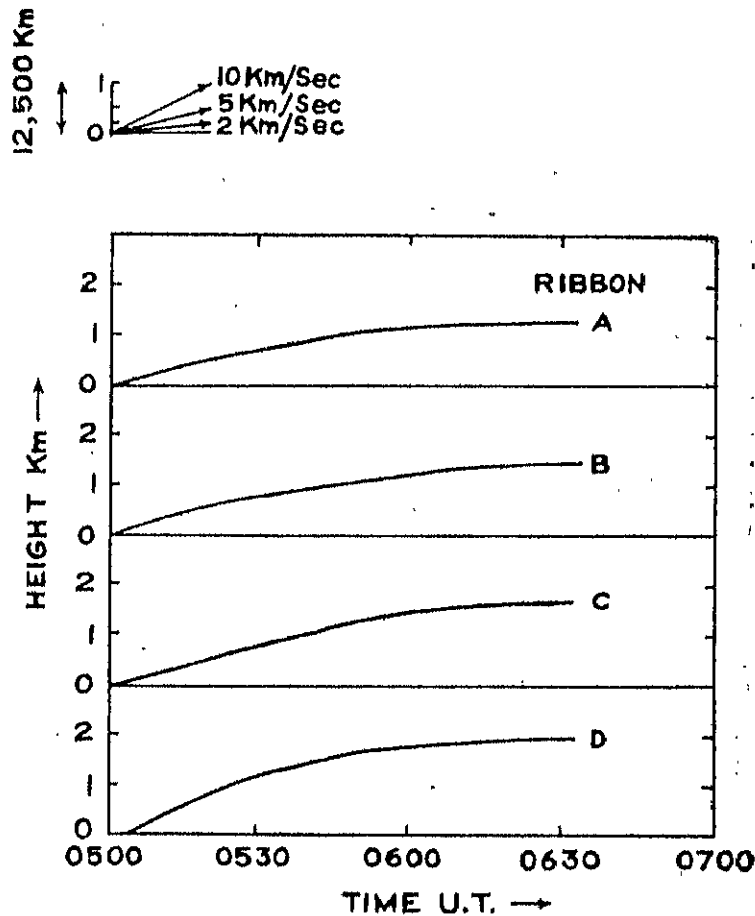


Figure 2: Time Height Graphs of Projected Height of Flare above the limb of four flare-elements. The drawing in the upper left hand corner gives the tangents for velocities of 10, 5 and 2 Km/Sec.

flare region towards an old prominence, formed on March 2-3 and situated to the north of the flare region. We now describe, the evolution of the main optical features in relation to the series of  $K_{232}$  spectroheliograms. In the first flare spectroheliogram taken at 0500 U.T. about 10 minutes after the flash phase, two very bright flare ribbons protruding beyond the solar limb were visible (A and B, Fig. 1). Their heights above



the limb at this instant were 11,000 km. and 9,300 km. respectively. The initial development of this flare, was almost opposite to the flare of May 4, 1960, where, the flare began as a brightening in an existing abnormally bright prominence at an elevation of 20,000 Km. above the limb (Ellison *et al* 1961). Assuming the start of upheaval of the flare ribbons to coincide with the flash phase of the flare, we find their mean projected velocity to be nearly 17 km/sec. This order of magnitude of the vertical velocity finds further support from the spectrohelioscope observations, where the line of sight velocities at two places were observed to be 145 km/sec. and 110 km/sec. at 0500 and 0505 U.T. respectively. Such high flare ribbon velocities are quite a rare phenomenon (Ellison 1949). The two rising flare ribbons at 0500 U.T. showed an initial conical shape. By 0501 U.T. they had become rectangular by expanding at their tips (at the rate of 62 km/sec.) but showed no change in height or the base line. At the same time, another bright ribbon C became conspicuous by moving away from the limb ( $V_h = 36$  km/sec.). The whole region then merged into one block and continued to expand southward at the rate of 55 km/sec. and gained in height ( $V_h = 19$  km/sec.) till 0508 U.T. Some part of the matter, thus brought forth in view was of a lesser intensity than the original flare ribbons, particularly at the southern end. This gave a frayed appearance to the ribbons. By 0508 a small streak D,  $1^\circ$ N of the three ribbons which had the brightness of a prominence became very bright and moved, away from the limb ( $V_h = 10$  km/sec.). The ribbon D and the ribbon C continued to move away from the limb, maintaining a rate of 10 km/sec. till 0513, without showing any decrease in their brightness. The rate of movement in the region of ribbons A and B and south of it was almost double (about 18 km/sec.) and hence, the portions near the limb and away from the limb, showed a decrease in intensity. In these regions the flare ribbons showed much filamentary structure. The rate of growth of the flare is shown by the time-height graphs for the elements A, B, C, & D. Fig. 2.

From 0513 to 0526 U. T. the whole region projected beyond the limb did not gain in dimensions, but continued to become fainter. At 0529 U. T. both the motion away from the limb and the south ward extension were seen to start again. Along with it, the whole region continued to become fainter, the bright intense regions being confined to few scattered patches which coincided with the original flare ribbons. This trend continued till 0633 U. T. when we have the last picture of the day. The average velocity away from the limb was about 4 km/sec. and the expansion rate was about 12 km/sec. These velocities showed an occasional rise by a factor of 3 to 4. Both the rate of rise and rate of expansion on the southern end were roughly twice, than at the northern end. In the spectroheliogram taken at 0626 U. T. the internal structures such as loops and arches became distinct in the flare; one end of the main loop apparently anchored on the biggest spot was also seen. Within the next 5 minutes, the typical condensations, knots and loops of a loop prominence were formed in the region, about  $1\frac{1}{2}$  hours after the flash phase. The knots at a mean height of 30,000 km. above the limb were connected with the chromosphere by thin, less bright curved threads.

Considering the flare from its intense geomagnetic effects, its influences on prominence activity were surprisingly trivial. To the north of the flare, there was an old prominence P, formed around March 2. From the beginning of the flare till 0610 U.T. the prominence remained almost quiescent except for the formation of few condensations in it, and the dispersion by diffusion or occasional lateral motion of these condensations. From 0615 U. T., the prominence changed its shape and curved towards the flare regions with condensations at the top. In this respect, it differed distinctly from the flare of July, 20, 1961, which caused violent changes in the prominence nearby. (Gaizauskas and Covington 1962; Bruzek 1965). This leads us to believe that there were no great changes in the configuration of the magnetic field following the flare, as according to Severney, this change in the configuration is often sufficient

to affect the stability of a nearby prominence. A prominence ray appeared with the flare at  $3^\circ$  north of the flare ribbon zone. This attained its maximum height at 0508 U. T. and thereafter decreased in height, merging into the background by 0517 U.T.

Among the secondary effects of this flare studied by Ellison (1961) were the outstanding magnetic crochets recorded at many stations, which showed an extremely abrupt start and rise to maximum. This has been taken to indicate the rapid rise of the flare to peak intensity.

The increase of cosmic ray intensity was also recorded at 4 stations, the maximum at Cheltenham (Maryland) being 9% above the pre-flare level and which lasted for about 12 hours.

No magnetic storm and consequently no Forbush decrease in cosmic rays were observed following the flare. This is to be expected according to Newton (1943) for, owing to the large heliocentric angle of the flare, the ejected corpuscular stream would invariably miss the earth.

It is a pleasure to thank Dr. M. K. Vainu Bappu, Director, for suggesting this study and for continued help during the course of the investigation.

KODAIKANAL OBSERVATORY, }  
November, 1966 }

#### References

- (1) Bruzek, A. (1965), AFCRL Special Report, No. 26, " Observations on Solar Flares ".
- (2) Ellison, M. A. (1949), M.N.R.A.S., **109**, 3.
- (3) Ellison, M.A., McKenna Susan M.P. and Reid J. H. (1961), Dunsink Obs. Pub. **1**, 53.
- (4) Gaizauskas V. and Covington, A.E. (1962) J. Geophys. Res., **67**, 4119.
- (5) Newton, H. W. (1943), M.N.R.A.S., **103**, 244.
- (6) Newton, H. W. (1947), J.B.A.A., **57**, 54.
- (7) Warwick, Constance S. (1966), Ap. J., **145**, 215.



# ERRATA FOR ODAIKANAL OBSERV FORM BULLETIN NO.180

Page	Line	For	Substitute
A 17	11	was	was < 30 metres
A 24	24	$V(\cos \phi \cos \gamma_2 - \sin \phi \cos \gamma_1)$	$V(\cos \phi \cos \gamma_2 - \sin \phi \cos \gamma_1)$
A 25	6	$\cos \gamma_3$	$\cos \gamma_2$
A 25	27	$\gamma_1 \gamma$	$\gamma_2$
A 25	28	$\gamma_{\lambda} = \int_0^{\infty} G \psi \left( \frac{K \lambda \gamma}{K \lambda_0} \right) \frac{d\gamma}{\mu}$	$\gamma_{\lambda} = \int_0^{\infty} G \psi \left( \frac{K \lambda \gamma}{K \lambda_0} \right) \frac{d\gamma}{\mu}$
A 26	17	log t scale	log $\tau$ scale
A 27	25	$K$	$\text{Dia}$
	2	(in eqn.13) $K_{\lambda}$	$K \lambda_0$
	7	$\gamma$	$\sum \gamma$
	9	$K$	$K$
	13	area	area
A 28	8	log t	log $\tau$
44	last line	- trial	- trical

bsraj/26.8.68.



## KODAIKANAL OBSERVATORY

BULLETIN Number 180

### The Evershed Effect and Line Asymmetry in Sunspot Penumbrae

A. Bhatnagar

#### Abstract

During the two successive passages of a sunspot across the solar disk, velocity field configurations have been obtained using three Zeeman insensitive lines ( $g=0$ ), 4912.027, NiI ; 5576.101, FeI and 5691.508 FeI (Ni). Large image resolution and high spectrographic dispersion have been used for the determination of sight-line velocities in the spot. The observed sight-line velocities have been resolved into three mutually perpendicular directions—the radial, tangential and the vertical components. The magnitude of the maximum radial velocity component,  $U_{\max}$ , depends on the disc position of the spot and on the strength of the line. For lines of Rowland intensity 1, the magnitude of  $U_{\max}$ , in the spot penumbrae near the disc centre is about 2.0 to 2.5 km/sec, directed radially outwards towards the photosphere. Well developed spots show large radial velocities compared to spots in the initial phases. From the knowledge of the mean depth of formation of lines in sunspot penumbrae (using Makita's sunspot penumbral model), a mean gradient of  $U_{\max}$  with depth, of the order of  $4 \times 10^{-3}$  km/sec. per km. in depth, has been obtained.

Small vertical velocities of the order of 0.2 km/sec., and less, directed downwards in the penumbral region, have been observed.

Sizable tangential velocities of the order of 0.6 to 1.0 km/sec. in the spot penumbrae have been detected. No definite direction of rotational motion in spots has been observed. The motion is both in clockwise and counter-clockwise directions, in the same spot. The present observations do not fully confirm the existence or otherwise of the tangential velocities in sunspot penumbrae. However, in the light of the recent measures of the azimuthal component of magnetic field in sunspots by Adam, the presence of the tangential velocities could be expected.

A photometric analysis of the asymmetry in lines in the penumbral region has been presented. The direction of asymmetry in lines is always directed towards the general Evershed flow and seems to end near the outer penumbral boundary, while the Evershed flow continues in the photospheric region. The magnitude of the asymmetry in lines is a function of the line strength and the location in the spot region. The stronger lines show small asymmetry compared to the weaker lines. Near the disc centre positions of the spots, the asymmetry in general decreases. It is suggested that the phenomenon of line asymmetry may be due to the relative Doppler displacements occurring in several strata of the line forming layer, superimposed on small scale motion within the layer.

In the photospheric region of the spectrum, lines show slight "flaring". This is conspicuous in the darker portions of the spectrum. In the bright regions, due to the solar granules, lines appear very asymmetrical and no "flaring" in lines is seen.

**Introduction:**—J. Evershed (1909a), while analysing sunspot spectra obtained at the Kodaikanal Observatory, noticed motion of sunspot gases in the penumbral region. The spectra clearly revealed a horizontal and radial outflow of gases in the penumbra. Further studies of Evershed (1909a, b, c, 1910, 1916) showed that the magnitude of the radial motion depends on the disc position of the spot and the strength of lines. Evershed's early observations of the radial motion in sunspots were later confirmed by the observations of St. John (1913). This discovery of radial horizontal flow of material in sunspot penumbrae, is now known as the Evershed Effect.

Much later Abetti (1932) observed 26 spots and reported that radial and tangential velocities vary from spot to spot. Abetti also showed that the radial velocity is a function of the spot area. Calamai (1934) suggested that the motion of gases in sunspots is of a logarithmic spiral type. During recent years, Kinman (1952, 1953), Bumba (1960), Holmes (1961), Servajean (1961) and Brekke and Per Maltby (1963) have extended the study of the Evershed Effect in sunspots. A detailed and precise knowledge of the velocity and magnetic fields in sunspots is essential for an understanding of the sunspot phenomenon.

For a precise understanding of the velocity fields in spots, it is necessary to have a large spectrographic dispersion, large image resolution and good seeing conditions. As suggested by Kinman (1953) the sight-line velocities in sunspots are affected by:

- (1) the horizontal apparatus function of the spectrograph,
- (2) The Zeeman broadening,
- (3) obliteration of solar image due to the telescope, spectrograph and atmospheric conditions, and
- (4) scattered light in the telescope and spectrograph.

To obtain an accurate velocity field configuration, it is necessary to minimise the above-mentioned obliterating effects. In the present study of the Evershed Effect, an image scale of 5.5" per mm and a spectrographic dispersion of approximately 6 to 8 mm per Angstrom were utilized. Table I, contains the details of dispersion, velocity factors, image scale, number of spots studied and exposure times used in the Evershed Effect studies. To completely avoid the influence of the magnetic field from the velocity field determinations, three Zeeman-insensitive lines were selected. These lines; 4912.027 NiI, 5576.101 FeI and 5691.509 FeI (Ni), cover a limited range in excitation potential and in Rowland intensity. The details of the lines are given in Table II.

TABLE I  
*Details of instrumentation used in the study of the Evershed Effect*

Author	Year	Dispersion $\text{\AA}/\text{mm}$	Doppler shift $\text{mm}/\text{km}/\text{sec}$	Image scale Sec. of $\text{arc}/\text{mm}$	No. of Spots	Exposure Time seconds	Wavelength Region $\text{\AA}$
Evershed	1909	1.1	0.014	16.3	12	30	4650
	1909	1.1	0.014	16.3	4	30	4650
	1916	1.1	0.014	22.0	2	5-30	4650
St. John	1913	0.56	0.025	11.0	11	60-180	
Abetti	1932	1.2	0.013	11.0	26	..	4000
Calamai	1934	1.5	0.013	11.0	5	..	..
Kinman	1952	1.5	0.013	10.3	1	5-6	5900
	1953	1.5	0.013	10.4	4	2-5	5900
Bumba	1960	0.29	0.068	5.9	22	1-2	5900
Servajean	1961	0.5	0.02	9.0	1	1-12	5000
Holmes	1961	0.17	0.109	5.8	1	30-60	5576
	1963	0.20	0.092	10.3	1	40-60	5576
Brekke and Per Maltby	1963	0.28	0.069	6.8	..	0.3-3	4754
Bhatnagar	1964	0.12	0.137	5.5	2	10-12	4912
		0.17	0.109	5.5	2	3	5576
		0.16	0.113	5.5	2	3	5691

TABLE 2

*Details of Zeeman-insensitive lines used for the velocity field determination*

Wavelength Å	Element	Rowland Intensity		E.P. in volts		Transition
		Disc	Spot	Low	High	
4912.027 . . . . .	NiI	1	1	3.75	6.26	$z^6F-e^6F$
5576.101 . . . . .	FeI	4	4	3.42	5.63	$z^6F-e^6D$
5691.509* . . . . .	FeI	2	2	4.28	6.45	$y^6F-g^6D$

The observed sight-line velocity fields reveal only the sight-line velocity variation in the spots. These measures are insufficient to present a complete velocity field distribution in spots, unless the true direction of the mass motion in spots is known. Further, the knowledge of depth dependence of the mass motion is essential for a velocity field model of sunspots. Methods are available for resolving the observed sight-line velocities into three component velocities; radial, tangential and vertical. With a suitable model of the sunspot penumbra and using the theory of line formation, it is now possible to determine the depth dependence of velocity fields in sunspot penumrae.

In this study the observed sight-line velocities in sunspot penumbrae, were resolved into three component velocities radial, tangential and vertical. The sunspot penumbra model of Makita (1963) was utilized for determining the mean depth of formation of lines. The spatial distribution of the longitudinal component of the spot magnetic field, was also determined for a study of a possible correlation between the velocity and the magnetic field configuration.

**The observations.**— The Kodaikanal solar tower telescope was utilized in this study. Light from a 60 cm aperture coelostat of fused quartz, was fed to a 38 cm aperture achromat of focal length 36.6 metres. A solar image of diameter 34.8 cms was formed on the spectrograph slit.

The 18 metre Littrow spectrograph in conjunction with the solar telescope, uses a grating ruled by Babcock as the dispersing unit. This grating of 600 grooves per mm is blazed in the fifth order green and has a ruled surface of  $200 \times 135$  mm. Tests performed with an Iodine absorption tube have shown that close Iodine doublets at  $5303 \text{ Å}$ , having approximately  $0.009 \text{ Å}$  separation are easily resolved in the fifth order. This shows that the theoretical resolving power of 600,000 of the grating is achieved.

To estimate the scattered light in the spectrograph, spectra were taken with different slit heights varying from 0.5 cm to 2.5 cms. Long exposures were given to greatly over expose the spectra. No blackening beyond the spectrum edges on these exposures were perceptible. Photoelectric determinations have also shown no perceptible contribution due to diffuse scattered light in the spectrograph. We have, therefore, assumed that the effect of the scattered light in the spectrograph on the observed velocities is negligible.

To determine the spatial variation of velocity and magnetic fields in sunspots five to six spectra were obtained with the slit of the spectrograph crossing various portions of the spot. To determine precisely the coordinates of the points where the Doppler displacements were measured on the spectrograms, two wires 300 microns thick were stretched over the slit jaws. These wires cast shadows on the spectrum

\* This line is identified as blend of Fe (Ni) in the Rowland table.



which serve as fiducial marks on the plate. The spot spectra were taken after bringing the desired portion of the spot between these two wires. A recording of the position of the wires, the slit position and the spot, was made immediately after each exposure. The heliographic coordinates of the points, at which the velocity measurements were made, were determined by using these sunspot maps and the white light photoheliograms taken daily at Kodaikanal, around the time of four observations.

**Measurement of Doppler shifts.**—The Fraunhofer lines become very broad and diffuse under high dispersion, such as the one used in this study. However, it is essential to have high dispersion for a precise determination of small Doppler displacements. In the case of wide diffuse lines it becomes very difficult, if not impossible, to use the conventional method of measuring line positions bisecting the spectral line with a micrometer crosswire. The method used in this study, for measuring the sight-line velocities, utilizes essentially the principle of photographic subtraction. The principle was first used for wavelength determinations by Evershed (1913). The present method is, however, an extension of the original Evershed's positive-on-negative method, and is capable of yielding greater precision and convenience of measurement. The essential advantage of this method is that, the accuracy of the setting is independent of the width of lines. A more or less similar technique for measuring small Doppler shift was also used by Servajean (1961).

The spectrum to be measured was mounted on the plate carriage of a Zeiss spectrum projector, and was magnified 21 times. The projector yields a distortion-free enlargement. On the magnified images of the spectra, the scale and velocity factors in the three spectral regions of interest were as follows:

Wavelength Å	Scale Å/mm.	Velocity factor km/sec/mm.
4912 . . . . .	0.0060	0.360
5576 . . . . .	0.0080	0.426
5691 . . . . .	0.0078	0.415

The enlarged image of the line of interest in the spectrum was focussed on a stage attached to a micrometer screw. On this stage was mounted a suitable density positive enlarged copy of the line to be measured. Care was taken to see that the magnification of the positive copy and the enlarged image of the spectrum was exactly the same. For setting on the line centre, the stage on which the positive enlargement of the line was mounted, was moved to obtain a 'grey' match. At this position of the micrometer screw the positive profile precisely matches the negative. With a little practice it was possible to obtain a match within 50 to 60 microns of the micrometer scale, thus giving an accuracy of velocity measures of about 30 meters per second. A velocity measure obtained on the plate, is the mean velocity over 1.6 seconds of arc over the solar disk.

The plate carriage of the spectrum projector is capable of moving in two perpendicular directions: one along the dispersion, the X-direction, and the other perpendicular to it, the Y-direction. A precision dial gauge was attached in the Y-direction to read the position of the measured point from the wire shadow on the plate. The velocity measures were made at intervals of approximately 1,100 km and on some plates at intervals of 1,900 km.

To determine the sight-line velocities in the sunspot, with respect to the velocity of a remote photospheric region, the following procedure was adopted. Line position settings on the two sides of spot were obtained using the 'grey' match technique. These

line positions were fitted into a straight line equation. Any deviation in the region of the spot, thus directly gives the sight-line displacement, due to the velocity field in the spot. This method enables one to smooth out small scale Doppler displacements due to the granular motion in the photospheric region:

This modified method of positive-on-negative, seems to be free from personal bias. However, matching becomes difficult when the line acquires an asymmetric profile, especially near the penumbral boundary.

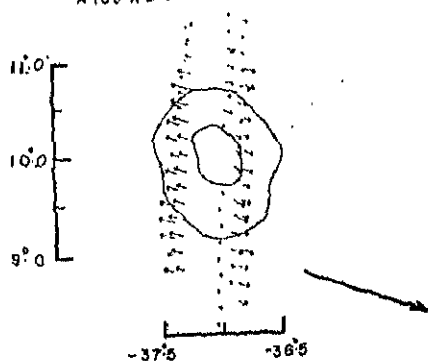
From the formulae given by Walker (1909) or Minkowski (1942) for the curvature of lines in grating spectrograph, the maximum deviation in wavelength over a slight height of 14 mm, for a 60-foot spectrograph and in the wavelength region of interest is, less than 0.7 mÅ. The solar differential rotation on two sides of the spot observed was per sec. Considering their small magnitude, both these corrections to the velocity measures have been neglected.

**Details of the sunspots studies and sight-line velocity field.**— The observations reported in this study were obtained during two successive passages of the same sunspot group. This investigation was aimed to study the changes in velocity field with the age of the spot. The Kodaikanal photoheliogram records show that Kodaikanal spot No. 12358 (KKL 12358), first appeared around December 18, 1962, at about  $14^\circ$  east of the central meridian, and receded beyond the western limb on December 25. The same spot group appeared around January 8, 1963 on the eastern limb and was designated as KKL 12368. Until January 13, no apparent change in the shape and size could be noticed in the spot group. Between January 9 and 14 only two small flares were reported. From January 14 onwards rapid changes in shape and size were observed until January 18. During this interval, more than 7 sub-flares were reported in the CRPL data. It appears that from January 19 onwards, the spot group KKL 12368 attained the stable phase of its life. During its second passage across the disc, sight-line velocities were determined on January 13, 19, 20 and 21. The observed sight-line velocity fields are given in Figure 1 which shows variations in velocity fields between the pre-development and post-development phases of the sunspot.

The same spot group again appeared on the eastern limb on February 3, and is designated in Kodaikanal records as KKL 12375 on its third passage. The observations of the spatial velocity and magnetic fields were made on February 9, 10, 11, 12, 14, 15 and 16. Sight-line velocity fields are given in Figure 1. On February 9, the umbra of this spot (KKL 12375) appeared split into two, surrounded by a common penumbra. This appearance of the spot remained till February 11, and around February 12 ( $L-L_0=0$ ) the two umbrae coalesced to form a single umbra. From the magnetic field plates and the shape of the spot, it was evident that the centre of the whole umbra was representative of the spot's centre.

JANUARY 13, 1963.  $(L-L_0) = 37^\circ\text{E}$

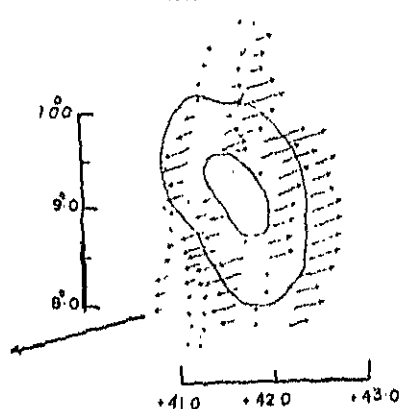
A153  $\lambda$  5576



(P)

JANUARY 19, 1963.  $(L-L_0) = 41.5^\circ\text{W}$

A173 & 172.  $\lambda$  4912



JANUARY 20, 1963.  $(L-L_0) = 56^\circ\text{W}$

A180  $\lambda$  5691

A181  $\lambda$  5576

A186  $\lambda$  4912

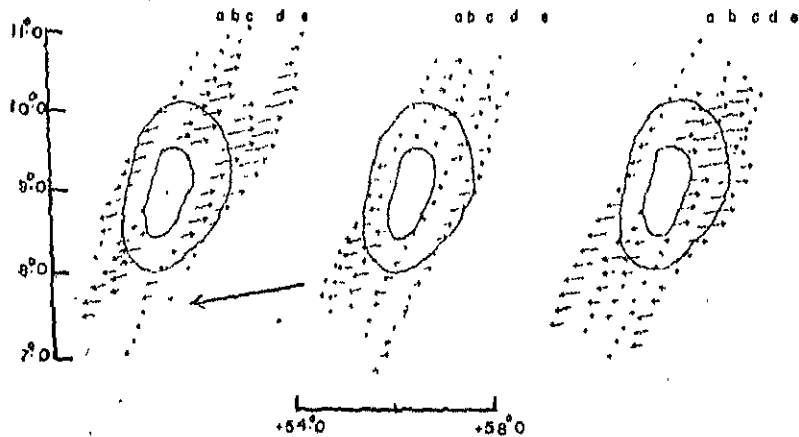


Figure 1 (a).—Sight line velocity field in Sunspots. Length of arrows are proportional to the magnitude of sight line velocity and the bold arrow indicates the approximate direction of the disc centre.

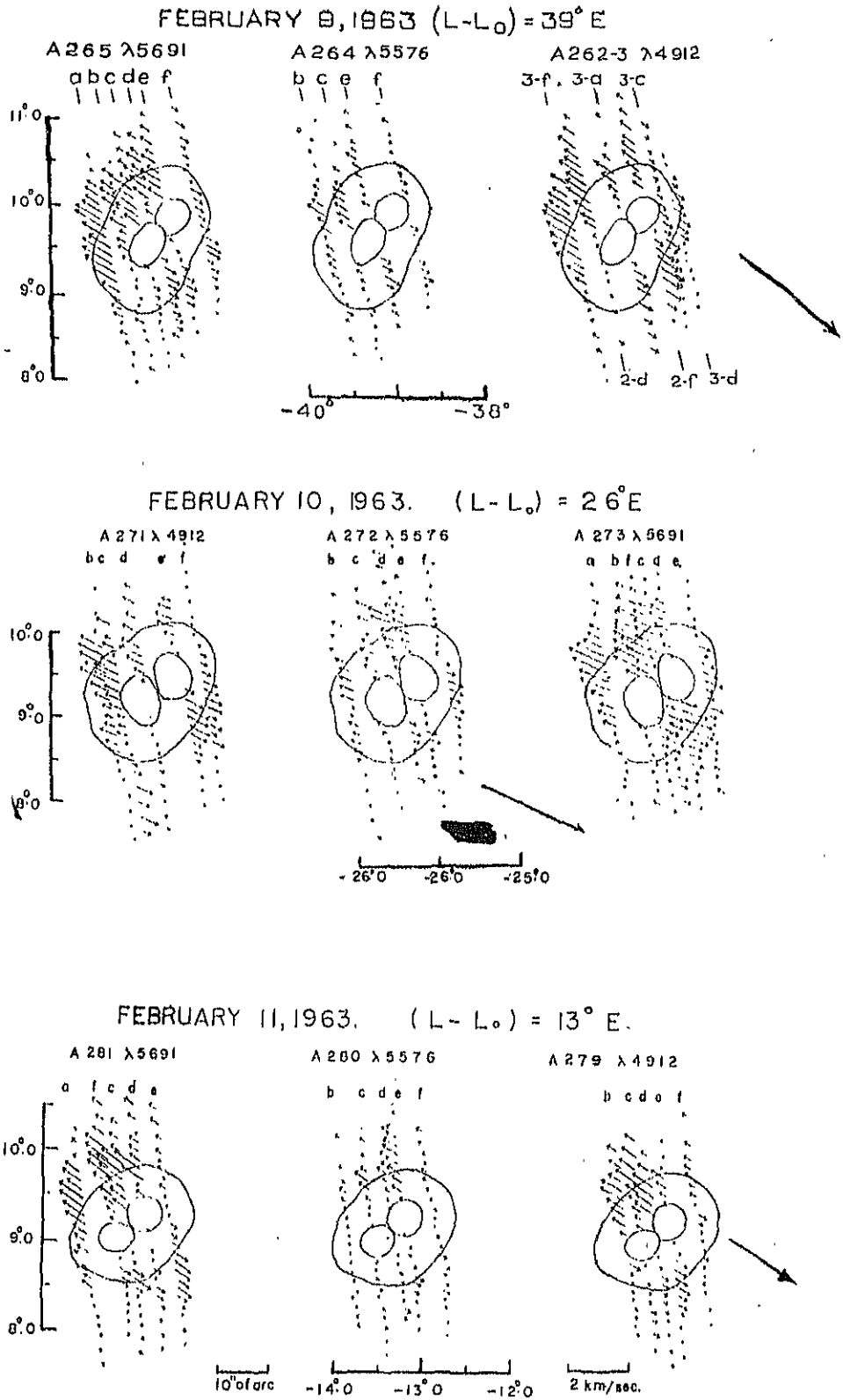


Figure 1 (b).—Sight line velocity field in Sunspots. Length of arrows are proportional to the magnitude of sight line velocity and the bold arrow indicates the approximate direction of the disc centre.

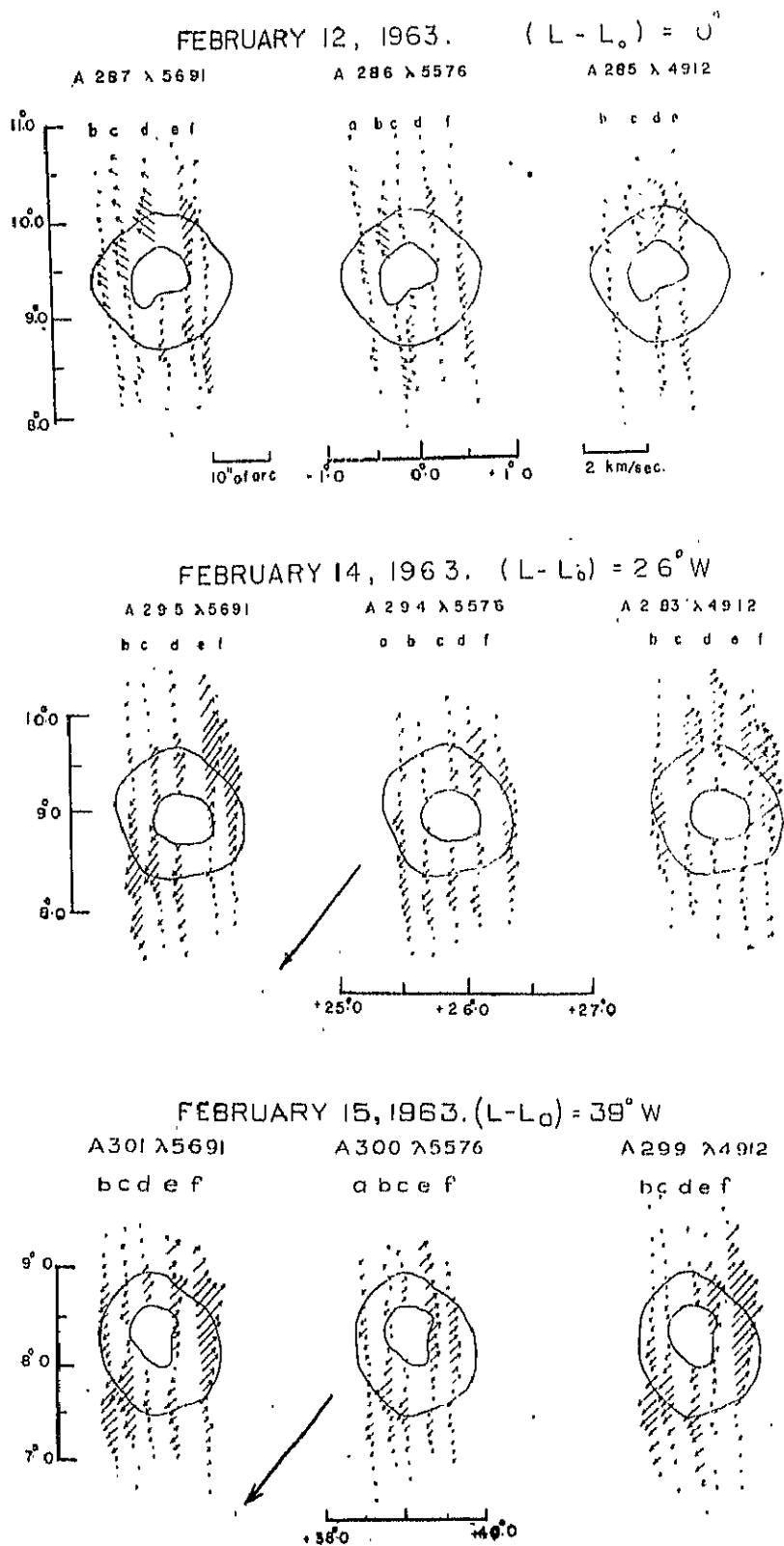
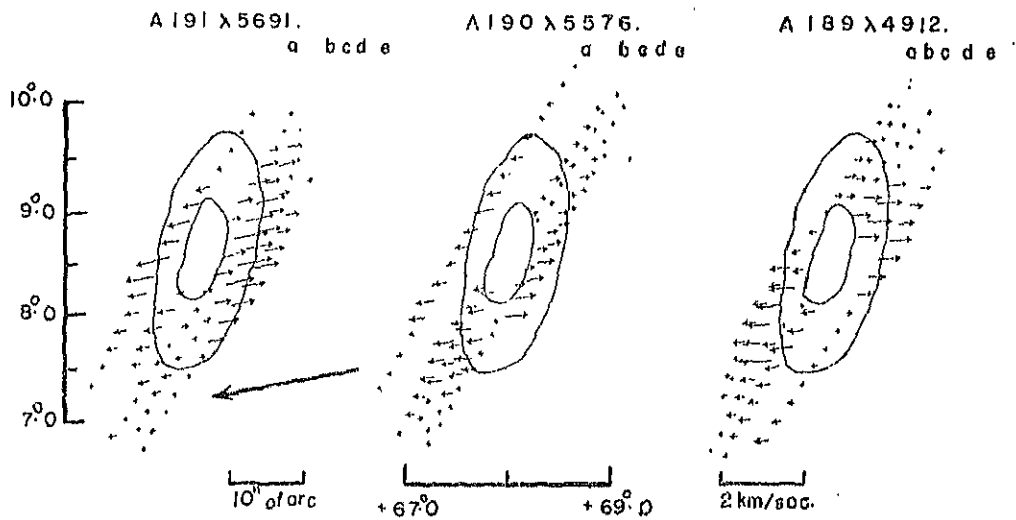


Figure 1 (c).—Sight line velocity field in Sunspots. Length of arrows are proportional to the magnitude of sight line velocity and the bold arrow indicates the approximate direction of the disc centre

JANUARY 21, 1963.  $(L-L_0) = 68^\circ W$



FEBRUARY 16, 1963.  $(L-L_0) = 52^\circ W$

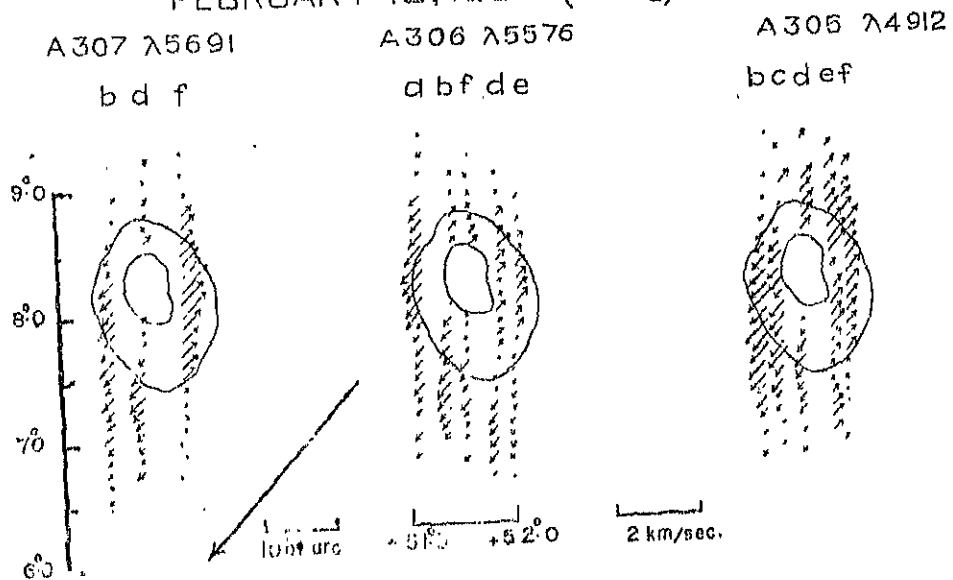
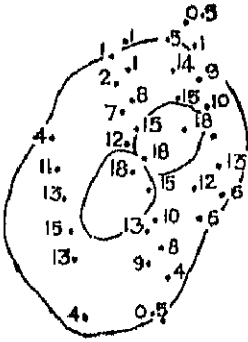


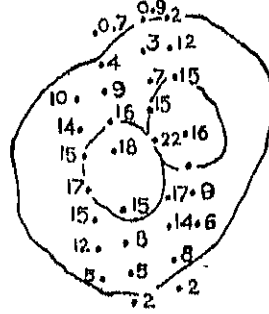
Figure 1 (d).—Sight line velocity field in Sunspots. Length of arrows are proportional to the magnitude of sight line velocity and the bold arrow indicates the approximate direction of the disc centre,

JAN. 19, A178 & 9.

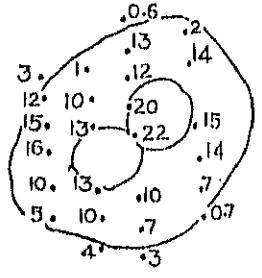
FEB. 9, A 269.



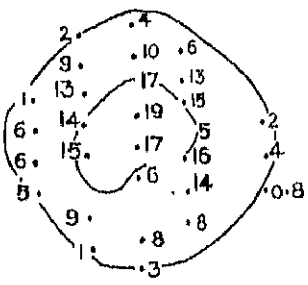
FEB. 10, A 270.



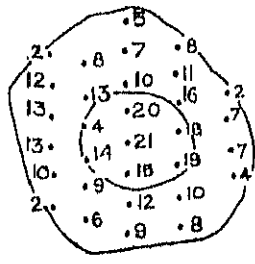
FEB. 11, A 283.



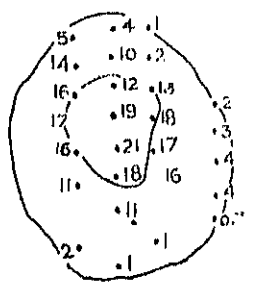
FEB. 12, A 284.



FEB. 14, A 286.



FEB. 15, A 298.



10.0

Figure 2.—Magnetic field in sunspots in units of 100 gauss.

The sunspot KKL 12375 disappeared beyond the western limb around February 19, and reappeared on March 3, on the eastern limb, with more or less the same shape that it had on the previous passage. Since March 5, until the spot vanished on the disc around March 14, 10 sub-flares of importance 1 to 1- were reported. From the flare data and the configuration of the sunspot group, it is definite that from January 19 through March 3, this spot was in a stable and well developed phase of its life.

The variation of the velocity field configuration during the two passages and at the same disc position is an indication of the change in the velocity with the age of the spot.

**Spatial magnetic field in sunspots:** The spatial distribution of magnetic field was determined for those spots for which velocity fields were obtained. The aim was to detect any inhomogeneity in the magnetic field greater than 100 gauss, that would affect the velocity field distribution.

The observations were made using a compound quarter wave plate and a polaroid mounted in front of the slit of the spectrograph. The Zeeman sensitive line, 6303 Å was used for these measurements. The polarity of the observed spot was tied in with the visual measures of the same spot obtained at the Mt. Wilson Observatory.\*

The spot's magnetic field, measured on seven days (January 19, February 9, 10, 11, 12, 14 and 15), shows a positive polarity indicating that the magnetic lines of force are directed outwards from the solar surface. The spatial magnetic field distribution for each day is given in Figure 2. The number against each point on these sunspot maps represents the magnetic field strength in units of hundred gauss.

---

\* I am thankful to Dr. R. Howard for kindly supplying the sunspot maps giving the magnetic field strength and polarity of some sunspots for comparison purposes.



**Determination of Component Velocities in sunspot penumbrae:** The sight-line velocity that we measure on a spot spectrum, is the velocity of the line-forming layers along the line of sight. For an understanding of the physical processes of motion in sunspots, it is essential to have a knowledge of the mode of flow of material in sunspots, independent of the line of sight.

In order to reduce the measured sight-line velocities to the component velocities (radial, tangential and vertical) in the spot, it is convenient to assume a polar coordinate system  $(r, \phi)$  with the centre of the umbra  $(B, L)$  as origin. The distance from the spot centre,  $r$ , and the position angle,  $\phi$  (measured from west through north) of any point (neglecting the curvature of the solar surface around the spot) are given by :

$$r = R_0 \left[ (\Delta \lambda \cos B)^2 + (\Delta B)^2 \right]^{\frac{1}{2}} \quad \text{and}$$

$$\tan \phi = \frac{\Delta B}{\Delta \lambda \cos B}$$

where  $R_0$  is the radius of the Sun, and  $\Delta B$  and  $\Delta \lambda$  are the differential heliographic coordinates of the point measured from the centre of the sunspot.

The three components of the sight-line velocity, which would completely define the velocity fields in a spot are the radial velocity  $u$ , component directed radially away from the spot centre, the tangential velocity  $v$ , directed normal to the radius vector of the spot and the vertical velocity  $w$ , directed perpendicular to the solar surface. It is convenient to use the cylindrical coordinate system to obtain the three component velocities in spots. The radial, tangential and vertical velocity components are given by

$$u = r, \quad v = r\phi \quad \text{and} \quad w = z$$

The corrected sight-line velocity is given by (Plaskett 1952)

$$V = u (\cos \phi \cos \gamma_1 + \sin \phi \cos \gamma_2) + V (\cos \phi \cos \gamma_2 - \sin \phi \cos \gamma_1) + w \cos \gamma_3 \quad \dots \dots \dots (1)$$

where  $\cos \gamma_1$ ,  $\cos \gamma_2$  and  $\cos \gamma_3$  are the direction cosines of the line of sight that depend on the position of the measured point and which are given by

$$\begin{aligned} \cos \gamma_1 &= \sin (L - L_0) \cos B_0 \sin (0 + \theta_1) \operatorname{cosec} \theta \\ \cos \gamma_2 &= [\sin B \cos B_0 \cos (L - L_0) - \cos B \sin B_0] \sin (0 + \theta_1) \operatorname{cosec} \theta \\ \cos \gamma_3 &= \cos (0 + \theta_1) \end{aligned}$$

For the spots observed, the value of  $\theta_1$  does not exceed  $0.1^\circ$  and is neglected. The heliocentric distance  $(L - L_0)$ , and the heliographic latitude  $B$  for any measured point on the solar disc were obtained from the sunspot maps.  $B_0$  and  $L_0$  are given for each day in the Nautical Almanac.

Equation (1) involves three unknown quantities  $u$ ,  $v$ , and  $w$ . To determine these unknowns, three equations of the type (1) are required. Following Kinman (1952, 1953), it was assumed that the motion has a cylindrical symmetry about the spot's centre and that all points equidistant from the centre of the spot, satisfy the equation of condition (1). The measured points around the spot were divided into annular zones of width 750 km to 1000 km, and for each annular zone we have the following equations,

$$\left. \begin{aligned} V_1 &= uX_1 + vY_1 + wZ_1 \\ V_2 &= uX_2 + vY_2 + wZ_2 \\ \vdots &\vdots \\ V_n &= uX_n + vY_n + wZ_n \end{aligned} \right\} \dots \dots \dots (2)$$

where

$$\begin{aligned} X &= (\cos \phi \cos \gamma_1 + \sin \phi \cos \gamma_2) \\ Y &= (\cos \phi \cos \gamma_2 - \sin \phi \cos \gamma_1) \\ Z &= \cos \gamma_3 = -\cos \theta \end{aligned}$$

In the polar coordinate system  $(r, \phi)$  with the spot centre as the origin, it is assumed that the spot surface is plane. In equation (1) the coefficient of  $w$ ,  $\cos \gamma_3$  ( $=\cos \theta$ ) is independent of  $\phi$  and is assumed constant over the spot surface. Following Servajean (1961), we have made  $\cos \gamma_3$  constant and the vertical velocity component  $w$  in the spot, is referred with respect to a distant point in the photosphere.

An IBM 1620 computer was used to obtain the component velocities  $u$ ,  $v$  and  $w$  from the solution of equations (2) for each annular zone. In the same programme instructions were coded to yield data required for the root square errors of  $u$ ,  $v$  and  $w$  velocities. The component velocities  $u$ ,  $v$  and  $w$ , were obtained for each of the three lines as measured on the spectra obtained on January 20 and 21 and February 9, 10, 11, 12, 14, 15 and 16.

**Determination of mean depths of formation of lines:** An absorption line in the solar spectrum is formed over a considerable thickness of the solar atmosphere. Individual strata contribute to the formation of a line, depending on the physical parameters of each layer. A knowledge of the model of the atmosphere, that is, the dependence of temperature, pressure and the continuous absorption coefficient on depth is essential for determining the mean depth of formation of a line. With the availability of a sunspot penumbra model given by Makita (1963), it was possible to determine the mean depth of formation of lines in the penumbral region.

The residual intensity of a point on the line profile is defined by

$$r_\lambda = \frac{I_{\lambda_0}(0, \mu) - I_{\Delta\lambda}(0, \mu)}{I_{\lambda_0}(0, \mu)} \quad \dots \dots \dots (3)$$

Writing in the form indicated by Pecker (1951) and making use of the weighting function,  $\eta_\lambda$  is given by the equation

$$r_\lambda = \int_0^\infty G \Psi \left( \frac{k_{\Delta\lambda}}{k_{\lambda_0}} \right) \frac{d\tau}{\mu} \quad \dots \dots \dots (4)$$

where the weighting function  $G$ , is given by

$$G = \frac{\int_0^\infty B(\tau) \left[ \exp - \left( \frac{\tau}{\mu} \right) \right] \frac{d\tau}{\mu} - B(\tau) \left[ \exp - \left( \frac{\tau}{\mu} \right) \right]}{\int_0^\infty B(\tau) \left[ \exp - \left( \frac{\tau}{\mu} \right) \right] \frac{d\tau}{\mu}} \quad \dots \dots \dots (5)$$

and  $\Psi$ , the saturation function

$$\Psi = \exp \left\{ - \int_0^\tau \left( \frac{k_{\Delta\lambda}}{k_{\lambda_0}} \right) \frac{d\tau}{\mu} \right\} \quad \dots \dots \dots (6)$$

where  $B(\tau)$  = Planck function,

$\mu = \cos \theta$ ,  $\theta$  being the angle between the solar radius at the point of observation on the disc and the line of sight,

$k\lambda_0$  = continuous absorption coefficient per hydrogen atom,

$k\Delta\lambda$  = selective absorption coefficient per hydrogen atom.

In equation (5) the source function is made equal to the Planck function at an optical depth  $\tau$ . The source function is given by the expression,

$$B(\tau) = a + b\tau + c E_2(\tau) \dots\dots\dots (7)$$

where  $E_2(\tau)$  is the exponential integral, and  $a$ ,  $b$ , and  $c$  are the limb darkening constants.

Integrating (7) and using the property of exponential integrals and substituting in (5), it can easily be shown that

$$G = \frac{\mu \exp \left[ -\frac{\tau}{\mu} \left\{ b + c \left[ E_1\left(\frac{\tau}{\mu} + \tau\right) - E_1(\tau) \right] \right\} \right]}{a + b\mu + c \left[ 1 - \mu \ln \left( 1 + \frac{1}{\mu} \right) \right]} \dots\dots\dots (8)$$

To determine the weighting function  $G$ , at five disc positions, use of the solar limb darkening observations at 5000 Å, of Pierce and Waddell (1961) was made.

Following ten Bruggencate *et al.* (1955), integration of equation (4) was carried over the  $\log \tau$  scale and equation (4) takes the form

$$r_{\lambda} = \int_{-\infty}^{\infty} \frac{G}{\mu} \left( \frac{k\Delta\lambda}{k\lambda_0} \right) \tau \cdot \frac{\Psi}{M_{od}} d(\log \tau) \dots\dots\dots (9)$$

where

$$\Psi = \exp \left[ -\int_{-\infty}^{\infty} \left( \frac{k\Delta\lambda}{k\lambda_0} \right) \cdot \frac{\tau}{\mu} \frac{1}{M_{od}} d(\log \tau) \right] \dots\dots\dots (10)$$

The selective absorption coefficient  $k\Delta\lambda$  per hydrogen atom is given by

$$k\Delta\lambda = \frac{\sqrt{\pi} e^2 \lambda_0^2}{mc^2} A. f. \frac{N_{la}}{N_a} \frac{1}{\Delta\lambda_D} \exp \left[ -\left( \frac{\Delta\lambda}{\Delta\lambda_D} \right) \right] \dots\dots\dots (11)$$

Assumption is made that the velocity measures refer only to the core of the line, where  $\Delta\lambda=0$ ,  $A$  is the number of atoms of the element per hydrogen atom,  $f$  is the oscillator strength,  $N$  is the number of atoms of the element in the energy level corresponding to the transition responsible for the line,  $N_a$  is the total number of atoms of that element, and  $\Delta\lambda_D$  is the Doppler width, given by

$$\Delta\lambda_D = \frac{\lambda}{c} \sqrt{\frac{2RT}{M} + \xi^2 t_n} \dots\dots\dots (12)$$

$\sqrt{\frac{2RT}{M}}$  gives the thermal velocity and  $\xi t_n$ , the turbulent velocity, was neglected because of its unknown contribution in the calculation of the Doppler width of lines.

The quantity  $\frac{(N_{la})}{(N_a)}$  in equation (11) was directly obtained from the combined Saha and Boltzmann equations, for each of the temperature and electron pressure values in the penumbra model.

The continuous absorption coefficient  $k_{\lambda_0}$  is given by

$$k_{\lambda_0} = \frac{N_{OH}}{N_H} \left( k_{\lambda_0} + k_{\lambda_0} p_e \right) \dots \dots \dots (13)$$

Contribution to the continuous absorption due to neutral hydrogen was neglected and only the contribution due to the negative hydrogen ion was considered.

The saturation function  $\Psi$ , was obtained by numerical integration of equation (10). The contribution curve is given by

$$\gamma = G \left[ \frac{K}{\mu} \cdot \frac{\tau}{\Delta \lambda_D} \cdot \frac{N_{ia}}{N_a} \cdot \frac{I}{k_{\lambda_0}} \right] \Psi$$

where

$$k = \frac{\sqrt{\pi} e^2 \lambda_0^2}{mc^3} A. f. \dots \dots \dots (14)$$

The abundance  $A$ , was obtained from Goldberg *et al.* (1961) and the oscillator strength  $f$ , of the lines from Wright's (1944) curve of growth.

Figure 3 shows the contribution curves for the line centre, for each of the two lines (4912 and 5691) at five disc positions. The bisector of the area under each contribution curve gave the mean optical depth of formation of the line and thus determined the mean geometrical depths of formation of each of the two lines. The mean depth of formation of 5576.101 Å Fe I, of Rowland intensity 4, in the sunspot penumbra seems to lie much higher than the other two lines, used in this study. The Makita penumbra model at our disposal does not permit us to obtain a complete contribution curve for this line.

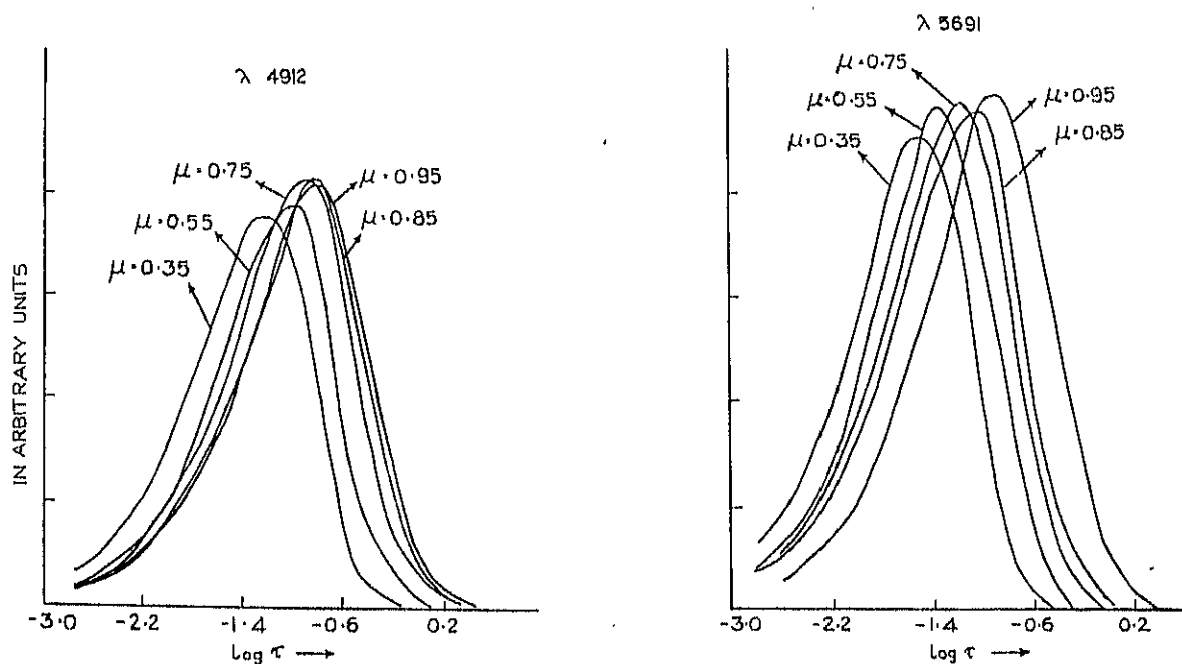


Figure 3.—Contribution curves for 4912 and 5691 in sunspot penumbra.

In Table 3 is given the mean depth of formation of lines 4912.027 Ni I Rowland intensity 1 and 5691.508 Fe I Rowland intensity 2 in the penumbral region.

TABLE 3

*Mean optical and geometrical depth of formation of 4912 and 5691 and the gradient of  $U_{\max}$  with depth at nine disc positions of the spot*

Date	$\mu$	Depth of formation of				Gradient of $U_{\max}$ in km/sec/km.
		4912 Ni I		5691 Fe I		
		log $t$	$\bar{z}$ km	log $t$	$\bar{z}$ km	
20 Jan.	0.55	-1.21	180	-1.42	145	$9.1 \times 10^{-3}$
21 Jan.	0.35	-1.36	155	-1.62	117	$4.5 \times 10^{-3}$
9 Feb.	0.75	-1.04	215	-1.29	166	$1.6 \times 10^{-3}$
10 Feb.	0.85	-0.98	230	-1.24	175	$0.3 \times 10^{-3}$
11 Feb.	0.95	-0.96	235	-1.18	188	$1.3 \times 10^{-3}$
12 Feb.	0.95	-0.96	235	-1.18	188	$6.2 \times 10^{-3}$
14 Feb.	0.85	-0.98	230	-1.24	175	$7.2 \times 10^{-3}$
15 Feb.	0.75	-1.04	215	-1.29	166	$3.8 \times 10^{-3}$
16 Feb.	0.55	-1.21	180	-1.42	145	$2.3 \times 10^{-3}$

**Discussion of the component velocities:** (a) *The radial velocity field*; The radial velocity component  $u$ , has the largest contribution to the mass motion in sunspot. The component velocity  $u$ , was determined using the three Zeeman insensitive lines, at two disc positions during the first passage and at seven disc positions during its second passage across the disc. Figure 4 gives the run of the component velocities  $u$ , and  $w$  and their r.m.s. errors obtained from each of the 3 lines and at 3 disc positions of the spot. At the top of each figure, the extent of the umbra and penumbra are represented by the dark and hatched regions respectively. Table 4 gives the magnitudes of radial, tangential and vertical velocities and their r.m.s. errors.

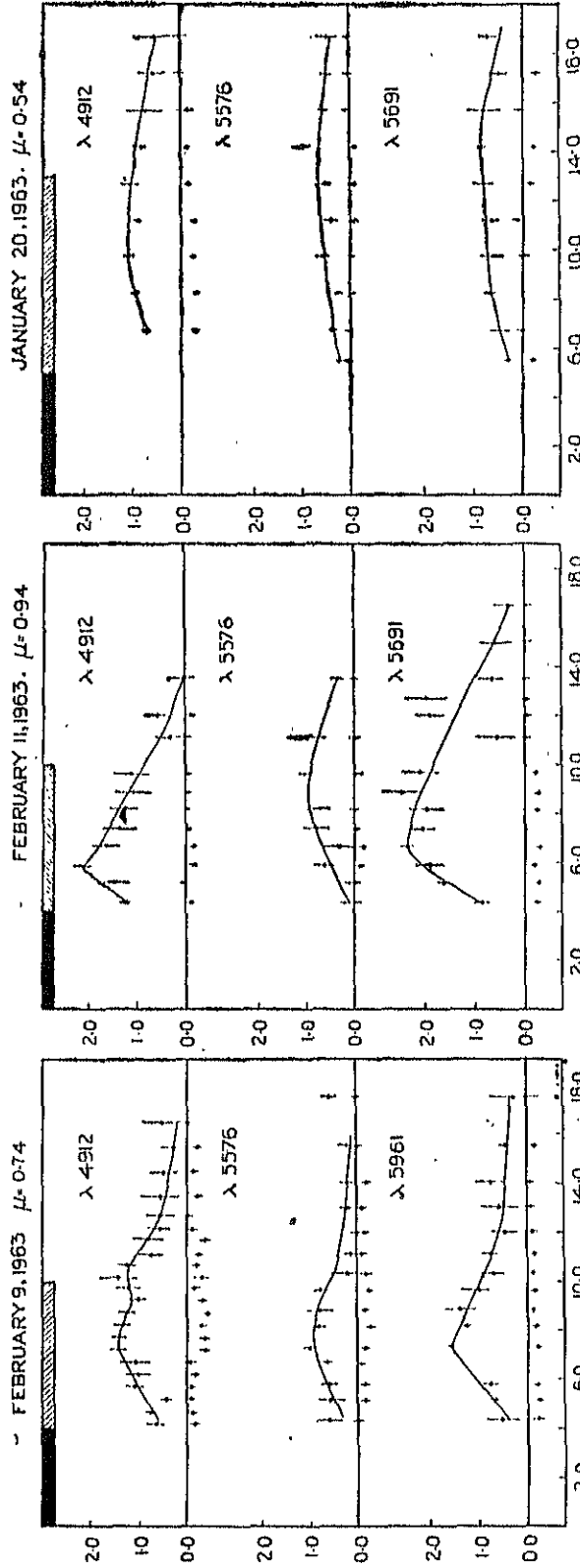


Figure 4—Run of radial and vertical velocities measured in three lines on three disc positions of the sunspot.  
 Ordinate — in units of km/sec.  
 Abscissa — in units of 1000 km.

TABLE 4

*Component velocities in km/sec. in Sunspot No. KKL 12375 on February 9,  
1963 at  $\mu = 0.74$*

Spectral line used		Distance from the centre of the spot in $10^3$ km.										
		4.25	4.75	5.25	5.75	6.25	6.75	7.25	7.75	8.25	8.75	9.25
4912 (A263)	u	+0.57	+0.82	+0.44	+1.14	+1.06	+1.13	+1.48	+1.46	+1.32	+1.24	+1.02
	r.m.s.	0.21	0.02	0.13	0.20	0.28	0.31	0.21	0.18	0.18	0.17	0.20
	v	+0.35	+0.07	-0.41	-0.06	+0.31	+0.56	-0.07	-0.31	-0.13	-0.60	-0.27
	r.m.s.	0.24	0.03	0.15	0.28	0.21	0.31	0.23	0.16	0.24	0.19	0.17
	W—W <sub>0</sub>	-0.15	-0.07	-0.07	-0.06	-0.17	+0.01	-0.36	-0.33	-0.26	-0.40	-0.32
	r.m.s.	0.09	0.01	0.02	0.12	0.12	0.15	0.11	0.08	0.10	0.08	0.09
Spectral line used		Distance from the Centre of the spot in $10^3$ km.										
		9.75	10.2	10.7	11.2	11.7	12.2	12.7	13.5	14.5	15.5	16.5
4912 (A263)	u	+1.37	+1.47	+1.30	+0.76	+0.18	+0.61	+0.60	+0.68	+0.51	+0.29	+0.64
	r.m.s.	0.28	0.42	0.21	0.20	0.32	0.25	0.33	0.43	0.22	0.30	0.40
	v	-0.36	-0.38	-0.34	+0.09	+0.05	-0.12	+0.18	-0.11	-0.09	+0.24	-0.11
	r.m.s.	0.26	0.35	0.15	0.20	0.20	0.17	0.30	0.28	0.16	0.27	0.29
	W—W <sub>0</sub>	-0.12	-0.25	-0.15	-0.20	-0.34	-0.16	-0.02	-0.14	-0.11	-0.22	-0.00
	r.m.s.	0.13	0.18	0.06	0.13	0.13	0.08	0.08	0.14	0.06	0.11	0.10

TABLE 4—(Contd.)

Component velocities in km/sec. in Sunspot No. KKL 12375 on February 9, 1963  
at  $\mu = 0.74$

Spectral line used				Distance from the centre of the spot in $10^3$ kms.								
				4.37	5.13	5.87	6.62	7.37	8.13	8.87		
5576 (A264)	u	.	.	+	0.67	+0.54	+0.58	+0.67	+1.02	+0.88	+0.77	
	r.m.s.	.	.	.	0.26	0.30	0.21	0.07	0.12	0.17	0.28	
	v	.	.	+	0.08	+0.12	+0.27	-0.02	-0.21	-0.38	-0.12	
	r.m.s.	.	.	.	0.23	0.18	0.22	0.07	0.10	0.16	0.16	
	W-W <sub>0</sub>	.	.	.	0.00	-0.16	-0.16	-0.06	-0.12	-0.24	-0.13	
	r.m.s.	.	.	.	0.10	0.11	0.10	0.03	0.05	0.07	0.09	
5691 (A265)	u	.	.	+	0.53	+0.69	+0.76	..	+1.57	+1.24	+1.37	
	r.m.s.	.	.	.	0.40	0.04	0.13	..	0.01	0.02	0.35	
	v	.	.	+	0.16	+0.37	+0.36	..	-0.06	-0.33	-0.25	
	r.m.s.	.	.	.	0.24	0.05	0.13	..	0.06	0.00	0.08	
	W-W <sub>0</sub>	.	.	.	-0.22	-0.25	-0.20	..	-0.21	-0.14	-0.10	
	r.m.s.	.	.	.	0.13	0.02	0.06	..	0.00	0.00	0.04	
Spectral line used				Distance from the centre of the spot in $10^3$ km.								
				9.62	10.3	11.1	12.0	13.0	14.0	15.5	17.5	
5576 (A264)	u	.	.	+	0.78	+0.24	+0.18	+0.07	+0.27	+0.25	+0.26	+0.60
	r.m.s.	.	.	.	0.14	0.35	0.14	0.18	0.20	0.21	0.20	0.20
	v	.	.	-	0.15	+0.29	+0.37	+0.11	+0.38	-0.11	+0.19	-0.03
	r.m.s.	.	.	.	0.13	0.33	0.11	0.10	0.40	0.17	0.23	0.09
	W-W <sub>0</sub>	.	.	-	0.23	-0.14	-0.08	-0.15	-0.09	-0.21	0.00	0.00
	r.m.s.	.	.	.	0.05	0.12	0.04	0.04	0.11	0.06	0.08	0.02
5691 (A265)	u	.	.	+	1.00	+0.71	+0.78	+0.49	+0.62	+0.78	+0.47	+0.30
	r.m.s.	.	.	.	0.43	0.23	0.15	0.30	0.42	0.30	0.17	0.53
	v	.	.	+	0.04	-0.02	0.00	-0.33	-0.19	-0.38	-0.02	-0.32
	r.m.s.	.	.	.	0.25	0.18	0.13	0.19	0.18	0.20	0.11	0.19
	W-W <sub>0</sub>	.	.	-	0.14	-0.04	-0.12	-0.11	-0.03	+0.06	-0.15	0.00
	r.m.s.	.	.	.	0.14	0.09	0.05	0.10	0.11	0.09	0.04	0.06



TABLE 4—(Contd.)

Component velocities in km/sec. in Sunspot No. KKL 12375 on February 10, 1963 at  
 $\mu = 0.86$

Spectral line used	Distance from the centre of the spot in 10 <sup>3</sup> km.						
	4.37	5.13	5.87	6.21	7.37	8.13	8.87
4912 (A271)	u						
	r.m.s.	+1.83 0.34	+1.54 0.35	+1.73 0.10	+1.64 0.10	+1.47 0.04	+1.20 0.17
	v						
	r.m.s.	+0.23 0.36	+0.15 0.36	+0.07 0.10	+0.16 0.11	+0.26 0.04	+0.36 0.20
	W—W <sub>0</sub>						
	r.m.s.	+0.29 0.12	+0.06 0.12	+0.01 0.03	+0.09 0.03	+0.07 0.01	+0.12 0.07
5576 (A272)	u						
	r.m.s.	+0.63 0.13	+0.73 0.14	+1.22 0.30	+1.03 0.14	+0.91 0.07	+1.02 0.12
	v						
	r.m.s.	+0.18 0.13	+0.05 0.02	+0.29 0.22	+0.25 0.13	+0.23 0.08	+0.12 0.14
	W—W <sub>0</sub>						
	r.m.s.	+0.02 0.05	+0.18 0.06	+0.06 0.09	+0.05 0.05	+0.08 0.02	+0.09 0.05
5691 (A273)	u						
	r.m.s.	+1.56 0.41	..	..	+1.55 0.25	+1.83 0.31	+1.43 0.24
	v						
	r.m.s.	+0.09 0.29	..	..	+0.18 0.28	+0.19 0.25	+0.09 0.22
	W—W <sub>0</sub>						
	r.m.s.	+0.20 0.12	..	..	+0.06 0.10	+0.05 0.09	+0.10 0.09

Spectral line used	Distance from the centre of the spot in 10 <sup>3</sup> km.							
	9.62	10.30	11.10	12.00	12.60	13.50	15.00	16.50
4912 (A271)	u							
	r.m.s.	+1.36 0.22	+0.93 0.44	+1.38 0.23	+0.75 0.56	+0.74 0.44	+0.74 0.31	+0.11 0.52
	v							
	r.m.s.	+0.28 0.24	+0.04 0.28	+0.15 0.40	+0.40 0.31	+0.24 0.37	+0.33 0.25	+0.31 0.37
	W—W <sub>0</sub>							
	r.m.s.	+0.09 0.09	+0.07 0.11	+0.15 0.12	+0.09 0.16	+0.10 0.13	+0.04 0.07	0.00 0.11
5576 (A272)	u							
	r.m.s.	+0.80 0.28	+0.89 0.08	+0.87 0.77	+0.90 0.11	+0.46 0.37	+0.69 0.35	+0.31 0.25
	v							
	r.m.s.	+0.01 0.23	+0.20 0.07	+0.03 0.50	+0.28 0.08	+0.01 0.28	+0.14 0.28	+0.20 0.30
	W—W <sub>0</sub>							
	r.m.s.	+0.18 0.09	+0.19 0.02	+0.28 0.17	+0.10 0.03	+0.19 0.06	+0.16 0.09	0.00 0.06
5691 (A273)	u							
	r.m.s.	+1.43 0.35	+1.35 0.25	+0.92 0.30	+0.55 0.30	+0.70 0.24	..	+0.07 0.38
	v							
	r.m.s.	+0.21 0.33	+0.22 0.20	+0.23 0.25	+0.12 0.24	+0.31 0.23	..	+0.01 0.29
	W—W <sub>0</sub>							
	r.m.s.	+0.21 0.12	+0.03 0.07	+0.12 0.07	+0.17 0.06	+0.01 0.06	..	+0.10 0.08

TABLE 4—(Contd.)

Component velocities in km/sec in Sunspot No. KKL 12375 on February 11, 1963  
at  $\mu = 0.94$

Spectral line used		Distance from the centre of the spot in $10^3$ km.						
		4.37	5.13	5.87	6.62	7.37	8.13	8.87
4912 (A279)	u	+1.25	+1.71	+2.15	+1.82	+1.38	+1.25	+1.09
	r.m.s.	0.11	0.34	0.15	0.30	0.36	0.30	0.39
	v	-0.29	+1.11	-1.09	-0.19	-0.07	+0.08	+0.14
	r.m.s.	0.14	0.54	0.23	0.44	0.34	0.34	0.46
	W—W <sub>0</sub>	-0.10	+0.07	-0.12	-0.16	+0.02	-0.01	-0.04
	r.m.s.	0.03	0.09	0.03	0.07	0.09	0.09	0.10
5576 (A280)	u	+0.18	+0.09	+0.63	+0.33	+0.81	+0.76	..
	r.m.s.	0.12	0.10	0.25	0.40	0.26	0.32	..
	v	+0.28	+0.26	+0.40	+0.28	+0.31	+0.40	..
	r.m.s.	0.14	0.10	0.33	0.36	0.30	0.37	..
	W—W <sub>0</sub>	-0.05	-0.04	-0.08	-0.18	-0.02	-0.01	..
	r.m.s.	0.03	0.02	0.07	0.09	0.07	0.08	..
5691 (A281)	u	+0.84	+1.69	+1.96	+2.42	+2.14	+2.01	+2.56
	r.m.s.	0.15	0.13	0.35	0.18	0.27	0.38	0.45
	v	+0.28	-0.31	-0.37	-0.27	+0.83	-0.27	-1.33
	r.m.s.	0.19	0.13	0.43	0.18	0.45	0.38	0.54
	W—W <sub>0</sub>	-0.25	-0.27	-0.17	-0.30	-0.01	-0.25	-0.26
	r.m.s.	0.03	0.03	0.08	0.04	0.09	0.08	0.10
Spectral line used		Distance from the centre of the spot in $10^3$ km.						
		9.62	11.10	12.00	12.60	13.50	15.00	17.50
4912 (A279)	u	+1.17	+0.31	+0.57	..	+0.07	..	..
	r.m.s.	0.35	0.32	0.30	..	0.30	..	..
	v	+0.06	+0.38	+0.24	..	+0.26	..	..
	r.m.s.	0.40	0.48	0.40	..	0.14	..	..
	W—W <sub>0</sub>	-0.05	+0.02	-0.10	..	0.00	..	..
	r.m.s.	0.07	0.07	0.07	..	0.03	..	..
5576 (A280)	u	+1.11	+1.00	..	..	+0.35	..	..
	r.m.s.	0.15	0.47	..	..	0.15	..	..
	v	-0.97	-0.11	..	..	+0.30	..	..
	r.m.s.	0.27	0.64	..	..	0.20	..	..
	W—W <sub>0</sub>	-0.04	-0.01	..	..	0.00	..	..
	r.m.s.	0.12	0.11	..	..	0.03	..	..
5691 (A281)	u	+2.15	+0.56	+1.98	+2.00	+0.68	+0.60	+0.30
	r.m.s.	0.39	0.41	0.30	0.47	0.26	0.36	0.32
	v	-0.78	0.00	-1.49	-1.95	-0.16	+0.28	-0.45
	r.m.s.	0.54	0.45	0.43	0.66	0.34	0.42	0.83
	W—W <sub>0</sub>	-0.21	-0.01	-0.05	-0.04	0.00	0.00	-0.04
	r.m.s.	0.09	0.07	0.05	0.07	0.04	0.04	0.08

TABLE 4—(Contd.)

Component velocities in km/sec in Sunspot No. KKL 12375 on February 12, 1963  
at  $\mu = 0.95$

Spectral line used	Distance from the centre of the spot in $10^3$ km.						
	4.37	5.12	5.87	6.62	7.37	8.13	
4912 (A285)	u	+0.89	+1.13	+1.67	+1.27	+1.69	+1.53
	r.m.s.	0.06	0.21	0.39	0.55	0.54	0.48
	v	-0.59	-0.81	-1.33	-0.18	+0.02	-0.04
	r.m.s.	0.13	0.25	0.49	0.09	0.92	0.21
	W-W <sub>0</sub>	-0.16	-0.02	-0.16	-0.16	-0.11	-0.13
	r.m.s.	0.01	0.04	0.08	0.19	0.13	0.10
5576 (A286)	u	+0.33	+0.93	+0.82	+0.97	+0.48	+0.88
	r.m.s.	0.13	0.41	0.22	0.24	0.24	0.21
	v	-0.64	-0.28	-0.11	-0.39	-1.06	-0.87
	r.m.s.	0.18	0.80	0.20	0.27	0.21	0.33
	W-W <sub>0</sub>	-0.03	-0.11	-0.12	-0.10	+0.04	-0.10
	r.m.s.	0.02	0.15	0.04	0.05	0.05	0.05
5691 (A287)	u	+1.10	+1.09	..	+1.26	+1.53	+0.30
	r.m.s.	0.27	0.27	..	0.44	0.36	0.10
	v	-1.06	+1.77	..	-0.50	-1.06	-0.86
	r.m.s.	0.19	0.22	..	0.37	0.46	0.11
	W-W <sub>0</sub>	-0.22	-0.34	..	-0.20	-0.21	+0.07
	r.m.s.	0.45	0.21	..	0.08	0.07	0.02

Spectral line used	Distance from the centre of the spot in $10^3$ km.							
	8.85	9.62	10.50	11.50	13.00	15.00	16.00	
4912 (A285)	u	+1.82	+1.19	+0.59	+0.96	..	+0.30	..
	r.m.s.	0.05	0.43	0.65	0.20	..	0.34	..
	v	-0.87	-0.89	-1.57	-1.89	..	+0.03	..
	r.m.s.	0.17	0.80	0.24	0.76	..	0.65	..
	W-W <sub>0</sub>	-0.30	0.00	0.00	-0.11	..	0.00	..
	r.m.s.	0.16	0.11	0.16	0.10	..	0.08	..
5576 (A286)	u	+0.49	+0.88	+0.35	+0.71	+0.63	+0.39	..
	r.m.s.	0.28	0.39	0.43	0.43	0.25	0.24	..
	v	+0.91	-0.37	+0.39	-0.36	+0.61	-0.33	..
	r.m.s.	0.49	0.56	0.80	0.57	0.53	0.72	..
	W-W <sub>0</sub>	-0.14	+0.12	+0.11	-0.09	+0.11	0.00	..
	r.m.s.	0.08	0.07	0.11	0.09	0.07	0.06	..
5691 (A287)	u	+1.14	+1.05	+0.93	+0.81	+0.53	+0.47	+0.26
	r.m.s.	0.38	0.22	0.19	0.39	0.33	0.15	0.16
	v	-0.79	-0.22	-1.43	-0.47	-0.64	-0.55	-0.57
	r.m.s.	0.53	0.33	0.30	0.25	0.92	0.45	0.62
	W-W <sub>0</sub>	+0.01	0.00	-0.05	-0.10	-0.07	+0.04	0.00
	r.m.s.	0.08	0.05	0.04	0.17	0.08	0.03	0.03

TABLE 4—(Contd.)

Component velocities in km/sec in Sunspot No. KKL 12375 on February 14, 1963  
at  $\mu = 0.86$

Spectral line used		Distance from the centre of the spot in $10^3$ km.						
		4.37	5.12	5.87	6.62	7.37	8.13	8.87
4912 (A293)	u	+0.81	+0.99	+1.47	+1.32	+1.13	..	+0.77
	r.m.s.	0.36	0.36	0.27	0.41	0.23	..	0.52
	v	-0.14	0.00	-0.07	-0.16	0.00	..	-0.06
	r.m.s.	0.30	0.35	0.26	0.29	0.25	..	0.35
	W-W <sub>0</sub>	-0.02	-0.13	+0.02	-0.01	+0.01	..	+0.03
	r.m.s.	0.12	0.11	0.10	0.11	0.06	..	0.11
5576 (A294)	u	+0.73	+0.89	+0.79	+0.91	+0.91	+0.65	+0.62
	r.m.s.	0.11	0.09	0.13	0.27	0.40	0.36	0.28
	v	-0.03	+0.15	+0.31	-0.03	-0.11	+0.09	+0.30
	r.m.s.	0.10	0.11	0.11	0.25	0.37	0.19	0.56
	W-W <sub>0</sub>	-0.37	-0.36	-0.34	-0.38	-0.39	-0.29	-0.36
	r.m.s.	0.03	0.03	0.04	0.09	0.13	0.07	0.21
5691 (A295)	u	+1.19	+1.52	+1.56	+1.78	+1.89	+1.58	+1.21
	r.m.s.	0.08	0.12	0.11	0.20	0.24	0.48	0.75
	v	-0.30	-0.30	-0.15	-0.27	-0.19	+0.11	-0.28
	r.m.s.	0.09	0.12	0.09	0.17	0.16	0.24	0.47
	W-W <sub>0</sub>	-0.16	-0.15	-0.10	-0.14	-0.09	+0.07	-0.14
	r.m.s.	0.03	0.04	0.03	0.06	0.06	0.09	0.15
Spectral line used		Distance from the centre of the spot in $10^3$ km.						
		9.62	10.50	11.50	12.50	13.50	15.00	17.00
4912 (S293)	u	+1.06	+1.15	..	+1.25	..	+0.95	..
	r.m.s.	0.45	0.61	..	0.67	..	0.34	..
	v	+0.40	+0.63	..	0.00	..	+0.01	..
	r.m.s.	0.31	0.34	..	0.45	..	0.68	..
	W-W <sub>0</sub>	+0.10	0.00	..	+0.06	..	0.00	..
	r.m.s.	0.10	0.28	..	0.13	..	0.16	..
5576 (A294)	u	+0.69	+1.27	+0.49	+0.86	+0.24	+0.19	..
	r.m.s.	0.29	0.54	0.45	0.30	0.39	0.20	..
	v	-0.41	+0.23	0.00	+0.41	-0.16	+0.40	..
	r.m.s.	0.19	0.26	0.34	0.40	0.22	0.12	..
	W-W <sub>0</sub>	-0.24	-0.22	-0.18	-0.08	-0.20	0.00	..
	r.m.s.	0.05	0.08	0.11	0.08	0.06	0.03	..
5691 (A295)	u	+1.18	+2.39	+1.93	+1.85	+1.41	..	+0.34
	r.m.s.	0.35	0.52	0.70	0.54	0.71	..	0.57
	v	+0.20	+0.66	+0.27	+0.56	+0.37	..	+0.05
	r.m.s.	0.14	0.27	0.42	0.30	0.40	..	0.32
	W-W <sub>0</sub>	+0.04	-0.14	-0.07	0.00	0.00	..	0.00
	r.m.s.	0.06	0.08	0.11	0.07	0.08	..	0.06

TABLE 4—(Contd.)

Component velocities in km/sec in Sunspot No. KKL 2375 on February 15, 1963  
at  $\mu = 0.75$

Spectral line used		Distance from the centre of the spot in $10^3$ km.						
		4.37	5.12	5.87	6.62	7.37	8.13	8.87
4912 ( $\lambda 299$ )	u	+0.80	+1.00	+0.61	+1.42	+1.27	+1.74	+0.94
	r.m.s.	0.20	0.28	0.32	0.19	0.30	0.20	0.33
	v	-0.40	-0.17	-0.22	0.02	-0.11	-0.21	-0.55
	r.m.s.	0.02	0.19	0.26	0.22	0.22	0.03	0.21
	W—W <sub>0</sub>	-0.26	-0.16	-0.19	-0.39	-0.30	-0.06	-0.01
	r.m.s.	0.09	0.10	0.16	0.10	0.11	0.01	0.10
5576 ( $\lambda 300$ )	u	+0.90	+1.05	+0.77	+0.47	+0.65	+0.55	+0.27
	r.m.s.	0.16	0.12	0.20	0.12	0.30	0.23	0.18
	v	+0.23	+0.33	-0.31	+0.17	+0.14	-0.11	+0.19
	r.m.s.	0.07	0.07	0.30	0.13	0.32	0.16	0.07
	W—W <sub>0</sub>	-0.06	0.00	0.00	-0.08	+0.01	+0.02	+0.10
	r.m.s.	0.05	0.01	0.12	0.06	0.16	0.08	0.04
5691 ( $\lambda 301$ )	u	+1.03	+1.81	+1.55	+1.28	+0.90	+0.92	+1.11
	r.m.s.	0.33	0.63	0.88	0.17	0.42	0.14	0.02
	v	-0.24	+0.31	+0.09	-0.13	-0.14	+0.24	-0.04
	r.m.s.	0.21	0.42	0.54	0.25	0.38	0.14	0.24
	W—W <sub>0</sub>	-0.10	+0.12	-0.09	+0.22	-0.02	+0.18	-0.09
	r.m.s.	0.11	0.24	0.28	0.09	0.19	0.07	0.12
Spectral line used		Distance from the centre of the spot in $10^3$ km.						
		9.62	10.50	11.10	11.80	13.20	15.00	
4912 ( $\lambda 299$ )	u	+1.25	+1.38	+1.02	+0.82	+1.03	+0.60	
	r.m.s.	0.63	0.40	0.28	0.09	0.55	0.25	
	v	+0.01	+0.10	-0.36	-0.01	-0.17	+0.11	
	r.m.s.	0.31	0.25	0.17	0.05	0.18	0.13	
	W—W <sub>0</sub>	-0.07	+0.06	-0.06	-0.02	-0.06	0.00	
	r.m.s.	0.18	0.13	0.09	0.02	0.11	0.04	
5576 ( $\lambda 300$ )	u	..	+0.53	+0.62	..	..	+0.33	
	r.m.s.	..	0.30	0.27	..	..	0.26	
	v	..	-0.07	-0.13	..	..	-0.07	
	r.m.s.	..	0.14	0.11	..	..	0.12	
	W—W <sub>0</sub>	..	+0.06	+0.08	..	..	0.00	
	r.m.s.	..	0.08	0.35	..	..	0.08	
5691 ( $\lambda 301$ )	u	+1.31	+1.19	+0.92	..	+0.90	+0.65	
	r.m.s.	0.42	0.21	0.18	..	0.22	0.14	
	v	-0.03	+0.04	-0.19	..	-0.72	0.00	
	r.m.s.	0.27	0.12	0.12	..	0.08	0.04	
	W—W <sub>0</sub>	-0.03	-0.02	-0.02	..	+0.34	0.00	
	r.m.s.	0.18	0.06	0.06	..	0.54	0.40	

TABLE 4—(Contd.)

Component velocities in km/sec in Sunspot No. KKL 12375 on February 16, 1963  
at  $\mu = 0.56$

Spectral line used		Distance from the centre of the spot in $10^3$ km.					
		4.37	5.12	5.87	6.62	7.37	8.13
4912 (A305)	u	+1.03	+1.46	+1.11	+2.09	+1.77	+1.61
	r.m.s.	0.18	0.21	0.21	0.61	0.46	0.50
	v	+0.18	+0.25	+0.07	+0.62	+0.13	+0.21
	r.m.s.	0.09	0.08	0.12	0.33	0.14	0.20
	W—W <sub>0</sub>	+0.06	+0.02	+0.05	+0.28	+0.05	+0.03
	r.m.s.	0.06	0.05	0.05	0.19	0.07	0.10
5576 (A306)	u	+0.70	+0.68	+0.72	+0.76	+0.22	..
	r.m.s.	0.19	0.23	0.29	0.78	0.34	..
	v	+0.09	+0.03	+0.12	+0.16	+0.14	..
	r.m.s.	0.11	0.14	0.11	0.18	0.14	..
	W—W <sub>0</sub>	+0.13	+0.13	+0.13	+0.01	+0.19	..
	r.m.s.	0.07	0.08	0.07	0.09	0.08	..
5691 (A307)	u	+1.70	+1.70	+1.83	+1.63	+2.00	+2.13
	r.m.s.	0.34	0.37	0.58	0.40	0.62	0.41
	v	+0.30	+0.27	+0.37	+0.22	+0.14	+0.41
	r.m.s.	0.12	0.15	0.23	0.56	0.15	0.42
	W—W <sub>0</sub>	+0.39	+0.30	+0.23	+0.25	+0.24	+0.08
	r.m.s.	0.08	0.08	0.12	0.16	0.10	0.16
Spectral line used		Distance from the centre of the spot in $10^3$ km.					
		8.87	9.62	10.50	12.00	14.00	
4912 (A305)	u	..	+0.24	+1.16	+1.22	+1.08	
	r.m.s.	..	0.61	0.46	0.47	0.72	
	v	..	+0.34	+0.02	+0.17	+0.10	
	r.m.s.	..	0.20	0.14	0.18	0.19	
	W—W <sub>0</sub>	..	0.00	+0.04	+0.06	0.00	
	r.m.s.	..	0.09	0.06	0.05	0.07	
5576 (A306)	u	+0.89	+0.90	+0.53	+0.79	+0.84	
	r.m.s.	0.50	0.37	0.32	0.09	0.59	
	v	+0.30	+0.08	+0.12	0.00	+0.07	
	r.m.s.	0.41	0.69	0.09	0.32	0.15	
	W—W <sub>0</sub>	0.00	+0.01	+0.01	+0.03	0.00	
	r.m.s.	0.25	0.31	0.05	0.13	0.06	
5691 (A307)	u	..	+1.95	..	+1.43	+0.87	
	r.m.s.	..	0.15	..	0.50	0.10	
	v	..	+0.26	..	+0.40	+0.24	
	r.m.s.	..	0.01	..	0.19	0.51	
	W—W <sub>0</sub>	..	+0.27	..	0.00	0.00	
	r.m.s.	..	0.09	..	0.07	0.34	

TABLE 4—(Contd.)

Component velocities in km/sec in Sunspot No. KKL 12368 on January 20, 1963  
at  $\mu = 0.54$

Spectral line used	Distance from the centre of the spot in $10^3$ km.				
	5.50	6.75	8.25	9.75	11.20
4912 (A186)	u	+0.66	+0.90	+1.04	+1.09
	r.m.s.	0.10	0.07	0.13	0.07
	v	+0.30	+0.55	+0.31	+0.04
	r.m.s.	0.12	0.08	0.08	0.18
	W—W <sub>0</sub>	—0.29	—0.38	—0.24	—0.20
	r.m.s.	0.07	0.04	0.06	0.09
5576 (A181)	u	+0.20	+0.35	+0.22	+0.57
	r.m.s.	0.05	0.08	0.14	0.14
	v	+0.13	—0.16	—0.12	—0.02
	r.m.s.	0.05	0.08	0.10	0.20
	W—W <sub>0</sub>	+0.03	+0.01	—0.06	—0.02
	r.m.s.	0.02	0.04	0.06	0.10
5691 (A180)	u	+0.28	+0.47	+0.66	+1.02
	r.m.s.	0.04	0.23	0.14	0.27
	v	—0.06	+0.52	+0.17	+0.29
	r.m.s.	0.04	0.22	0.19	0.29
	W—W <sub>0</sub>	—0.21	0.00	0.00	—0.03
	r.m.s.	0.01	0.03	0.10	0.16
Spectral line used	Distance from the centre of the spot in $10^3$ km.				
	12.70	14.20	15.70	17.20	18.70
4912 (A186)	u	+1.03	+0.79	+0.73	+0.56
	r.m.s.	0.21	0.12	0.42	0.31
	v	+0.31	—0.14	+0.51	+0.13
	r.m.s.	0.20	0.18	0.39	0.30
	W—W <sub>0</sub>	—0.11	—0.12	—0.12	0.00
	r.m.s.	0.09	0.07	0.20	0.11
5576 (A181)	u	+0.53	+1.00	+0.52	+0.47
	r.m.s.	0.16	0.24	0.18	0.14
	v	+0.17	+0.43	+0.18	+0.18
	r.m.s.	0.20	0.17	0.25	0.23
	W—W <sub>0</sub>	—0.08	—0.08	+0.09	0.00
	r.m.s.	0.10	0.07	0.10	0.06
5691 (A180)	u	+0.74	+0.69	+0.77	+0.43
	r.m.s.	0.23	0.03	0.38	0.21
	v	—0.06	—0.68	0.00	—0.94
	r.m.s.	0.22	0.05	0.28	0.57
	W—W <sub>0</sub>	+0.18	—0.28	+0.13	—0.31
	r.m.s.	0.14	0.03	0.12	0.12

TABLE 4—(Contd.)

Component velocities in km/sec Sunspot No. KKL 12368 on January 21, 1963  
at  $\mu = 0.35$

Spectral line used		Distance from the centre of the spot in $10^3$ km.				
		5.50	6.75	8.25	9.75	11.20
4912 (A189)	u	+0.69	+0.40	+0.66	+0.38	+0.31
	r.m.s.	0.16	0.16	0.13	0.21	0.22
	v	+0.13	-0.08	+0.02	-0.12	-0.18
	r.m.s.	0.19	0.14	0.08	0.22	0.30
	W—W <sub>0</sub>	-0.17	-0.21	-0.02	-0.08	-0.07
	r.m.s.	0.07	0.08	0.05	0.06	0.08
5576 (A190)	u	+0.59	+0.45	+0.44	+0.51	+0.62
	r.m.s.	0.19	0.14	0.13	0.14	0.26
	v	+0.25	+0.24	+0.32	+0.11	+0.31
	r.m.s.	0.14	0.13	0.21	0.13	0.17
	W—W <sub>0</sub>	+0.13	-0.08	-0.04	0.00	0.00
	r.m.s.	0.09	0.07	0.09	0.04	0.09
5691 (A191)	u	+0.91	+0.80	+0.82	+0.96	+0.61
	r.m.s.	0.09	0.12	0.19	0.41	0.19
	v	+0.52	+0.35	+0.38	+0.39	+0.33
	r.m.s.	0.06	0.11	0.22	0.28	0.18
	W—W <sub>0</sub>	+0.09	0.00	+0.01	0.00	-0.08
	r.m.s.	0.05	0.08	0.15	0.12	0.09

Spectral line used	Distance from the centre of the spot in $10^3$ km.					
	12.70	14.20	15.70	17.20	19.00	
4912 (A189)	u	+0.53	..	+0.03	..	..
	r.m.s.	0.13	..	0.10	..	..
	v	+0.24	..	-0.19	..	..
	r.m.s.	0.12	..	0.08	..	..
	W—W <sub>0</sub>	+0.08	..	0.00	..	..
	r.m.s.	0.04	..	0.02	..	..
5576 (A190)	u	+0.22	..	+0.32	+0.23	+0.16
	r.m.s.	0.24	..	0.18	0.23	0.18
	v	-0.13	..	0.00	+0.03	+0.05
	r.m.s.	0.19	..	0.14	0.18	0.15
	W—W <sub>0</sub>	+0.09	..	+0.06	+0.02	0.00
	r.m.s.	0.06	..	0.05	0.05	0.03
5691 (A191)	u	+0.35	+0.49	..	+0.31	+0.08
	r.m.s.	0.27	0.24	..	0.23	0.11
	v	+0.09	+0.19	..	+0.14	-0.01
	r.m.s.	0.30	0.17	..	0.16	0.09
	W—W <sub>0</sub>	+0.02	+0.05	..	-0.01	0.00
	r.m.s.	0.13	0.08	..	0.06	0.03



The run of the radial velocity  $u$ , shows that the radial velocity steeply increases near the umbral border, to attain its maximum value near the middle of the penumbral region. From the peak value, the radial velocity gradually declines to become nearly zero, far out in the photosphere. Recently Brekke and Per Maltby (1963) have shown, from observations of a single spot that the radial velocities abruptly cease at the outer boundary of the penumbra. However, observations of Evershed (1916), Kinman (1952, 1953), Holmes (1961), Servajean (1961) and this study, show that the material flow continues far out into the photosphere.

The rise of the radial velocity to the peak value is generally very steep compared to the decline. A slight shift in the location of the peak velocity across the penumbra could be due to the errors in locating the boundaries of the umbra and the penumbra. The magnitude of the maximum radial velocity  $U_{\max}$  in all the three lines, shows a decrease towards the disk positions of the spot near the limb. Michard (1951) and recently Servajean (1961) have reported such a decrease of  $U_{\max}$  near the limb position and have interpreted this decrease as due to the decrease of  $U_{\max}$  with increasing height in the photosphere. Holmes (1963a) has shown that the observed velocities in spots are affected more towards the limb by the scattered light and the observed decrease of  $U_{\max}$  may not wholly be due to the level difference in the photosphere. A plot between  $U_{\max}$  and the disc positions, for each of the three lines, is given in Figure 5. The slope of  $U_{\max} : \mu$  for 5691 and 4912 lines is almost the same, while for the stronger line 5576 (Rowland intensity 4) the slope is different. The 5576 line is formed at a higher level than either of the two lines.

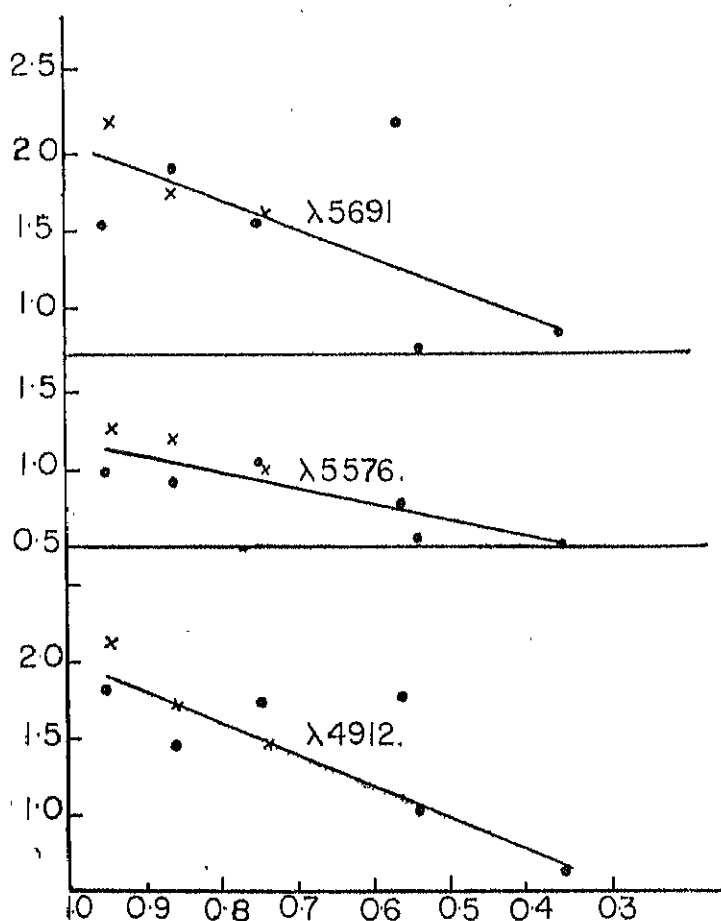


Figure 5.— $U_{\max}$  versus disc position ( $\mu$ ) of spots. Crosses indicate the velocities measured in the eastern quadrant; dots indicate the velocities measured in the western quadrant.  
Ordinate —  $U_{\max}$  in Km/sec. Abscissa — disc position of the spot.

Comparing the pattern of radial velocity curves for different disc positions of the spot, it is noticed that the velocity patterns flatten out for the spot-positions near the limb. For spots located near disc centre, the radial velocity curves show a steep rise and relatively slow decline. The velocity run for all the three lines at one disc position appears to be similar. On some disc positions of the spot, a small hump appeared near the outer edge of the penumbra. This hump in velocity curve was visible in all the three lines. A similar double peak in the radial velocity curve was also observed by Kinman (1953) in the case of Mount Wilson spot No. 10955. Sunspot spectra obtained on January 20 ( $\mu = 0.54$ ) and February 16 ( $\mu = -0.54$ ) refer to the same spot group, but on two different passages and almost at the same central meridian distance. Hence the velocity fields obtained on January 20 and February 16 can be compared for possible effects of age difference. These observations reveal that the spots show large radial velocities during their well developed phase, compared to the early phases.

Comparing the radial velocity field and the magnetic field maps, it is evident that the radial velocity increases in the penumbra with increasing distance from the umbral border. The velocity attains its maximum value about half way in the penumbral region, and then gradually decreases to zero well outside the penumbral limit. The magnetic field however, decreases monotonically with increasing distance from the spot centre to attain less than or equal to half its peak value near the middle of the penumbra. In this study of the Evershed effect and the spatial magnetic field, it was not possible to obtain a point-to-point correlation between the velocity and magnetic field pattern. It is planned to investigate the interaction of magnetic and velocity fields in the sunspot atmosphere from the observations of high resolution spatial magnetic and velocity fields.

The variation of the maximum radial velocity  $U_{\max}$  with depth in spots was first suggested by Evershed (1910) and later a detailed investigation was made by St. John (1913). From the calculations of the mean depth of formation of lines, gradients of  $U_{\max}$  with depth were obtained at nine disc positions of the spot and are given in Table 3.

(b) *Vertical velocity,  $w$*  ; The vertical velocity  $w$ , is the component directed outwards and normal to the solar surface. The measures of the vertical velocity are referred to the vertical velocity  $w_0$ , of a far removed point in the photosphere. The quantity  $(w - w_0)$  and their r.m.s. errors are plotted in the lower halves of Figure 4. The direction of these small vertical velocities is systematically negative in the penumbra and the maximum amplitude is of the order of  $-0.3$  km/sec. This indicates a descending motion of matter, in the penumbral region.

The variation of the vertical velocity with disc position is evident from Table 3. A decrease of maximum vertical velocity towards the limb positions of the spot, is observed for all the three lines.

(c) *Tangential velocity,  $v$*  ; The existence or otherwise of the tangential component of velocity or a rotational motion, in sunspots is yet to be confirmed. There are reliable and convincing observations in the literature that indicate the presence as well as absence of the tangential velocities in sunspots. Evershed (1910, 1916) detected tangential velocities of the order of 0.25 to 0.35 km/sec and even higher. Abetti (1932) found irregular tangential velocities of the order of 0 to 5 km/sec and suggested that the tangential motion varied from spot to spot. Kinman (1952) found that the tangential component  $v$  was random in nature and was well within the errors of measurements. Servajean (1961) has also shown that the magnitude of  $v$ , on most of the spot positions on the disc was very small. In his Table III (Servajean 1961) sizable tangential velocities ( $-0.33$  to  $+0.55$  km/sec) occur on April 27 and 30.

Our results of the tangential velocities and their r.m.s. errors, are given in Table 3. Figure 6 shows the run of tangential velocity component and their r.m.s. errors, on February 9 and 10, measured in all three lines. The tangential velocity measured from the spectra of January 20, 21 and February 9 & 10, show a slight systematic pattern of velocity variation over and above the large r.m.s. errors. At positions near the disc centre, the tangential velocity patterns show no systematic trend. At a few points in the spot, the component velocity  $v$  was found to be as high as  $1.5 \pm 0.6$  km/sec. An exact correspondence between the tangential velocity run in all the three lines is not found.

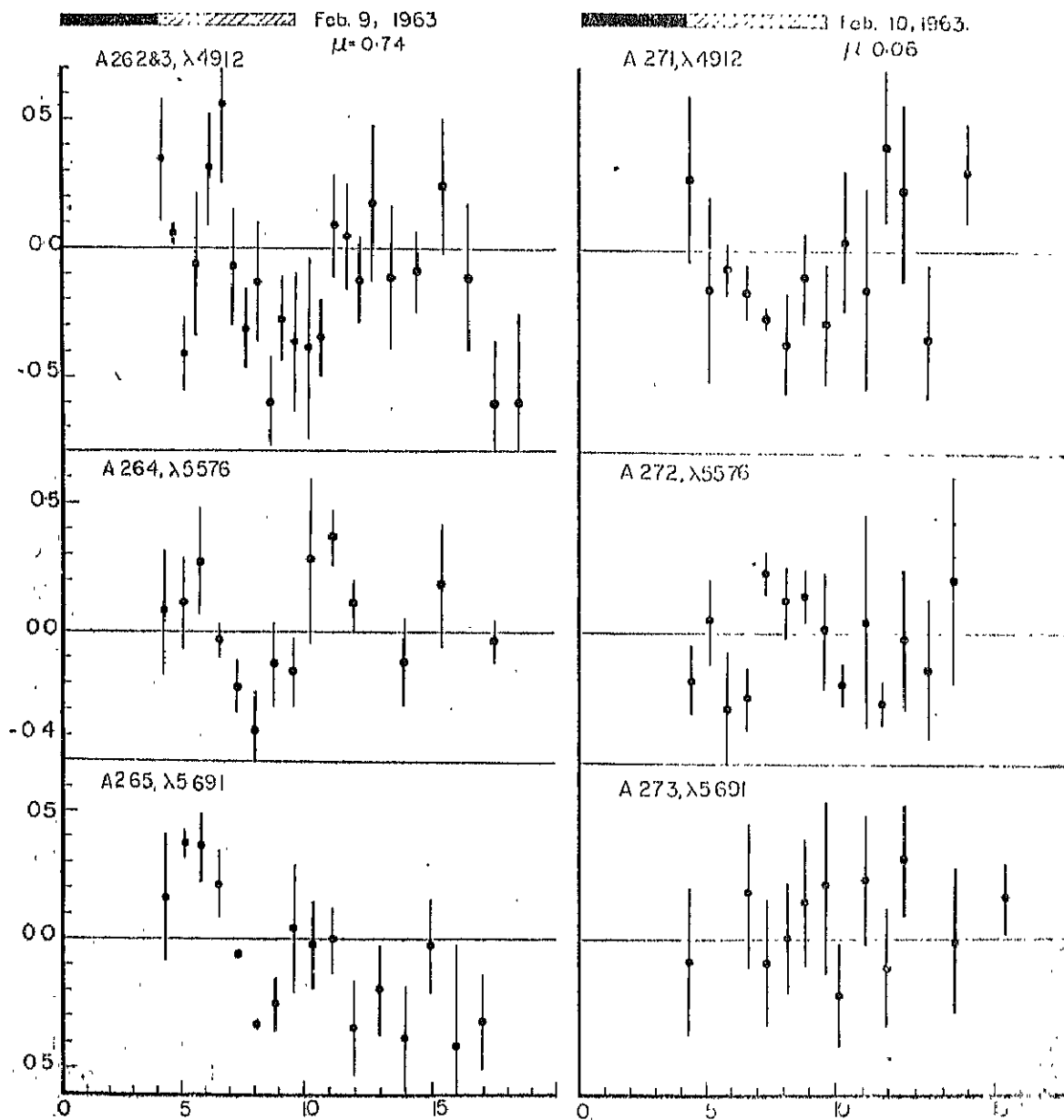


Figure 6.—Run of tangential velocity component and r.m.s. errors.  
Ordinate --- in km/sec  
Abscissa --- in 1000 km

From our observations of the tangential velocity and also on the basis of the work briefly reviewed earlier, it will be realized that further observational corroboration is necessary before we can definitely recognize the contribution of the tangential component to the velocity fields in sunspots. Adam's (1963) recent measures of the magnetic field in spots and the detection of the azimuthal component of magnetic field indicate the possibility of the presence of tangential and vertical velocities. Adam (1963) has shown that while the field strength remains stable, the direction of magnetic field varies from day to day.

As shown earlier, the largest contribution to the mass motion in spot penumbra comes from the radial component only. Nevertheless, the existence of the tangential motion has not been repudiated and on the other hand its presence may be in agreement with the recent observations of Adam (1963). Considering the high conductivity of the solar material, the flow of material has to be along the magnetic lines of force. It would be impossible for the conducting material to 'slip-cross' perpendicularly the magnetic lines of force. With the existence of the azimuthal component of magnetic field in sunspot penumbrae, it implies that the motion should have a tangential component also.

In some of the radial and tangential velocity measures, large r.m.s. errors are noticed. These large r.m.s. errors could be due to the following reasons ;

- (1) the number of the measured velocity points in each annular zone may be small,
- (2) our basic assumption that the motion has a cylindrical symmetry about the centre of the spot, may not be wholly valid.

**The phenomenon of line profile asymmetry in sunspot penumbrae.** The important phenomenon of asymmetry of spectral lines in the sunspot penumbral regions, was first discovered by Evershed (1916). He showed that near the outer boundary of a spot penumbra, the spectral lines develop a strong diffuse wing, which is always directed towards the Evershed displacement. A diffuse asymmetric wing in lines is easily seen on the spot spectra taken by McMath et al. (1956). Recently, Bumba (1960) at the Crimean Observatory has studied this phenomenon. He used high spectrographic dispersion and a large solar image. He termed this diffuse asymmetry in spectral lines as 'Flag' and has resolved this 'Flag' into a separate 'Satellite' line. This satellite line indicates Doppler shifts of the order of 5 km/sec or more. Servajean (1961) has studied changes in the asymmetric nature of lines in the spot region and also at different spot locations on the solar disk. It seems that Bumba (1960), Servajean (1961) and other workers in reporting the phenomenon of asymmetry in sunspot lines 'seem to have overlooked its first discovery by Evershed in 1915. It is remarkable for Evershed (1916) to have observed the diffuse wing in lines near the penumbral region, even though he had at his disposal a small solar image (44 mm diameter) and relatively low spectrographic dispersion.

**Observations and the photometric analysis of the line asymmetry.** Some of the best spectra were selected from a collection of spot spectra for a detailed photometric study of the variation of the line asymmetry; (1) over the spot region, (2) with the location of spot on the disc, (3) at two places on the line profile and (4) with the strength of the line. A term "flag factor (F.F.)" is defined as a measure of the asymmetry in a line, and is given by

$$F.F. = (\lambda_1 - \lambda_0)$$

where  $\lambda_0$  is the wavelength of the central intensity point and  $\lambda_1$  is the wavelength of the centre of the line joining equal intensity points on the line profile. The flag factor' F.F., is measured at half intensity and at one-tenth intensity points on the line profile.

The spectra obtained under good seeing conditions on February 9 at  $L-Lo=39^{\circ}.0$  E., on February 12 at  $L-Lo=0^{\circ}$ : and on February 15 at  $L-Lo=39^{\circ}.0$  W., in the three spectral regions 4912, 5576 and 5691 were used for this study. For the spatial variation of F.F. over the spot region, three slit positions, crossing the umbra centrally and on either sides of the umbra crossing only the penumbra were used. These three slit positions for the three disc positions of the spot, yield a picture that is very representative of the spatial aspect of the line asymmetry in spots. All the spectrograms used were calibrated with the aid of a Hilger step wedge filter. Microphotometer scans of the three Zeeman insensitive lines (4912.027, 5571.101 and 5691.508) were obtained at several places in the spot region and at a point far removed from the spot in the photosphere. The chart speed was adjusted to give a magnification of 25 times, thus yielding a dispersion of about 200 mm per Å on the traces. The positions of the scanned regions on the spot spectrum were determined using the wire shadows, registered while obtaining the spot spectra. The microphotometer scanning slit used was about  $0''.8$  of arc in height and  $0''.3$  of arc in width on the solar disk.

On six spectrograms and for one slit position, line profiles were obtained for 4912.027 and 5691.508 lines. These are given in Figure 7, as representative of some typical asymmetric line profiles. The 'flag factors' were determined at one-half and one-tenth intensity points on the line profile. Figure 8 gives the variation of flag factor in milliangstrom, over the spot region, in all the three lines (except for spectra obtained on February 9), and in three slit positions. In these figures the positions of spot and the slit are given to indicate the approximate location of the slit orientation and also the sight-line velocities measured along the length of the slit. The positive values of F.F., indicate flagging towards the long wavelength side, while the negative values indicate flagging towards the short wavelength side. The line profiles given are not corrected for the errors introduced by the instrumental profile of the 18-metre Littrow spectrograph. Using an iodine absorption tube, it was found that the instrumental profile of this spectrograph is very narrow (less than 12 mÅ) and fairly symmetrical.

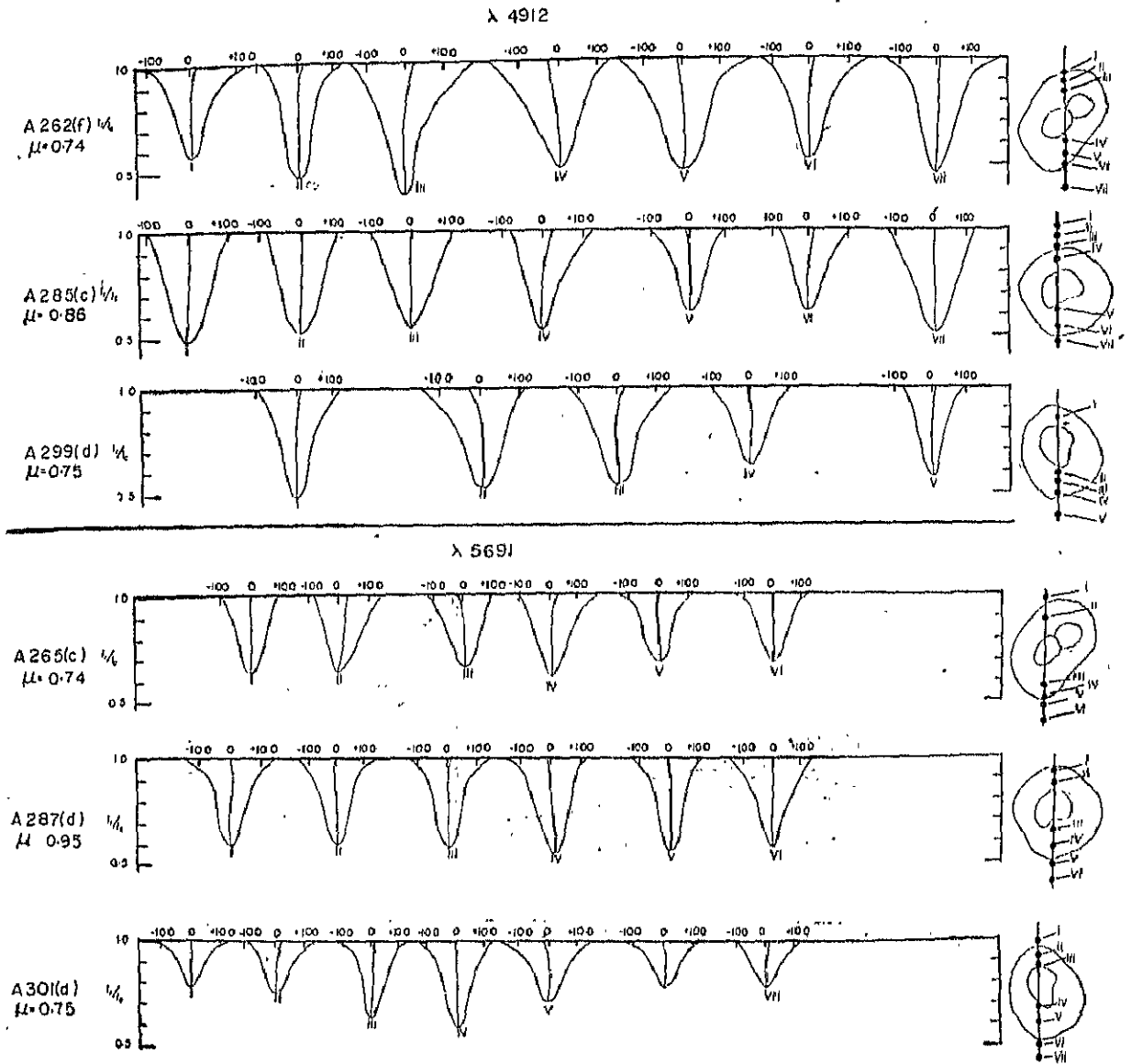


Figure 7—Variation of line profiles in sunspots.

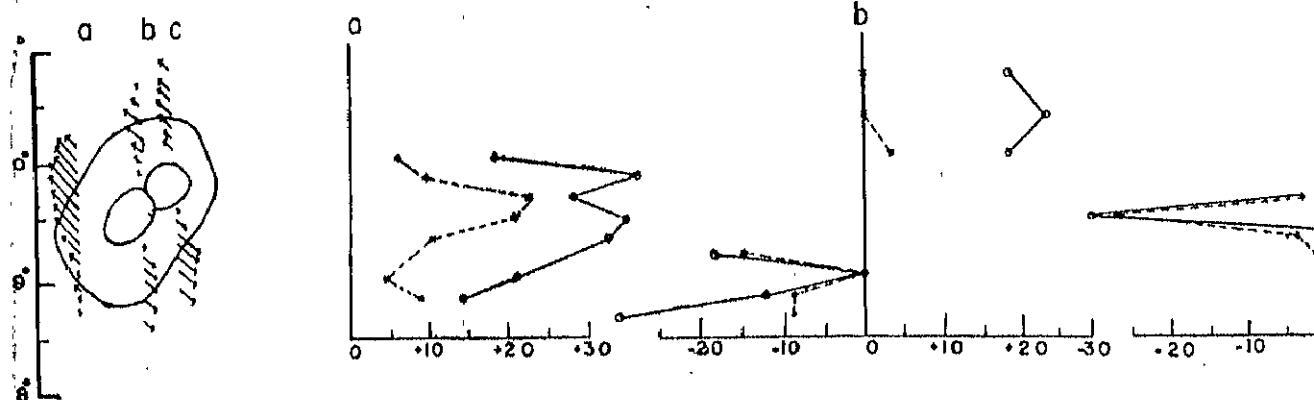
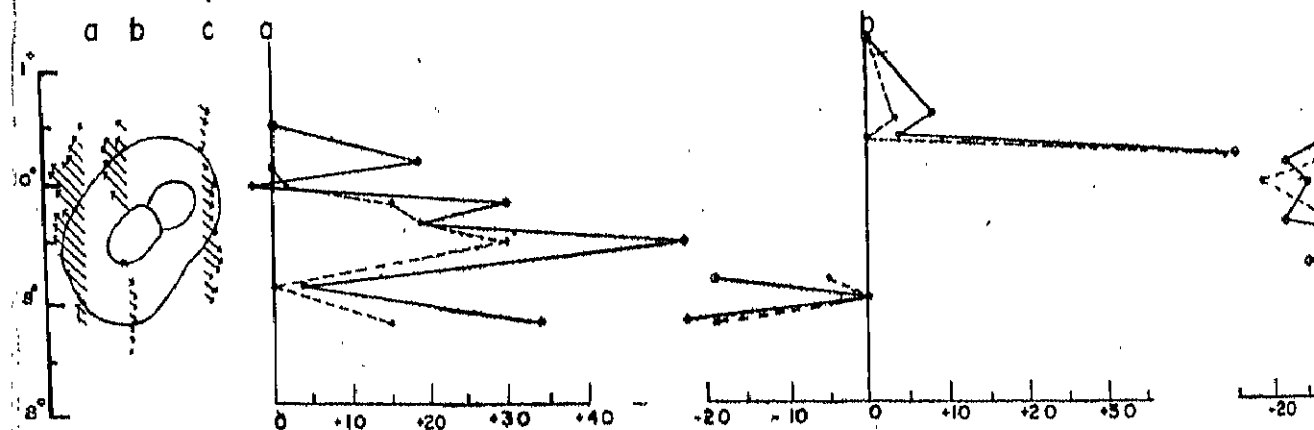
FEBRUARY 9, 1963.  $(L-L_0) \approx 39^\circ \text{E}$ , KKL 12375A262  $\lambda 4912$ A265  $\lambda 5691$ 

Figure 8 (a)—Variation of 'Flag factor' in sunspots, in units of milliangstrom. The sight-line velocities are indicated on the left.

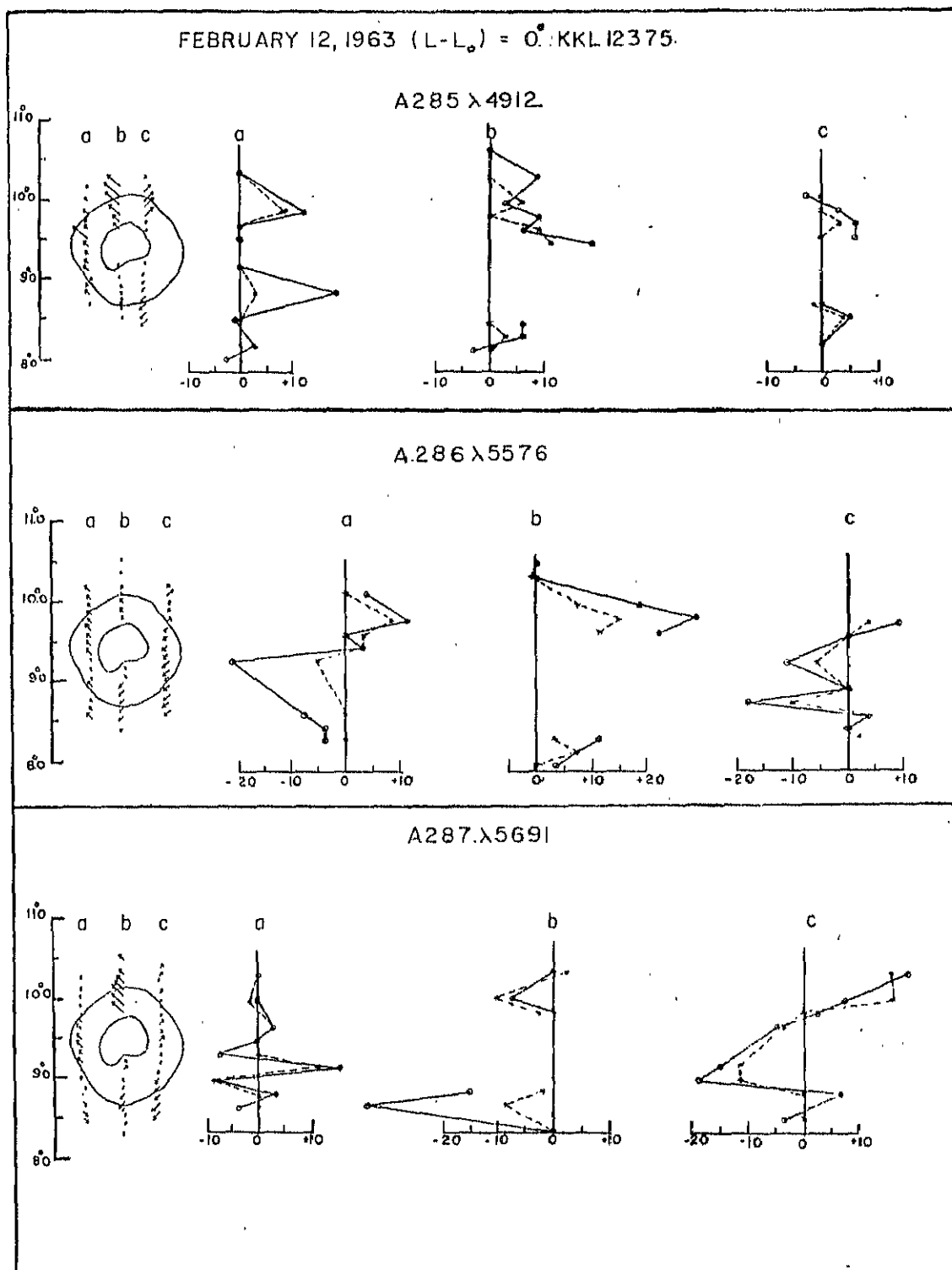


Figure 8 (b)—Variation of 'Flag factor' in sunspots, in units of milliangstrom. The sight-line velocities are indicated on the left.



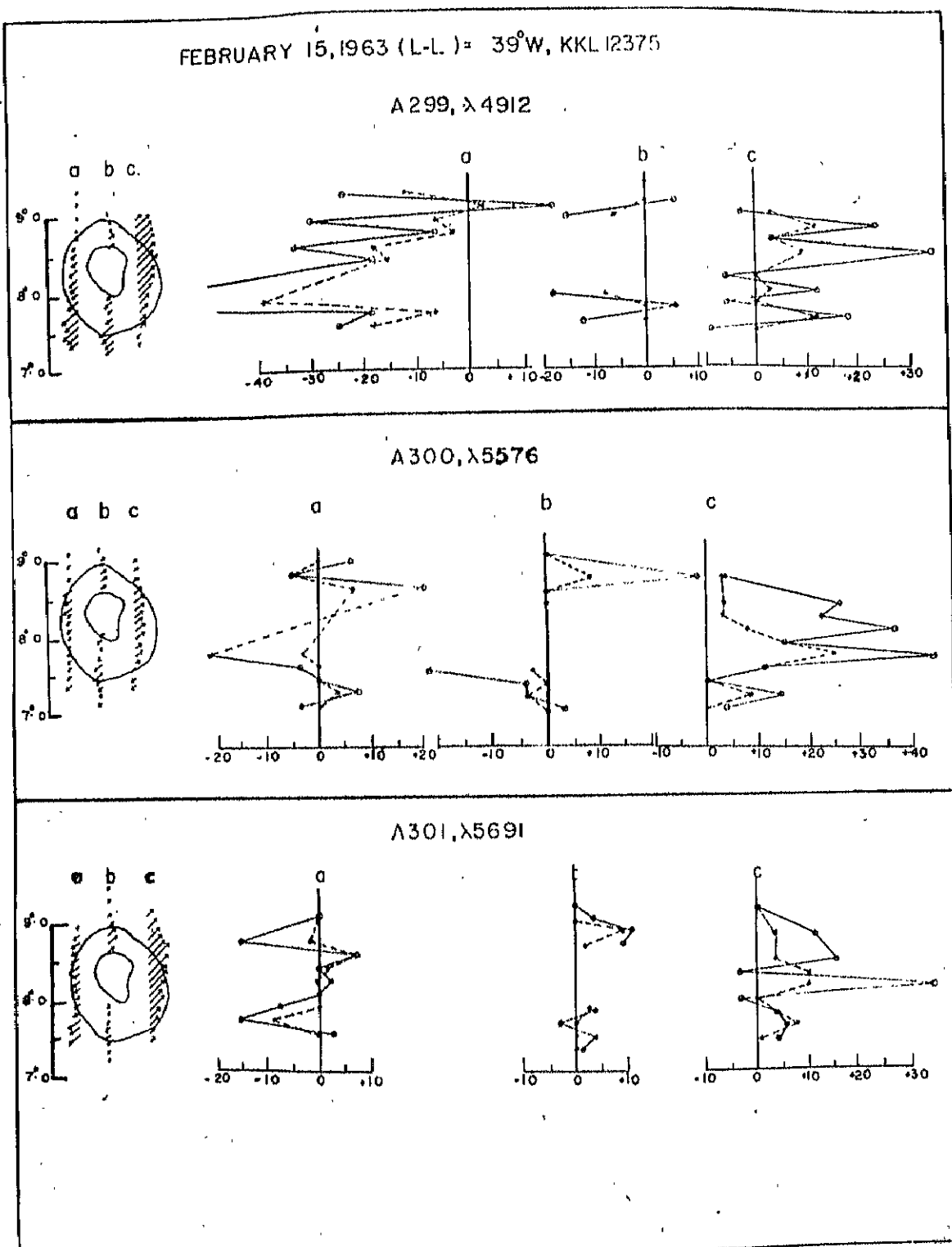


Figure 8 (c).—Variation of 'Flag factor' in sunspots, in units of milliangstrom. The sight-line velocities are indicated on the cft.

**Discussion of the line asymmetry ;** From the 'flag factor' plots and the variation of the line profiles, it is noticed that the line profiles in the photosphere are symmetrical. In the region of the penumbra, the asymmetry increases to attain its maximum value around the middle of penumbral region. The magnitude of the 'flag factor' fluctuates considerably in the penumbral region. In some spot regions maximum asymmetry of about 60 mÅ at one-tenth central dip is noted. The maximum 'flag-factor' is a function of the disc position of the spot. In spot positions near the disc centre, the value of maximum 'flag-factor' is smaller compared to the spots near the limb. A variation of the 'flag factor' is noted with line strength. The 5576 line shows systematically a smaller 'flag factor' compared to the weaker lines,  $\lambda$  4912 and  $\lambda$  5691. A visual examination of some spot spectra taken by Dr. M.K.V. Bappu, at the Kitt Peak National Observatory, Arizona, using a large solar image (33 inches in diameter) and a spectrographic dispersion of 12 mm/Å, indicates a decrease in flagging with increasing line strength. The 4903 and 4919 lines of Rowland intensity 5 and 6, show marked decrease in asymmetry, compared to the weaker lines. The direction of flagging in the strong and weak lines is the same and in no case the flagging extends beyond the penumbral limit.

The spot spectra obtained at Kodaikanal and those obtained at Kitt Peak, under good to very good seeing conditions, do not show any indication of satellite line, as reported by Bumba (1961, 1963). The diffuse wing always appears to be joined with the parent line. Perhaps the appearance of the faint satellite line depends on some other rigorous factors of observation.

Some of the spectra obtained under extremely fine seeing conditions show brightness variation in the penumbral region. The 'flagging' in lines occur more conspicuously in the darker regions of the penumbra. In the brighter regions the lines appear, more or less symmetrical. It seems that the agency responsible for the asymmetry or flagging in lines is more efficient in the darker (cooler) penumbral regions, compared to the brighter (hotter) penumbral regions.

From the asymmetric appearance of the line profiles and their variation in the spot region it seems that this phenomenon is associated with velocity fields, either on the surface or deep in the sunspot atmosphere. Two plausible explanations have been put forward, one by Servajean and the other by Bumba. Servajean (1961) has suggested that asymmetry occurs due to the difference in velocities of different strata in the line forming layers while Bumba (1963) suggests, an upstreaming of material at the umbral-penumbral boundary, which bends to become horizontal in the penumbral region and turns downwards again near the outer penumbral border. It appears that the line asymmetries in the penumbra may be due to the velocity fields of some kind. It was noted earlier that the flagging is always directed towards the general Evershed flow. Therefore it seems that the motion responsible for the asymmetry in lines is an additional motion superimposed on the Evershed flow. This additional motion in various layers, responsible for the asymmetry in lines, perhaps ceases abruptly at the outer boundary of the penumbra, while the Evershed flow continues well out into the photospheric region.

**Diffuse wing in lines in the Photospheric regions;** A similar phenomenon of diffuse asymmetric wings in lines as that observed in the penumbral region, is noticed in the photospheric region also. On our best spectra that show, "wiggles" due to the solar granulation, one can see slight diffusion or 'flaring' in one of the wings of Fraunhofer lines. A diffuse wing develops invariably in the same direction, as the Doppler displacement due to the granular motion and in the darker (cooler) regions of the spectrum. In the brighter (hotter) photospheric regions, the lines appear symmetrical and also slightly narrow. A detailed quantitative analysis of this phenomenon is required. Servajean (1961) has also reported the presence of a similar phenomenon in granulation spectra.

**Acknowledgements :** The author is greatly indebted to Dr. M.K. Vainu Bap-  
 Director, Astrophysical Observatory, Kodaikanal, for suggesting this problem and  
 constant encouragement and guidance. The author wishes to thank Miss. N. Subra-  
 manyan, for stimulating discussions and for the cooperation during this investigation.  
 The work reported in this paper was done during the tenure of the author as a Sen-  
 Research Fellow of the Ministry of Education, Government of India.

KODAIKANAL OBSERVATORY, }  
*November, 1966.* }

#### REFERENCES

- Abetti, G. 1932, Mem. Soc. Astr. Ital., 6, 353.  
 Adam, M. G. 1963, M. N. **126**, 135.  
 Brekke, K., and Maltby, P. 1963, Ann. Astr. **26**, 383.  
 Bruggencate, P. ten, Lust, Kulka, R., and Voight, H. 1955, Veröffentlichung  
 der Universitäts-Sternwarte zu Göttingen, No. 110.  
 Bumba, V. 1960, Izvestiya Krym, Astro. Obs., **23**, 253.  
 Bumba, V. 1963, B. A. C., **14**, 1937.  
 Calami, G. 1934, Oss. Mem. Arcetri, **52**, 39.  
 Evershed, J. 1909a, M. N. **69**, 454.  
 Evershed, J. 1909b, Bull. Kodaikanal Obs. **2**, No. 15, 63.  
 Evershed, J. 1909c, Mem. Kodaikanal Obs., **1**.  
 Evershed, J. 1909d, The Observatory, **32**, 291.  
 Evershed, J. 1910, M. N. **70**, 217.  
 Evershed, J. 1913, Bull. Kodaikanal Obs., **3**, No. 32, 17.  
 Evershed, J. 1916, Bull. Kodaikanal Obs., **3**, No. 51, 167.  
 Edmonds, F. N. 1962, Ap. J., **136**, 507.  
 Goldberg, L., Muller, E. A., and Aller, L. H., 1960, Ap. J., Suppl. 5, 1.  
 Holmes, J. 1961, M. N., **122**, 301.  
 Holmes, J. 1963a, The Observatory, **86**, 163.  
 Holmes, J. 1963b, M. N. **126**, 155.  
 Kinman, T. D. 1952, M. N., **112**, 425.  
 Kinman, T. D. 1953, M. N., **113**, 613.  
 Makita, M. 1963, Pub. Astr. Soc. Japan, **15**, 145.  
 McMath, R. R., Mohler, O. C., Pierce, A. K., and Goldberg, L. 1956, Ap.  
**124**, 1.  
 Michard, R. 1951, Ann. Astr. **14**, 101.  
 Minkowski, R. 1942, Ap. J., **96**, 306.  
 Pierce, A. K., and Waddell, J. H. 1961, Mem. R. A. S., **68**, 89.  
 Plaskett, H. H. 1952, M. N., **112**, 414.  
 Servajean, R. 1961, Ann. Astr., **24**, 1.  
 St. John, C. E. 1913, Ap. J., **37**, 322.  
 Walker, G. T. 1909, Bull. Kodaikanal Obs. **2**, No. 16, 71.  
 Wright, K. O. 1944, Ap. J., **99**, 249.

# KODAIKANAL OBSERVATORY

## BULLETIN Number 181

### Photoelectric light curve of YY Eridani

J. C. Bhattacharyya

#### Abstract

Photoelectric light curves in B and V of the W Ursa Majoris star YY Eridani have been determined. Gradual lengthening of the period has been observed.

The light curve of the star YY Eridani, HD 26609, an eclipsing binary was obtained by a photoelectric photometer employing an RCA 1P21 photomultiplier tube, on twelve nights during December 1965—March, 1966 at Kodaikanal. The telescope used was a 20cm refractor. The signal from the photomultiplier was amplified by a linear D.C. amplifier and recorded on a potentiometric type stripchart recorder. The observations were taken in two colours, blue and yellow using standard glass filters of the UBV system with pass bands centred around 4500Å and 5500Å. For comparison, two other nearby stars were observed. The details of the three stars are given below:

Star	HD No.	(1950)	(1950)	Spectral type
YY Eridani	26609	4h 9m 46s.525	- 10° 35' 43" .58	G5, G5
Comparison	26650	1h 10m 9s.980	- 10° 41' 35" .20	A5
Check	26902	1h 12m 25s.410	- 10° 14' 36" .56	K0

Altogether 468 comparisons in blue and 422 in yellow light were obtained during this period. Six primary and three secondary minima were observed. It is found that to fit our observation with earlier ones by Cillie (1951) Haruhata (1953), Kwee (1958) and Purgathofer (1961), a further change in the period must be assumed.

The new period is found to be near the value obtained by Purgathofer. The elements are well represented by the equation

$$\text{Min.} = \text{JD } 2433617^{\text{d}} - 5197^{\text{h}} - 0^{\text{m}} - 32149630^{\text{E}}$$

the epoch being counted from Cillie's well determined minima of JD 2433617.51. The observed minima timings were found to be in excellent agreement to those calculated by the above equation.

The table below gives the residuals (O-C) for the six primary minima recorded

TABLE I  
*Primary Minima of YY Eridani*

Heliocentric J.D.	Computed Times	Residual O-C
2439120.2503 . . . . .	2439120.2501	-.0001
124.1085 . . . . .	124.1083	-.0002
165.2596 . . . . .	165.2599	-.0003
166.2241 . . . . .	166.2243	-.0002
167.1886 . . . . .	167.1888	-.0002
187.1216 . . . . .	187.1216	0.0000

The times of the three secondary minima were also determined and are tabulated in Table II. It is seen that the mean time interval between the secondary minima and the preceding primary minima is  $0^{\text{d}} - 1611$  which is  $0^{\text{d}} - 0003$  later than the midpoint of the cycle. This value is within the limits of error of the measurement and hence secondary minima may be considered equidistant from the two nearby primary minima.

TABLE II  
*Secondary Minima of YY Eridani*

Heliocentric J.D.	Computed time of previous primary min.	Residual O-C
2439162.2058 . . . . .	2439162.0449	.1609
165.0999 . . . . .	164.9384	.1615
181.1742 . . . . .	181.0132	.1610

The previous observers have noted a gradual lengthening of the period of particular system. Our results also corroborate their findings. The results of period change are represented in Fig. 1 where periods determined by several authors over the 33 year interval are plotted against the measured epochs. All the photometric observations can be fitted by a smooth curve. Considering the uncertainty in determining the actual times of minima by the photographic technique, the earlier photographic observations by Bodokia (1938) and Jensch (1934) can also be considered to be contained in the extended curve.

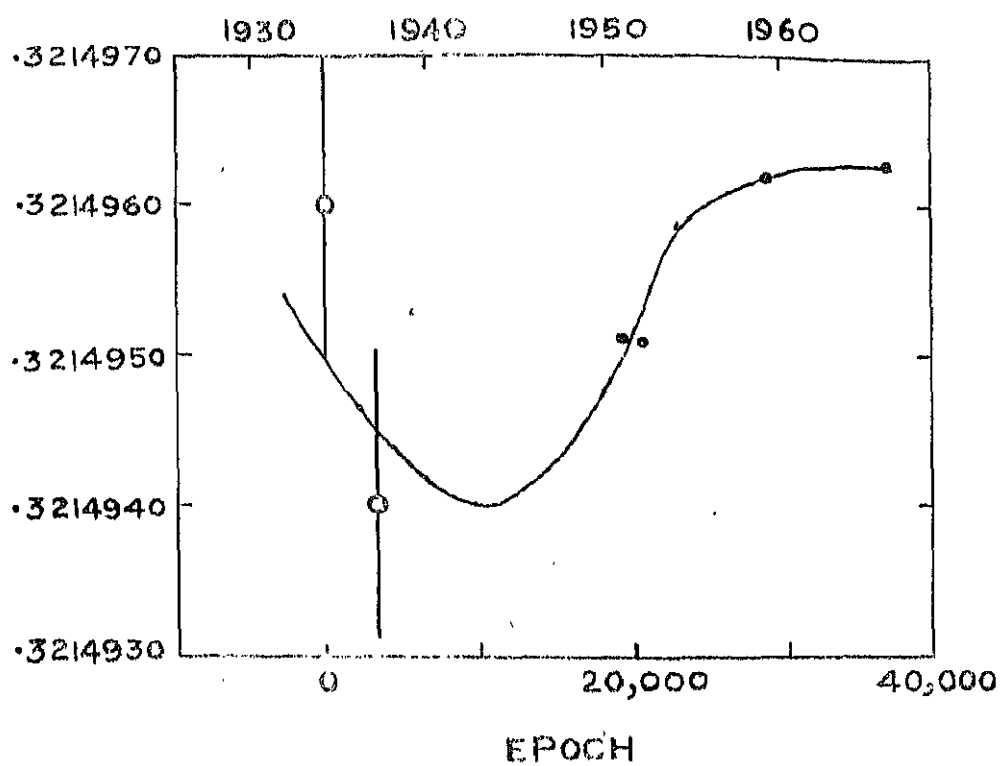


Fig. 1 Period Variation of YY Eridani

TABLE III

J.D.	$\Delta m$	J.D.	$\Delta m$
<i>Blue</i>			
2439120.1642	-.017*	2439120.3253	-.189
.1656	.125	.3260	.215
.1677	.125	.3309	.116
.1712	.087	.3323	.169
.1788	.169	.3337	.121
.1808	.185	.3350	.164
.1933	.126	.3378	.163
.1955	.093	.3385	.168
.2024	+.007	.3431	.196
.2051	.015	.3461	.123
.2128	.125	.3489	.175
.2156	.031	.3515	.062
.2219	.091	.3566	.097
.2226	.058	.3586	.082
.2246	.081	.3593	.012
.2260	.195	.3649	.032
.2337	.347	.3670	.015
.2357	.558	.3697	.099
.2371	.408	.3701	.032
.2434	.417	.3746	.025
.2462	.624	.3753	.080
.2482	.600	.3774	.111
.2515	.477	.3795	-.008
.2572	.509	2439162.0925	+.324
.2579	.451	.0953	.140
.2607	.530	.0994	.097
.2614	.517	.1008	.107
.2635	.559	.1022	.101
.2705	.306	.1092	.068
.2725	.379	.1112	.035
.2733	.309	.1126	.116
.2705	.191	.1168	.063
.2802	.157	.1182	.078
.2823	.229	.1196	.053
.2830	.169	.1230	.106
.2892	.068	.1251	.080
.2927	.033	.1265	.079
.2911	.013	.1314	.222
.2976	-.032	.1328	.270
.2990	+.026	.1425	.120
.3010	-.007	.1452	.077
.3052	.026	.1466	.089
.3080	.097	.1480	.126
.3128	.010	.1598	.201
.3149	.024	.1612	.267
.3163	.061	.1702	.193
.3205	.185	.1730	.236
.3226	.190	.1751	.273
.3232	.241		

\*Observations on JD 2439120 were through a narrow band interference filter ( $\pm 1\%$ ) centred round 4200Å.

TABLE III (Contd.)

J.D.	$\Delta m$ .	J.D.	$\Delta m$ .
2439162.1827	.344	2439165.1187	.406
.1831	.368	.1193	.427
.1897	.433	.1200	.381
.1910	.533	.1263	.295
.1924	.539	.1284	.289
.1994	.712	.1298	.249
.2001	.700	.1367	.180
.2015	.663	.1381	.178
.2022	.646	.1395	.148
.2028	.677	.1485	.138
.2035	.656	.1499	.120
.2042	.655	.1517	.080
.2056	.626	.1561	.085
.2077	.632	.1603	.022
.2084	.614	.1632	.030
.2160	.729	.1707	.193
.2167	.561	.1728	.122
.2174	.461	.1712	.095
.2230	.459	.1811	.033
.2257	.531	.1832	.038
.2278	.501	.1867	.013
.2382	.281	.1891	.019
.2389	.350	.1929	.036
.2400	.087	.1964	.025
.2507	.278	.1999	.074
.2521	.152	.2026	.101
.2618	.007	.2047	.112
.2632	.050	.2103	.144
.2709	.025	.2130	.138
2439165.0784	.480	.2332	.403
.0798	.475	.2339	.360
.0812	.538	.2401	.473
.0819	.531	.2415	.494
.0840	.561	.2436	.487
.0853	.592	.2450	.554
.0867	.571	.2470	.605
.0881	.637	.2484	.617
.0902	.600	.2505	.656
.0916	.613	.2519	.707
.0944	.711	.2533	.735
.0951	.753	.2554	.720
.0958	.733	.2575	.706
.0971	.735	.2595	.647
.0985	.811	.2609	.676
.1006	.745	.2637	.691
.1020	.742	.2651	.629
.1041	.698	.2665	.640
.1055	.737	.2706	.546
.1069	.652	.2734	.502
.1082	.656	.2755	.325
.1096	.622	2439166.1936	.351
.1159	.515	.1964	.295
.1173	.469	.1998	.423



TABLE III (Contd.)

J.D	$\Delta m$	J.D	$\Delta m$
2439166.2033	.479	2439174.1013	.707
.2040	.472	.1055	.673
.2009	.506	.1381	.162
.2110	.545	.1436	.144
.2130	.610	.1457	+.122
.2151	.612	.1561	-.003
.2165	.690	.1575	+.110
.2172	.748	.1589	.105
.2193	.812	.1645	.023
.2207	.853	.1658	.024
.2248	.783	.1700	.057
.2262	.822	.1714	.050
.2276	.788	.1756	.053
.2290	.784	.1769	.062
.2318	.732	.1889	.031
.2332	.735	.1901	.126
.2373	.619	.1929	.056
2439167.1511	.174	.1964	.078
.1518	.240	.2033	.085
.1553	.242	.2054	.080
.1567	.272	.2123	.090
.1587	.274	.2144	.110
.1608	.300	.2165	.141
.1657	.458	.2227	.107
.1664	.494	.2248	.162
.1685	.525	.2304	.176
.1698	.549	.2325	.190
.1719	.602	.2345	.246
.1747	.661	.2359	.252
.1761	.709	.2380	.350
.1775	.759	.2401	.415
.1789	.705	.2443	.414
.1802	.782	2439175.0859	.446
.1816	.800	.0894	.350
.1837	.799	.0977	.163
.1851	.833	.0998	.209
.1865	.806	.1026	+.196
.1893	.843	.1421	-.008
.1920	.788	.1435	.002
.1927	.816	.1491	+.078
.1941	.769	.1539	.050
.1955	.762	.1615	.096
.1976	.738	.1629	.093
.2018	.642	.1713	-.147
.2032	.588	.1740	.104
.2053	.537	.1851	.039
.2073	.505	.1872	+.018
.2108	.409	.1900	.027
.2122	.357	.1921	.039
.2156	.339	.1942	.211
.2198	.273	.1962	.204
.2267	.149	.1983	.208
.2281	.135	.2004	.375
.2323	.088	.2032	.439

TABLE III (Contd.)

J.D	$\Delta m$	J.D	$\Delta m$
2439175.2053	.471	2439181.0846	.023
.2112	.625	.0909	.023
.2143	.716	.0930	.027
2439176.0775	.228	.0999	.015
.0837	.083	.1013	.030
.0851	.061	.1075	.056
.0879	.059	.1103	.017
.0900	.091	.1131	.033
.0962	.038	.1145	.059
.1011	.092	.1159	.050
.1039	.069	.1173	.085
.1122	.149	.1193	.050
.1150	.098	.1207	.052
.1226	.117	.1235	.075
.1268	.068	.1256	.079
.1337	.080	.1277	.084
2439180.1007	.124	.1291	.098
.1012	.133	.1304	.102
.1076	.195	.1318	.118
.1104	.118	.1339	.183
.1201	.079	.1353	.152
.1215	-.068	.1367	.157
.1285	-.012	.1402	.202
.1305	-.118	.1415	.213
.1333	.046	.1429	.252
.1351	.006	.1450	.261
.1368	.007	.1461	.285
.1403	.041	.1478	.286
.1416	.084	.1499	.347
.1465	.013	.1513	.353
.1486	.061	.1526	.378
.1500	.041	.1575	.453
.1514	.031	.1589	.517
.1534	.039	.1603	.508
.1562	.125	.1624	.561
.1604	.206	.1638	.564
.1618	.193	.1651	.577
.1625	.159	.1665	.599
.1645	.110	.1686	.625
.1659	.100	.1749	.676
.1680	.139	.1769	.616
.1701	.132	.1783	.611
.1757	.151	.1818	.611
.1777	.191	.1832	.584
.1826	.242	.1880	.469
.1888	.333	.1901	.455
.1916	.466	.1922	.104
.1986	.589	.1936	.379
.1999	.575	.1965	.327
.2062	.693	.2005	.292
2439181.0770	.081	.2047	.237
.0832	.011	.2061	.189
		.2082	.174
		.2137	.134

TABLE III (Contd.)

J.D.	$\Delta m$	J.D.	$\Delta m$
2439187.0841	.227	2439187.1368	.577
.0883	.240	.1382	.578
.0917	.284	.1452	.456
.0952	.413	.1519	.349
.0991	.508	.1556	.318
.1008	.526	.1618	.225
.1077	.629	.1632	.240
.1105	.670	.1695	.150
.1119	.694	.1709	.144
.1153	.753	.1778	.125
.1160	.738	.1792	.090
.1174	.762	.1868	.034
.1188	.790	.1882	+ .019
.1202	.740	.1938	- .010
.1223	.773	.1951	+ .011
.1237	.751	.1986	.033
.1250	.769	.2000	.026
.1271	.743	.2014	.057
.1290	.727		

*Yellow*

2439124.1001	.380	2439124.2382	.101
.1022	.400	.2403	.096
.1050	.430	.2424	.009
.1126	.425	2439162.0919	- .141
.1154	.402	.0933	.073
.1181	.354	.0961	.126
.1258	.254	.1002	.132
.1292	.157	.1009	.171
.1320	.117	.1099	.182
.1383	+ .011	.1120	.186
.1410	- .026	.1134	.177
.1438	.012	.1176	.264
.1605	.195	.1190	.268
.1626	.203	.1204	.283
.1646	.225	.1238	.226
.1714	.108	.1259	.227
.1764	.118	.1266	.271
.1869	.250	.1315	.211
.1903	.247	.1342	.191
.1931	.235	.1410	.265
.1945	.253	.1446	.206
.2021	.210	.1453	.282
.2012	.240	.1474	.141
.2091	.252	.1606	.088
.2111	.234	.1627	.134
.2160	.212	.1710	.073
.2202	.202	.1731	.043

TABLE III (Contd.)

J.D	$\Delta m$	J.D	$\Delta m$
2439162.1759	---043	2439165.1096	---272
.1821	1.021	.1152	.153
.1828	.036	.1180	.131
.1812	.071	.1186	.089
.1904	.182	.1207	.069
.1918	.197	.1256	---002
.1932	.191	.1277	---033
.1988	.253	.1291	.062
.1995	.259	.1360	.134
.2002	.270	.1374	.147
.2009	.263	.1388	.167
.2022	.268	.1471	.212
.2029	.272	.1485	.189
.2036	.278	.1540	.229
.2050	.310	.1554	.231
.2057	.332	.1658	.304
.2070	.305	.1693	.308
.2085	.346	.1714	.276
.2175	.146	.1728	.232
.2182	.157	.1804	.270
.2221	1.059	.1818	.272
.2245	.019	.1874	.262
.2279	1.036	.1894	.236
.2376	---141	.1936	.241
.2383	.110	.1971	.233
.2487	.228	.2005	.213
.2501	.237	.2040	.200
.2508	.226	.2109	.161
.2515	.300	.2137	.155
.2612	.351	.2325	.019
.2626	.384	.2352	.056
.2703	.428	.2394	.169
2439165.0777	1.019	.2408	.177
.0791	.117	.2422	.183
.0805	.143	.2443	.259
.0819	.154	.2463	.279
.0826	.174	.2477	.328
.0846	.191	.2491	.351
.0860	.223	.2512	.391
.0874	.232	.2526	.416
.0895	.296	.2540	.422
.0909	.305	.2561	.410
.0923	.345	.2588	.416
.0944	.376	.2602	.405
.0964	.368	.2616	.390
.0978	.390	.2644	.401
.0985	.383	.2658	.393
.1013	.370	.2679	.358
.1027	.370	.2713	.318
.1048	.333	.2734	.244
.1062	.352	.2762	.172
.1075	.309	2439166.1929	---053
.1089	.286	.1957	.032

TABLE III (Contd.)

J.D.	$\Delta m$	J.D.	$\Delta m$
2439166-1998	-1.047	2439167-2129	-.006
2026	.119	2156	.041
2033	.123	2212	.119
2075	.121	2226	.175
2096	.185	2274	.171
2116	.197	2288	.198
2130	.263	2439174-1013	-1.250
2151	.330	1018	.214
2165	.345	1381	.119
2179	.462	1413	-.116
2193	.483	1461	.141
2207	.502	1568	.319
2255	.458	1582	.250
2269	.452	1596	.228
2283	.303	1651	.205
2297	.378	1658	.288
2325	.388	1707	.273
2339	.365	1721	.203
2380	.253	1763	.211
2408	.266	1783	.228
2439167-1518	-.081	1832	.212
1525	.062	1853	.246
1560	.032	1908	.236
1573	+1.008	1936	.241
1594	.059	1971	.248
1608	.083	2026	.237
1650	.131	2031	.216
1657	.143	2068	.226
1671	.156	2130	.219
1691	.207	2159	.197
1705	.241	2172	.191
1712	.268	2231	.166
1726	.275	2255	.114
1754	.319	2311	.051
1768	.371	2332	-.033
1782	.395	2352	+1.022
1796	.426	2373	.056
1809	.406	2387	.097
1830	.417	2408	.145
1844	.412	2450	.190
1858	.435	2439175-0852	.153
1900	.442	0887	.096
1920	.407	0981	-.116
1934	.381	1019	.142
1948	.387	1414	.307
1962	.317	1435	.290
1976	.314	1484	.192
2025	.222	1532	.217
2038	.186	1615	.248
2045	.147	1629	.221
2059	.139	1727	.228
2073	.120	1747	.168
2108	.026	1865	.117

TABLE III (Contd.)

J.D.	$\Delta m$	J.D.	$\Delta m$
2439175-1886	-.097	2439180-1784	-.142
.1907	-.093	.1833	-.079
.1928	-.098	.1995	+ .013
.1949	-.111	.1923	-.077
.1969	-.044	.1992	-.214
.1997	-1 .010	.2013	-.262
.2018	-.048	.2069	-.319
.2016	-.108		
.2115	-.242	2439181-0742	-.176
.2136	-.324	.0763	-.191
2439176-0754	-.203	.0784	-.209
.0782	-.198	.0846	-.258
.0844	-.248	.0860	-.244
.0858	-.231	.0923	-.291
.0886	-.218	.0944	-.291
.0907	-.214	.1013	-.228
.0955	-.272	.1027	-.236
.0969	-.281	.1096	-.233
.1018	-.347	.1124	-.229
.1015	-.387	.1138	-.229
.1129	-.195	.1159	-.211
.1157	-.226	.1186	-.215
.1240	-.197	.1200	-.207
.1275	-.291	.1221	-.268
.1344	-.273	.1248	-.202
2439180-1014	-.176	.1270	-.185
.1049	-.174	.1291	-.177
.1083	-.134	.1304	-.170
.1111	-.215	.1318	-.168
.1187	-.218	.1332	-.168
.1208	-.237	.1353	-.140
.1222	-.254	.1367	-.141
.1292	-.334	.1381	-.116
.1312	-.307	.1415	-.057
.1340	-.311	.1429	-.064
.1361	-.303	.1443	-.036
.1375	-.314	.1464	-.032
.1410	-.273	.1478	-.028
.1423	-.240	.1492	-.007
.1472	-.282	.1513	+ .007
.1486	-.252	.1527	-.035
.1507	-.296	.1540	-.094
.1521	-.274	.1589	-.173
.1541	-.279	.1603	-.181
.1569	-.203	.1617	-.227
.1611	-.092	.1638	-.230
.1625	-.158	.1651	-.263
.1639	-.207	.1665	-.270
.1652	-.220	.1679	-.288
.1673	-.196	.1706	-.330
.1687	-.194	.1769	-.366
.1708	-.174	.1783	-.310
.1763	-.156	.1797	-.332
		.1832	-.303

TABLE III (Contd.)

J. D.	$\Delta m$	J. D.	$\Delta m$
2439181-1846	.261	2439187-1230	-.433
.1901	.128	.1244	-.442
.1936	.096	.1250	-.442
.1998	-.016	.1278	-.441
.2019	.043	.1299	.383
.2061	.069	.1375	.290
.2075	.091	.1389	.222
.2096	.106	.1459	+ .102
.2151	.157	.1556	- .025
2439187-0848	.134	.1563	.026
.0890	.105	.1625	.072
.0924	-.007	.1639	.093
.0959	+ .055	.1702	.122
.1001	.153	.1715	.138
.1013	.172	.1785	.173
.1084	.324	.1799	.202
.1112	.365	.1875	.260
.1126	.376	.1889	.266
.1153	.419	.1914	.301
.1167	.433	.1951	.278
.1181	.457	.1993	.259
.1195	.426	.2007	.213
.1209	.457	.2021	.257

TABLE V

Phase	mb	n	Phase	mb	n
.019	.776	10	.013	1.428	7
.039	.700	6	.026	1.371	7
.055	.540	6	.047	1.251	6
.115	.283	4	.066	1.112	5
.175	.106	11	.118	1.052	5
.203	.027	10	.175	1.182	11
.305	.016	15	.235	1.266	18
.360	.110	11	.306	1.231	21
.403	.244	9	.370	1.161	12
.427	.358	5	.408	1.012	9
.445	.157	4	.410	1.101	12
.460	.558	11	.465	1.231	10
.483	.628	3	.482	1.317	4
.509	.662	3	.503	1.374	7
.516	.625	5	.512	1.327	4
.550	.448	4	.540	1.221	5
.580	.285	3	.563	1.084	5
.614	.149	5	.591	1.044	7
.703	.025	6	.617	1.136	8
.777	.038	8	.685	1.238	17
.841	.007	7	.770	1.249	16
.900	.250	7	.837	1.207	13
.925	.433	4	.893	1.079	9
.933	.520	3	.932	1.162	12
.962	.651	5	.973	1.389	14
.985	.766	8	.997	1.461	6



TABLE IV

Phase	m <sub>b</sub>	m <sub>y</sub>	m <sub>b</sub> - m <sub>y</sub>
.000 m <sub>1</sub>	-0m. 790	+0m. 465	-0.325
.250	+0.005	-0.270	+0.275
.500 m <sub>2</sub>	+0.662	+0.375	+0.287
.750	+0.005	-0.262	+0.267

To get an idea of the magnitude of uncertainty in the determination of our period we may note that the periods have been calculated over 20,000 cycles. An error of one minute in the minima determination which is expected in a photoelectric method will give an uncertainty of  $\pm 0^d.00000008$ . The earlier photoelectric observers also have indicated comparable figures. The photographic observations by Jensch and Bodokia were somewhat handicapped by lack of well determined minima timings over a long interval and the uncertainties may be estimated to about  $\pm 0^d.0000012$  on similar basis.

In Table III, the observed differences in magnitudes in two colours between the variable and the comparison stars have been tabulated against the heliocentric Julian moments.

Normal points of the light curve were calculated from 173 comparisons in blue light and 253 comparisons in yellow light from data recorded in Table IV. Figure 2 shows the normal light curve in blue and yellow light respectively.

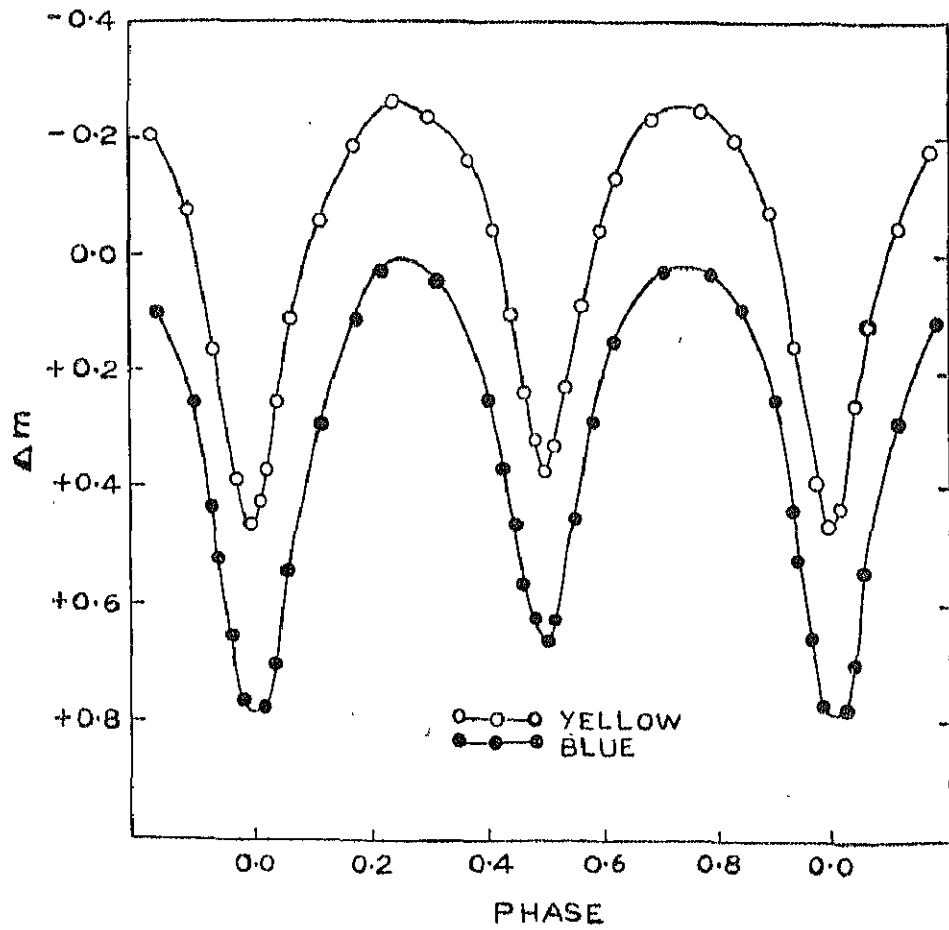


Fig. 2—Light Curve of YY Eridani

From the normal curve the maxima and minima values have been determined and tabulated in Table V. It is seen that the amplitude of the primary minimum exceeds that of the secondary minimum by  $+0^m.13$  in blue and  $+0.20$  in yellow while the brightness of the system is the same outside eclipses at either elongation.

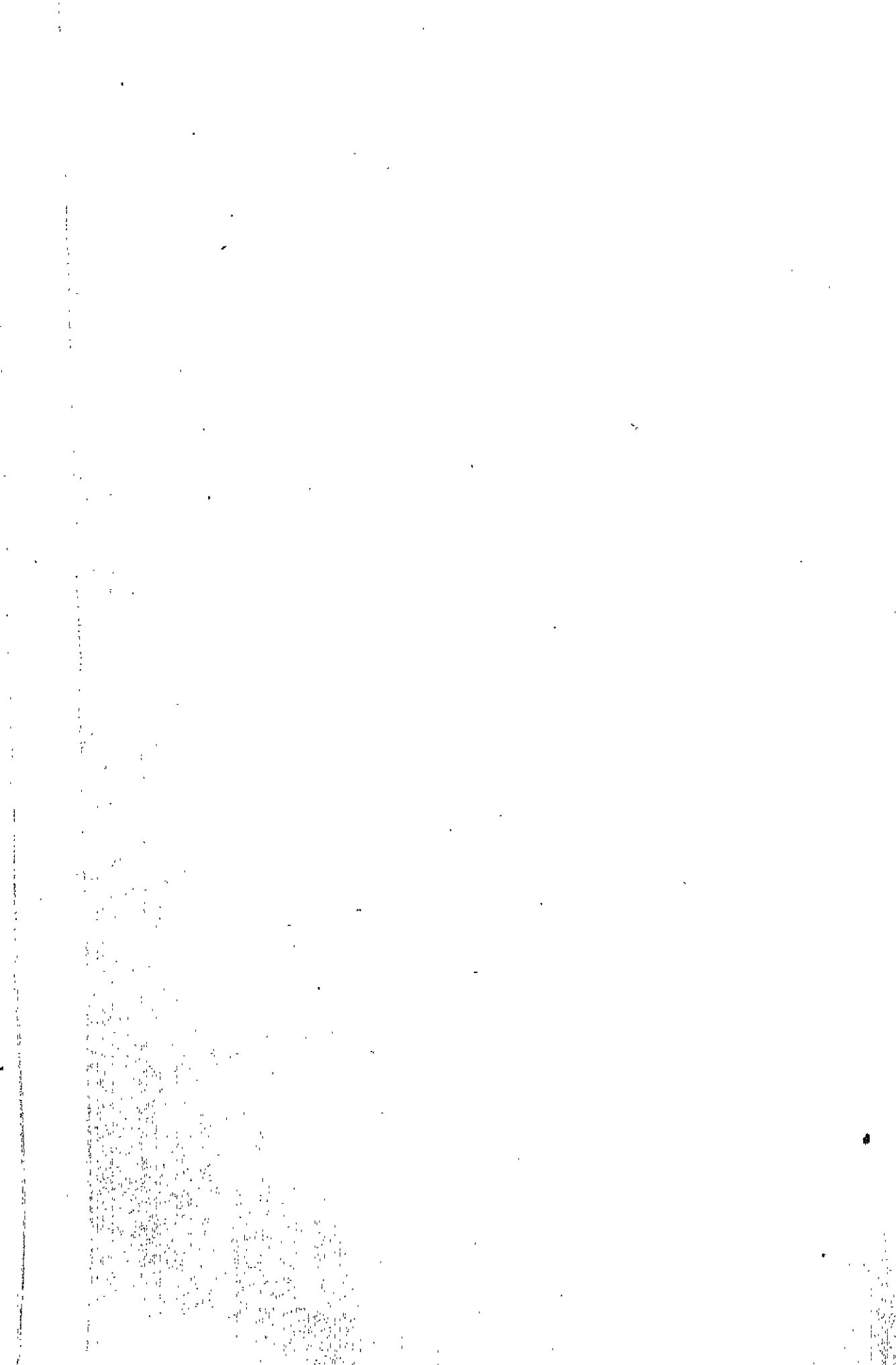
### Acknowledgement

The author is extremely grateful to Dr. M. K. V. Bappu, Director, Kodaikanal Observatory for suggesting the problem and for valuable help and guidance during the whole project.

KODAIKANAL OBSERVATORY, }  
December, 1966.

### REFERENCES

- Bodokia, V. M., (1938)—*Bull. Ap. Obs. Abastumani*—No. 3, 9.  
 Cilie G. G. (1951)—*Harvard Obs. Bull.* No. 920.  
 Haruhata, M. Dambara T., and Kitammna M. (1953)—*Annals Tokyo Astr. Obs.*  
 Sec. Ser. Vol. III—4,227.  
 Jensch A, (1934) —*A. N.* 251, 329  
 Kwee, K. K., (1958)—*BAN XIV*, 485.  
 Purgathofer, A. u. I (1961)—*Mitt. Wein Band* 10.



## KODAIKANAL OBSERVATORY

### BULLETIN Number 182

#### Two Colour Photoelectric observations of the eclipsing variable UW Canis Majoris

A.T. Doss

#### Abstract

Photoelectric light curves of the eclipsing binary UW Canis Majoris have been obtained in the blue and yellow. A new ephemeris is given for the system. The depth of the primary minimum is about  $0^m.45$  in B and  $0^m.47$  in V and that of the secondary is about  $0^m.43$  in B and  $0^m.42$  in V.

#### Introduction

The variability of UW Canis Majoris was discovered by Frost (1906). Later spectroscopic orbits of this system have been published by several authors. Gaposchkin (1936) first observed the light variation from Harvard patrol plates and published its photographic light curve. Struve (1958) has given a schematic model of UW CMA with gas streaming from the the primary that encircles the secondary and envelopes the whole system. The only photoelectric observations that were carried out so far on this system are those by Elvey and Rudnick and their results were utilized by Kuiper (1938) and by Sahade (1959) who has given an alternate model of UW CMA. Seyfert (1941) has obtained a photographic light curve of this star and made three solutions for the ellipticity and eclipses of the components.

The star UW CMA is one of the massive systems known with O7f and O9III stars as components. The present project has been undertaken mainly to obtain accurate photoelectric light curves of UW CMA in B and V of the U, B, V system and to improve the available ephemeris. The results of an analysis of the light curve will be published later.

#### The Observations

The star was observed photoelectrically at Kodaikanal between January 1964 and March 1966 with a photometer attached to the 20cm Cooke refractor. The photo-multiplier tube used was an unrefrigerated RCA 1P21. The out-put from the photo-multiplier was amplified by a linear D.C. amplifier and recorded on a Brown recording

potentiometer. The observations were taken in two colours. The blue deflections were obtained through a Corning 5030 and 2mm Schott GG13 filter combination and the yellow deflections through a Corning 3384 filter. These are the standard filters of the UBV system.

30 CMa was observed as comparison star. The following are the details of the variable and the comparison star as given in the Yale Bright Star Catalogue.

Star	HD	RA (1900)	Dec. (1900)	Vis. Mag.	Spectral Class
29 UW CMa . . . . .	57060	7 <sup>h</sup> 14 <sup>m</sup> 31 <sup>s</sup>	-24° 23'	4.5 †	O7f
30 $\tau$ CMa . . . . .	57061	7 14 34	-24 46	4.39*	O9III

\*Visual magnitude in the standard UBV system.

†Original HR visual magnitude.

The variable was observed for 37 days during the period between January 1964 and March 1966 and 221 points in yellow and 208 points in blue were obtained. The values have been reduced to magnitudes outside the atmosphere by applying suitable extinction corrections. These have been converted into standard B, V magnitudes using linear transformations.

#### New ephemeris

It is seen that the primary minimum occurs about 2.5 hours earlier than the computed epoch with the Gaposchkin (1936) ephemeris (JD 2426326.76 + 4.3934E). From the present set of observations an exact epoch of primary minimum was determined to be JD 2439164.176. Harper's (1917) epoch of JD 242482.207 combined with a period of 4.3934 seems to be nearly correct as can be inferred from Seyfert's (1941) light curve of UW CMa, who has computed phases with the above value. Hence, between Harper's (1917) epoch and the present epoch 3228 cycles have elapsed from which an accurate period was computed.

The new ephemeris is JD (Hel) 2439164.176 + 4.393423E.

It is with this new ephemeris that all the phases (heliocentric) were computed. These are given in Table I for B magnitudes and Table II for V magnitudes. The individual points are plotted in Figures 1 and 2 for getting the light curves of UW CMa in blue and yellow respectively.

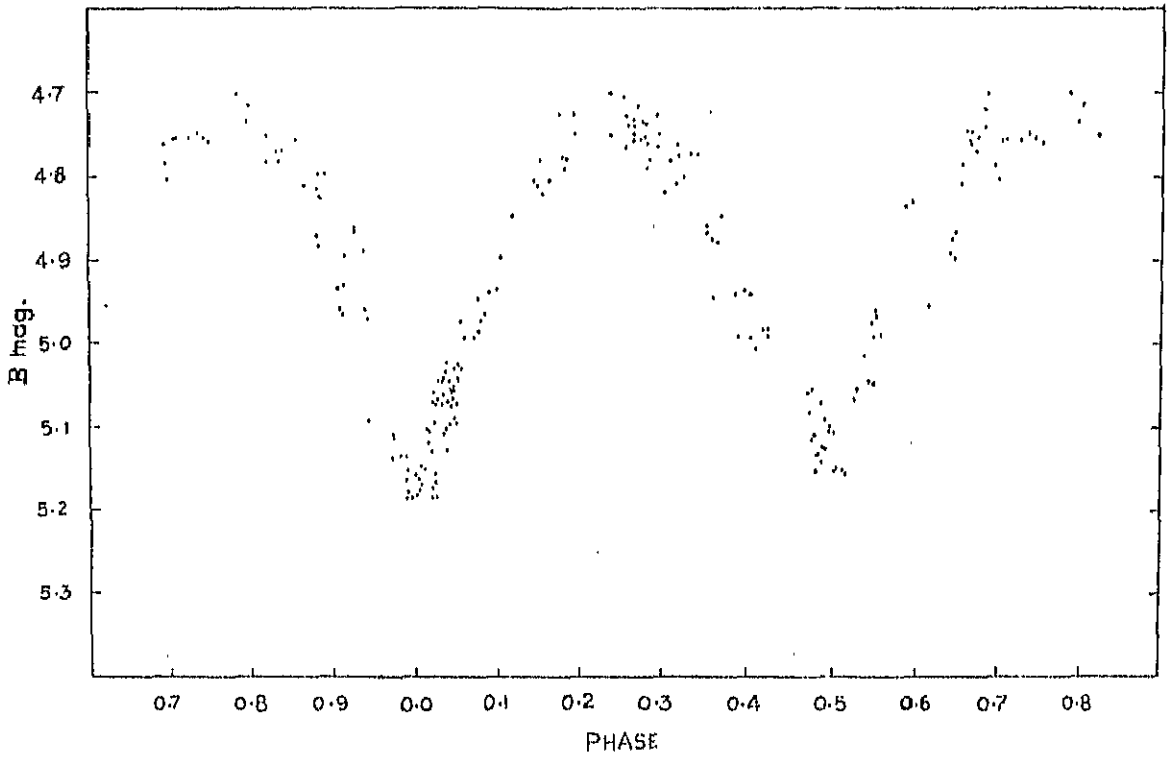


Figure 1—Light curve of UW CMa in blue.

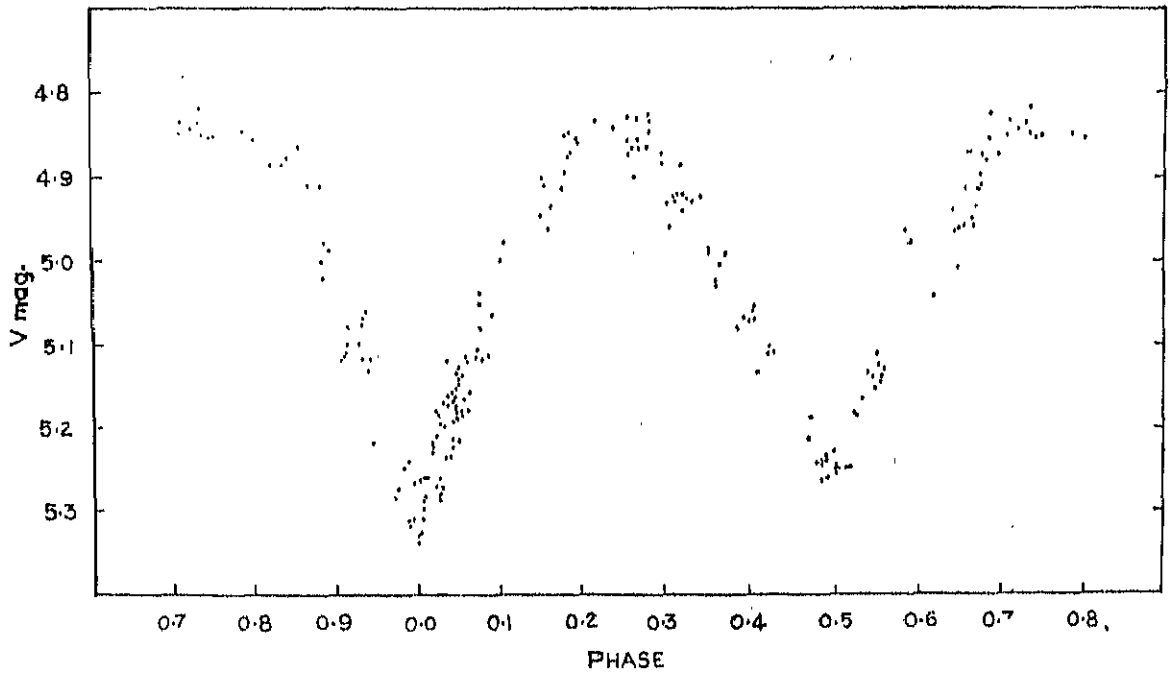


Figure 2—Light curve of UW CMa in yellow.

TABLE I  
*Blue observations of U W Canis Majoris*

J.D. Heliocentric	Phase	B	J.D. Heliocentric	Phase	B
2438000+			2438000+		
411.2143	0.6162	4.955	434.3550	0.8833	4.882
413.2240	0.0736	4.914	435.0765	0.0475	5.096
414.1032	0.2737	4.756	435.0876	0.0500	5.010
414.2928	0.3169	4.759	435.0974	0.0523	5.030
415.2025	0.5239	5.088	435.1013	0.0538	4.972
415.2331	0.5309	5.056	435.1751	0.0699	4.992
415.2636	0.5378	5.016	435.1967	0.0719	4.986
415.2817	0.5419	5.045	435.2092	0.0777	4.973
415.3053	0.5473	5.048	435.2974	0.0978	4.934
416.1602	0.7419	4.752	435.3147	0.1017	4.896
416.1997	0.7509	4.757	435.3765	0.1158	4.817
416.3470	0.7844	4.700	436.0918	0.2786	4.753
425.1809	0.7951	4.732	436.0987	0.2802	4.730
425.2010	0.7997	4.715	436.1696	0.2963	4.766
425.2899	0.8200	4.750	436.2599	0.3169	4.808
426.1746	0.0213	5.173	437.3063	0.3550	4.966
426.2198	0.0316	5.061	437.3116	0.3569	4.990
426.2531	0.0392	5.053	442.0749	0.6404	4.892
426.2719	0.0435	5.031	442.0798	0.6415	4.875
427.1205	0.2366	4.749	442.0902	0.6439	4.898
427.2010	0.2540	4.727	442.0992	0.6460	4.868
427.2274	0.2610	4.738	442.1784	0.6640	4.758
427.2434	0.2646	4.733	442.1847	0.6654	4.760
427.2489	0.2659	4.749	459.2422	0.5479	4.971
427.3017	0.2779	4.735	459.2477	0.5492	4.992
427.3156	0.2810	4.761	459.2575	0.5514	4.959
428.1469	0.4702	5.057	461.0997	0.9707	5.137
428.1635	0.4740	5.054	461.1046	0.9718	5.110
428.2121	0.4851	5.069	461.1088	0.9728	5.113
428.2295	0.4890	5.128	461.1129	0.9737	5.113
428.2739	0.4992	5.152	464.1037	0.6545	4.808
428.2851	0.5017	5.149	464.1099	0.6559	4.784
428.3302	0.5120	5.152	464.1294	0.6603	4.744
428.3434	0.5150	5.156	464.1342	0.6614	4.744
429.1371	0.6956	4.786	464.1717	0.6700	4.770
429.1503	0.6986	4.802	464.1815	0.6722	4.753
429.1809	0.7056	4.755	464.2106	0.6787	4.740
429.1920	0.7081	4.756	464.2211	0.6812	4.717
429.2705	0.7260	4.755	464.2329	0.6839	4.699
429.3052	0.7339	4.748	465.1037	0.8821	4.816
431.1162	0.1461	4.806	465.1086	0.8832	4.826
431.1315	0.1496	4.810	465.1090	0.8833	4.798
431.1426	0.1521	4.779	465.1342	0.8890	4.791
431.1613	0.1563	4.817	465.2092	0.9061	4.933
431.1843	0.1616	4.806	465.2127	0.9067	4.958
431.2398	0.1742	4.725	465.2204	0.9087	4.929
431.2530	0.1772	4.783	465.2231	0.9093	4.965
431.2634	0.1796	4.778	465.2363	0.9123	4.894
431.2752	0.1823	4.790	470.1027	0.0199	5.184
431.2940	0.1866	4.780	470.1096	0.0215	5.164
431.3183	0.1921	4.724	470.1124	0.0221	5.184
431.3280	0.1943	4.750	470.1166	0.0231	5.155
432.2530	0.4018	4.992	470.1194	0.0237	5.095
432.2704	0.4088	5.004	470.1201	0.0239	5.072
432.3190	0.4199	4.983	470.1228	0.0245	5.068
432.3329	0.4230	4.982	470.1367	0.0277	5.044
432.3419	0.4251	4.990	470.1402	0.0285	5.073
434.0828	0.8212	4.782	470.1430	0.0291	5.042
434.1314	0.8324	4.767	470.1714	0.0356	5.123
434.1397	0.8343	4.779	470.1742	0.0362	5.103
434.1571	0.8382	4.767	470.1784	0.0371	5.046
434.2244	0.8535	4.754	470.1819	0.0379	5.022
434.2737	0.8648	4.809	470.1944	0.0408	5.107
434.3307	0.8798	4.870	470.1951	0.0409	5.097

J.D. Heliocentric	Phase	B
2438000+		
470.1978	0.0416	5.066
470.2006	0.0422	5.064
470.2041	0.0430	5.075
470.2089	0.0441	5.089
470.2374	0.0505	5.073
470.2409	0.0514	5.046
471.1966	0.2552	1.701
471.1762	0.2643	4.755
471.1811	0.2654	4.732
471.2172	0.2734	4.714
472.1164	0.4783	5.152
472.1254	0.4803	5.132
472.1324	0.4819	5.124
472.1353	0.4871	5.091
472.1928	0.4956	5.105
472.1956	0.4963	5.100
472.2074	0.4989	5.108
2439000+		
155.3364	0.9880	5.164
155.3406	0.9890	5.179
155.3489	0.9908	5.186
155.3816	0.9983	5.186
155.3857	0.9992	5.182
155.3962	0.0016	5.163
155.4003	0.0025	5.175
155.4024	0.0030	5.178
155.4107	0.0049	5.167
161.1169	0.3037	4.820
161.1502	0.3113	4.779
161.1843	0.3190	4.776
161.2113	0.3252	4.801
161.2565	0.3355	4.772
161.2843	0.3418	4.773
161.3336	0.3530	4.867
161.3627	0.3597	4.941
164.0940	0.9813	5.135
164.1079	0.9845	5.135
164.1384	0.9914	5.152
164.1794	0.0008	5.158
164.1975	0.0019	5.148

J.D. Heliocentric	Phase	B
2439000-		
164.2141	0.0087	5.150
164.2363	0.0137	5.103
164.2419	0.0150	5.104
164.2454	0.0158	5.118
164.2558	0.0182	5.129
164.2641	0.0201	5.071
164.2690	0.0212	5.057
164.2870	0.0253	5.046
164.3155	0.0318	5.032
164.3419	0.0378	5.045
164.3600	0.0419	5.057
164.3697	0.0441	5.055
170.1202	0.3550	4.860
170.1445	0.3585	4.874
170.1702	0.3644	4.877
170.1875	0.3683	4.845
170.2618	0.3852	4.940
170.2896	0.3915	4.991
170.3188	0.3982	4.934
170.3408	0.4032	4.941
171.1444	0.5861	4.835
171.1708	0.5921	4.828
173.1027	0.0318	5.107
173.1256	0.0371	5.070
173.1513	0.0429	5.055
173.1805	0.0496	5.026
173.2124	0.0568	4.993
173.3208	0.0815	4.965
173.3451	0.0870	4.937
209.1535	0.2375	4.700
209.2264	0.2541	4.766
210.1718	0.4692	5.083
210.1864	0.4726	5.112
210.2083	0.4776	5.110
210.2278	0.4820	5.142
212.1783	0.9260	4.865
212.1818	0.9267	4.863
212.2186	0.9351	4.887
212.2318	0.9381	4.957
212.2456	0.9413	4.971
212.2505	0.9424	5.093



TABLE II  
*Yellow observations of UW Canis Majoris*

J.D. Heliocentric	Phase	V	J.D. Heliocentric	Phase	V
2438000+			2438000+		
411.2129	0.6159	5.042	435.0786	0.0480	5.216
413.2261	0.0711	5.079	435.0897	0.0505	5.182
414.2060	0.2971	4.806	435.0946	0.0516	5.161
414.2240	0.3012	4.931	435.1057	0.0541	5.116
414.3011	0.3187	4.885	435.1758	0.0701	5.105
415.2004	0.5234	5.182	435.1980	0.0752	5.117
415.2296	0.5373	5.166	435.2112	0.0782	5.093
415.2615	0.5373	5.133	435.3001	0.0984	4.999
415.2803	0.5176	5.139	435.3198	0.1029	4.978
415.3067	0.5416	5.151	436.0904	0.2783	4.865
416.1622	0.7424	4.853	436.1001	0.2805	4.844
416.2011	0.7512	4.851	436.1710	0.2966	4.872
416.3483	0.7817	4.848	436.2612	0.3172	4.919
425.2024	0.8000	4.856	437.3035	0.5544	5.141
425.3260	0.8282	4.900	437.3167	0.5574	5.130
426.1767	0.0218	5.281	442.0728	0.6400	4.941
426.2212	0.0319	5.161	442.0819	0.6420	4.965
426.2545	0.0395	5.166	442.0923	0.6444	5.007
426.2732	0.0415	5.132	442.1016	0.6465	4.962
426.3406	0.0391	5.157	442.1791	0.6642	4.949
427.2031	0.2554	4.872	442.1860	0.6657	4.958
427.2281	0.2611	4.861	442.2152	0.6724	4.909
427.2552	0.2673	4.861	442.2666	0.6841	4.824
427.3031	0.2782	4.825	442.2450	0.5486	5.124
427.3170	0.2814	5.831	442.2505	0.5498	5.113
428.1239	0.4650	5.213	442.2602	0.5520	5.146
428.1476	0.4704	5.187	461.1011	0.9710	5.282
428.1649	0.4743	5.165	461.1067	0.9723	5.273
428.2135	0.4851	5.206	464.1051	0.6548	4.907
428.2760	0.4996	5.251	464.1092	0.6557	4.913
428.2857	0.5018	5.249	464.1308	0.6606	4.871
428.3316	0.5123	5.249	464.1349	0.6616	4.871
428.3455	0.5155	5.247	464.1724	0.6701	4.916
428.3854	0.5245	5.186	464.1829	0.6725	4.897
429.1392	0.6961	5.875	464.2002	0.6764	4.876
429.1823	0.7059	4.850	464.2113	0.6790	4.877
429.1934	0.7084	4.836	464.2238	0.6818	4.855
429.2503	0.7214	4.843	464.2342	0.6842	4.822
429.2830	0.7288	4.836	465.1063	0.8827	5.020
429.2948	0.7315	4.817	465.1105	0.8832	5.000
429.3066	0.7342	4.850	465.1204	0.8859	4.981
431.1190	0.1467	4.945	465.1356	0.8894	4.988
431.1329	0.1499	4.899	462.2106	0.9064	5.118
431.1412	0.1518	4.910	465.2141	0.9072	5.114
431.1620	0.1565	4.962	465.2217	0.9089	5.111
431.1836	0.1614	4.936	465.2252	0.9097	5.099
431.2412	0.1745	4.912	465.2377	0.9126	5.079
431.2523	0.1771	4.894	470.1041	0.0202	5.270
431.2641	0.1797	4.849	470.1110	0.0218	5.286
431.2759	0.1824	4.876	470.1117	0.0220	5.279
431.2926	0.1862	4.871	470.1138	0.0224	5.277
431.3197	0.1924	4.855	470.1180	0.0234	5.260
431.3273	0.1941	4.860	470.1214	0.0242	5.195
432.2502	0.4042	5.058	470.1381	0.0280	6.198
432.2725	0.4093	5.133	470.1437	0.0292	5.167
432.3204	0.4202	5.108	470.1770	0.0368	5.234
432.3343	0.4233	5.102	470.1798	0.0375	5.222
432.3475	0.4263	5.109	470.1958	0.0411	5.190
434.0842	0.8216	4.885	470.1992	0.0419	5.174
434.1411	0.8346	4.884	470.2027	0.0427	5.178
434.1585	0.8385	4.878	470.2062	0.0435	5.179
434.2258	0.8539	4.862	470.2103	0.0444	5.187
434.2758	0.8652	4.909	470.2381	0.0507	5.179
434.3418	0.8803	4.910	471.1318	0.2542	4.830

J.D. Heliocentric	Phase	V
2438000-[-		
471-1352	0-2519	4-854
471-1718	0-2639	4-851
471-1804	0-2652	4-829
472-1282	0-4809	5-264
472-1344	0-4824	5-245
472-1490	0-4857	5-239
472-1515	0-4862	5-231
472-1942	0-4960	5-227
472-1976	0-4967	5-247
472-2011	0-4976	5-256
2439000-[-		
129-1642	0-0309	5-449
129-1670	0-0315	5-458
129-2253	0-0418	5-448
129-2316	0-0462	5-444
129-2906	0-0596	5-478
129-2969	0-0611	5-416
129-3510	0-0734	5-050
129-3559	0-0736	5-037
130-3920	0-3103	4-923
130-3948	0-3110	4-931
130-4017	0-3125	4-949
130-4337	0-3198	4-939
135-2032	0-4054	5-054
155-3351	0-9877	5-309
155-3385	0-9885	5-318
155-3476	0-9905	5-309
155-3802	0-9980	5-337
155-3837	0-9988	5-329
155-3871	0-9995	5-326
155-3969	0-0018	6-307
155-3982	0-0024	5-298
155-4031	0-0032	5-288
155-4114	0-0051	5-283
161-1204	0-3045	4-959
161-1539	0-3149	4-919
161-1856	0-3193	4-915
161-2134	0-3257	4-921
161-2579	0-3358	4-927
161-2856	0-3421	4-922
161-3350	0-3533	4-904
161-3641	0-3593	5-024
164-0926	0-9810	5-248
164-1126	0-9856	5-239
164-1398	0-9918	5-268
164-1808	0-0041	5-263
164-1995	0-0073	5-259

J.D. Heliocentric	Phase	V
2439000 [-		
164-2155	0-0090	5-261
164-2377	0-0140	5-220
164-2433	0-0153	5-223
164-2468	0-0161	5-230
164-2572	0-0185	5-211
164-2662	0-0205	5-182
164-2701	0-0215	5-183
164-2891	0-0257	5-175
164-3169	0-0321	5-173
164-3433	0-0381	5-150
164-3613	0-0422	5-153
164-3711	0-0444	5-128
170-1218	0-3533	4-981
170-1461	0-3589	5-027
170-1709	0-3645	5-004
170-1889	0-3686	4-991
170-2632	0-3855	5-089
170-2910	0-3919	5-068
170-3209	0-3937	5-072
170-3471	0-4036	5-071
171-1458	0-5864	4-964
171-1722	0-5924	4-981
173-0877	0-0284	5-270
173-1014	0-0322	5-231
173-1263	0-0372	5-212
173-1527	0-0432	5-166
173-1812	0-0497	5-138
173-2138	0-0571	5-118
173-2569	0-0669	5-115
173-3222	0-0818	5-113
173-3472	0-0875	5-067
178-1573	0-1823	4-848
178-3080	0-2166	4-832
209-1539	0-2380	4-810
209-2278	0-2511	4-872
209-2532	0-2602	4-901
210-2097	0-4779	5-243
210-2285	0-4822	5-240
210-2493	0-4869	5-260
212-1790	0-9261	5-099
212-1831	0-9270	5-117
212-1929	0-9293	5-067
212-1956	0-9299	5-074
212-2200	0-9351	5-061
212-2331	0-9384	5-130
212-2463	0-9414	5-117
212-2512	0-9425	5-217

The zero phase given by Struve *et al* (1958) refers to the epoch of the periastron passage. Since the phase of the periastron passage was given, the epoch of the corresponding primary minimum can be known. Combining the Struve *et al*, (1958) epoch of the primary minimum with the new period of 4.393423, we find a good agreement with the present epoch.

### The light curves

The present light curves shows the same anomalies already pointed out by Seyfert (1941). From the Figures 1 and 2, it can be noted that the depth of the primary minimum is about  $0^m.45$  in B and  $0^m.47$  in V and that of the secondary is about  $0^m.43$  in B and  $0^m.42$  in V. The (B-V) colour at primary minimum is  $-0^m.13$  and at secondary minimum it is  $-0^m.10$ . It is also seen that the duration of the secondary minimum is more than that of the primary minimum. The general shape of the light curve indicates opacity effects caused by electron scattering in an extended envelope.

### Acknowledgements

I am greatly indebted to Dr. M.K.V. Bappu for suggesting this programme and for his continued guidance. I want to thank Mr. P. Viswanadham for his help during the 1964 observations.

KODAIKANAL OBSERVATORY, }

January, 1967. }

### REFERENCES

- FROST, E.B., (1906), AP.J., 23, 265.  
 GAPOSCHKIN, S., (1936), HARVARD BULL. NO. 902, p. 17.  
 HARPER, W. E., (1917), PUB. DOM. OBS. 4, 115.  
 KUIPER, G. P., (1938), AP. J., 88, 503.  
 SAHADE, J., (1959), PUB. A.S.P., 71, 151.  
 SEYFERT, CARL, K. (1941), AP. J., 93, 442.  
 STRUVE, O., (1958), A. J. 63, 346.  
 STRUVE, O., SAHADE, J., HUANG, S.S., AND ZEBERGS, V. (1958),  
 AP. J., 128, 328.

# KODAIKANAL OBSERVATORY

BULLETIN Number 183

## The Wolf-Rayet binary HD 68273

K. S. Ganesh and M. K. V. Bappu

### Abstract

A series of 127 spectrograms of this binary obtained at Kodaikanal during 1965 and 1966 have been used for a study of radial velocities of the emission and absorption lines. The period is found to be 78.5 days. The spectral type of the O component is O7.5 as determined from a single high dispersion Mount Stromlo coude spectrogram. The velocity curves of the Wolf-Rayet component are determined for HeII 4686, the CIII complex at 4652Å and CIV 4441. The velocity curve for the O component is from measures of the absorption line H5. Arguments are presented to show that the velocity curve of CIII 4652 is the best suited for the study of masses of the components. The eccentricity of the orbit is 0.17. The gamma-axis for HeII 4686 is red-shifted with respect to that of H5 by 82 km/sec. The values of  $m_o \sin^3 i$  and  $m_w \sin^3 i$  are 46.3 and 13.0 solar masses respectively. The inclination of the orbit is likely to be such that the system exhibits eclipses. The W-component seems to be the most massive yet known among the very small group of Wolf-Rayet stars.

### Introduction

The spectrum of HD 68273 has long been known to be composite and variable. The spectrum has been described by Cannon (1901) and Worszel (1916) from objective prism spectra obtained at Arequipa and the Cape respectively. Perrine (1918) first announced the striking spectral variations of both emission and absorption lines. These have been confirmed in a recent study by Smith (1955) who found that the variations were both short-lived and infrequent. Smith also gives a list of wavelengths of both emission and absorption lines, as seen in high contrast low dispersion slit spectra obtained by him, with the 60-inch reflector at Boyden station. Sahade (1955) announced that radial velocities measured indicated the star to be a binary that exhibits the spectra of two components, with most of the absorption lines associated with a companion of spectral type O. From the few measures that Sahade had at his disposal, a period of the order of 24 days was indicated. Gaposchkin (1959) estimated from radial velocities obtained at Mount Stromlo that a tentative period of 16.2 days could be assigned for the orbital motion. His visual estimates indicated light variability with a small range, thus holding out promise of the system being an eclipsing binary.

The brightness of HD 68273 enables the examination of its spectrum in the far ultraviolet by the techniques of rocket spectroscopy. Stecher and Milligan (1962) from objective grating spectra find the energy distribution from 1600 Å

to  $3000 \text{ \AA}$  to depart substantially from that of a black body at  $30000^\circ\text{K}$ . Aller and Faulkner (1964) have determined photoelectrically the energy distribution in the domain  $3400\text{--}5900 \text{ \AA}$ . They estimate a colour temperature of  $32000^\circ\text{K}$  on the basis of measures of monochromatic magnitudes made at Mount Stromlo on five nights. One needs to recognize in such continuum flux measurements, the role played by the continuum of the O star.

HD 68273 is the brighter star of the optical double Gamma-Velorum. The fainter component HD 68243 is of MK type B2IV and is 2.4 mag. fainter than HD 68273. The absolute magnitude of the Wolf-Rayet star is  $M_V = -5.6$ , if a value of  $M_V = -3.3$  is ascribed to HD 68243 on the basis of the MK classification type assigned. One assumes also, following Schlesinger and Jenkins (1940) that both HD 68243 and HD 68273 form a proper motion system. This Wolf-Rayet star along with Zeta Puppis probably excites the Gum nebula, which is the largest HII region known in our galaxy.

The number of Wolf-Rayet binary systems that exhibit the spectra of both components is very small. Of these, the best studied is V444 Cygni which has a Wolf-Rayet star of the nitrogen sequence along with an early type star. Sahade has shown that the absorption lines indicative of an early type star are seen on the spectra of HD 68273. Since HD 68273 contains a WC7 star with an early type companion, presumably an O star, it furnishes the possibility of determination of a reliable mass for the WC7 star and an O star, if the orbital parameters can be derived in detail and also, if the orbital plane is favourably inclined for detection of an eclipse. Only one other system HD 168206 (WC7+O) has preliminary spectroscopic orbits available for both the components. It, therefore, is of great interest to study the system of HD 68273 in detail and increase our information pertaining to the masses of these early stars.

### The spectroscopic observations

The spectra were obtained at Kodaikanal over the period February-April 1965 and November 1965-April 1966. A total of 127 spectrograms, obtained with the cassegrain spectrograph attached to the 51 cm reflector, have been measured for radial velocity. The spectra have a dispersion of  $125 \text{ \AA/mm}$ . They were obtained in the second order of a 600 lines/mm Bausch and Lomb grating blazed in the first order at  $7500 \text{ \AA}$ . Most of the spectra were obtained on Ilford N-40 process plates. A few spectra were obtained in 1965 in Ilford Thin Film Half Tone plates. The spectra have a width of 300 microns. A projected slit width in the camera focal plane of 15 microns was used. The velocity measures of the emission lines were confined to those of HeII 4686, CIV 4441 and the emission complex at  $4652 \text{ \AA}$  originating predominantly from CIII. The velocity measures of the O component depend entirely on the measures of the hydrogen lines  $4340 \text{ \AA}$ ,  $4100 \text{ \AA}$ , with occasional measures on HeII 4200 and HeI 4471. These are all listed in Table 1. Previous investigators of this system have reported on the appreciable scatter in the velocity measures made by them. We find this to be prevalent even in our measures. The emission lines are in general weak and diffuse, but the high contrast photographic emulsion used enables the spectra show up the emission features with appreciable contrast.

TABLE I  
*Velocity measures of HD 68273*

Plate	JD of observa- tion	Phase (in period)	Velocities in Km/Sec.						
			4686e	4652e	4441e	4340a	4200a	4101a	
1	2	3	4	5	6	7	8	9	
27	2438817.20	0.04	+ 97.9	+ 57.4	..	- 31.1	..	..	..
33a	818.17	0.05	+154.2	+ 73.5	..	- 65.6	- 15.7	- 21.9	..
33b	818.18	0.05	+ 41.6	+ 09.0	-150.5	- 13.8	-104.9	- 58.5	..
40	820.12	0.07	+149.7	+ 49.0	..	+ 4.1	- 46.4	- 90.6	..
45	820.27	0.08	+ 88.9	+ 16.8	-108.7	- 22.8	..	+ 32.9	..
49	821.26	0.09	+121.6	- 7.7	..	..	..	- 31.4	..
54	822.28	0.09	+ 65.3	0.0	-108.7	- 40.1	- 34.3	- 59.2	..
55	824.23	0.09	- 70.4	..	-150.5	..	..	..	..
58	825.29	0.14	+ 49.3	+ 8.4	-142.4	+ 03.5	..	+ 32.9	..
65	827.22	0.17	+ 09.0	- 32.2	..	- 57.3	..	- 03.7	..
66	827.27	0.17	- 39.7	- 56.8	-201.8	+ 38.0	..	- 22.7	..
69	828.23	0.18	+ 9.0	- 96.7	- 134.3	+ 38.0	+ 47.0	..	..
73	830.12	0.20	- 41.0	0.0	..	+ 29.0	+ 02.1	-132.3	..
76	831.24	0.22	+ 56.9	- 07.7	- 49.3	+ 72.5	..	-22.7	..
80	834.18	0.25	-103.7	- 57.4	-219.4	- 05.5	..	+ 05.1	..
82	834.24	0.25	+ 15.4	+ 89.0	-236.3	- 40.1	+ 20.0	- 13.2	..
87	837.13	0.29	- 31.4	-129.6	- 58.1	+ 72.5	+ 2.1	+ 69.4	..
92a	843.10	0.37	+ 01.0	+ 33.0	+ 35.0	+ 11.7	..	- 59.2	..
92b	843.13	0.37	+ 09.0	+ 08.4	-253.0	- 57.3	..	- 22.7	..
95	851.22	0.47	+ 56.9	+ 97.4	-108.7	- 22.8	+ 28.6	- 29.2	..
99	858.19	0.56	+121.6	+ 49.0	- 41.2	+ 03.4	..	- 77.5	..
100	859.17	0.57	+ 72.9	+ 40.6	+ 27.0	- 22.8	..	- 49.7	..

TABLE 1—*contd.*

1	2	3	4	5	6	7	8	9
150	2439083.34	0.43	-47.4	-15.5	+168.1	+03.5	+47.1	-31.4
151	083.38	0.43	+17.3	+16.8	-133.7	-13.8	..	-141.1
152	083.41	0.43	-23.0	+09.0	-218.7	-57.3	+47.1	-68.0
153	084.40	0.44	+145.9	+60.6	-06.7	+64.2	..	+51.9
156	085.37	0.45	-47.3	+32.9	-201.8	..	+55.7	..
158	086.31	0.47	+121.6	-56.1	..	-57.3	..	-95.8
159	086.35	0.47	+09.0	0.0	-168.1	-57.3	+109.9	-95.8
161	086.44	0.47	-23.0	-47.7	-08.0	-04.8	+127.8	-21.9
163	087.36	0.48	+25.6	+09.0	-66.2	+03.5	+101.4	-31.4
167	108.28	0.75	+121.5	+146.5	+120.2	+11.7	..	-77.5
168	108.28	0.75	+177.9	+194.8	+94.5	+11.7	..	-141.8
169	108.34	0.75	+153.6	+178.6	+18.2	-40.0	+28.6	-87.0
171	111.35	0.78	+105.6	+146.4	+69.5	..	..	-114.0
176	112.24	0.80	+225.9	+178.6	-24.3	+11.7	+10.7	-59.2
177	112.27	0.80	+193.9	+146.4	..	-22.8	+2.1	-151.3
181	112.32	0.80	+145.2	+130.3	+171.5	-109.8	+15.0	-132.3
185	119.23	0.89	+202.2	+187.0	+128.9	-82.9	..	+5.9
186	119.26	0.89	+154.2	+219.3	+171.5	-4.8	+28.3	-58.5
187	119.28	0.89	+129.9	+154.8	+120.8	-82.9	+02.1	-114.0
193	120.26	0.90	+298.8	+211.5	+128.9	-40.1	+29.3	-114.0
194a	120.29	0.90	+242.5	+195.4	+154.6	-118.1	..	-178.3
194b	120.31	0.90	+210.5	+179.3	..	-22.1	+20.7	-68.0
197	124.27	0.95	+113.9	+81.9	-31.7	-48.4	..	..
198a	124.30	0.95	+121.6	+49.0	-57.4	-57.4	+02.1	-205.4
198b	124.32	0.95	..	+57.4	+104.0	-57.3	..	-168.8

TABLE I—*contd.*

1	2	3	4	5	6	7	8	9
198c	.	.	.	+154.8	-184.9	-31.1		-196.6
202	.	.	+226.5	+138.7	-66.2	-126.4	-60.0	-150.6
203a	.	.	.	+130.3	+61.4	-31.1	+20.7	-42.4
208	.	.	-71.0	-153.5	-185.0	-65.6		+104.5
213a	.	.	-47.4	-96.7	-295.0	+29.7	+227.0	-22.0
213b	.	.	-55.0	-96.7	-303.8	-31.1		-32.9
214	.	.	-79.3	-104.5	-235.6	-48.4	+97.1	-40.2
215a	.	.	-07.0	-88.3	-150.5	-13.8		+24.1
215b	.	.	+01.3	-64.5	-116.8	+12.4	+272.0	+42.4
218a	.	.	-71.0	-40.0	-83.0	+29.7	+137.1	-68.0
218b	.	.	-47.4	-104.5	-125.6	-22.1		+24.1
221	.	.	-95.3	-88.4	-261.2	-13.8		-58.5
223	.	.	-79.3	-96.7	-133.7	-65.6	+20.7	-187.1
228	.	.	-23.0	-104.5	-14.9	-57.3		-214.9
231b	.	.	.	-80.6	-66.2	-23.5	+11.4	-49.7
236a	.	.	-86.8	-121.2	-57.4	-48.4	+83.5	+155.0
236b	.	.	-25.2	-72.2	+10.1	+38.7	+177.7	+42.4
241	.	.	-130.9	-40.0	-116.8	-4.8	+101.4	-24.1
247	.	.	-104.3	-72.2	-185.0	-4.8	+11.4	-12.4
249	.	.	-194.5	+32.9	-99.9	+29.7	+65.0	-40.2
249	.	.	+198.2	+36.6	-96.2	+26.0		-36.5
252c	.	.	.	+25.3	-21.2	+57.5		+34.7
252d	.	.	.	+21.0	-02.9	+15.4		+82.1
254	.	.	+95.1	+20.3	-68.7	-08.3		-16.4
255	.	.	+103.5	+30.7	-68.7	-18.0		..



TABLE 1—*contd.*

	1	2	3	4	5	6	7	8	9
258a .	.	2439164.14	0.46	..	- 06.4	- 90.3	..	..	- 76.5
262a .	.	165.14	0.47	+ 19.3	+ 35.5	- 46.7	..	..	- 122.0
262b .	.	165.15	0.47	- 14.3	+ 24.2	- 33.3	..	..	- 97.4
267a .	.	167.26	0.50	+ 66.0	+ 58.0	- 64.0	+ 40.5	..	- 20.5
267b .	.	167.27	0.50	+ 56.7	+ 51.3	- 62.5	- 04.8	..	- 130.0
267c .	.	167.28	0.50	+ 61.1	+ 69.3	- 24.8	..	..	- 156.6
269 .	.	168.18	0.51	+ 69.3	+ 61.4	- 03.0	..	..	- 44.2
274 .	.	170.09	0.53	+ 62.5	+ 95.1	- 08.3	..	..	- 137.3
275 .	.	170.12	0.53	+ 35.7	+ 67.4	- 43.8	+ 28.7	..	- 105.8
276 .	.	170.15	0.53	+ 40.0	+ 72.5	- 56.9	+ 12.0	..	- 79.6
284a .	.	173.10	0.57	+ 140.8	+ 100.5	+ 103.6	- 34.2	..	- 47.7
284c .	.	173.11	0.57	+ 136.6	+ 104.7	+ 45.8	- 38.4	..	- 89.1
288a .	.	174.13	0.58	+ 112.4	+ 104.8	+ 98.3	- 15.3	..	- 93.4
288c .	.	174.16	0.58	+ 105.2	+ 105.3	+ 65.3	- 17.3	..	..
291a .	.	174.12	0.60	+ 141.5	+ 113.3	+ 81.6	- 22.4	..	- 143.0
291c .	.	175.16	0.60	+ 150.3	+ 126.3	+ 81.4	- 44.3	..	- 198.4
293b .	.	176.13	0.61	+ 143.8	+ 127.4	+ 91.3	- 85.7	..	+ 27.4
293c .	.	176.14	0.61	+ 126.0	+ 110.1	+ 100.5	..	..	+ 10.2
296a .	.	177.12	0.62	+ 143.9	+ 135.9	+ 100.7	+ 17.7	..	+ 163.2
302a .	.	181.09	0.67	+ 203.5	+ 185.6	+ 135.9	..	..	- 187.7
302b .	.	181.10	0.67	+ 185.2	+ 178.1	+ 112.2	- 36.1	..	- 179.9
305 .	.	181.27	0.68	+ 166.7	+ 200.1	+ 110.8	- 49.3	..	- 104.4
306 .	.	181.37	0.68	+ 211.5	+ 155.6	+ 101.2	- 61.1	..	- 159.6
307a .	.	182.15	0.69	+ 158.0	+ 77.3	+ 115.8	..	..	..
307b .	.	182.16	0.69	+ 125.2	+ 182.8	+ 55.5	..	..	- 136.1

311a	.	.	.	.	.	2439183.12	0.70	+165.8	+174.7	+55.8	-63.2	..	-238.8
311b	.	.	.	.	.	183.13	0.70	+197.0	+189.4	+87.4	-74.6	..	-278.1
315a	.	.	.	.	.	185.31	0.73	+188.6	+197.6	+147.6	-90.3	..	-249.2
315b	.	.	.	.	.	185.32	0.73	+182.0	+191.0	+166.7	-116.4	..	-98.6
318a	.	.	.	.	.	186.83	0.75	+240.6	+217.2	+119.0	..	..	-171.7
318b	.	.	.	.	.	186.84	0.75	+169.6	+194.7	+85.0	-41.6	..	-227.3
321a	.	.	.	.	.	187.60	0.76	+222.5	+191.3	+109.3	-70.9	..	-209.0
321c	.	.	.	.	.	187.61	0.76	+238.3	+191.1	+109.2	-70.7	..	-128.2
327a	.	.	.	.	.	191.67	0.81	+238.3	+207.2	+137.3	-55.4	..	-132.9
328c	.	.	.	.	.	191.72	0.81	+240.7	+217.5	+137.9	-57.1	..	-55.6
329b	.	.	.	.	.	191.75	0.81	+245.3	+222.1	+159.8	-32.2	..	-93.2
330c	.	.	.	.	.	191.80	0.81	+253.8	+239.0	+168.4	-60.6	..	-48.8
336a	.	.	.	.	.	193.78	0.83	+202.8	+203.7	+150.3	-77.3	..	+129.9
336b	.	.	.	.	.	193.79	0.83	+252.2	+245.7	+131.7	-49.9	..	+180.8
338a	.	.	.	.	.	194.70	0.85	+247.9	+232.9	+149.1	-41.1	..	+180.8
338b	.	.	.	.	.	194.73	0.85	+265.8	+217.8	+162.9	-41.1	..	..
344	.	.	.	.	.	202.59	0.92	+191.2	+183.7	+73.5	-78.3	..	-185.8
345b	.	.	.	.	.	202.62	0.92	+178.7	+171.8	+80.3	-64.5	..	-204.1
345c	.	.	.	.	.	202.62	0.92	+162.2	+154.5	..	-53.0	..	+00.8
349	.	.	.	.	.	207.66	0.01	+100.6	+44.1	+22.0	..	..	+30.5
350	.	.	.	.	.	207.68	0.01	+79.5	+22.8	+14.6	-78.0	..	+00.4
351	.	.	.	.	.	207.72	0.01	+85.3	+36.9	+16.0	-71.9	..	-06.2
352	.	.	.	.	.	207.74	0.01	+95.5	+31.3	+18.2	-68.8	..	-11.2
353a	.	.	.	.	.	207.77	0.01	+100.3	+59.7	+3.0	-64.3	..	-27.6
354	.	.	.	.	.	215.65	0.11	-12.7	-102.3	..	+06.4	..	..

### The orbital elements

The almost continuous series of observations from November 1965 to April 1966 indicate a period of 78.5 days. Figure 1 is a plot of the velocities of

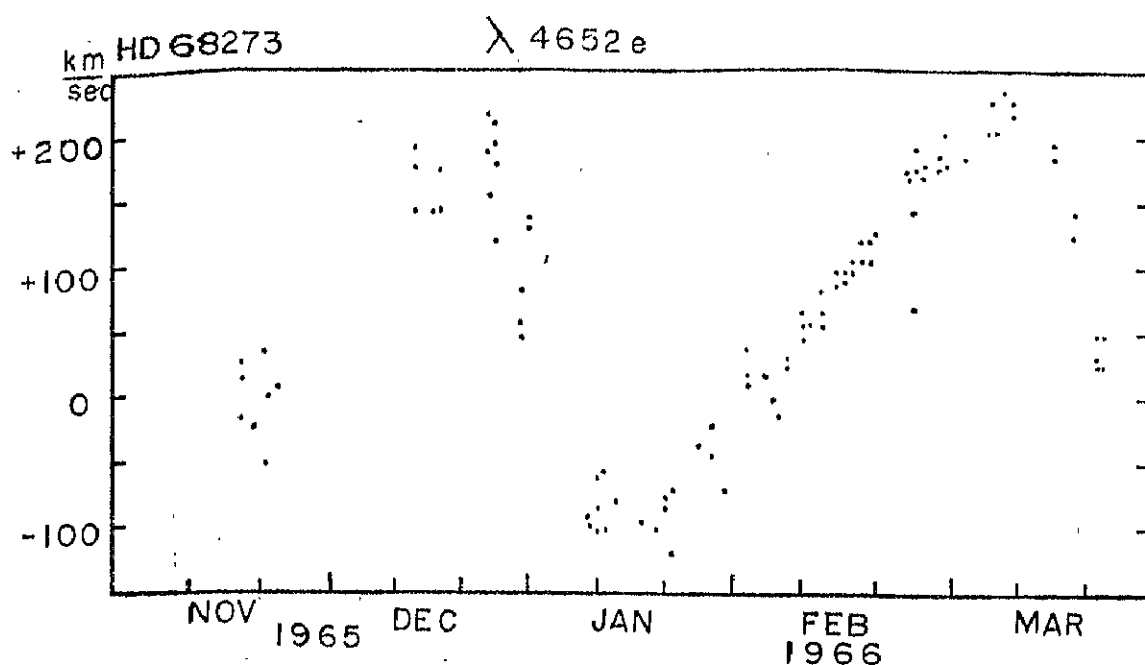


Figure 1:—Velocity variations of HD 68273—November 1965—March 1966

4652 $\text{\AA}$ , covering the period November 1965 to March 1966. In combination with our velocity measures, we used a few values of velocities obtained by the Lick Observers from Chile. We also have utilized radial velocity measures of the absorption lines of the O star from a single high dispersion (6.7 $\text{\AA}/\text{mm}$ ) Coude spectrogram. This spectrogram was obtained by one of us with the Mount Stromlo 188 cm reflector through the courtesy of Director Bok and ANZAAS. The zero phase is assumed to be JD 2439128.25. The observations on two nights seem to rule out the possibility of a period close to a day. It is difficult at this stage to derive a more exact period of this system. Extended observations for some time will be necessary for a more correct spectroscopic determination of the period.

The observations of the emission lines 4686 $\text{\AA}$ , 4652 $\text{\AA}$ , 4441 $\text{\AA}$  and the absorption line 4340 $\text{\AA}$  grouped into 20 normal points are given in Table 2. Figure 2

TABLE 2  
*Velocity measures—normal points*

No.	Mean phase	Mean Velocities			
		4686	4652	4441	4340
1	2	3	4	5	6
1	0.02	+101.20	+ 45.90	+ 19.10	— 64.00
2	0.10	— 39.80	— 88.60	—181.03	— 10.65

TABLE 2—*Contd.*

1	2	3	4	5	6
3 . . . . .	0.12	— 61.30	— 72.09	—163.90	+ 13.63
4 . . . . .	0.17	— 77.16	— 38.92	—162.99	+ 39.92
5 . . . . .	0.24	—109.80	— 80.20	—217.26	— 31.90
6 . . . . .	0.29	— 83.09	— 89.62	—114.46	+ 33.96
7 . . . . .	0.34	— 38.25	— 76.75	—173.60	+ 9.36
8 . . . . .	0.44	— 25.00	+ 27.35	— 89.50	+ 21.93
9 . . . . .	0.46	— 8.07	+ 31.33	—130.45	+ 30.65
10 . . . . .	0.48	+ 23.64	+ 39.21	— 47.99	+ 40.47
11 . . . . .	0.53	+ 51.86	+ 74.11	— 27.99	+ 20.35
12 . . . . .	0.57	+114.33	+107.04	+ 71.37	— 27.23
13 . . . . .	0.62	+137.90	+139.75	+108.27	+ 17.65
14 . . . . .	0.68	+175.02	+180.45	+115.17	— 48.83
15 . . . . .	0.71	+183.34	+188.18	+135.56	— 86.12
16 . . . . .	0.75	+217.82	+198.61	+105.63	— 61.07
17 . . . . .	0.80	+214.40	+197.45	+143.51	— 56.43
18 . . . . .	0.87	+206.09	+208.46	+152.74	— 59.81
19 . . . . .	0.91	+201.70	+187.30	+114.30	— 40.96
20 . . . . .	0.95	+180.52	+123.61	+ 94.25	— 34.53

contains the plots of radial velocities of  $\lambda 4441$ ,  $\lambda 4652$  and  $\lambda 4686$ . The plots of radial velocities show that the orbits are near-circular. Hence Sterne's method was utilized to solve for the elements. These elements were treated again as preliminary values in the case of  $4686\text{\AA}$  and  $4652\text{\AA}$  and final elements calculated by the method of Lehman-Filhes. The elements derived from the three emission lines are given in Table 3.

TABLE 3

	HeII 4686 $\text{\AA}$	CIII complex 4652 $\text{\AA}$	CIV 4441 $\text{\AA}$
$\gamma$ (km/sec)	$+63.9 \pm 2.4$	$+59.9 \pm 3.0$	$-26.5 \pm 11.4$
K (km/sec)	$163.7 \pm 3.5$	$153.5 \pm 4.4$	$196.7 \pm 15.4$
$e$	$0.16 \pm .02$	$0.17 \pm .03$	$0.13 \pm .08$
$\omega$	$96^\circ \pm 8^\circ$	$87^\circ \pm .9^\circ$	$78^\circ \pm 43^\circ$

In the derivation of a velocity from a measurement of the CIII emission complex, we have assumed a wavelength of  $4652.0\text{\AA}$  as the mean wavelength of the band and the shifts from this arbitrary value denote the velocities. While this prevents the assignment of an exact value for the systemic velocity as inferred from measures of this line, it is useful in providing a set of parameters that define the orbital motion.

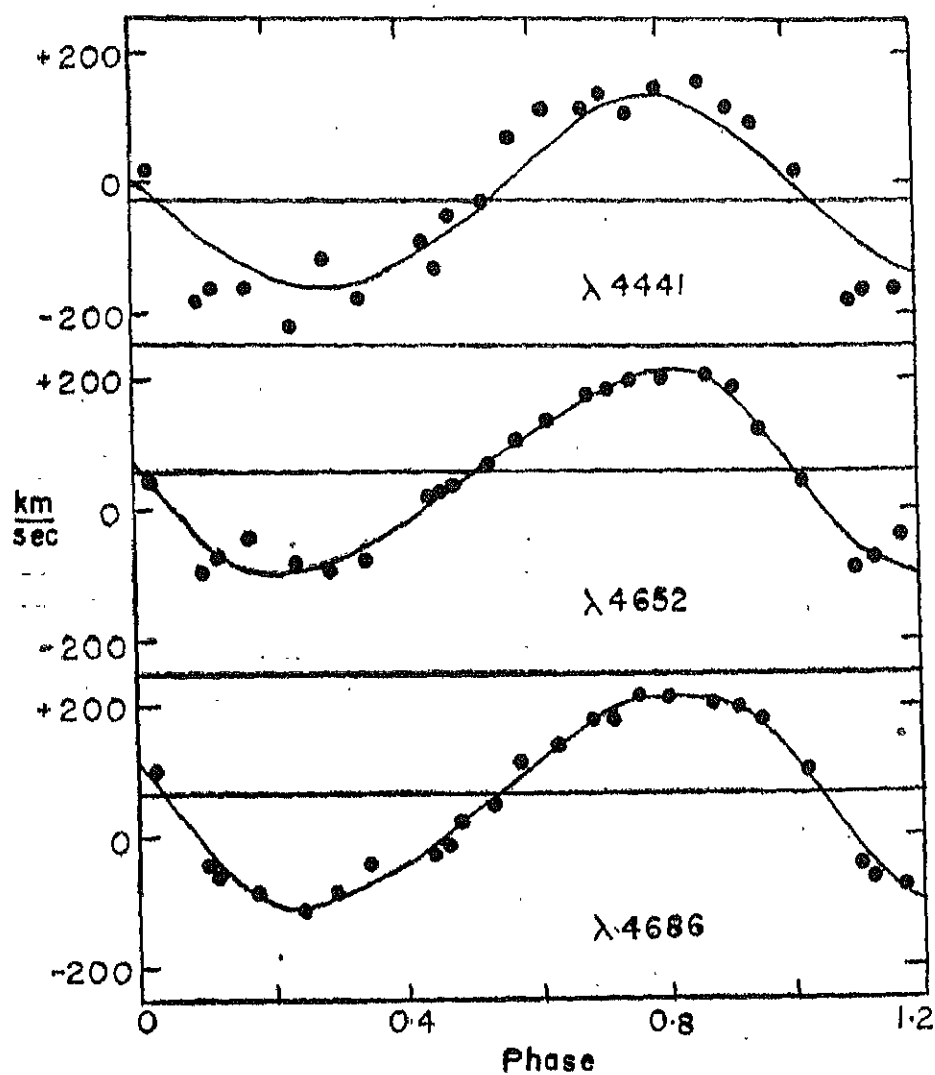


Figure 2.—The Radial velocity curves of HD 68273 for the emission lines.

The measures of the hydrogen absorption line at  $4340\text{\AA}$  are utilized to study the orbit of the O star. A large scatter of the measures, together with the relatively smaller amplitude in velocity of the more massive O star, made it difficult for us to carry through an independent analysis of the orbit. We have, therefore, solved for the values of  $\gamma$  and  $K$  which give the best theoretical fit for the observed points. The final elements derived from the velocity measures of  $4340\text{\AA}$  are as follows:

$$\gamma = -18.0 \pm 1.80 \text{ km/sec.}$$

$$K = 43.1 \pm 2.6 \text{ km/sec.}$$

$$e = 0.17$$

### Discussion

The orbital elements obtained for all the three emission lines are remarkably similar. This result can be contrasted with HD 214419, CQ Cephei, where according to Bappu *et al* (1967), there is a considerable difference in the orbital characteristics, denoted by the velocity curves of NIV 4058 and HeII 4686. A disparity exists only in the values of  $K$ , with CIV 4441 having the largest value of 196 km/sec. and the  $4652\text{\AA}$  complex having a value of 154 km/sec. The large amplitude in the velocity curve of CIV 4441 seems certainly to originate from an apparent shift to the violet at some phases caused by the absorption line on the long wavelength side.

In the case of HeII 4686, Sahade (1958) has shown that at certain phases a narrow emission is seen superposed on the broad emission feature of  $4686\text{\AA}$ . Sahade has interpreted this feature as due to material streaming from the Wolf-Rayet star through the inner Lagrangian point. The presence of this narrow feature is likely to upset within a small limit, the value of the semi-amplitude of the velocity curve. It could also affect the value of the derived systemic velocity, though, if it is seen at more phases than a restricted range, it is quite probable that the effect will be nullified.

We have, therefore, preferred using the value of  $K$  derived from  $4652\text{\AA}$ , since it is least likely to be affected by possible distortions that are usually present in Wolf-Rayet systems. In fact,  $4652\text{\AA}$  may have proved also to be unsuitable for this purpose, were it not for the fact that a violet edge, normally seen associated with this line in most WC spectra, is totally absent in HD 68273, as was pointed out first by Smith (1955).

Along with the measures of the H-gamma line, we have made measures of the absorption line HeII 4200 as well as the hydrogen line at  $4100\text{\AA}$ . The helium absorption line is seen only weakly in the spectra and hence the helium contribution to the overall absorption of the Balmer series is not likely to be greater than 20 to 30 per cent. In the reduction of velocity measures of  $4340\text{\AA}$  we have assumed that it has the wavelength of the hydrogen gamma line and have ignored possible contamination by the corresponding member of the Pickering series. In doing so, the results will be affected, if at all, in the value of the systemic velocity without altering  $K$ . Figure 3 contains plots of radial velocities measured in the absorption lines  $4340\text{\AA}$ ,  $4200\text{\AA}$  and  $4101\text{\AA}$ . If the velocity curve of  $4340\text{\AA}$  is made to pass through the points of the absorption lines  $4200\text{\AA}$  and  $4100\text{\AA}$ , and systemic velocities derived, then one finds the velocity of  $4200\text{\AA}$  to be about 62

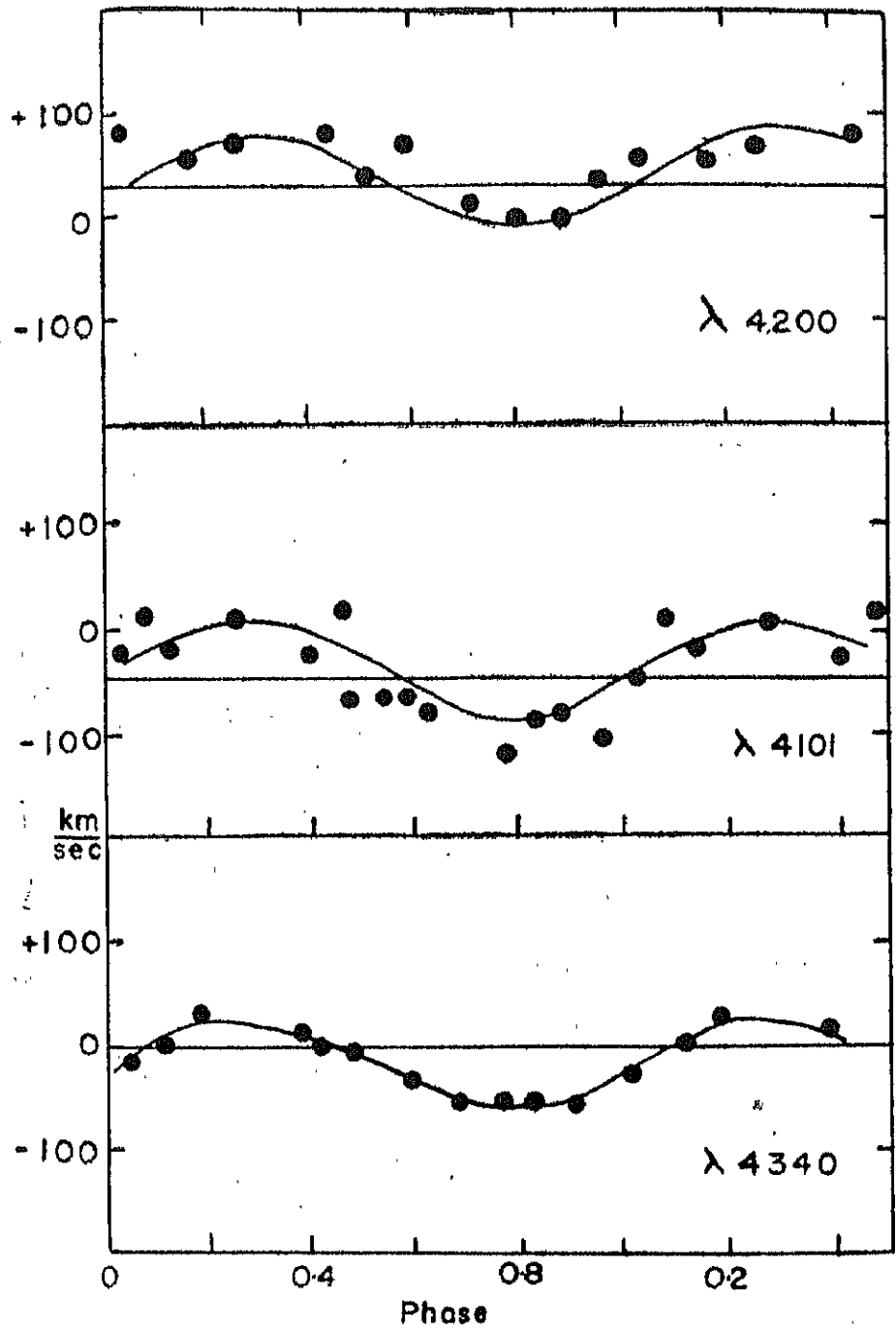


Figure 3.—The Radial velocity curves of HD 68273 for the absorption lines.

km/sec. more positive than  $4340\text{\AA}$ . This raises the question whether the discrepancy thus observed is due to our neglect of the HeII contribution towards the wavelength of the absorption feature at  $4340\text{\AA}$ . If it were so, and if HeII has contributed appreciably, then the mean wavelength would be shifted more to the violet causing thereby the occurrence of a value of systemic velocity that is more negative than what we have measured. Hence, we feel justified that the wavelength of the absorption feature at  $4340\text{\AA}$  is correctly taken, if one assigns to it the wavelength of the hydrogen-gamma line. An explanation of the more positive value of the systemic velocity from HeII 4200 is its likely contamination with  $4200\text{\AA}$  emission originating from the Wolf-Rayet atmosphere. The plots of the velocity measures of the absorption feature at  $4101\text{\AA}$ , when fitted with the theoretical curve for  $4340\text{\AA}$ , shows a systemic velocity very much more negative than  $4340\text{\AA}$ . Clearly, the wavelength used for this absorption feature is not correct and the absorption is the sum total of the effect of, not only the hydrogen-delta line, but also, of some other ions that have a transition near about this wavelength. An examination of the spectra shows that this line is broad and intense, upsetting the decrement of the Balmer series at this particular wavelength.

It is necessary at this stage to be able to determine the spectral type of the O companion. The single high dispersion blue spectrogram obtained at Mount Stromlo shows no trace of MgII 4481 and OIII 3960. Also HeI 4387 is seen marginally. Hence the spectral type is earlier than O8 and closer to O7. The ratios  $\frac{4542}{4471}=0.4$ ;  $\frac{4542}{4340}=0.2$  and  $\frac{3819}{3813}=0.25$  make it earlier than O8, but later than O7. Hence a spectral type of O7.5 seems best to adopt. The Balmer series are seen on the high dispersion plate until H16 with certainty.

In Table 4 we give the values of  $m_{O7.5} \sin^3 i$  and  $m_w \sin^3 i$  based on the mass ratios determined from the hydrogen-gamma line and each of the other three emission lines used. Since  $K$  is an important quantity in the evaluation of the masses,

TABLE 4  
*Values of  $m_o \sin^3 i$  and  $m_w \sin^3 i$*

HD 68273	HeII 4686	CIII 4652 Complex	CIV 4441
$m_o \sin^3 i$	54.9	46.3	89.8
$m_w \sin^3 i$	14.5	13.0	19.7

we have to use that value which is the most dependable from the results we have on the three emission lines. It has been pointed out before that CIV 4441 is the least reliable of the three. The presence of emission from the inner Lagrangian point superimposed on the normal  $4686\text{\AA}$  profile and the absence of a violet edge for the emission complex  $4652\text{\AA}$  make the latter, despite the wavelength uncertainty, more dependable than the other for an evaluation of the masses. Proceeding on this reasoning, we find that the values of  $M_o \sin^3 i$  and  $M_w \sin^3 i$  as 46.3 and 13.0 solar masses are in the range of values, obtained for equivalent spectral types.



There are very few well determined masses of the O stars available in the literature. The values obtained in this study are in good agreement with those listed by Allen (1963) and can provide an independent estimate of the mass of an O7.5 star, if the inclination of the orbit can be evaluated with certainty. The masses derived on the assumption of  $\sin^3 i = 1$  come within the range of values that we know to be valid for the Wolf-Rayet stars and the O stars. However, the detection of emission near the inner Lagrangian point at almost all phases would necessarily imply that the inclination has a value of  $70^\circ$  or smaller. If this is true, then not only would the chances of an eclipse be ruled out, but the lower limits to the masses of the W and O star would be 14 and 48 solar masses respectively. While this would make the Wolf-Rayet star the most massive of the very small number we know of, the mass of the O star would make it intermediate between those found among the O dwarfs and O subgiants. It is obvious that much of this speculation can be eliminated, if a light curve is available for the system.

As indicated earlier, HD, 68273 has long been known for the variations in its spectra. The Kodaikanal Observations cover over 3 cycles of the star and a feature that is most strikingly seen is the variation in the absorption of HeI 3889. This has been reported earlier by Smith, who observed a displaced absorption component of this line on a few nights during 1953 and also on a few nights during 1954. Due to the fact that the star has never been subjected to a systematic study before, it has always been assumed that the occurrence of displaced HeI 3889 absorption is sporadic in nature. Our observations of the system show that the violet edges are seen on two cycles chiefly between phases 2 days and 30 days. This fact seems to suggest that the displaced absorption of HeI 3889 can be observed only in a selected range of phases of the binary system. However, we must point out that in the second of the 3 continuous cycles we have observed at Kodaikanal, no displaced absorption was seen even though we had good coverage of the star over a range of phase from 2 days to 35 days. It seems likely that this displaced absorption originates from material flow with a velocity of about 1500 km/sec. in the vicinity of the inner Lagrangian point from the advancing hemisphere of the Wolf-Rayet star. The gas streams are visible from phase 2 days to atmost 40 days. However, it is not necessary that, in every cycle over this phase range, the displaced absorption be present. We believe that the gas streaming giving rise to the intense and displaced HeI absorption 3889Å is sporadic. Sahade's findings in 4686Å emission also seem to support such a conclusion. With a period of 78.5 days, the phases at which Smith observed displaced 3889Å have been 18 days in 1953 and 33 days in 1954.

*Acknowledgement:* It is a pleasure to acknowledge the help rendered by V. Natarajan in the computations.

KODAIKANAL OBSERVATORY, }

October 1967. }

## REFERENCES

- Allen, C.W. 1963 . . . Astrophysical Quantities 203
- Aller, L.H., and Faulkner, D.J., 1964 Astrophys. J., **140**, 167.
- Bappu, M.K.V., Viswanadham P. In preparation.  
and Natarajan V. 1967
- Cannon, A.J. 1901. . . Harv. Ann., **28**, 148.
- Gaposchkin, S., 1959 . . . Astr. J., **64**, 127.
- Perrine, C.D., 1918 . . . Astrophys. J., **120**, 22.
- Sahade, J., 1955 . . . Publ. Astr. Soc. Pacific, **67**, 348.
- Sahade, J., 1958 . . . Mem. Soc. R.Sc. Liege, **XX**, 404.
- Schlesinger, F. and Jenkins, L.F., Yale Bright Star Catalogue.  
1940.
- Smith, H.J. 1955. . . Ph.D. thesis, Harvard University.
- Stecher, T.P., and Milligan, J.E. Astrophys. J., **136**, 1.  
1962.
- Worsell, W.M. 1916 . . . Mon. Not. R. Astr. Soc. **76**, 418.



# KODAIKANAL OBSERVATORY

BULLETIN Number 184

## The Wolf-Rayet eclipsing binary HD 193576

K. S. Ganesh, M. K. V. Bappu and V. Natarajan

### Abstract

Low dispersion spectra ( $75 \text{ \AA/mm}$  at  $4300 \text{ \AA}$ ) of HD 193576 have been utilized for radial velocity measures as well as line profile determinations of some of the emission lines. Using such measures for HeII 4686, the elements derived are,  $\gamma$ -axis =  $\pm 16.2 \text{ km/sec}$ ,  $K=282.8 \text{ km/sec}$ ,  $e=0.11$ ,  $\omega = 163^\circ$ . The velocity measures of NIV 4058 are combined with earlier measures of Munch to yield the following values:  $\gamma$ -axis (NIV 4058) =  $-41.5 \text{ km/sec}$ ,  $K = 302.6 \text{ km/sec}$ ,  $e = 0.09$ ,  $\omega = 130^\circ$ ,  $T_0 = 0.26$ ,  $T=0.62$ . The velocity measures of the absorption lines  $4340 \text{ \AA}$  and  $4100 \text{ \AA}$  that originate from the O component show much scatter. A combination of the K values of NIV 4058, H $\delta$  yield masses of the O and W stars as 23.3 and 8.2 solar masses respectively. If  $4058 \text{ \AA}$  is used with the K value derived by Munch from measures of the higher members of the Balmer series these are 25.0 and 9.9 solar masses respectively.

Line profiles of  $4058 \text{ \AA}$ ,  $4686 \text{ \AA}$ ,  $4861 \text{ \AA}$  from low dispersion spectra are discussed. A few coude spectrograms ( $10 \text{ \AA/mm}$ ) of this star were obtained at primary and secondary minima and outside eclipse. The emission line NIV 3483 shows a violet absorption edge at primary minimum. Profiles of H9, H11 and H13 show clearly the increase in width at primary minimum caused by electron scattering. The intensities of the hydrogen lines are also found to increase slightly at this phase.

### Introduction

The binary nature of HD 193576 (V444 Cygni) was discovered by Wilson (1939). Gaposchkin (1941) showed subsequently that the star is also an eclipsing variable. Precise light curves for this system have been obtained photo-electrically by the Krons (1950) and Hiltner (1949).

The most recent spectrographic orbit is by Munch (1950). Very soon after the discovery of the binary nature Wilson (1940) had shown that the  $4686 \text{ \AA}$  line originating from the Wolf-Rayet component of this system experienced little eclipse when occulted by the O companion. Kuhi (1956) has recently scanned photo-electrically the spectrum of HD 193576 from  $3400 \text{ \AA}$  to  $11000 \text{ \AA}$  with a spectrum scanner used as a narrow band photometer. He finds that in the process of the eclipse of the Wolf-Rayet component by the O star, the lines of ionized He, NIII and NIV do not share in the eclipse but actually undergo a brightening. This behaviour is most conspicuously seen in  $4686 \text{ \AA}$ . On the other hand, the line identified as CIV 5808 decreases in intensity as the Wolf-Rayet star is eclipsed by the O star. Apparently a similar behaviour is indicated in the case of the HeI line at  $10830 \text{ \AA}$ . The interesting feature is that the CIV line goes into eclipse two hours before the neutral helium line does.

In this investigation we present new orbital parameters for the binary system from radial velocity data. We also present the line profiles for different lines at different phases.

### The observations

Twenty-eight spectra of this binary system were obtained in 1952 with the Mount Wilson 60-inch telescope and single prism spectrograph. The spectra have a dispersion of  $75 \text{ \AA/mm}$  at  $4340 \text{ \AA}$  and can be used to study the orbits of both components. The phases of the observations have been computed from the epoch of primary minimum when the Wolf-Rayet star eclipses the O star. The elements provided by Kron and Gordon (1950) are

$$\text{Phase zero} = \text{JD } 2428771.379 + 4.21238E$$

The measures of radial velocity were of the emission line  $\text{HeII } 4686$  and  $\text{NIV } 4058$  along with the Balmer absorption lines  $4861 \text{ \AA}$ ,  $4340 \text{ \AA}$  and  $4101 \text{ \AA}$ . The accompanying table gives the velocity measures of this system.

### The orbital elements

The earlier spectrographic investigations of this system had assumed a circular orbit. We obtained a set of preliminary elements on the same basis from the velocity curve of  $4686 \text{ \AA}$ . We next applied Sterne's method and determined the corrections necessary to the preliminary orbit. The orbital elements obtained from the  $4686 \text{ \AA}$  velocity curve are

$$\begin{aligned}\gamma &= +16.2 \text{ km/sec} \\ K &= 282.8 \text{ km/sec} \\ e &= 0.11 \\ \omega &= 163^\circ \\ T_0 &= 0.24 \\ T &= 0.69\end{aligned}$$

In the case of  $\text{NIV } 4058$  we combined our velocity measures with those of Munch (1950) in order to obtain a set of well defined orbital elements, using Sterne's method. The elements thus obtained are

$$\begin{aligned}\gamma &= -41.5 \pm 6.2 \text{ km/sec} \\ K &= 302.6 \pm 9.3 \text{ km/sec} \\ e &= 0.09 \pm .04 \\ \omega &= 130^\circ \\ T_0 &= 0.26 \\ T &= 0.62\end{aligned}$$

The presence of a certain degree of eccentricity of the orbit has been speculated on for some time. The photo-electric measures of Kron and Gordon show that the secondary minima occur slightly earlier than the midpoint between the primary minima. The eccentricity derived spectroscopically is 0.09 and is of the right order of magnitude to explain the observation of Kron and Gordon. The systemic velocity derived from measures of  $4058 \text{ \AA}$  is  $-42 \text{ km/sec}$  as against  $+16 \text{ km/sec}$  for  $4686 \text{ \AA}$ , or a difference of  $58 \text{ km/sec}$ .

Plate	J.D. of observation	Phase (in period)	Velocities in Km/Sec					
			4686e	4603e	4058e	4861a	4340a	4101a
32596	.	0.64	-183.6	-193.7	-311.8	..	+102.6	+112.3
32597a	.	0.64	-248.3	-209.9	-323.1	+107.3	+130.3	+43.9
32597b	.	0.65	-308.9	-236.4	-338.2	+77.2	+103.3	+151.6
32602	.	0.91	-24.1	-73.7	-191.2	..	+124.7	..
32631a	.	0.79	-310.8	-229.8	-352.6	+158.6	+26.3	+168.2
32631b	.	0.80	-270.1	-191.1	-313.7	+68.2	+96.5	+141.5
32634a	.	0.03	+117.0	+67.0	-28.0	..	-17.1	+15.3
32636a	.	0.08	+164.6	+86.0	+36.6	..	-39.0	+59.9
32636b	.	0.08	+198.5	+176.7	+41.0	-120.6	-49.8	+37.5
32642a	.	0.53	+35.4	-36.5	-115.0	-60.3	+36.5	+37.4
32642b	.	0.54	-121.0	+34.3	-201.5	-60.3	-6.6	-28.5
32649a	.	0.80	-318.7	-333.5	-319.0	-165.0	..	..
32649b	.	0.80	-298.3	-308.3	-319.0	-113.5	+111.7	+198.5
32654b	.	0.00	+69.1	+79.3	-106.6	+142.7	+74.1	+23.7
32654c	.	0.01	+62.2	..	-102.3	..	+122.6	+32.4
32654d	.	0.02	+69.0	+38.3	-132.6	+7.1	+90.2	..
32661a	.	0.24	+259.4	+324.5	+359.0	..	-28.6	-88.7
32661b	.	0.24	+259.3	+298.3	+248.1	-113.4	-66.4	-61.8
32669a	.	0.50	+88.0	+85.2	-107.0	-8.4	+30.4	-3.8
32669b	.	0.51	+27.7	+85.1	-128.8	-1.0	-34.5	+9.6
32681a	.	0.47	+168.0	..	-23.1	+27.0	-22.4	+25.1
32683a	.	0.51	-43.1	-59.7	-88.3	-109.2	-37.3	+83.2
32683c	.	0.53	-83.9	-40.4	-70.9	-139.3	+49.1	+20.3
32746b	.	0.59	-97.6	-66.6	-255.5	+42.1	+63.8	..

Figure 1 is a plot of our measured velocities of the two emission lines 4686 Å and 4058 Å as well as the velocities derived from the absorption lines. These absorption line velocities show a certain degree of scatter and indicate a range in location of the  $\gamma$ -axis. This originates presumably by contamination caused by the emission lines that are present in the spectrum of the Wolf-Rayet component. We have used separately the velocity measures of 4340 Å and 4101 Å to determine the orbit of the O star. A least squares solution was made to obtain corrections to initial values for  $K$  as well as  $\gamma$ . The values obtained are the following :

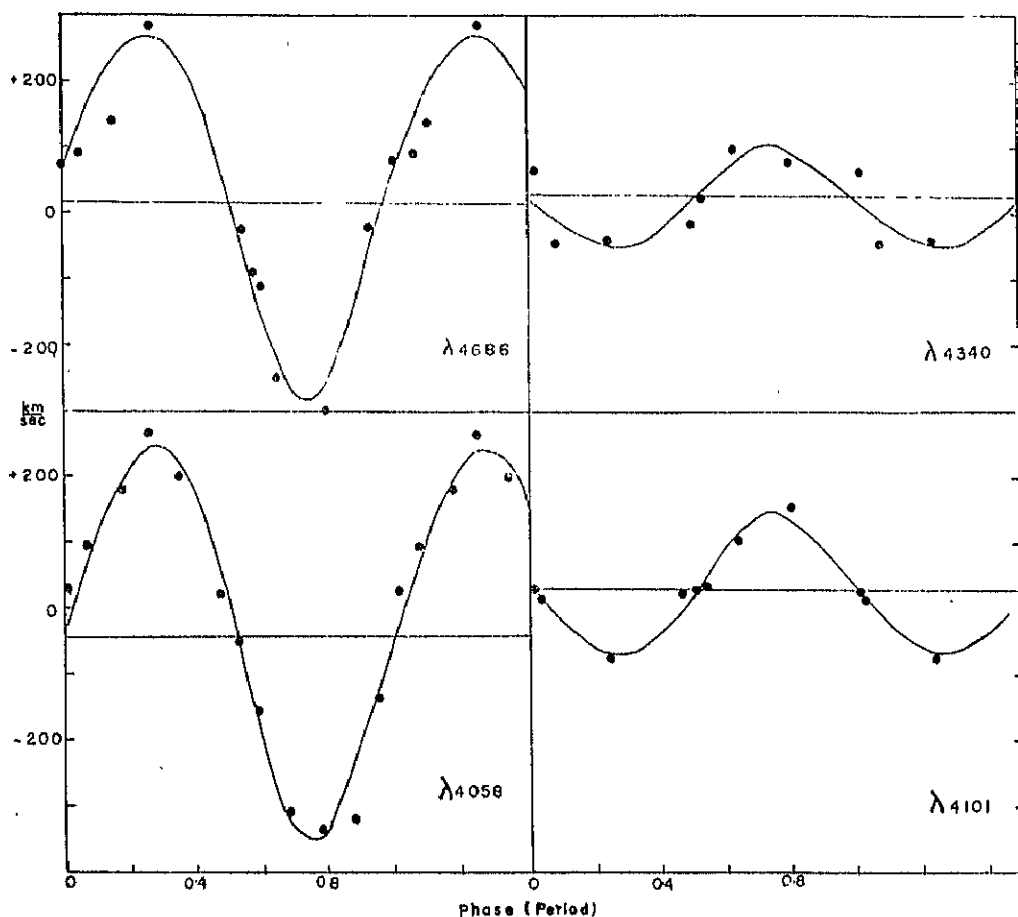


Figure 1.—The Radial velocity curve of HD 193576

	H $\gamma$	H $\delta$
$\gamma$ -axis (km/sec)	+22.1	+32.2 $\pm$ 6.7
$K$ (km/sec)	76.9	106.0 $\pm$ 11.7

The large discrepancy between the values of  $K$  of the two velocity curves indicates that either one or both are affected seriously by emission from the Wolf-Rayet component. Since the value of  $K$  is very important in the determination of the masses of the components, it is doubtful if our values of  $K$  from the absorption lines at 4340 Å and 4101 Å would add to the reliability of a mass determination. In this respect, measures of the higher members of the Balmer series as carried out by Munch, would have been more useful. In the calculation of the

values of  $m_o \sin^3 i$  and  $m_w \sin^3 i$  we, therefore, use in addition to our values of  $K$  for the O component those obtained by Munch. The values of  $m_o \sin^3 i$  obtained are the following :

Emission line		Absorption line		
		H $\gamma$	H $\delta$	Munch H $\delta$ , H9, H10
HeII 4686	$m_o \sin^3 i$	15.7	18.4	19.7
	$m_w \sin^3 i$	4.3	6.9	8.4
NIV 4058	$m_o \sin^3 i$	18.8	21.8	23.3
	$m_w \sin^3 i$	4.8	7.7	9.3

A value of mass determined from the velocity curve of HeII 4686 is questionable since this line in a close binary system is liable to have complications by virtue of gas streaming near the inner Lagrangian point. We are, therefore, limited to using 4058 Å and the absorption lines, preferably the higher members of the Balmer series.

There are very few mass determinations of the O stars available in the literature. Using a value of  $i=78^\circ$  derived by Kron and Gordon (1950) as well as the values of  $m_o \sin^3 i$  and  $m_w \sin^3 i$  determined from a combination of 4058 Å and H $\delta$  we get the masses of the O and W components as 23.3 and 8.2 solar masses respectively. If we use the combination of 4058 and Munch's value of  $K$  from the higher members of the Balmer series these become 25.0 and 9.9 solar masses respectively.

### The line profiles

It is well known that the Wolf-Rayet spectrum of 193576 shows very striking changes in the line contours of its various emission lines at various phases. A study of these contours help us in building a picture of the binary system as a whole. Figure 2 depicts the variations experienced at various phases by NIV 4058, HeII 4686 and HeII 4860, as measured from low dispersion spectra. In the case of HeII 4686, we find that at the conjunctions a narrow hump appears at about the peak of the profile and this hump which is on the red side at phases close to the primary minimum, moves over to the violet side at phases close to the secondary minimum when the Wolf-Rayet star is eclipsed. This variation in HeII 4686 was first pointed out by Wilson in 1942. In general, the overall widths of the lines are essentially the same. But in the vicinity of the conjunctions, the second hump caused by the superposed narrow emission seems to be primarily responsible for the changes in the profile. Sahade has shown (1958) that this narrow emission originates at the inner Lagrangian point and the observations reported here substantiate his point of view.

The profile of HeII 4860 essentially portrays the variations in location of the H $\beta$  absorption line of the O star and the consequent effects that it has on the appearance of the overall structure. However, the total emission width seems



to be greater near secondary minimum than it is at primary minimum. The profile at phase 0.02P has the absorption component on the violet side caused by an approaching O star but the narrowness of the overall emission cannot just be explained by a heavy mutilation of the emission line by the  $H\beta$  profile of the O star. It, therefore, seems that the emission line itself has a difference in width near about primary and secondary minimum, or in other words the emission line is narrower when the Wolf-Rayet star is closest to the observer than it is when it is farthest away.

The profiles of 4058 Å are also displayed in Figure 2. We have given six of these profiles to indicate the fact that no serious changes in the structure have been observed during the period when these plates were obtained. Hence, we can adopt the values obtained from the radial velocity measures of this line with a good degree of confidence. However, a few minor changes in the appearance of the profile need further mention. The profile close to primary minimum is fairly sharp peaked, differing from that near secondary minimum.

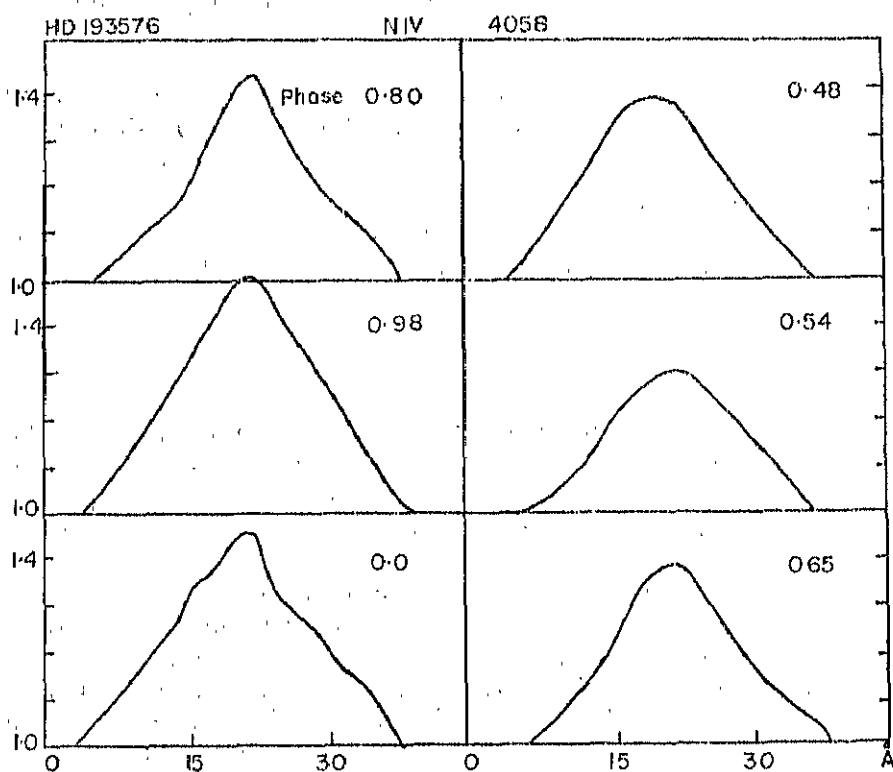


Figure 2 (a).—Profiles of NIV 4058 in the spectrum of HD 193576 at various phases.

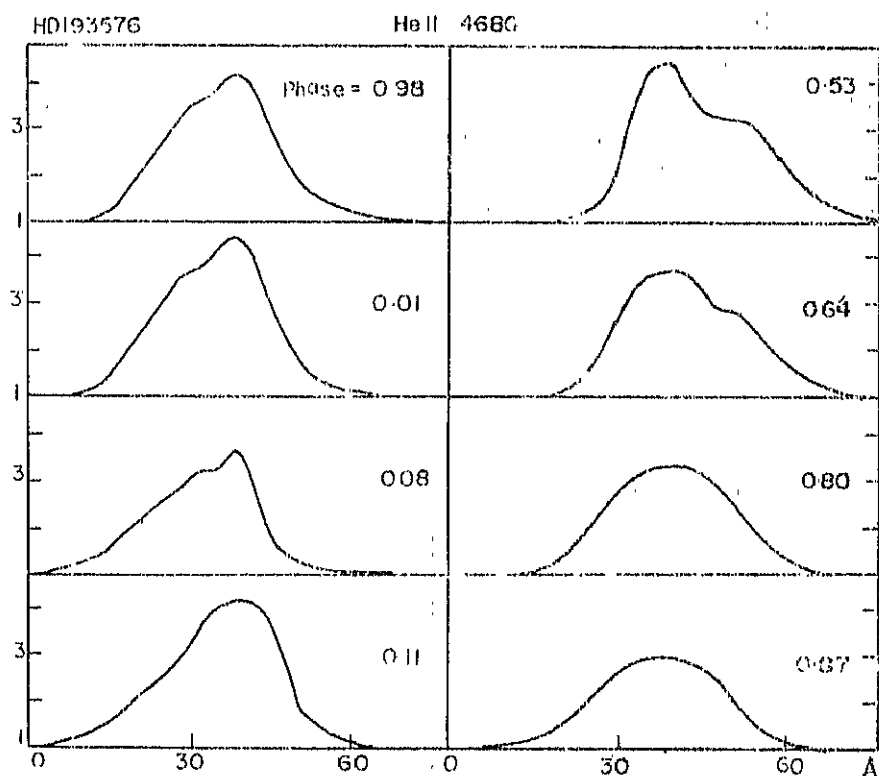


Figure 2 (b). --Profiles of He II 4686 in the spectrum of HD 193576 at various phases.

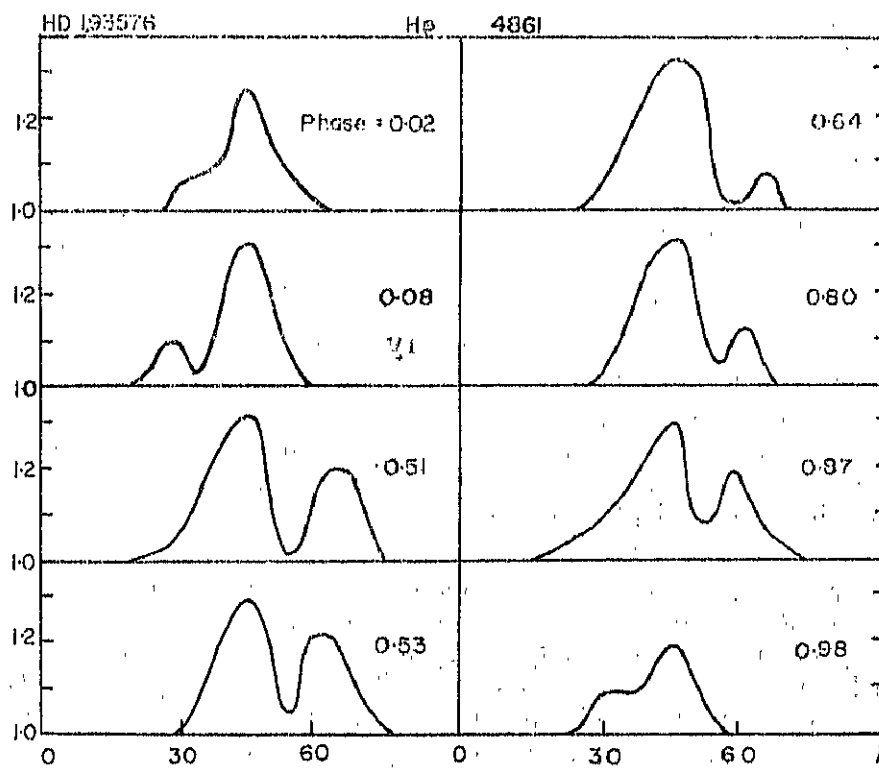


Figure 2 (c). --Profiles of He I 4861 in the spectrum of HD 193576 at various phases.

High dispersion spectra obtained at phases 0.02, 0.48, 0.71 and 0.95P are available, for the study with better resolution, of some of these characteristic changes. These spectra obtained at  $10 \text{ \AA/mm}$  with the 100-inch coude spectrograph extend into the ultra-violet to about  $3300 \text{ \AA}$ . In fact these plates at selected phases, more especially at conjunctions, were exposed to study the profiles of the higher members of the Balmer series and how these have been affected by the electron scattering envelope around the Wolf-Rayet star.

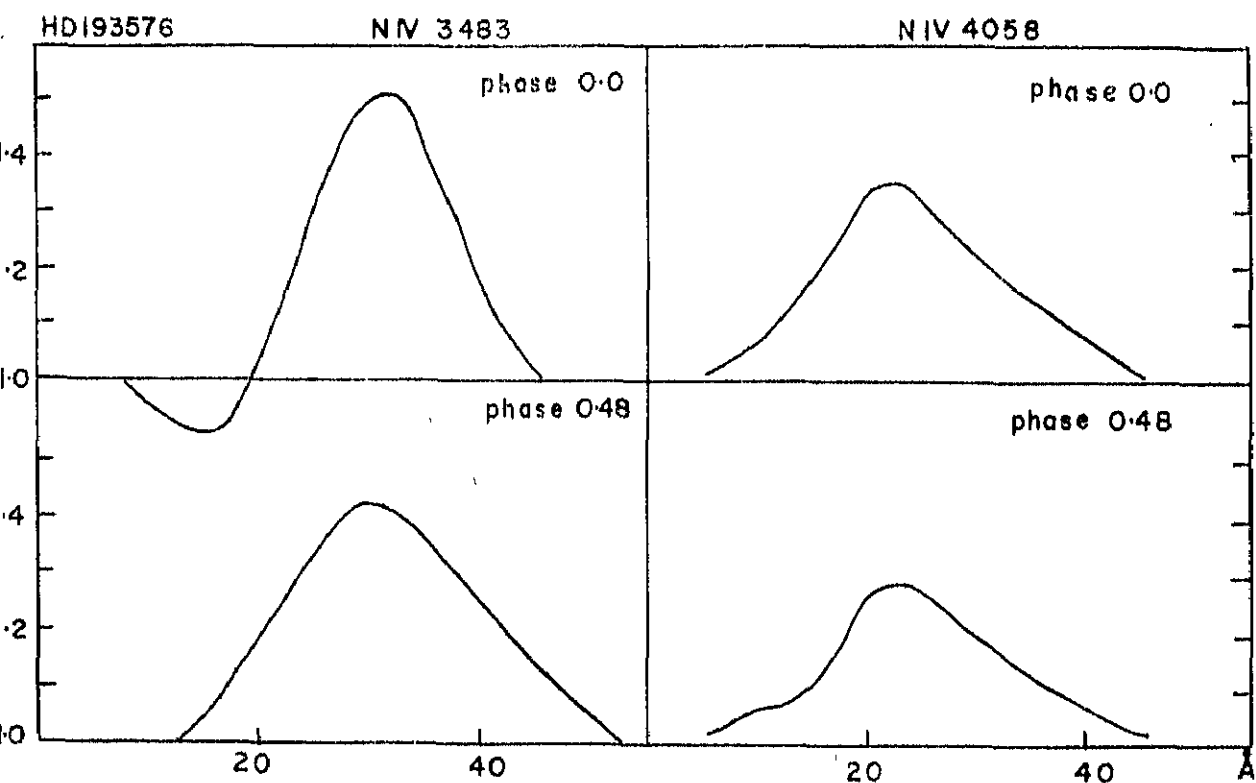


Figure 3—Profiles of NIV 3483 and NIV 4058 in the spectrum of HD 193576 at primary and secondary minimum.

In Figure 3, the profiles of the NIV multiplet  $3s^3S-3p^3P$  at  $3479 \text{ \AA}$ ,  $3483 \text{ \AA}$  and  $3485 \text{ \AA}$  can be seen at primary minimum and secondary minimum alongside the profiles at corresponding phase of the  $3p^1P-3d^1D$  multiplet at  $4058 \text{ \AA}$ . The kinematic conditions in the Wolf-Rayet envelope are such as to broaden the individual transitions of the triplet considerably, so that we see them unresolved separately. The main characteristic of interest is the presence of a violet absorption edge displaced with respect to the centre of the emission at  $3482 \text{ \AA}$  by  $1160 \text{ km/sec}$ . This feature is seen only at primary minimum when the Wolf-Rayet star eclipses the O component. The surprising fact is that, at this phase, the Wolf-Rayet spectrum should have the normal characteristics of a WN5 star. The appearance of a violet absorption edge for NIV 3483 is not seen on any of the high dispersion spectra of HD 192163, HD 191765 or HD 193077. It, therefore, seems to be a characteristic stimulated by the component of the binary system. The multiplet  $3p^1P-3d^1D$  at  $4058 \text{ \AA}$  does not show the absorption feature.

The higher members of the Balmer series that originate in the atmosphere of the O star are widened at primary minimum when the O star shines through the electron scattering envelope of the Wolf-Rayet star. This property was first observed by Munch. Figure 4 indicates the differences in profile for H9, H11

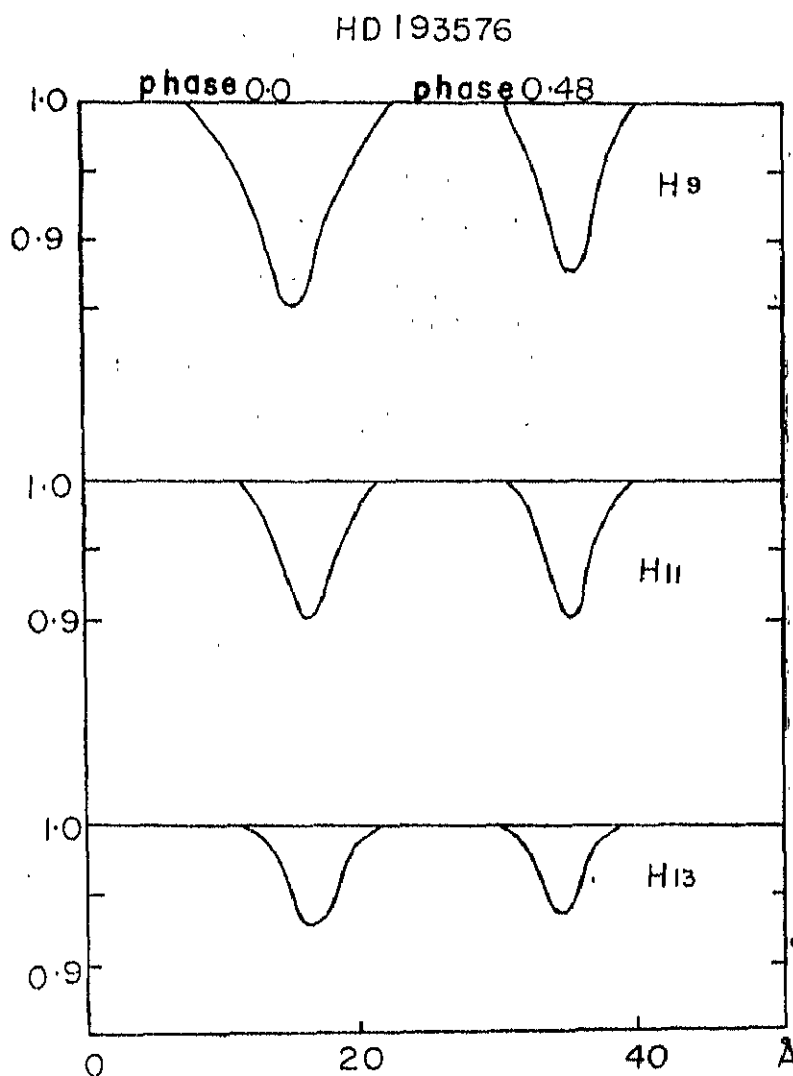


Figure 4.—Profiles of H<sub>9</sub>, H<sub>11</sub> and H<sub>13</sub> in the spectrum of HD 193576 at primary and secondary minimum.

and H13 for the two phases representing primary and secondary minima. The increase in widths is obvious, confirming our speculations regarding the electron scattering envelope. However, the intensities of the hydrogen lines increase by a small amount at this phase. More quantitative information would be necessary before we consider this as definite evidence of enhanced hydrogen absorption in the Wolf-Rayet atmosphere.

The observations reported herein were obtained by one of us (MKVB) during the tenure of a Carnegie Fellowship at the Mount Wilson and Palomar Observatories.

KODAIKANAL OBSERVATORY }  
October 1967

## REFERENCE

- |                                |   |
|--------------------------------|---|
| Gaposchkin, S.,                | 1941, Astrophys. J., <b>93</b> , 202          |
| Hiltner, W. A.,                | 1949, Astrophys. J., <b>110</b> , 95          |
| Kron, G. E. and<br>Gordon, K., | 1950, Astrophys. J., <b>111</b> , 454         |
| Kuhi, L. V.,                   | 1966, Astr. J. <b>71</b> , 167                |
| Munch, G.,                     | 1950, Astrophys. J., <b>112</b> , 266         |
| Sahade, J.,                    | 1958, Mem. Soc. R. Sc. Liege <b>20</b> , 404  |
| Wilson, O. C.,                 | 1939, Publ. Astr. Soc. Pacific <b>51</b> , 55 |
| Wilson, O. C.,                 | 1940, Astrophys. J., <b>91</b> , 379          |

# KODAIKANAL OBSERVATORY

## BULLETIN Number 185

### Three Wolf-Rayet binaries

K. S. Ganesh and M. K. V. Bappu

#### Abstract

Radial velocities and line profiles are studied of the three Wolf-Rayet binaries HD 193928 HD 186943 and HD 211853.

**HD 193928:** A new orbit has been determined from radial velocity measures of HeII 4686. The orbital elements are as follows:  $\gamma$  axis =  $\pm 60$  km/sec,  $K = 147$  km/sec,  $e = 0.12$ ,  $\omega = 51^\circ$ ,  $f(m) = 4.62$  solar masses. The NIV 4058 velocities can be represented by the HeII 4686 velocity curve displaced in phase by 0.1P. A displacement of 185 km/sec in the gamma-axis suffices to fit the 4686 Å curve onto the NV 4603 velocities. Line profile variations with phase of the emission lines are described. This system is likely to have an orbital inclination that will enables the detection of eclipses.

**HD 186943:** A revised period of 9.5594 days is derived for this system. Orbital elements are derived using velocity curves HeII 4686, NV 4603 and NIV 4058. The orbital elements derived from HeII 4686 are as follows:

$\gamma$  axis =  $\pm 107$  km/sec,  $K = 212$  km/sec,  $e = 0.04$ ,  
 $\omega = 151^\circ$ ,  $\gamma$  (NIV 4058) =  $\pm 70$  km/sec,  $\gamma$  (NV 4603) =  $\pm 30$  km/sec.

**HD 211853:** Preliminary elements are derived from velocity curves of HeII 4686, NV 4603 and NIV 4058. These are as follows:  $\gamma$  (HeII 4686) =  $\pm 15$  km/sec,  $\gamma$  (NV 4603) =  $\pm 35.0$  km/sec,  $\gamma$  (NIV 4058) =  $-120$  km/sec,  $e$  (HeII 4686) = 0.12,  $K$  (HeII 4686) = 220 km/sec,  $f(m)$  (HeII 4686) = 7.25.

The observation are discussed in terms of some of the current ideas on the nature of the Wolf-Rayet phenomenon.

#### HD 193928

This faint Wolf-Rayet star has a spectral type on the Beals classification between WN5 and WN6. It is categorized by Hiltner (1966) as WN6-B on his new classification scheme. The emission lines are broad and quite intense and hence are easier to measure than in any other Wolf-Rayet binary of the WN sequence. The only existing orbit of the star is that derived by Hiltner (1945) in which he has used radial velocity measures of HeII 4686 and NV 4603. Hiltner has pointed out that NIV 4058 experiences severe changes in line profile and on numerous occasions displaced absorptions of HeI 3888 and HeI 4471 can be seen.

Our determination of the orbit of the star rests on eighteen spectrograms obtained at Mount Wilson with the single prism spectrograph on the 60 inch reflector. The spectra have a dispersion of  $\text{\AA}/\text{mm}$  in the region of  $4300\text{\AA}$ . We have measured the emission lines  $4686\text{\AA}$ ,  $4603\text{\AA}$  and  $4058\text{\AA}$  for a study of the radial velocity changes. Because of the faintness of the star, the spectra could not be over-exposed to show up the absorption lines conspicuously. The spectra were primarily obtained for the purpose of spectrophotometry of the emission lines. In Table 1 we present our radial velocity measures for this star. Phases have been calculated with phase zero as JD 2434179.77 and Hiltner's value of the period of 21.64 days. The orbital elements derived from the  $4686\text{\AA}$  velocity curve using Sterne's method are,

TABLE 1

*The velocity measures of HD 193928*

Plate	J.D. of observation	Phase	Velocities in km/sec.		
			4058e	4603e	4696e
32598	2434144.97	0.60	-138.5	+62.5	+221.4
32601a	145.95	0.56	-173.1	-53.5	+98.1
32601b	145.98	0.56	-186.2	-92.4	+132.2
32605	146.90	0.51	-147.1	-98.7	+91.3
32632	170.92	0.40	-270.0	-195.3	-4.6
32635	171.88	0.36	-265.8	-288.0	-97.0
32643	173.95	0.26	-261.0	..	-61.2
32655	175.97	0.17	-265.5	-228.7	-53.0
32660	176.83	0.13	-205.7	-307.6	-80.0
32668	177.93	0.08	-132.5	-172.4	-19.2
32684	194.94	0.29	-265.7	-266.1	-90.5
32688	195.91	0.25	..	-276.0	-47.0
32724	200.98	0.00	-80.0	-264.1	+37.2
32728	201.91	0.97	-29.0	-222.5	+23.6
32732	202.96	0.92	-29.4	-119.4	+70.8
32747	224.73	0.92	..	-83.9	+27.2
32754	225.85	0.87	-39.7	-67.5	+76.5
32762	227.93	0.77	-28.2	+61.6	+187.4

$$\gamma = +60 \pm 8 \text{ km/sec}$$

$$K = 147 \pm 9 \text{ km/sec}$$

$$e = 0.12 \pm 0.05$$

$$\omega = 51^\circ \pm 21^\circ$$

$$f(m) = 4.62 \text{ solar masses.}$$

The  $\gamma$ -axis of the  $4686\text{\AA}$  velocity curve has a value of 60 km/sec, in exact agreement with the value derived by Hiltner. However, the value of  $K$  differs by about 17 km/sec. No orbit analysis has been carried out with the velocity measures off  $4058\text{\AA}$ . We show in Figure 1, the velocity curve of  $4686\text{\AA}$  in the upper half of the diagram. In the lower half of the diagram the solid curve is the theoretical curve of  $4686\text{\AA}$ , the filled circles are the observed velocities of  $4058\text{\AA}$ , and the dashed curve is the  $4686\text{\AA}$  curve displaced by 0.1P to have a good fit with the  $4058\text{\AA}$  velocities.

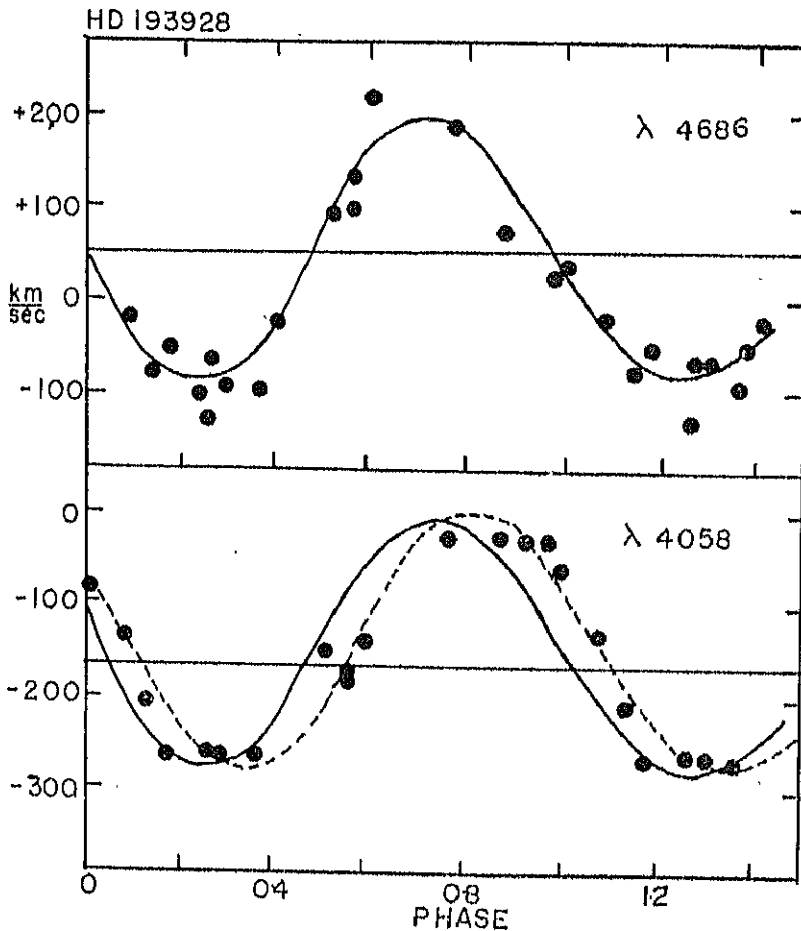


Figure 1.—Velocity curve of HD 193928. The top half of the diagram gives the HeII 4686 curve. In the lower half the solid circles are the observed velocities of NIV 4058, the solid curve is the theoretical curve of HeII 4686 and the dashed curve is the HeII 4686 curve displaced by 0.1P so as to fit the NIV 4058 velocity values.



It is difficult to explain the nature of this phase shift as seen in 4058 Å. It is likely that over the duration of the observations there has been activity on the star seen in NIV 4058 causing such a displacement.

Figure 2 is a plot of the emission line NV 4603 with the solid curve representing the variation of 4686 Å. It is seen that the curve fits the points well out for a displacement in the  $\gamma$ -axis by 185 km/sec.

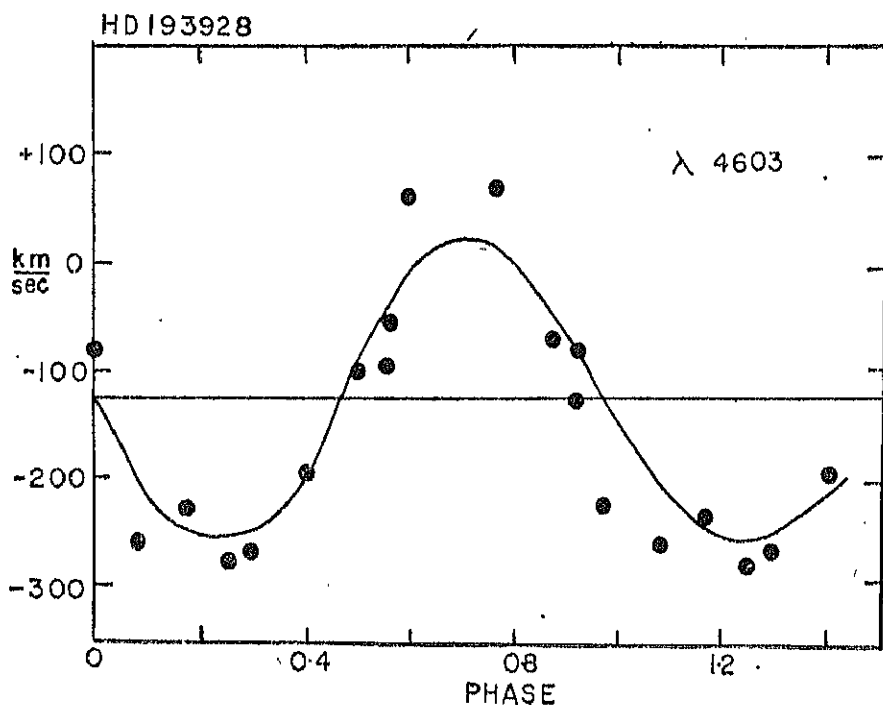


Figure 2.—Velocity observations of HD 193928. The points are the measured velocities of NV4603 while the solid curve is the velocity curve of HeII 4686.

The study of the profiles in a system of this kind is obviously of considerable interest. Figure 3 shows the variations experienced by HeII 4686 at four different phases. At phase zero, the Wolf-Rayet star is farthest from the observer. At this phase, the profile of 4686 Å is narrow with a slight hump on the longward side. At a phase when the Wolf-Rayet star is closest to the observer, which happens to be at phase 0.5, the profile is almost symmetrical and narrow. The profile is broad at phases 0.77 and 0.60 and the hump seen near phase zero continues to prevail. Figure 4 depicts the variations experienced by HeII 4200. Here again, the lines are narrow at phase zero. The profiles at elongations are wider than at phase zero and on some occasions, as seen in 4200 Å, there are suggestions of displaced humps in the structure. At phase 0.51 a hump on the shorter wavelength side is seen. However, the reliability of the presence of this hump cannot be affirmed with any degree of certainty because there has been no additional plate taken on the same day to confirm it.

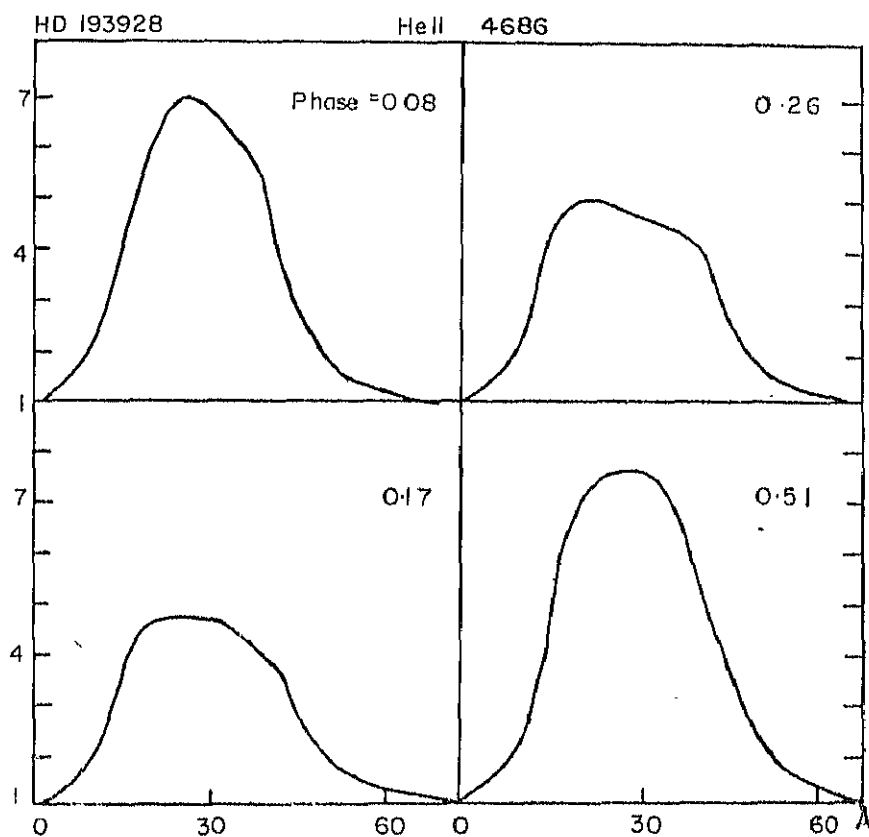


Figure 3.—HD 193928, Line profiles of He II 4686 at four different phases.

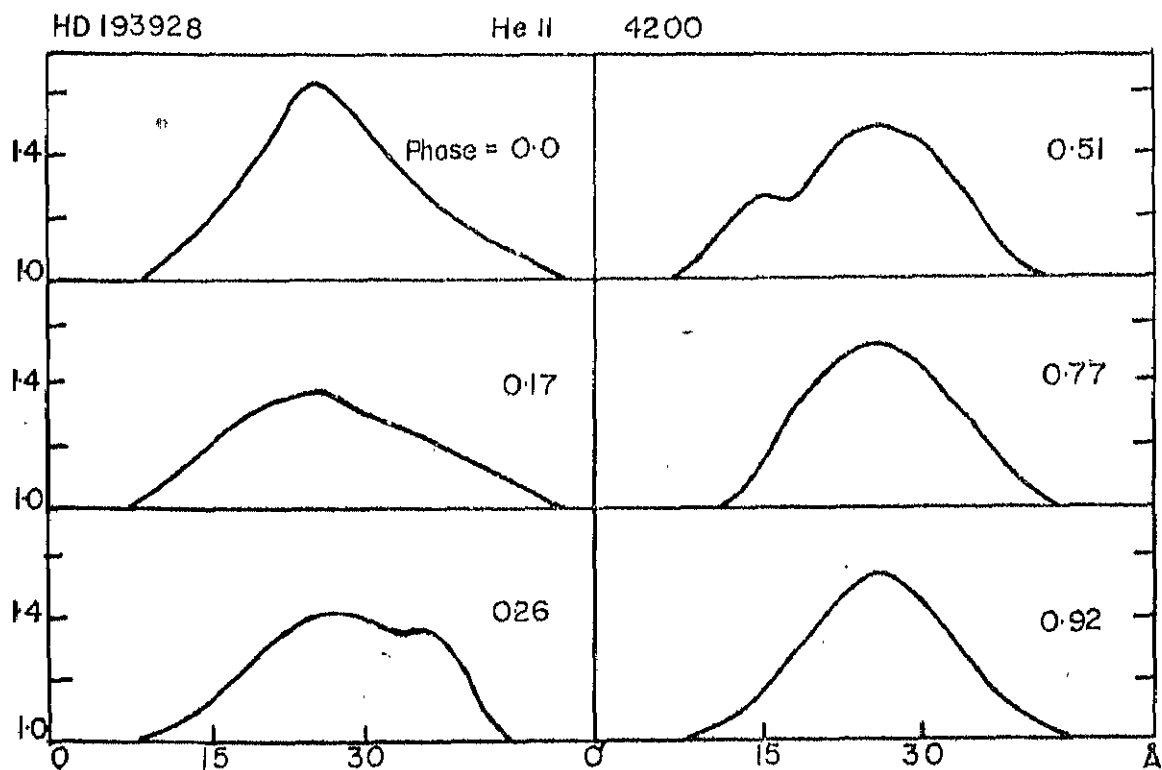


Figure 4.—HD 193928, Line profile variations of He II 4200.

The variations experienced by 4058 Å have been striking during the period of observation by Hiltner. Our observations shown in Figure 5 indicate that there are changes in the profile of this emission line. The line is more narrow near phase zero, similar to the pattern set by the others. However, at phase 0.51 it is quite wide and indicates a rather intense hump on the longward side. This perhaps, is the kind of variation noted by Hiltner and it is the presence of this distortion in the profile that prevented us from the calculation of orbital elements from the velocity measures of this line.

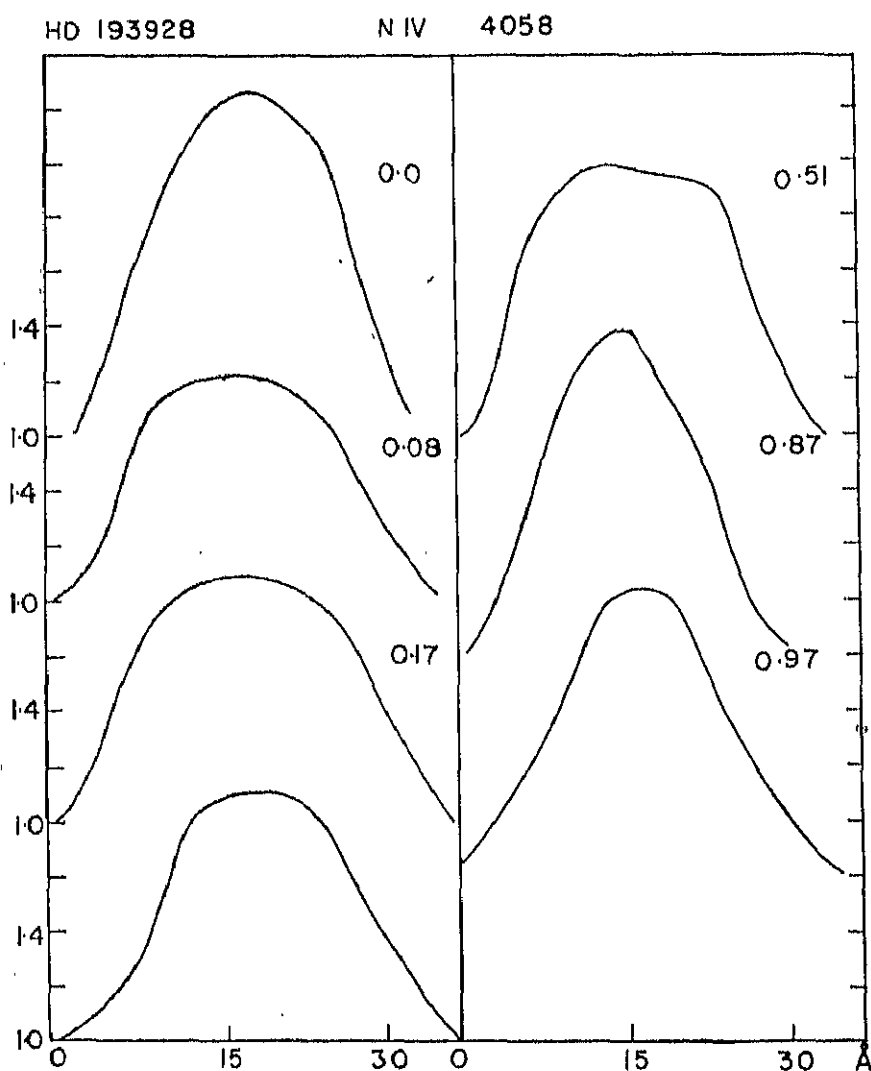


Figure 5.—HD 193928. Line profiles of NIV 4058.

The system of HD 193928 is, therefore, one which seems to have striking spectral variations. One is reminded of the variations seen in HD 50896 which, of course, is not an established binary system. The amplitude of velocity variation is appreciable and it is quite likely that this star is an eclipsing variable. If it is so, however, it would have only grazing eclipses. A comparison of the mass function with that of CQ Cephei ( $f(m)$ -4.4 solar masses) is of interest. It does seem possible that HD 193928 can be a good candidate in any search programme of eclipsing binaries among the Wolf-Rayet stars.

## HD 186943

The spectrum of this star on the Beals classification is WN 5. Hiltner (1966) classifies it as WN5-A. The emission lines seen in the blue region of the spectrum are HeII 4686, the two NV lines at 4619 Å and 4603 Å, as well as NIV 4058. The Pickering series of HeII are also present, in emission, but are quite faint for accurate measurements. The NV lines do not seem to have violet absorption edges. There are some absorption features seen in the spectrum. The spectra available for this study were obtained with a glass prism spectrograph and hence it was not possible to observe the higher members of the Balmer series. According to Hiltner(1945), these absorption features are extremely weak.

The only orbit of the star that is available is the one derived by Hiltner (1945). This study yielded a period of 9.55 days on the basis of velocity measures of 4686 Å, the NV emission lines and NIV 4058. The elements were determined from the velocity curve of HeII 4686. Hiltner reported a phase shift between the velocity curves of 4686 Å and 4603 Å. He also derived a velocity curve from the hydrogen absorption lines.

We have only ten spectra well distributed in phase of this star. We had exposed these for spectrophotometry of NIV 4058 since a variation with phase was apparent from Hiltner's work. The measures of radial velocity are given in Table 2. Preliminary orbits were obtained for 4058 Å, 4686 Å and 4603 Å. The  $\gamma$ -axes derived from NIV 4058 and NV 4603 are 75 km/sec and 30 km/sec respectively. On the other hand, HeII 4686 has a  $\gamma$ -axis value of 105 km/sec. The fact that the NV 4603 line has a systemic velocity nearly equivalent to that of NIV 4058 indicates that the NV lines have little or no violet absorption edges. The observations reported here were combined with those of Hiltner to yield a revised value of period of 9.5594 days. The phases were computed with the formula.

TABLE 2

*The Velocity measures of HD 186943*

Plate	J.D. of Observation	Phase	Velocities in km/sec		
			4686e	4603e	4058e
32653	2434175.75	0.78	-122.4	-116.2	-212.2
32659	176.78	0.89	- 6.8	- 32.3	-212.2
32667	177.87	0.01	+149.6	- 38.8	- 43.3
32686	195.79	0.88	+102.0	-180.8	-324.8
32720	200.74	0.39	+136.0	+103.3	-129.9
32725	201.71	0.50	- 27.2	- 58.1	-160.3
32730	202.84	0.61	-102.0	- 90.4	-316.1
32748	224.80	0.91	+ 20.4	- 6.5	-285.9
32761	227.86	0.23	+292.4	+219.6	-199.3
32766	228.90	0.33	+170.0	+ 38.8	+ 4.3

Phase zero = JD 2431253.041  $\pm$  9.5594E.

The Hiltner observations of 4686 Å were combined with our measures and a least squares solution obtained of the orbital elements. Table 3 lists these elements along with similar values derived from the preliminary orbits of NIV 4058 and NV 4603. The velocity curve for HeII 4686 is shown in Figure 6.

TABLE 3

*The orbital elements of HD 186943*

4686A	4058A	4603A
P = 9.5594 days	P = 9.5594 days	P = 9.5594 days
e = 0.0361 $\pm$ 0.02	e = 0	e = 0.0162
= 150°54' $\pm$ 6°54'	= 150°	= 149°
K = 211.5 $\pm$ 12.9 Km/sec	K = 165 Km/sec	K = 162.5 Km/sec
= 106.7 $\pm$ 6.7 Km/sec	= +70 Km/sec	= +40 Km/sec

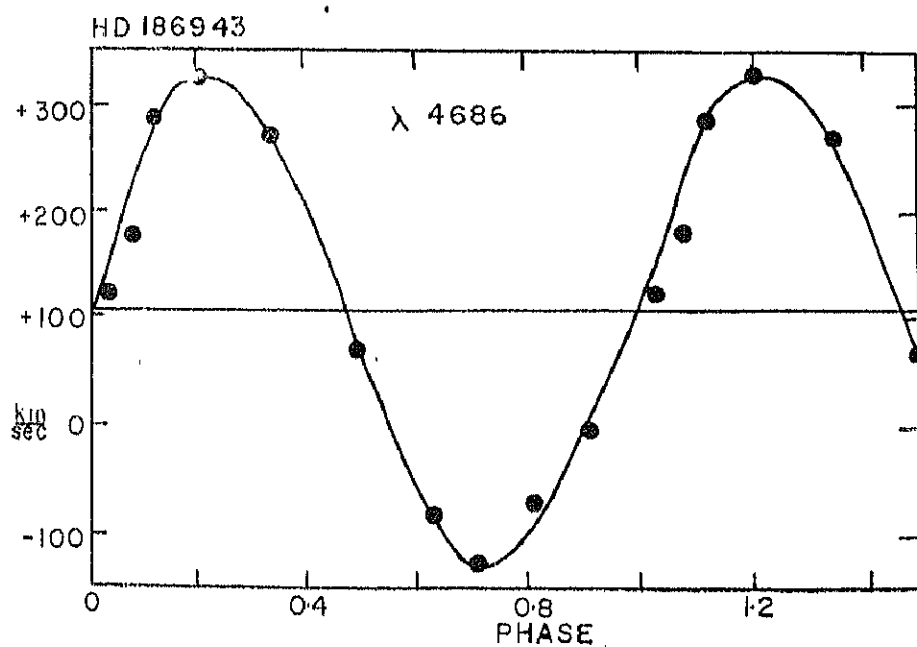


Figure 6.—HD 186943 Velocity curve of HeII 4686

The 4058 Å emission line is extremely weak in this star. In order to obtain this with the correct density, it was necessary to over-expose the 4686 Å region. As such, we have no line profiles of 4686 Å for this star. The 4058 Å line at the time of observation did not exhibit the striking changes reported on by Hiltner.

At a phase close to zero in Figure 7, the line is sharper and more intense than at other phases. It is quite possible that our spectra were exposed during a quiescent spell of the system. Hiltner reported on a phase shift between the velocity curves of  $4686 \text{ \AA}$  and  $4603 \text{ NV}$ . Based on our observations alone, we fail to find such a phase shift. This is also an added confirmation of the fact that the spectra available for this study were obtained at a particularly quiescent phase.

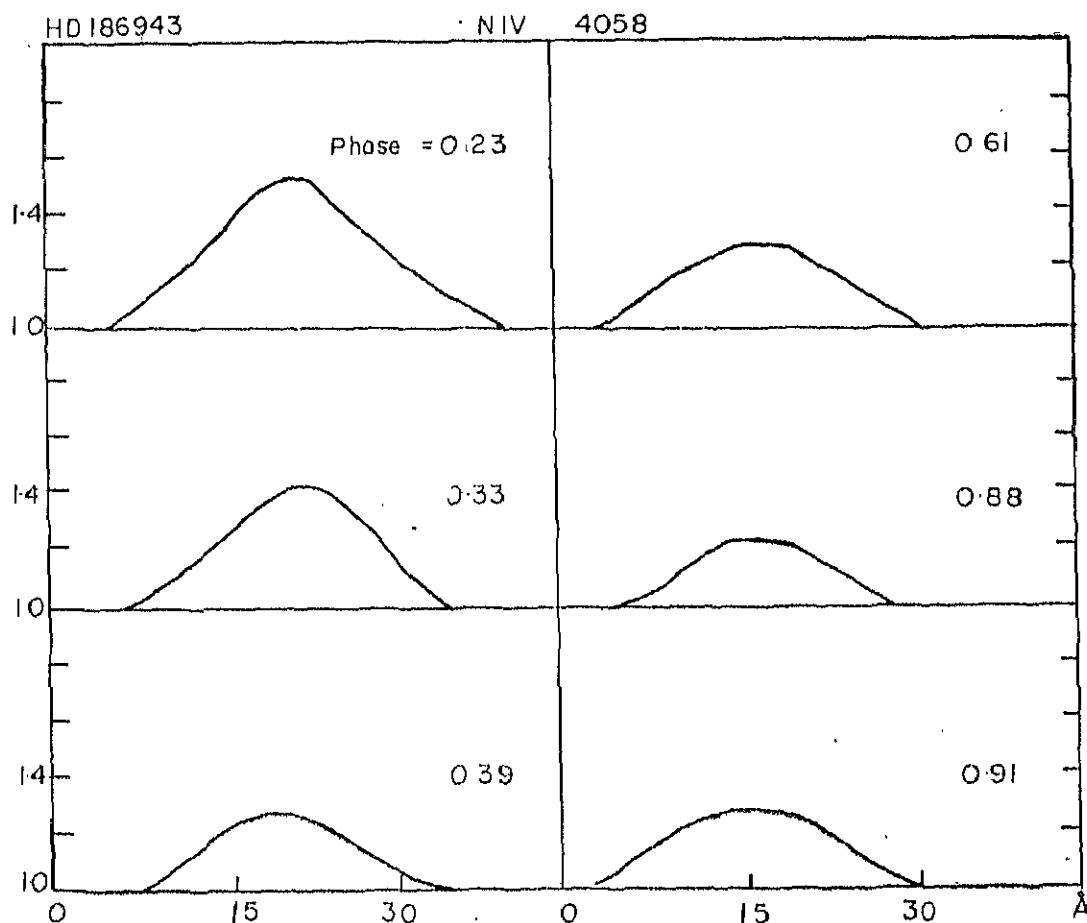


Figure 7.—NIV 4058 Profile changes in HD 186943

### HD 211853

The spectral type of this star is WN6. Hiltner (1966) classifies it as WN6.5-A. The predominant line is HeII  $4686 \text{ \AA}$ . The rest of the emission lines are fairly weak. Absorption lines at  $H\beta$ ,  $H\gamma$  and  $H\delta$  are present. The velocity changes of these lines indicate that they originate from the companion. Occasionally a violet shifted  $4471 \text{ \AA}$  is seen. Hiltner (1945) has given an orbit for the star utilizing the velocity measures of  $4686 \text{ \AA}$ ,  $4058 \text{ \AA}$  and  $4603 \text{ \AA}$ . His measures of the H-lines were not such as to give a confident measure of the velocity curve of the companion. Recently Hjellming and Hiltner (1963) have reported on the light variation of this star. The obvious characteristic of the light curve is the intrinsic variability of the system shown by a lack of repeatability from cycle to cycle. An improved period of the binary has also been derived by Hiltner. This is one of the stars in which Hiltner (1950) has measured the emission line intensities photoelectrically and found that when the Wolf-Rayet star was eclipsed by

the companion, the emission intensity was the greatest. The observations of light variations by Hiltner through UBV filters indicate that an eclipse of the system does take place, but the intrinsic variation in the Wolf-Rayet star is such as to prevent easy study of this light curve by conventional methods.

We have only 10 spectra, primarily obtained for spectrophotometry, available for velocity measures. However, these have been utilized for measuring the velocities of 4686 Å, NIV 4058, NV 4603 and the hydrogen lines of Hγ and Hδ of the companion. These measures are given in Table 4. Only preliminary elements have been derived on the basis of the three emission lines. These indicate that the system is one of small eccentricity. The preliminary elements and the mass function values derived are given in Table 5. There is close agreement between the mass functions derived from HeII 4686 and NV 4603 while that derived from 4058 Å, deviates considerably from the other two emission lines. This is in agreement with the findings of Hiltner that NIV 4058 lacks repeatability.

TABLE 4  
*The radial velocity measures of HD 211853*

Phase	Velocities (km/sec)		
	4686A	4603A	4058A
0.06	+ 15	— 145	— 105
0.09	0	..	— 160
0.20	+ 95	— 80	0
0.34	+ 180	+ 125	+ 20
0.48	+ 250	+ 280	+ 65
0.58	+ 40	+ 125	— 160
0.64	+ 30	+ 120	— 145
0.92	— 225	— 200	— 290
0.93	— 140	— 200	— 225

TABLE 5  
*The orbital elements of HD 211853*

4686A	4058A	4603A
K = 220.00 km/sec	155.00 km/sec	235.00 km/sec
= +15.00 km/sec	—120 km/sec	+35.0 km/sec
e = 0.12	0.20	0.24
= 79°	64°	315°
a sin i = 2.01 x 10 <sup>7</sup>	1.39 x 10 <sup>7</sup>	2.10 x 10 <sup>7</sup>
f(m) = 7.2460	2.4010	8.239

The velocity measures of the hydrogen lines plotted are seen in Figure 8. One sees a general scatter of the points but the trend of velocity is similar to what has been noticed by Hiltner, many years ago. It is rather difficult to fit a velocity curve of the companion, through the points that are available and therefore, we have made no attempt to estimate the mass of the companion.

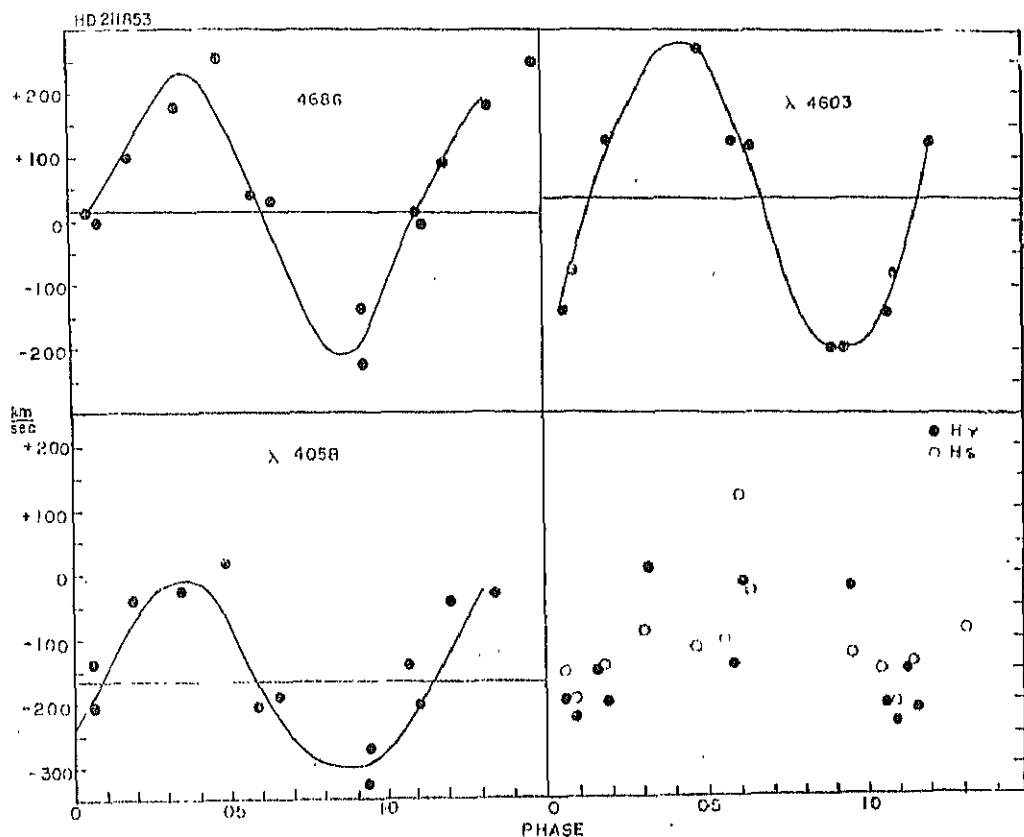


Figure 8. HD 211853 Velocities of the emission and absorption lines

We have derived line profiles for this system for 4686 Å, 4058 Å and 4861 Å (Figures 9a, b, c). The variations seen in H $\epsilon$  4686 are reminiscent of those seen in V444 Cygni. At a phase close to zero corresponding to the position when the Wolf-Rayet star is closest to the observer, the profile is narrower than when the Wolf-Rayet star is farthest from the observer. At phase 0.47, there is a double hump structure in 4686 Å. This double hump is seen even at phases 0.60 and 0.61 and one can speculate on its existence even at phase 0.09. However, the fact that at phase 0.31 the profile is symmetrical indicates that this change of profile is more due to the intrinsic variations in the system than one caused by the variation of phase. The 4058 Å profiles show in general that in the vicinity of phase zero, the profile is narrower than it is elsewhere. The intensity of 4058 Å is extremely weak in this star and hence it is not easy to derive a reliable profile of this emission line. The profile of the emission line at 4680 Å is affected considerably by the presence of the H $\beta$  line of the companion. In general, the emission intensity of ionized helium in the vicinity of phase zero seems to be much less than what it is in the vicinity of phase 0.50 to 0.60. The double hump structure at 0.6 is typical of what one would expect of a receding O star and an approaching Wolf-Rayet star, with the absorption line of H $\beta$  of the O star mutilating the smooth structure of the emission line originating from the Wolf-Rayet star.



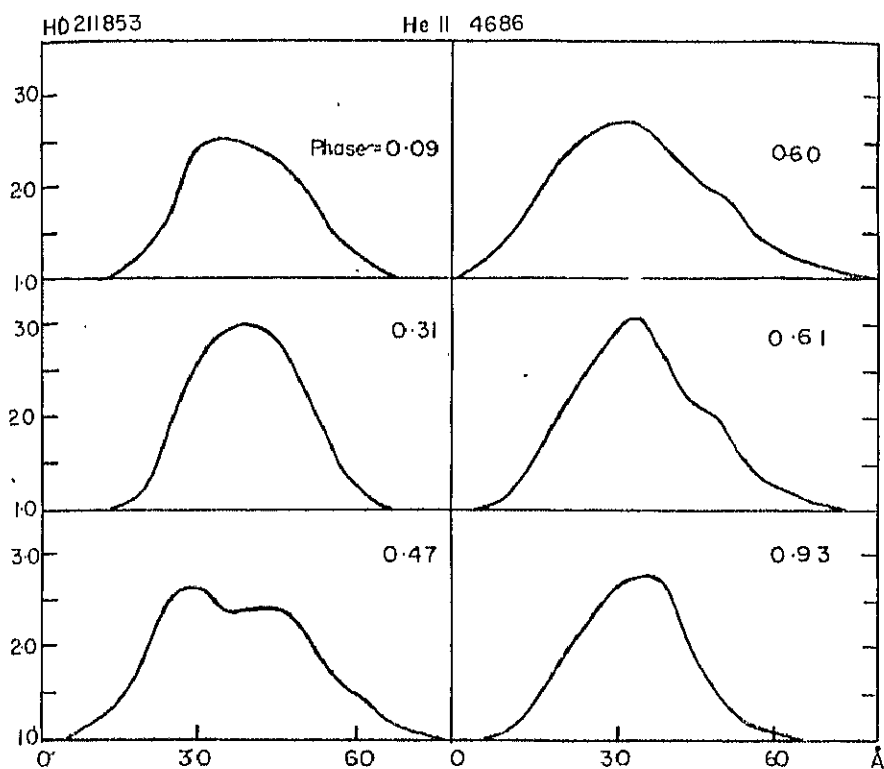


Figure 9 (a).—HD 211853 Line profiles of emission lines in HeII 4686

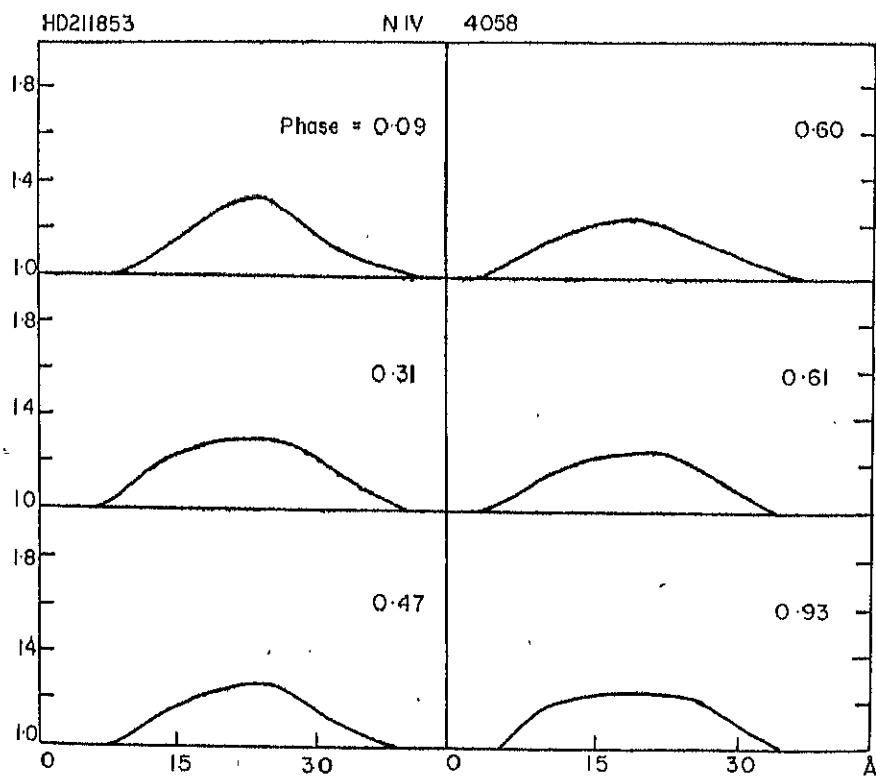


Figure 9 (b).—HD 211853 Line profiles of emission lines in NIV 4058

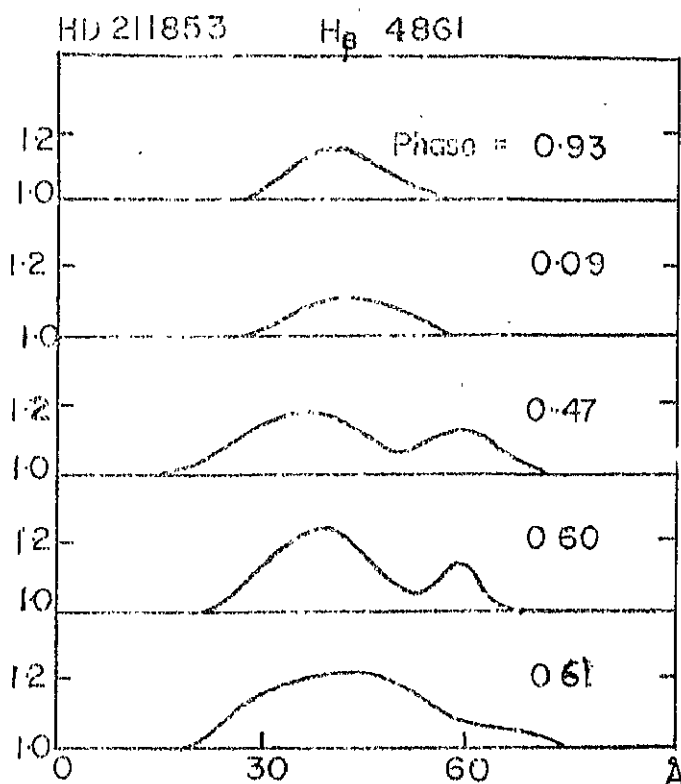


Figure 9 (c).--HD 211853 Line profiles of emission lines in HeII 4861

### Discussion

The observations of five binary systems that we have studied (Ganesh and Bappu, 1967a, Ganesh, Bappu, Natarajan 1967b) provide us with a set of information which can be usefully examined to obtain a picture of the Wolf-Rayet atmosphere. We have attempted to derive orbital elements for the different systems using different lines. While these orbital elements are liable to be affected by mass motions in the binary system, the availability of line profile data simultaneously, enables a judicious selection of the orbital elements to be made. Four of the systems have orbital elements with a least squares fitting of the observations. The system of V444 Cygni is the only one that has a well established light curve. It, therefore, provides the best mass estimate for the Wolf-Rayet star as well as the companion O star. The values obtained for HD 68273 satisfactorily agree with the present day concepts of masses of the Wolf-Rayet stars. It remains to be seen whether HD 68273 is also an eclipsing binary.

A striking feature observed in most of the binary systems examined is that there are large-scale changes in the line profiles caused either by intrinsic variability in the atmosphere of the Wolf-Rayet star or a phase-dependent variation depending on the geometry of the situation. Many of these systems have a structure in HeII 4686, at phases of conjunction, that are typical of material flow through the inner Lagrangian point. It is present even in such a well separated system like HD 68273. Hence, we may conclude that in almost all cases of Wolf-Rayet binary systems, gas flow through the inner Lagrangian point is likely to be

present. Many of the systems examined show large-scale changes in intensity of emission. These are apparent in the HeII lines of the Pickering series in V444 Cygni, in HD 193928 and also in HD 211853. This is suggestive of the fact that it is likely that in a Wolf-Rayet atmosphere, specially of a Wolf-Rayet star that is a member of a binary system with an early type component, the longitudinal distribution of emission is by no means uniform. We have ample justification for this presumption, not only from the data given here but also from the study of CQ Cephei. In general, there seems to be more emission present near the conjunctions than at elongations. The question of course, is whether such a peculiar longitude distribution of emission intensity is stimulated by the presence of the companion. It is difficult to answer this question with any degree of certainty with the present state of observation.

The red-shift experienced by HeII 4686 seems more or less a certainty for the systems examined. HD 68273 with its large separation of components and a period of 78.5 days also shows the phenomenon. This puzzling aspect of the enhanced systemic velocity determined from HeII 4686 is likely to be a vital clue in any explanation of the origin of the emission of HeII 4686. Could it be due to fluorescence as a result of which selective excitation is possible only when the gases that give rise to 4686 Å emission have a certain velocity of recession with respect to the exciting source? This is a problem that needs careful consideration. For the present, the reality of the phenomenon is established beyond doubt.

The binary systems have been an automatic choice for examination of several of the hypotheses advanced earlier concerning the nature of the Wolf-Rayet atmosphere. HD 193576 stimulated Wilson to show that a "transit time effect" would be present if the Beals hypothesis was valid. The Beals picture of a simple expanding shell suffers from various defects. Alternative models postulated have their own difficulties. Many years ago, Bappu (1951) showed that rotational instability could explain the large widths in the emission line in the stars. He also showed that this would call for an excitation gradient of the Wolf-Rayet atmosphere in such a way that the widest lines have the highest excitation. Quite independently, Limber (1964) has postulated that the wide emission in the Wolf-Rayet star can be explained in terms of forced rotational instability consequent to the continual gravitational contraction in a post main-sequence stage. Limber has examined this hypothesis quantitatively and he has shown that it is very attractive when compared to Beal's old hypothesis. A significant aspect of this theory is that the narrow lines originate farther away from the stellar surface than the lines which have enhanced widths. Limber also pointed out that there is a surprising coincidence between the volume occupied by the electron scattering envelope of HD 193576 and that formed by the inner Lagrangian lobe about this component.

While the rotational instability hypothesis has many attractive features which indicate a situation closer to reality than any achieved so far, nevertheless, several difficulties exist that need explanation. In Figure 10, we have plotted the individual velocities of 4686 Å for three binary systems. If rotation is an important feature, then for the eclipsing system V444 Cygni or even for the other systems it would be necessary to observe the Rossiter effect, caused by rotation. It will be seen that an examination of these curves shows that Rossiter effect cannot be detected. Limber, of course, postulates that the absence of a Rossiter effect is not likely to invalidate the hypothesis, since several mechanisms could mask the feature. The broadest emission lines in the system of HD 68273 are

identical to those seen in V444 Cygni. The observations listed above on the broadening of the higher members of the Balmer series at the phase when the O star is eclipsed by the Wolf-Rayet star clearly indicate the definite manifestation of electron scattering. Therefore, one can postulate with sufficient degree of confidence, the fact that such an electron scattering envelope exists in every Wolf-Rayet atmosphere. Several of the binary systems studied have different values of  $K$ . It is very likely that some of them may be systems with high orbital inclinations and some with a small value of  $\sin i$ . In general, it seems as though there is very little difference in the line widths of  $4686 \text{ \AA}$  for the various systems. On the basis of the rotational instability hypothesis, it is necessary to find a change with the inclination. However, the lack of decrease in the emission widths is likely to be offset, by the postulate of electron scattering envelopes of differing properties in such a way that the electron scattering more than offsets the narrowness of the emission lines.

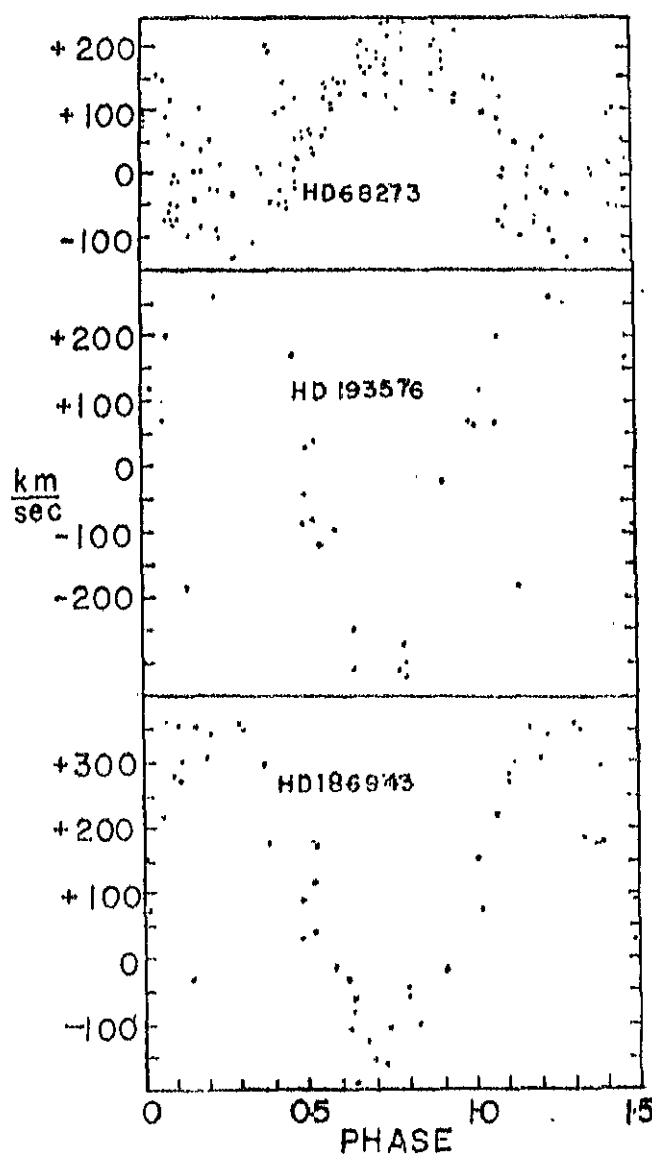


Figure 10.—Velocities of HeII 4686 in the Wolf-Rayet binaries HD 68273, HD 193576 and 186943.

It seems that a profitable avenue for study of the Wolf-Rayet phenomenon, is to study in detail the binary systems. We need to detect many more binary systems than we have so far, in order to find among them systems that have favourable inclinations for an eclipse, systems that can provide reliable information on the masses of the stars and also those that can be usefully utilized in enabling the easy conjecture of a model of the Wolf-Rayet atmosphere.

### Acknowledgement

The observations reported herein were obtained by one of us (MKVB) during a tenure as Carnegie Fellow at the Mount Wilson and Palomar Observatories.

KODAIKANAL OBSERVATORY,

*October, 1967.*

### REFERENCES

- Bappu, M. K. V. 1951, Ph.D. Thesis, Harvard University.  
 Ganesh, K. S., and Bappu, M. K. V. 1967a, Kodaikanal Obs. Bull., Number 183.  
 Ganesh, K. S., and Bappu, M. K. V., 1967b, Kodaikanal Obs. Bull., Number 184.  
 Hjellming R. M., and Hiltner, W. A., 1963, *Astrophys. J.*, **137**, 1080.  
 Hiltner, W. A. 1945, *Astrophys. J.*, **101**, 356.  
 Hiltner, W. A. 1950, *Astrophys. J.*, **112**, 477.  
 Hiltner, W. A. 1966, *Astrophys. J.*, **143**, 770.  
 Limber, D. N. 1964, *Astrophys. J.*, **140**, 1391.

KODAIKANAL OBSERVATORY  
BULLETIN Number 186

Line Profile Analysis of Carbon Molecules in the Sun

Nirupama Raghavan\*

Abstract

Thirteen molecular lines of CN, C<sub>2</sub> and CH have been photoelectrically observed at six disc positions each. The observed trends fall into two categories; one for strong lines and another for weak lines, irrespective of the molecule of their origin. Detailed profile calculations have been made for six selected lines. LTE methodology and an anisotropic model of turbulence have been assumed. In the region of line formation for these molecules ( $\tau=0.1$  to  $0.04$ )  $\xi_{rad}$  and  $\xi_{turb}$  are 3.0 km/sec and 3.6 km/sec respectively. An interesting variation of the factor F, used for fitting central intensities with  $\mu$  is found. It is strongly suspected that important physical reasons underlie this variation.

Ever since Peckers group (1949, 1950, 1952) studied the centre-limb variation of equivalent widths of resolved and unresolved CN, CH and C<sub>2</sub> lines, the problem of correctly interpreting these variations has remained. Calculations based both on pure scattering and pure absorption mechanisms of line formation have predicted equivalent widths that are larger than the observed ones at the limb.

The following ideas have been put forward to remove the discrepancy:

(a) Existence of non-LTE effects as are present in the formation of atomic lines (Pecker and Praderie 1960).

and (b) Presence of unsuspected polyatomic molecules involving carbon (Laborde 1961).

Although these have changed the equivalent widths in the right direction, the agreement has not been improved significantly.

This problem has been heightend by more recent observations by Newkirk (1957) Laborde (1961) and Cowley (1964). Newkirk's analysis of excellent observations of CO lines has shown that the Aller-Pierce model along with the mechanism of pure absorption explains the C-L observations very satisfactorily. Using Minnaert's photospheric model, Laborde predicts the C-L variation of MgH lines correctly, while for C<sub>2</sub> the observed and predicted variations are very different. Cowley's results for CN proves that LTE calculation of equivalent width is entirely adequate for the centre of the disc observations. We are led to conclude, therefore, that:

- (i) A conventional model of the photosphere is adequate for both a molecule like MgH formed relatively lower in the atmosphere ( $\tau_0(\text{MgH}) > 0.1$ ) and a molecule like CO formed higher up ( $\tau_0(\text{CO}) \leq 0.01$ )

\*Now at the Department of Physics, Indian Institute of Technology, Kanpur.

- (ii) Calculations based on a similar frame work are also correct at  $\mu=1.0$  for molecules like CN ( $\tau_0(\text{CN}) \approx 0.06$ )
- (iii) It has *not* been possible to predict the C-L variations of CN, CH and  $\text{C}_2$  on the basis of LTE methodology, coupled with conventional models.

It is evident that the cause for the discrepancy lies in a direction that has not yet been explored and a re-examination of the problem is necessary. The crucial question is, why is LTE methodology inadequate for all observed carbon constituent molecules except CO? In fact CO being formed in the highest layers, should be affected more by deviations from LTE. Also is  $T_{\text{exc}} \neq T_{\text{el}}$  the only way in which non LTE effects enter the molecular problem? These are the questions that must be looked into.

Another aspect of interest regarding carbon molecules, arises from the fact that they exist in a narrow layer in the transition region between the photosphere and the chromosphere. This enables one to use these molecules for studying the structure of this region; especially of interest is the determination of turbulence velocity as can be appreciated from Fig. 1. In the hatched region there are no velocity determinations and it is

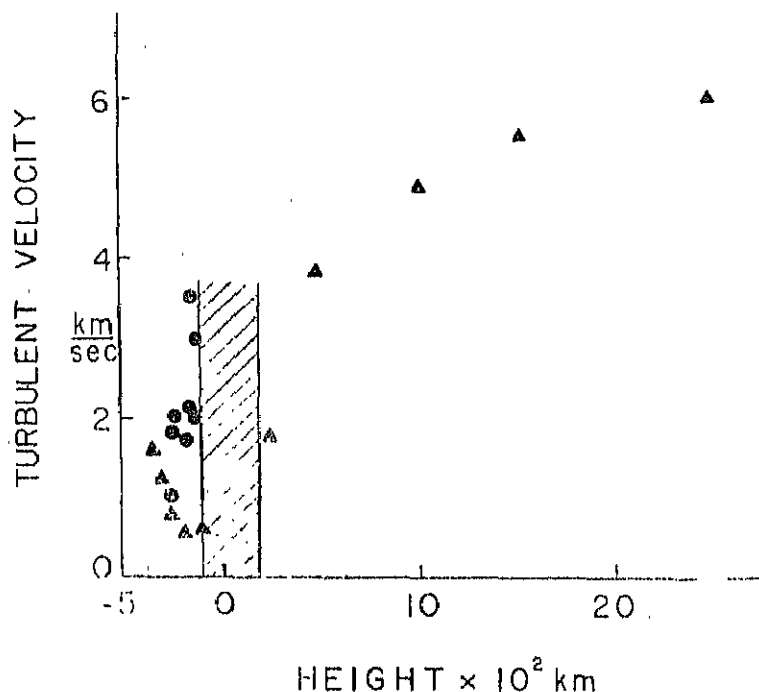


Fig. 1. The known variation of turbulent velocities with height in the solar atmosphere. The shaded area is the region of interest in this investigation; triangles represent Unno's results and circles the results of other workers.

precisely here that the molecules are formed. In his fine analysis of CN lines, Cowle states that his results are insensitive to both the model of turbulence and its magnitude. While this may be true for equivalent widths, profile shapes are sensitive to both.

The object of this investigation has, therefore been:

- (1) to study differentially, C-L variation of line profiles of the Carbon molecule CN, CH and  $\text{C}_2$
- (2) to derive turbulence velocity from these profiles, on the basis of LTE methodology.

## OBSERVATIONS

The solar tower telescope of 38cm aperture of the Kodaikanal Observatory has been used in this work. This gives a 34 cm image (scale 5" arc/mm). The image is guided by an electro-mechanical system, with respect to a pattern of circles drawn at specific  $\mu$  values, and mounted at the plane of the focussed image.

The 18.3 meter Littrow spectrograph has a  $200 \times 135$  mm Babcock grating. The 4th, 5th and 6th orders were used in this study. The dispersion in the 5th order at  $5000\text{\AA}$  is  $10 \text{ mm}/\text{\AA}$ .

The profiles were traced photoelectrically. The scanner had a speed of  $3 \text{ mm}/\text{minute}$  so that scanning rate of  $5 \text{ m}\text{\AA}/\text{sec}$  is achieved. At the dispersion used the scanning slit isolated  $3 \text{ m}\text{\AA}$  of the spectrum. The output was amplified by a D. C. amplifier and fed to a Brown recorder with a  $\frac{1}{2}$  sec time constant. The sky transparency was monitored by a stationary photomultiplier tube, centred on the nearby continuum.

## Instrumental Profile

The instrumental profile was derived by tracing an iodine absorption line at  $5318.610\text{\AA}$  in the 5th order. A 10 cm column of iodine vapour was placed in the Solar beam just ahead of the slit. The pressure of Iodine was controlled by visually examining whether very close doublets at ( $\Delta\lambda \approx 10 \text{ m}\text{\AA}$ ) at  $5330.10$ ,  $5330.33$  and  $5333.57\text{\AA}$  were well resolved. The half width of the instrumental profile with a 2.4 normal slit was  $13 \text{ m}\text{\AA}$ .

The observed profiles were corrected for finite resolving power by the graphical method suggested by Bracewell (1955), which is quick and of useful accuracy. The maximum correction to the central intensity for resolving power was 0.8% of the continuum intensity.

## Scattered Light

If 'g' gives the excess scattered light, the true relative intensity at any point on the profile is given by

$$i_{\text{true}} = (i_{\text{obs}} - g) / (i_{\text{cont, obs}} - g)$$

Diffuse scattered light was taken into account by registering the signal with the ruled area of the grating masked and the scanning slit centred on the continuum. This signal was used as the reference dark level, over which all measurements were made.

To correct for Rowland ghosts, g is obtained from the above equation by combining the observed central intensities of  $\text{H}\gamma$ ,  $\text{Mg } b_1$  and  $\text{Na } D_1$  and  $D_2$  in the 6th, 5th and 4th orders with the Sacramento Peak double pass observations of the same lines (White 1962, Waddell 1962 and 1963). To check the accuracy of this method, 'g' was evaluated from the central intensity of  $\text{Mg } b_1$  and the other parts of the line were corrected using this 'g'. Double pass and the corrected single pass profiles, coincided with each other, over the entire profile, within one percent.

Table I sets out the details of observations. The profiles were measured in all cases with respect to the local continuum which is the same as the general continuum given by the Utrecht Atlas except for CN lines at  $3864\text{\AA}$  and  $3879\text{\AA}$ . Profile measurements for these two lines were referred to an arbitrary continuum which matched the general continuum of Utrecht atlas. This amounted to changing the residual intensities referred to the local continuum by a factor of 0.95.



TABLE I  
Details of the Photoelectric observations included in this study

Date of Observation	Wavelength	Mole- cule	Transition	Rowland Intensity	Seeing	Trans- mission	Location of local continuum
1 April 1964	3864.307Å	CN	$2\Sigma - 2\Sigma$	3	$> 2$ Average	V. Fair	3863.25
2 April 1964	3879.578Å 3879.661Å 3879.716Å	CN	$2\Sigma - 2\Sigma$	1 0 0	2 to 3	Good	3880.55
30 March 1964	4192.917Å	CN	$2\Sigma - 2\Sigma$	-1	2 to 3	V. Fair	4192.80
11 March 1964	4207.409Å		$2\Sigma - 2\Sigma$	1	2 to 3	Good	4207.65
14 March 1964	4212.236Å 4212.407Å	CN	$2\Pi - 2\Pi$ u g	-1 -1	about 2	Fair	4212.50
18 March 1964	5086.251Å 5086.399Å	C <sub>2</sub>	$2\Pi - 2\Pi$ u g	-1 -2	about 2	V. Fair	5086.15
17 March 1964	5094.029Å	C <sub>2</sub>	$2\Pi - 2\Pi$ u g	-2	$< 3$	Good	5093.90
24 March 1964	5147.106Å	C <sub>2</sub>	$2\Pi - 2\Pi$ u g	2 -2	2 to 3	Good	5145.95
26 March 1964	5159.467Å 5159.609Å	C <sub>2</sub>	$2\Pi - 2\Pi$ u g	-3	2 to 3	Fair	5158.25
14 March 1964	4210.970Å	CH	$2A - 2\Pi$	-3	2 to 3	Fair	4212.50
15 March 1964	4218.726Å	CH	$2A - 2\Pi$	-3	$> 2$	V. Fair	4218.60
16 March 1964	4281.974Å	CH	$2A - 2\Pi$	-2	$> 2$	V. Fair	4281.65
28 March 1964	4378.915Å	CH	$2A - 2\Pi$	-2	2 to 3	Good	4378.75

Pencilled copies of the profile on transparent graph sheets were obtained and measured at every millimeter, dispersion on the traces ranging from  $.007\text{\AA}/\text{mm}$  to  $.005\text{\AA}/\text{mm}$ . The average of atleast six such traces was plotted to a large working scale and corrected for instrumental profile and scattered light.

#### Description of the observed profiles

**3864.307 $\text{\AA}$  CN:** This is a close spin doublet with a separation of less than  $15\text{m}\text{\AA}$  and rotational quantum number  $K=14$ . The central intensity increases from centre to limb, slowly at first and steeply later. The half width also increases towards the limb, so that the equivalent width remains nearly constant. The profile takes a characteristic U-shape towards the limb.

$\left. \begin{array}{l} 3879.579\text{\AA} \\ 3879.661\text{\AA} \\ 3879.716\text{\AA} \end{array} \right\}$  CN is a triplet of the 0—0 vibrational transition;  $K=9, 48$  and 48 respectively.

Towards the limb, the profiles become shallow and broad keeping the total absorption due to the three lines effectively constant.

4192.917 $\text{\AA}$  CN comprises of three lines of 4192, 898 $\text{\AA}$ . 4192.898 $\text{\AA}$  and 4192.962 of the 0—1 vibrational transition.

The latter two have  $K=40$  of the P branch and the former  $K=0$  of the R branch. The profile has a pronounced red asymmetry, as is to be expected in view of the presence of the 4192.962 $\text{\AA}$  line. Central intensity decreases in going towards the limb. The half widths, however, increase and the profile becomes U shaped towards the limb.

4207.409 $\text{\AA}$  line of CN is a doublet of 4207.399 and 4207.468 $\text{\AA}$ . Central intensity rises steeply with decreasing  $\mu$ . At the limb, the profiles are U shaped, broader and shallower.

4212.215 $\text{\AA}$ , 4212.275 $\text{\AA}$  and 4212.399 $\text{\AA}$  are CN lines with  $\Delta V=-1$ . The first two are spin doublets with  $K=38$  and 4212.399 $\text{\AA}$  has  $K=7$ . The C-L decrease of the central intensity of the unresolved spin doublet is more rapid than that of 4212.399 $\text{\AA}$ .

4210.970 $\text{\AA}$  of CH has  $K=16$  and is a doublet of  $R_{2cd}$  and  $R_{1cd}$  components. The line has a violet asymmetry. Like the strong lines of CN,  $r_c$ , the central intensity increases towards the limb and the profile is once again U shaped at the limb. 4218.726 $\text{\AA}$  of CH is a doublet comprising of the  $R_{1dc}$  and the  $R_{2dc}$  components of  $K=15$ . This has a slight red asymmetry and has the same characteristic C-L variation of central intensity and half width as the 4210 $\text{\AA}$  line of CH.

4281.974 $\text{\AA}$  of CH also behaves similarly on going from centre to limb. This line comprises of the  $Q_{1d}+Q_{2d}$  components of  $K=22$ .

4378.915 $\text{\AA}$  of CH is in the P branch of 1—1 vibrational transition with  $K=15$  and is made up of the  $P_{1dc}$  and the  $P_{2dc}$  components. The line has a C-L variation of  $r_c$  and half width similar to the weaker lines of CN, i.e., 4192 and 4212 $\text{\AA}$ .

5086.251 $\text{\AA}$ , 5086.399 $\text{\AA}$  are partially resolved  $C_2$  triplet of the Swan system. 5086.251 is the unresolved  $R_{23}(37)$  line and 5086.399 $\text{\AA}$ , the  $R_1(37)$  line. The lines are broader and deeper towards the limb, following the pattern of the weak lines of CN. 5094.029 of  $C_2$  comprises of the unresolved  $P_{23}(62)$  at 5094.002 and  $P_1(62)$  at 5094.025.

This weak line has a central intensity of 91.7% at the centre, which decreases to 90.6% at  $\mu = 0.25$ . Again the half width increases towards the limb and the profile becomes markedly U shaped on going from  $\mu = 0.35$  to  $\mu = 0.25$ . 5147.106 Å of  $C_2$  is a  $R_1(11)$  line and is blended on both wings. The slight violet asymmetry may be an atomic blend effect. Neither the central intensity nor the half width increase very much until  $\mu = 0.35$ . From  $\mu = 0.35$  to  $\mu = 0.25$  the increase in  $r_c$  and half width is relatively more marked.

5159.467 Å and 5759.609 Å of  $C_2$  are  $P_{21}(28)$  and  $P_1(28)$  lines of the Swan system. Their G-L variation follows the same pattern set by other weak lines of CN and  $C_2$  described above.

The observed profiles are given in numerical form in Table II. Fig 2, gives the observed G-L variation of central intensities  $r_c$  for strong and weak lines. Summarising the general trends, we find that lines are broader at the limb than at the centre in all cases.  $r_c$  shows a decrease up to  $\mu = 0.45$  and then increases slowly for weak lines. For all strong lines irrespective of the parent molecule,  $r_c$  increases slowly up to  $\mu = 0.7$  and then increases more steeply.

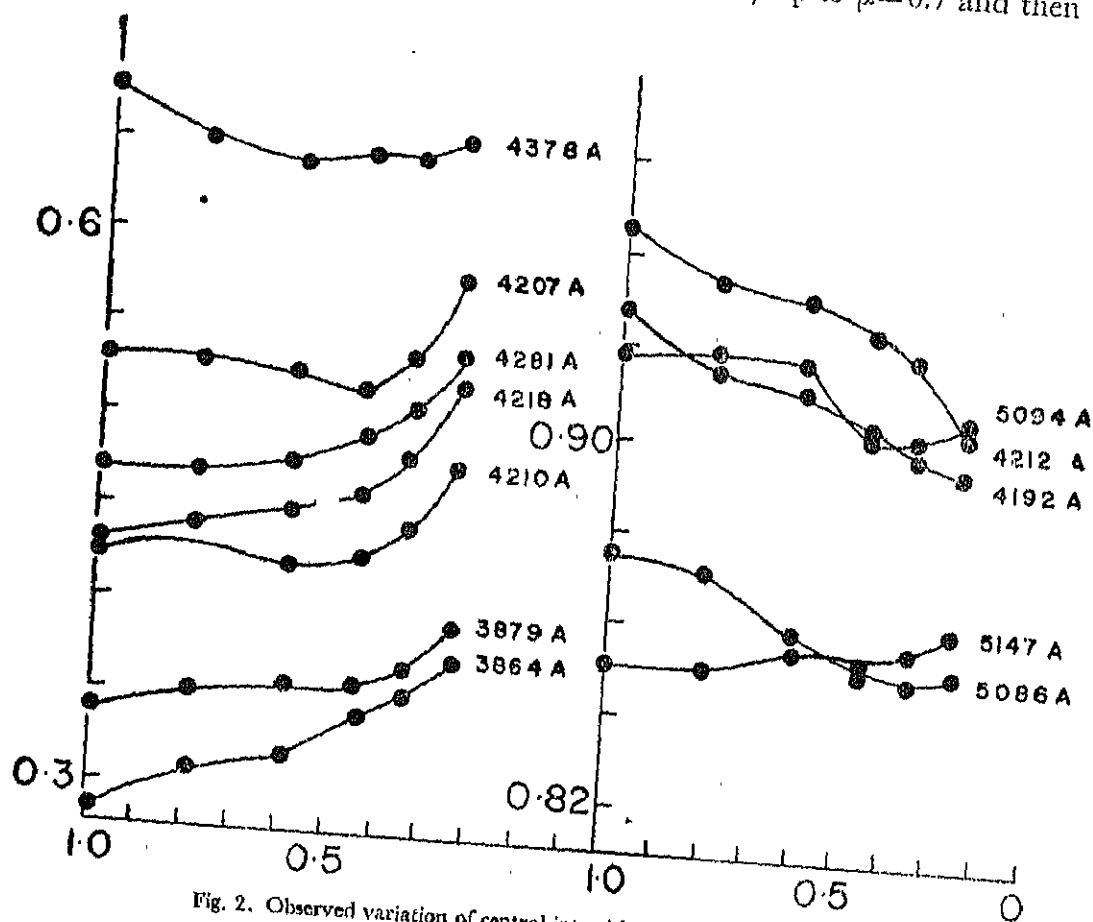


Fig. 2. Observed variation of central intensities for strong and weak lines.

The generality of the trends indicates that the G-L variations are characteristic of the physical structure of the solar atmosphere rather than a property of the particular molecule concerned. Some factor affecting all three molecules identically could, however, be the reason for the similarity in the G-L variation.

TABLE II.

$\Delta\lambda$ in mÅ	$\mu = 1.00$		$\mu = 0.80$		$\mu = 0.60$		$\mu = 0.45$		$\mu = 0.35$		$\mu = 0.25$	
	Violet	Red	Violet	Red	Violet	Red	Violet	Red	Violet	Red	Violet	Red
3864.307 Å *CN												
0	0.295	0.295	0.310	0.310	0.315	0.315	0.340	0.340	0.350	0.350	0.370	0.370
20	0.355	0.355	0.355	0.355	0.395	0.385	0.387	0.380	0.390	0.385	0.405	0.405
40	0.560	0.560	0.525	0.520	0.555	0.530	0.545	0.535	0.530	0.525	0.535	0.535
60	0.778	0.763	0.730	0.695	0.730	0.695	0.700	0.710	0.695	0.690	0.710	0.700
80	0.825	0.815	0.810	0.810	0.815	0.800	0.807	0.805	0.815	0.800	0.780	0.762
100	0.835	0.825	0.820	0.825	0.835	0.820	0.830	0.825	0.830	0.820	0.812	0.810
120											0.820	0.820
4192.917 Å *CN												
0	0.926	0.926	0.913	0.913	0.911	0.911	0.903	0.903	0.898	0.898	0.894	0.894
20	0.938	0.933	0.928	0.924	0.919	0.921	0.912	0.912	0.902	0.902	0.904	0.903
40	0.966	0.948	0.957	0.939	0.940	0.941	0.941	0.934	0.925	0.923	0.924	0.924
60	0.987	0.963	0.984	0.956	0.963	0.962	0.966	0.955	0.961	0.953	0.962	0.950
80	0.996	0.979	0.993	0.975	0.984	0.985	0.985	0.978	0.984	0.977	0.987	0.978
100	1.000	0.990	0.998	0.993	0.994	0.997	0.996	0.991	0.998	0.994	0.997	0.996
120	1.000	0.998	1.000	1.000	1.000	0.999	1.000	0.998	1.000	1.000	1.000	1.000
140		1.000			1.000	1.000		1.000				
4207.409 Å *CN												
0	0.530	0.530	0.530	0.530	0.525	0.525	0.515	0.515	0.535	0.535	0.580	0.580
20	0.560	0.555	0.570	0.565	0.540	0.545	0.540	0.545	0.550	0.560	0.598	0.598
40	0.640	0.640	0.642	0.625	0.620	0.615	0.595	0.620	0.605	0.620	0.660	0.655
60	0.750	0.750	0.750	0.740	0.730	0.728	0.695	0.710	0.700	0.700	0.755	0.735
80	0.855	0.845	0.857	0.845	0.825	0.815	0.792	0.800	0.790	0.810	0.860	0.830
100	0.932	0.900	0.926	0.900	0.900	0.890	0.870	0.870	0.882	0.875	0.913	0.890
120	0.955	0.940	0.955	0.937	0.940	0.925	0.920	0.913	0.920	0.920	0.955	0.937
140	0.950	0.960	0.960	0.962	0.955	0.945	0.930	0.940	0.917	0.950	0.965	0.960
160		0.970	0.940	0.980	0.950	0.960	0.925	0.950	0.910	0.965	0.935	0.975
180		0.975	0.980	0.980		0.965	0.960	0.960		0.975		0.980

\*Refers to the wavelength of the centre of the line as given in the Revised Rowland Table.

TABLE II—Contd.

$\Delta\lambda$ in $m\mu$	$\mu = 1.00$ Violet	Red	$\mu = 0.80$ Violet	Red	$\mu = 0.60$ Violet	Red	$\mu = 0.45$ Violet	Red	$\mu = 0.35$ Violet	Red	$\mu = 0.25$ Violet	Red
5094.029 Å * C <sub>2</sub>												
0	0.917	0.917	0.918	0.918	0.918	0.918	0.901	0.901	0.901	0.901	0.906	0.906
20	0.927	0.926	0.929	0.925	0.931	0.925	0.912	0.910	0.913	0.914	0.914	0.913
40	0.942	0.938	0.931	0.935	0.947	0.937	0.932	0.924	0.936	0.927	0.932	0.924
60	0.963	0.951	0.955	0.947	0.964	0.948	0.953	0.935	0.957	0.939	0.953	0.937
80	0.978	0.962	0.975	0.957	0.981	0.959	0.971	0.945	0.974	0.950	0.969	0.949
100	0.992	0.973	0.991	0.967	0.993	0.969	0.985	0.957	0.988	0.960	0.983	0.961
120	0.997	0.982	0.998	0.975	0.999	0.976	0.994	0.963	0.994	0.969	0.992	0.971
140	0.999	0.989	0.999	0.982	1.000	0.984	0.999	0.978	0.999	0.976	0.997	0.979
160	1.000	0.994	1.000	0.988		0.990	1.000	0.986	1.000	0.983	1.000	0.985
180		0.997		0.993		0.995		0.992		0.988		0.990
200		0.999		0.996		0.998		0.997		0.993		0.994
220		1.000		0.999		1.000		1.000		0.996		0.997
240				1.000						0.999		0.999
5147.106 Å * C <sub>2</sub>												
0	0.850	0.850	0.851	0.851	0.856	0.856	0.851	0.851	0.854	0.854	0.860	0.860
20	0.862	0.862	0.859	0.862	0.870	0.870	0.865	0.864	0.870	0.869	0.869	0.869
40	0.890	0.888	0.884	0.890	0.897	0.903	0.890	0.894	0.891	0.890	0.890	0.897
60	0.920	0.932	0.913	0.926	0.928	0.938	0.918	0.924	0.924	0.918	0.916	0.924
80	0.946	0.953	0.937	0.943	0.953	0.962	0.942	0.947	0.943	0.944	0.940	0.947
100	0.962	0.964	0.952	0.964	0.965	0.974	0.956	0.963	0.952	0.960	0.959	0.965
120	0.971	0.973	0.962	0.974	0.973	0.978	0.965	0.973	0.960	0.969	0.963	0.975
140	0.974	0.976	0.971	0.978	0.976	0.982	0.968	0.979	0.962	0.977	0.961	0.981
160	0.969	0.980	0.974	0.980	0.970	0.980	0.965	0.980	0.956	0.981	0.958	0.982

\*Refers to the wavelength of the centre of the line as given in the Revised Rowland Table.

TABLE II—Contd.

$\Delta\lambda$ in mÅ	$\mu = 1.00$		$\mu = 0.80$		$\mu = 0.60$		$\mu = 0.45$		$\mu = 0.35$		$\mu = 0.25$	
	Violet	Red	Violet	Red	Violet	Red	Violet	Red	Violet	Red	Violet	Red
4210.970Å* CH												
0	0.425	0.425	0.430	0.430	0.420	0.420	0.430	0.430	0.442	0.442	0.435	0.485
20	0.440	0.445	0.450	0.447	0.435	0.437	0.442	0.447	0.460	0.460	0.497	0.495
40	0.500	0.535	0.515	0.535	0.495	0.460	0.472	0.485	0.477	0.487	0.537	0.530
60	0.595	0.670	0.595	0.645	0.575	0.603	0.555	0.595	0.565	0.605	0.610	0.605
80	0.700	0.795	0.715	0.760	0.680	0.723	0.655	0.735	0.650	0.705	0.692	0.703
100	0.785	0.865	0.793	0.855	0.705	0.810	0.765	0.825	0.740	0.807	0.775	0.798
120	0.855	0.895	0.875	0.905	0.840	0.875	0.842	0.875	0.825	0.862	0.840	0.868
140	0.917	0.910	0.925	0.920	0.897	0.907	0.887	0.900	0.885	0.895	0.890	0.907
160	0.937	0.915	0.935	0.925	0.922	0.925	0.925	0.915	0.923	0.907	0.925	0.920
180	0.950	0.930	0.945	0.925	0.925	0.927	0.940	0.910	0.925	0.910	0.925	0.920
200			0.950									
4218.726Å* CH												
0	0.430	0.430	0.440	0.440	0.450	0.450	0.460	0.460	0.480	0.480	0.517	0.517
20	0.462	0.458	0.478	0.473	0.478	0.475	0.490	0.485	0.500	0.505	0.535	0.538
40	0.575	0.565	0.570	0.563	0.585	0.580	0.582	0.570	0.565	0.565	0.597	0.600
60	0.735	0.730	0.730	0.710	0.715	0.710	0.710	0.690	0.695	0.700	0.700	0.717
80	0.870	0.875	0.870	0.830	0.832	0.845	0.830	0.812	0.820	0.815	0.810	0.850
100	0.945	0.930	0.955	0.955	0.935	0.925	0.930	0.890	0.915	0.895	0.915	0.917
120	0.992	0.948	0.990	0.975	0.978	0.960	0.965	0.940	0.960	0.940	0.970	0.950
140	0.997	0.972	0.998	0.985	0.992	0.973	0.982	0.965	0.997	0.962	0.987	0.967
160	1.000	0.975	1.000	0.965	1.000	0.982	0.992	0.972	1.000	0.970	0.997	0.972
180							1.000				1.000	

\*Refers to wavelength of the centre of the line as given in the Revised Rowland Table.

TABLE II—Contd.

$\Delta\lambda$ in mÅ	$\mu = 1.00$		$\mu = 0.80$		$\mu = 0.60$		$\mu = 0.45$		$\mu = 0.35$		$\mu = 0.25$	
	Violet	Red	Violet	Red	Violet	Red	Violet	Red	Violet	Red	Violet	Red
4231.974 Å* CH												
0	0.467	0.467	0.470	0.470	0.475	0.475	0.490	0.490	0.505	0.505	0.535	0.535
20	0.490	0.495	0.497	0.500	0.490	0.495	0.507	0.512	0.522	0.525	0.550	0.560
40	0.565	0.560	0.565	0.570	0.555	0.557	0.565	0.570	0.580	0.570	0.595	0.600
60	0.697	0.690	0.680	0.680	0.665	0.660	0.650	0.665	0.665	0.665	0.670	0.685
80	0.822	0.820	0.795	0.800	0.790	0.780	0.780	0.810	0.810	0.751	0.770	0.770
100	0.903	0.895	0.915	0.880	0.895	0.860	0.890	0.862	0.895	0.845	0.865	0.855
120	0.965	0.930	0.965	0.915	0.950	0.910	0.950	0.920	0.945	0.902	0.930	0.900
140	0.982	0.945	0.990	0.930	0.977	0.930	0.975	0.935	0.975	0.930	0.960	0.930
160	0.997	0.915	1.000	0.945	0.992	0.935	0.990	0.935	0.990	0.935	0.985	0.930
180	1.000	0.915	1.000	0.945	1.000	0.935	1.000	0.935	0.995	0.935	0.995	0.915
200									1.000		1.000	
4378.915 Å* CH												
0	0.675	0.675	0.650	0.650	0.640	0.640	0.645	0.645	0.640	0.640	0.655	0.655
20	0.700	0.702	0.680	0.680	0.665	0.665	0.670	0.667	0.665	0.658	0.675	0.670
40	0.780	0.752	0.752	0.727	0.740	0.710	0.740	0.712	0.725	0.698	0.732	0.710
60	0.870	0.805	0.850	0.780	0.835	0.760	0.832	0.757	0.805	0.752	0.818	0.755
80	0.950	0.855	0.915	0.832	0.955	0.810	0.990	0.807	0.898	0.802	0.895	0.807
100	0.980	0.890	0.962	0.872	0.980	0.855	0.907	0.850	0.942	0.842	0.945	0.845
120	0.995	0.905	0.975	0.898	0.992	0.878	0.983	0.880	0.970	0.865	0.975	0.870
140	1.000	0.915	0.983	0.915	0.997	0.890	0.992	0.898	0.980	0.882	0.990	0.888
160		0.930	0.992	0.922	1.000	0.902	1.000	0.912	0.992	0.895	0.997	0.900
180									1.000		1.000	

\*Refers to the wavelength of the centre of the line as given in the Revised Rowland Table.

TABLE II—Contd.

$\Delta\lambda$ in $m\text{\AA}$	$\mu=1.00$	$\mu=0.80$	$\mu=0.60$	$\mu=0.45$	$\mu=0.35$	$\mu=0.25$
3879.418 $\text{\AA}$ * CN						
0	0.845	0.847	0.855	0.840	0.847	0.823
20	0.845	0.845	0.835	0.847	0.840	0.842
40	0.842	0.837	0.835	0.840	0.840	0.835
60	0.832	0.830	0.820	0.815	0.825	0.812
80	0.810	0.805	0.760	0.760	0.762	0.740
100	0.720	0.730	0.675	0.645	0.660	0.620
120	0.575	0.515	0.515	0.485	0.525	0.495
140	0.400	0.390	0.395	0.385	0.405	0.410
160	0.335	0.350	0.360	0.360	0.365	0.390
180	0.420	0.390	0.390	0.375	0.390	0.410
200	0.475	0.432	0.410	0.395	0.402	0.412
220	0.395	0.390	0.370	0.360	0.370	0.387
240	0.355	0.350	0.355	0.343	0.355	0.382
260	0.390	0.365	0.355	0.350	0.362	0.390
280	0.375	0.360	0.372	0.372	0.380	0.405
300	0.385	0.385	0.420	0.425	0.420	0.455
320	0.515	0.490	0.570	0.535	0.560	0.595
34	0.790	0.690	0.720	0.720	0.690	0.725
360	0.850	0.790	0.805	0.800	0.795	0.810
380	0.850	0.812	0.845	0.812	0.820	0.815
400		0.760	0.760	0.810		
4212.116 $\text{\AA}$ * CN						
0	0.980	0.983	0.982	0.982	0.979	0.976
20	0.992	0.985	0.985	0.984	0.977	0.977
40	0.989	0.977	0.981	0.974	0.964	0.972
60	0.976	0.962	0.962	0.957	0.948	0.951
80	0.959	0.949	0.946	0.943	0.932	0.928
100	0.949	0.938	0.935	0.939	0.922	0.911
120	0.914	0.934	0.931	0.923	0.919	0.904
140	0.951	0.940	0.935	0.929	0.924	0.910
160	0.961	0.952	0.948	0.942	0.938	0.925
180	0.972	0.966	0.962	0.962	0.955	0.958
200	0.982	0.979	0.977	0.989	0.980	0.978
220	0.988	0.986	0.983	0.996	0.983	0.983
240	0.981	0.970	0.973	0.977	0.969	0.968
260	0.963	0.952	0.957	0.957	0.947	0.951
280	0.950	0.951	0.949	0.947	0.938	0.938
300	0.961	0.970	0.964	0.963	0.953	0.952
320	0.980	0.984	0.978	0.979	0.975	0.973
340	0.993	0.995	0.994	0.992	0.992	0.991
360	0.998	1.000	1.000	1.000	0.998	1.000
380	1.000				1.000	

\*Indicates that residual intensities have been measured from this position, in steps of 20m $\text{\AA}$  towards the long wavelength.



TABLE II—Contd.

$\Delta\lambda$ in $m\text{\AA}$	$\mu=1.00$	$\mu=0.80$	$\mu=0.60$	$\mu=0.45$	$\mu=0.35$	$\mu=0.25$
5085.071 $\text{\AA}$ * $\text{Cl}_2$						
0	1.000	0.998	0.998	0.998	1.000	1.000
20	1.000	1.000	1.000	1.000	0.998	0.998
40	0.999	0.996	0.998	0.998	0.994	0.992
60	0.993	0.991	0.991	0.993	0.983	0.980
80	0.984	0.982	0.976	0.970	0.970	0.960
100	0.968	0.964	0.958	0.948	0.944	0.938
120	0.946	0.941	0.934	0.912	0.912	0.911
140	0.912	0.911	0.900	0.976	0.883	0.881
160	0.888	0.884	0.874	0.860	0.859	0.862
180	0.874	0.871	0.863	0.852	0.848	0.852
200	0.886	0.883	0.875	0.863	0.858	0.862
220	0.906	0.906	0.893	0.882	0.880	0.884
240	0.929	0.927	0.914	0.910	0.904	0.909
260	0.946	0.948	0.932	0.931	0.922	0.926
280	0.951	0.954	0.943	0.940	0.933	0.933
300	0.951	0.947	0.945	0.934	0.934	0.930
320	0.942	0.938	0.941	0.926	0.926	0.927
340	0.942	0.938	0.937	0.931	0.923	0.929
360	0.949	0.950	0.946	0.942	0.934	0.939
380	0.964	0.965	0.959	0.956	0.951	0.954
400	0.979	0.978	0.974	0.971	0.969	0.969
420	0.989	0.988	0.986	0.984	0.983	0.983
440	0.998	0.995	0.995	0.994	0.993	0.993
460	1.000	0.998	0.998	0.999	0.998	0.999
480		1.000	1.000	1.000	1.000	1.000
5159.327 $\text{\AA}$ * $\text{Cl}_2$						
0	0.964	0.964	0.965	0.963	0.964	0.963
20	0.964	0.964	0.964	0.963	0.963	0.960
40	0.961	0.961	0.958	0.959	0.958	0.950
60	0.956	0.957	0.948	0.946	0.938	0.937
80	0.938	0.944	0.922	0.926	0.908	0.910
100	0.910	0.907	0.890	0.894	0.882	0.882
120	0.881	0.872	0.869	0.863	0.855	0.854
140	0.864	0.861	0.863	0.853	0.843	0.841
160	0.877	0.871	0.872	0.862	0.854	0.852
180	0.900	0.895	0.888	0.879	0.874	0.876
200	0.920	0.912	0.908	0.899	0.895	0.892
220	0.928	0.920	0.914	0.910	0.900	0.900
240	0.921	0.916	0.910	0.904	0.898	0.894
260	0.902	0.908	0.903	0.894	0.890	0.884
280	0.910	0.902	0.898	0.892	0.889	0.886
300	0.928	0.908	0.906	0.904	0.900	0.893
320	0.942	0.930	0.923	0.918	0.914	0.914
340	0.951	0.946	0.939	0.933	0.945	0.930
360	0.955	0.954	0.946	0.941	0.937	0.940
380		0.954	0.948	0.947	0.945	0.942

\*Indicates that residual intensities have been measured from this position, in steps of  $20m\text{\AA}$  towards the long wavelength region.

## THEORETICAL LINE PROFILES

Calculation of line profiles requires that  $I_c(\lambda, \mu)$  the continuum intensity and  $I_l(\lambda, \mu)$  the line intensity be computed. These calculations have been based on the assumption that:

1. Local thermodynamic equilibrium conditions are valid in this problem.
2. Lines are formed by pure absorption.
3. Molecular lines are not affected by damping, so that only pure Doppler profiles are calculated.

*Continuum Intensity*

In choosing the model atmosphere two factors were considered. Firstly that the carbon constituent molecules are formed in the transition region between the photosphere and the chromosphere and all three molecules under study have been observed in emission. Therefore, the model atmosphere covering very small values of optical depth is required. Secondly the ability of standard photospheric models to explain observations of CO and MgH molecules indicate that cold models with  $T \approx 3900^\circ \text{K}$  advocated by Pecker (1957) are probably ruled out. Also an analytical model based on observations is more suitable. Therefore, from  $\log \tau_0 = -1.6$  to  $\log \tau_0 = +0.6$  Pierce-Waddell (1961) model was used. This model was extended beyond  $\log \tau_0 = -1.6$  by combining it with the model given for the lower Chromosphere by Thomas and Athay (1961). This extends upto  $\log \tau_0 = -5.0$ . Table III gives the adopted model. The last column gives the total absorption coefficient  $K_\lambda$  per atom of neutral Hydrogen in the continuum.

TABLE III  
Pierce-Waddell HAO Model

$\log \tau_0$	T in degrees K	$P_g$ in $\times 10^4$ dynes/cm	$P_e$ in $10^2$ dynes/cm	$K$ in $10^{-25}$ per neutral hydrogen atom
-5.0	6150	0.0071	0.0040	0.1482
-4.8	6060	0.0089	0.0039	0.1537
-4.6	5940	0.0123	0.0038	0.1616
-4.4	5820	0.0182	0.0038	0.1753
-4.2	5675	0.0275	0.0039	0.1934
-4.0	5585	0.0427	0.0038	0.2064
-3.8	5490	0.0646	0.0036	0.2106
-3.6	5300	0.0977	0.0035	0.2200
-3.4	5230	0.1413	0.0037	0.2593
-3.2	5140	0.2130	0.0040	0.2988
-3.0	5050	0.3167	0.0045	0.3642
-2.8	4955	0.4365	0.0054	0.4700
-2.6	4870	0.5957	0.0062	0.5863
-2.4	4790	0.7943	0.0072	0.7316
-2.2	4720	1.0720	0.0087	0.9407
-2.0	4680	1.4130	0.0108	1.2119
-1.8	4690	1.8520	0.0132	1.4695
-1.6	4740	2.3990	0.0164	1.7394
-1.4	4842	2.9240	0.0211	2.0457
-1.2	4976	3.7760	0.0280	2.4831
-1.0	5141	4.8870	0.0404	3.0148
-0.8	5339	6.3100	0.0598	3.7945
-0.6	5575	8.0540	0.0944	5.1547
-0.4	5805	10.0000	0.1660	7.6028
-0.2	6130	11.9900	0.3206	12.0860
-0.0	6469	13.9900	0.6622	20.5280
+0.2	6858	15.6700	1.4660	36.2100
+0.4	7362	17.2200	3.5240	56.9560
+0.6	8005	18.4500	9.3760	131.2600

$$K_{\lambda} = R_{\lambda} (H^{-}) \cdot Pe + K_{\lambda} (H) \quad (1)$$

$K_{\lambda} (H^{-})$  were taken from Gingerich (1960)

$K_{\lambda} (H^{-})$  and  $K_{\lambda} (H)$  are the absorption coefficients due to  $H_{\lambda}$  and  $H$  respectively and  $Pe$  the electron pressure.

$$K_{\lambda} (H) = \frac{C}{y^3} \left(1 - e^{-\frac{hy}{kT}}\right) e^{-\frac{x}{kT}} \sum_{n=3}^{\infty} \frac{e^{\frac{x}{n^2 kT}}}{n^3} + \frac{e^{\frac{x}{81kT}}}{2xkT}$$

is evaluated for every level of the model.

The emergent intensity in the continuum is given by (2)

$$I_c(\lambda, \mu) = \int_0^{\infty} S_{\lambda} e^{-\frac{\tau_{\lambda}}{\mu}} d\tau_{\lambda} / \mu \quad (3)$$

where  $S_{\lambda}$  is the source function

Replacing  $S_{\lambda}$  by  $B_{\lambda}$  the Planck function,

$$I_c(\lambda, \mu) = \int_0^{\infty} B_{\lambda} e^{-\frac{\tau_{\lambda}}{\mu}} d\tau_{\lambda} / \mu \quad (4)$$

$$\text{with } d\tau_{\lambda} = \frac{K_{\lambda}}{K_0} d\tau_0 \quad ; \quad \tau_{\lambda} = \int_0^{\tau_0} \frac{K_{\lambda}}{K_0} d\tau_0$$

$\tau_0$  being the optical depth at  $\lambda = 5000\text{\AA}$

$$I_c(\lambda, \mu) = \int_0^{\infty} B_{\lambda} e^{-\frac{\tau_{\lambda}}{\mu}} \frac{K_{\lambda}}{K_0} \frac{d\tau_0}{\mu} \quad (5)$$

The integration is performed over  $\log \tau_0$  rather than  $\tau_0$ . Numerical integration was performed using Gregory's formula upto the first difference. It is seen from the expression for  $\tau_{\lambda}$  that to obtain  $\tau_{\lambda}$  at any level, it is necessary to integrate over all overlying layers.  $\tau_{\lambda}$ 's have, therefore, been calculated only for  $\log \tau_0 = -4.2$  and downwards.

Table IV gives the continuum intensities so calculated.

TABLE IV  
Continuum Intensities,  $I_c(\lambda) \times 10^{-5}$

Wavelength	$\mu=1.00$	$\mu=0.80$	$\mu=0.60$	$\mu=0.45$	$\mu=0.35$	$\mu=0.25$
3860Å*	2.037	1.861	1.599	1.340	1.139	0.915
4220Å*	2.403	2.193	1.892	1.603	1.381	0.134
5000Å*	3.059	2.799	2.438	2.115	1.869	1.593

## Line Intensity

The emergent intensity in the line is given by

$$I_l(\lambda, \mu) = \int_0^\infty B_\lambda e^{-\frac{t_\lambda}{\mu}} dt_\lambda / \mu \quad (6)$$

the line optical depth is defined by

$$dt_\lambda = (1 + \eta_\lambda) d\tau_\lambda \quad \eta_\lambda = \alpha_{\Delta\lambda} / K_\lambda \quad (7)$$

$\alpha_{\Delta\lambda}$  the line absorption coefficient at a distance  $\Delta\lambda$  from the line centre  $\lambda_0$  is expressed in terms of the Doppler width  $\Delta\lambda_D$  as

$$\alpha_{\Delta\lambda} = \frac{\sqrt{\pi} e^2}{m c^2} \int \lambda_0^2 \frac{N_{AB}}{\Delta\lambda_D} \exp\left(-\frac{\Delta\lambda^2}{\Delta\lambda_D^2}\right) d\lambda, \quad \frac{\Delta\lambda_D}{\lambda} = \frac{\xi}{c} \quad \text{and} \quad \xi^2 = \frac{2RT}{M} + \xi_t^2 \quad (8)$$

$\xi_t$  being the line of sight turbulence velocity; other symbols have their conventional meaning. The assumption of a Maxwellian distribution for turbulence is one of convention. Further this seems reasonable in so far as it provides a numerical estimate of turbulence velocity, for eddy sizes of the order of  $L$ ; here  $L$  is the length of the line forming region.

$f$  values adopted for CN,  $C_2$  and CH were .026, .024 and .005 respectively. For CH the arbitrarily low value of .005 had to be chosen following Pecker and Praderic (1960) because with  $f_{CH} = .06$  (de Jager and Neven 1957) the absorption coefficients obtained were high by a factor of 100.

The fraction of molecules capable of absorbing the frequency corresponding to the line of interest,  $N_{AB}$

$$N_{AB} = i \times p(AB) \frac{(2J+1)}{Z(AB)} \exp(-B_J J(J+1) hc/kT) \quad (9)$$

where

$$p(AB) \text{ --- Partial pressure of AB} = \frac{p(A) \times p(B)}{K(AB)}$$

$Z(AB)$  --- Partition function

$i$  --- Strength factor depends on the coupling scheme

$B_J$  --- rotational constant

TABLE V  
Relative Partial Pressures—CN, CH and C<sub>2</sub>

Log $\tau_0$	P <sub>CN</sub> /p <sub>g</sub>	P <sub>CH</sub> /p <sub>g</sub>	P <sub>C<sub>2</sub></sub> /p <sub>g</sub>
-5.0	338.3E-14	106.0E-12	162.1E-14
-4.8	590.7E-14	170.2E-12	245.6E-14
-4.6	915.5E-14	266.5E-12	437.7E-14
-4.4	226.2E-13	481.8E-12	844.8E-14
-4.2	513.7E-13	888.1E-12	178.8E-13
-4.0	102.4E-12	157.7E-12	344.2E-13
-3.8	206.4E-12	273.1E-11	660.1E-13
-3.6	440.3E-12	489.7E-11	132.7E-12
-3.4	103.3E-11	900.8E-11	288.2E-12
-3.2	212.0E-11	158.2E-10	562.7E-12
-3.0	429.6E-11	273.0E-10	108.3E-11
-2.8	936.7E-11	446.1E-10	199.4E-11
-2.6	156.9E-10	711.4E-10	355.0E-11
-2.4	284.5E-10	110.2E-09	611.9E-11
-2.2	505.6E-10	170.0E-09	103.7E-10
-2.0	778.8E-10	241.7E-09	155.5E-10
-1.8	979.2E-10	311.1E-09	196.8E-10
-1.6	102.9E-09	362.9E-09	214.0E-10
-1.4	844.5E-10	364.7E-09	187.6E-10
-1.2	661.8E-10	368.8E-09	159.6E-10
-1.0	478.9E-10	359.2E-09	127.1E-11
-0.8	321.9E-10	336.7E-09	950.5E-11
-0.6	199.9E-10	301.8E-09	663.7E-11
-0.4	129.9E-10	272.6E-09	479.2E-11
-0.2	676.9E-11	216.7E-09	285.6E-11
0.0	359.5E-11	171.1E-09	172.2E-12
0.2	180.9E-11	129.2E-09	986.8E-12
0.4	793.3E-12	901.1E-10	501.9E-10
0.6	309.4E-12	584.7E-10	230.9E-12

Table V gives the partial pressures calculated by solving simultaneously the equations,

$$P(H) = p(H) [(1 + 2 p(H)) / K(H_2)] \quad (10)$$

$$P(C) = p(C) [(1 + p(H)) / K(CH) + p(O) / K(CO)] \quad (11)$$

$$P(N) = p(N) [(1 + 2p(N)) / K(N_2) + p(H) / K(NH)] \quad (12)$$

$$P(O) = p(O) [(1 + p(C)) / K(CO) + p(H) / K(OH)] \quad (13)$$

$$\text{and } K_{AB} = g_A g_B \left( \frac{2\pi m k T}{h^2} \right)^{\frac{3}{2}} \frac{h^2}{8\pi^2 I} \left( 1 - e^{-\frac{\omega h c}{k T}} \right) e^{-\frac{D_0}{k T}} \quad (14)$$

where fictitious pressures  $P(H)$ ,  $P(N)$ ,  $P(C)$  and  $P(O)$  are derived from a system of assumed abundances (Goldberg, Muller and Aller 1960) of these elements. The dissociation potentials  $D_0$  were taken from P.G. Wilkinson (1964).

$$\alpha_{\Delta\lambda} = \frac{\sqrt{\pi} e^2}{mc^2} f \frac{\lambda_0^2}{\Delta\lambda_0} \frac{P_{(AB)}}{P_{(H)}} \frac{1}{Z_{(AB)}} \exp(-B_J J \overline{J+1} \frac{hc}{kT}) e^{-\frac{(\Delta\lambda)^2}{\Delta\lambda_0^2}} \quad (15)$$

### Turbulence

Since the effective layer of molecular line formation is narrower than that of atomic lines, a depth independent anisotropic model was chosen.

$$\xi_1^2 = \xi_{tan}^2 - \mu^2 (\xi_{tan}^2 - \xi_{rad}^2) \quad ; \quad \Delta\lambda_0^2 = \frac{\lambda_0^2}{c^2} \left( \frac{2RT}{M} + \xi_1^2 \right) \quad (16)$$

$\xi_{rad}$  is obtained by fitting the observed and calculated profile at  $\mu = 1.0$  while  $\xi_{tan}$  was fixed by a fit at  $\mu = 0.25$ .

The calculation of line contours for doublets or triplets were essentially the same, except that for each level the absorption coefficients of constituent lines were added, with the appropriate wavelength shift. If  $\Delta\lambda_i$  is the separation in wavelength between two lines at  $\lambda_1$  and  $\lambda_2$  then the total absorption coefficient  $\alpha_{\Delta\lambda}$  at  $\Delta\lambda$  from  $\lambda_1$  is given by

$$\alpha_{\Delta\lambda} = \alpha_1 \exp[-(\Delta\lambda/\Delta\lambda_0)^2] + \alpha_2 \exp[-(\Delta\lambda \mp \Delta\lambda_2)^2 / \Delta\lambda_0^2] \quad (17)$$

$\alpha_1$  and  $\alpha_2$  are the absorption coefficients at the two line centres. This involves no approximation; in all cases of molecular blending, the two lines have very close initial and final energy states. So the blending lines have identical conditions of excitation and the total line absorption coefficient at any wavelength is the sum of all the absorption coefficients at that wavelength

$$\alpha_{\Delta\lambda} = \sum_i \alpha_{\Delta\lambda_i}$$

It is important to note that  $\Delta\lambda_i$  is not measured from the central wavelength of the blend, but from the centre of one of the constituent lines. With an IBM 1620 Computer calculation of a single residual intensity took 225 seconds for a singlet and 290 seconds for a doublet.

### Calculations and Comparison with observations

Trends in observed centre—limb variations emphasise that these variations are very similar for strong lines on the one hand and weak lines on the other, irrespective of the molecule of their origin. So computations were performed for a restricted set of lines, so that characteristic features of the observed variations could be studied. The CN lines of 3864A, and 4207A, C<sub>2</sub> lines of 5094A and 5147A and CH lines of 4210A and 4281A were selected for extensive computation.

Each of these lines is a spin doublet except 5094.029A of C<sub>2</sub> which is a triplet. The hyperfine structure of atomic lines widens the line considerably and simulates the effect of turbulence. Therefore, fine structure due to spin doubling has to be properly accounted for in order to arrive at the correct values for  $\xi_i$ .

The construction of an unresolved doublet profile to which the correct turbulent velocity must be fitted is complicated. The contour is very sensitive to the separation between the lines and a very small change in this separation changes the profile considerably. Preliminary calculations also indicated that the use of the rigorous doublet approach is necessary for separations larger than about 25mA. Also the relative intensities of the two component lines is very important in reproducing exactly the asymmetries observed and the location of the central wavelength.

Published data on separations for spin doubling are probably accurate upto 10mA corresponding to 0.75 km/sec at 4000Å. Also the smallest resolvable separation in wavelength is 15mA. Therefore, a spin doublet of separation of 15mA or less may be treated as a coincident doublet with the absorption coefficients of the two lines added, without any wavelength shift.

The 3864.307Å line of CN has a spin separation of less than 15mA.,  $\xi_{rad}$  was first calculated by choosing the appropriate numerical fitting factor  $F$ , to match the observed central intensity.  $F$  would generally give a measures of the uncertainties in the transition probabilities. The value of  $\xi_{rad}$  was then adjusted to give the best fit for the entire profile. The adjusted value of  $\xi_{rad} = 3$  km/sec.

With this  $\xi_{rad}$  and  $F$ , the observed half width at  $\mu = 0.25$  was matched by adjusting  $\xi_{tan}$ . A good overall fit was difficult to obtain, because if the half width were exactly matched the central intensities were too low.  $\xi_{tan}$  giving the correct central intensity at  $\mu=0.25$  was improbably large and gave very broad profiles. In order to fix  $\xi_{tan}$  therefore, the observed C-L variations of the profile over the disc, had to be considered. The optimum value of  $\xi_{tan}$  giving the observed trends was 3.6 km/sec (Fig.3). When the numerical fitting factor  $F$  was changed to fit the central intensity at every  $\mu$  and  $\xi_{rad}=3$  km/sec and  $\xi_{tan}=3.6$  km/sec were used in computing profiles, the theoretical profiles matched the observed ones remarkably well. A plot of  $F\mu$  versus  $\mu$  is a straight line with  $F_{1.00} = \frac{1}{2}F_{0.25}$ . This is a surprising result in as much as  $F$  was expected to characterise uncertainties in physical constants. This also indicates that a change in the assumed turbulence velocity field will not improve the agreement significantly and in fact the values derived for  $\xi_{tan}$  and  $\xi_{rad}$  above are certainly the appropriate ones.

4207.409 of CN and 5094.029Å of  $C_2$  were chosen for detailed multiplet calculations as these seemed to have the most reliable separations available in literature. For the first line, wavelengths of the constituent lines were measured by Heurlinger (1918)\*.

Detailed calculations showed that this separation of 69mA could not reproduce the observed profile exactly, for any value of  $\xi_{rad}$  at the centre of the disc. Further calculations showed that with this separation, the best overall match was obtained with  $\xi_{rad}=3$  km/sec. So, to improve the agreement, the only other alternative was to change the value of the separation. For  $\Delta\lambda = 60$ mA the fit at the centre of the disc is very good. That a decrease of 10mA in  $\Delta\lambda$ , improves the fit to such a large extent, emphasizes the need for knowing these separations very accurately.

As in the case of 3864.307Å of CN the fit at  $\mu = 0.35$  could not be made exactly and  $\xi_{tan} = 3.6$  km/sec provided the best over-all agreement from centre to limb.

The 5094.029Å line of  $C_2$  consists of a triplet of the P branch  $J=62$ .  $P_2(62)$  and  $P_3(62)$  are coincident for all practical purposes and  $P_1(62)$  is 93 mA away at 5094.095Å

\* I am indebted to Mrs. Moore-Sitterly for loaning a copy of Heurlinger's results from his Lund thesis.

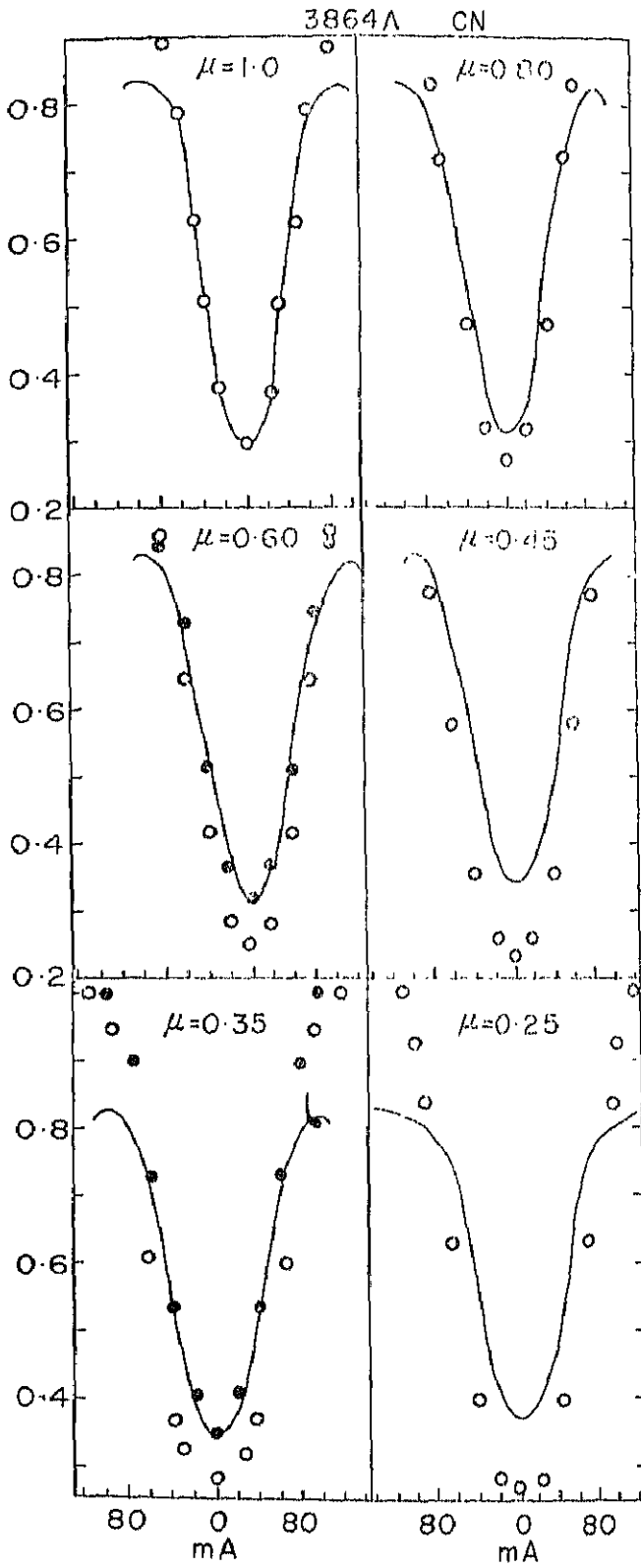


Fig. 3. Observed and calculated profiles,  $\xi_{\text{rad}}$  and  $\xi_{\text{tan}}$  are 3.0 km/sec. and 3.6 km/sec respectively. Observed—continuous line; calculated—open circles. At  $\mu = 0.60$  and  $0.35$ , filled circles give the calculated profile with different fitting factors.



Fig. 4a gives the computed and observed profiles, for the two lines, at three disc positions.

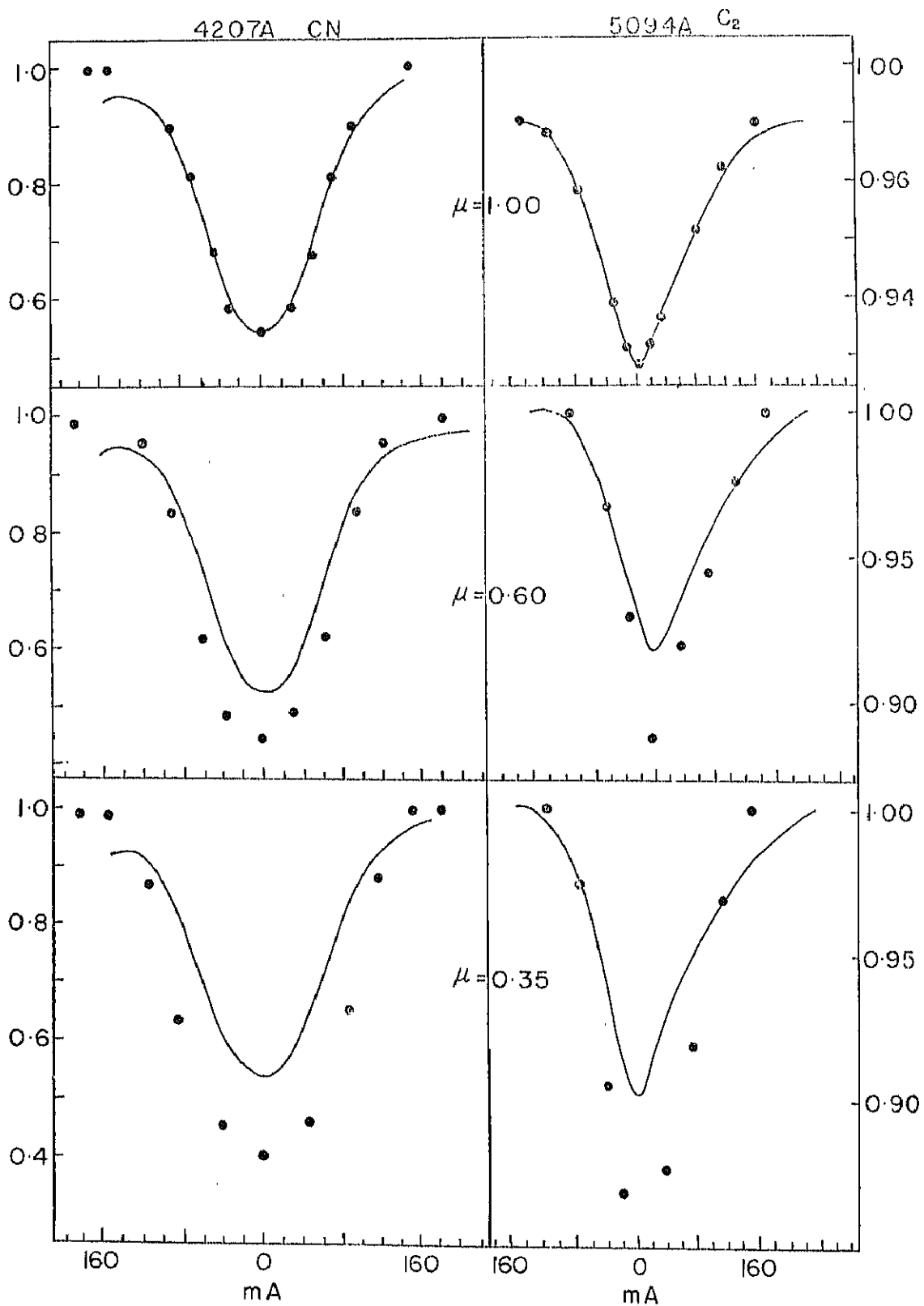


Fig. 4(a). Observed and calculated profiles on the doublet assumption.

Detailed calculations of doublets showed that:

- (1) the half width and shape of a profile is fixed by a unique combination of  $\Delta\lambda$ ,  $\xi_{rad}$  and  $\xi_{tan}$
- (2) the actual value of  $\Delta\lambda$  is very critical in exactly reproducing the observed profile, if  $\Delta\lambda$  is the same order of magnitude as  $\Delta\lambda_D \approx 50\text{mÅ}$ .
- (3)  $\Delta\lambda \leq 20\text{mÅ}$  leads to a situation where turbulence broadening dominates and the line may be treated as single.
- (4) For  $\Delta\lambda > 80\text{mÅ}$ , doublet calculations correctly reproduce, the asymmetries in the wing and the half widths are not affected.

Considering the fact that spin separations are so ill known, time consuming doublet calculations on a medium speed computer were not justified. The rest of the selected profile were calculated as singlets. As a tie-in with the doublet calculations,  $\xi_{tan}$  and  $\xi_{rad}$  were re-determined for  $4207\text{Å}$  CN and  $5094\text{Å}$  C<sub>2</sub>, treating them as single lines.  $\xi_{rad} = 4\text{ km/sec}$  and  $\xi_{tan} = 5\text{ km/sec}$  were obtained for the best fits. This incidentally shows that the ratio of  $\xi_{tan}/\xi_{rad}$  has remained more or less the same in both cases giving an anisotropy factor of 1.2. This is an indication of the reality of the existence of anisotropy in the transition region between the photosphere and the chromosphere.

The same set of turbulence velocities were used in obtaining fits for the lines  $4210\text{Å}$  of CH,  $4281\text{Å}$  CH, and  $5147\text{Å}$  of C<sub>2</sub>. The results are given in Fig. 4b, Fig. 5a, and Fig. 5b.

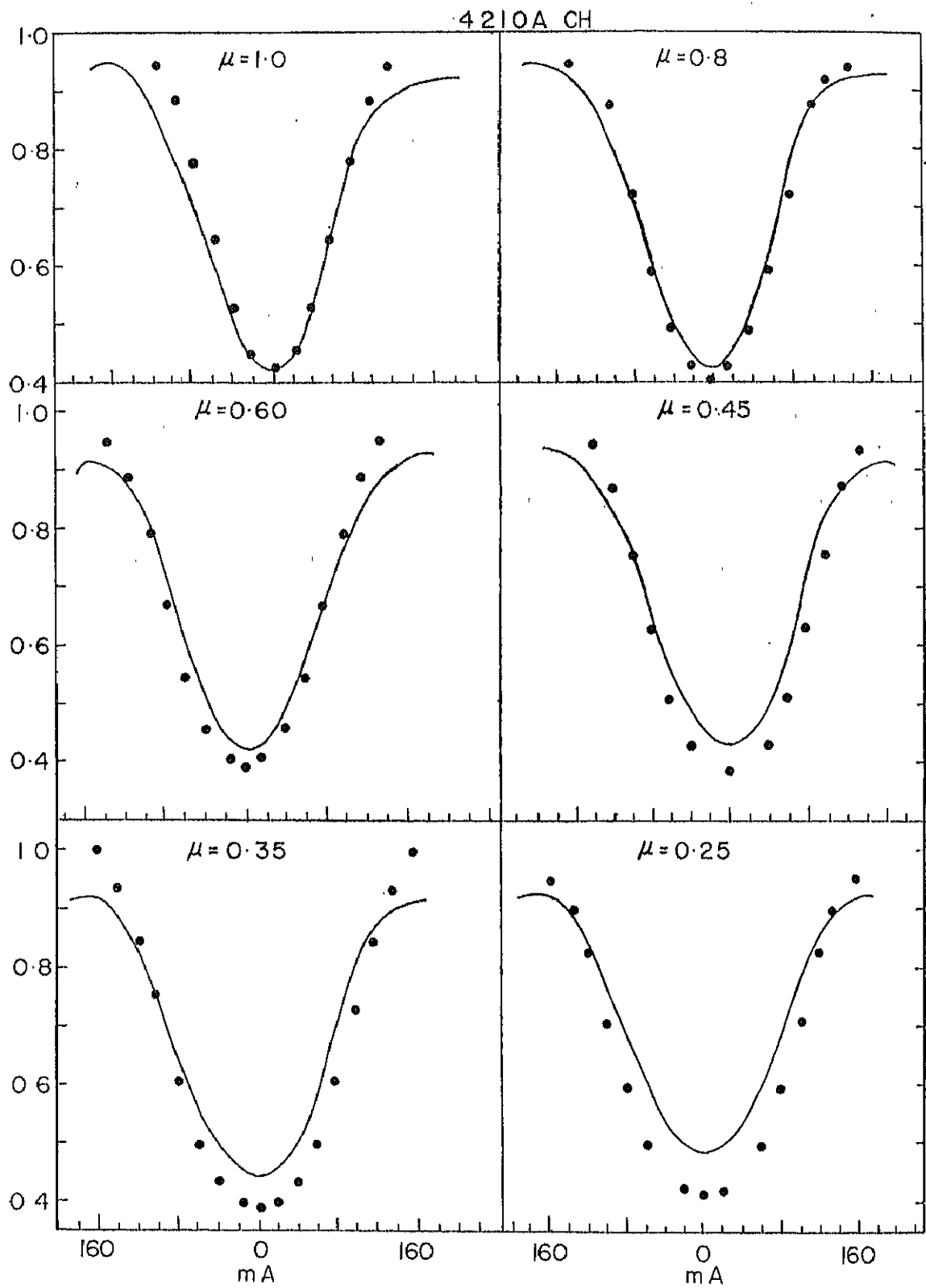


Fig. 4(b). Observed and calculated profile on the singlet assumption.

4281A CH

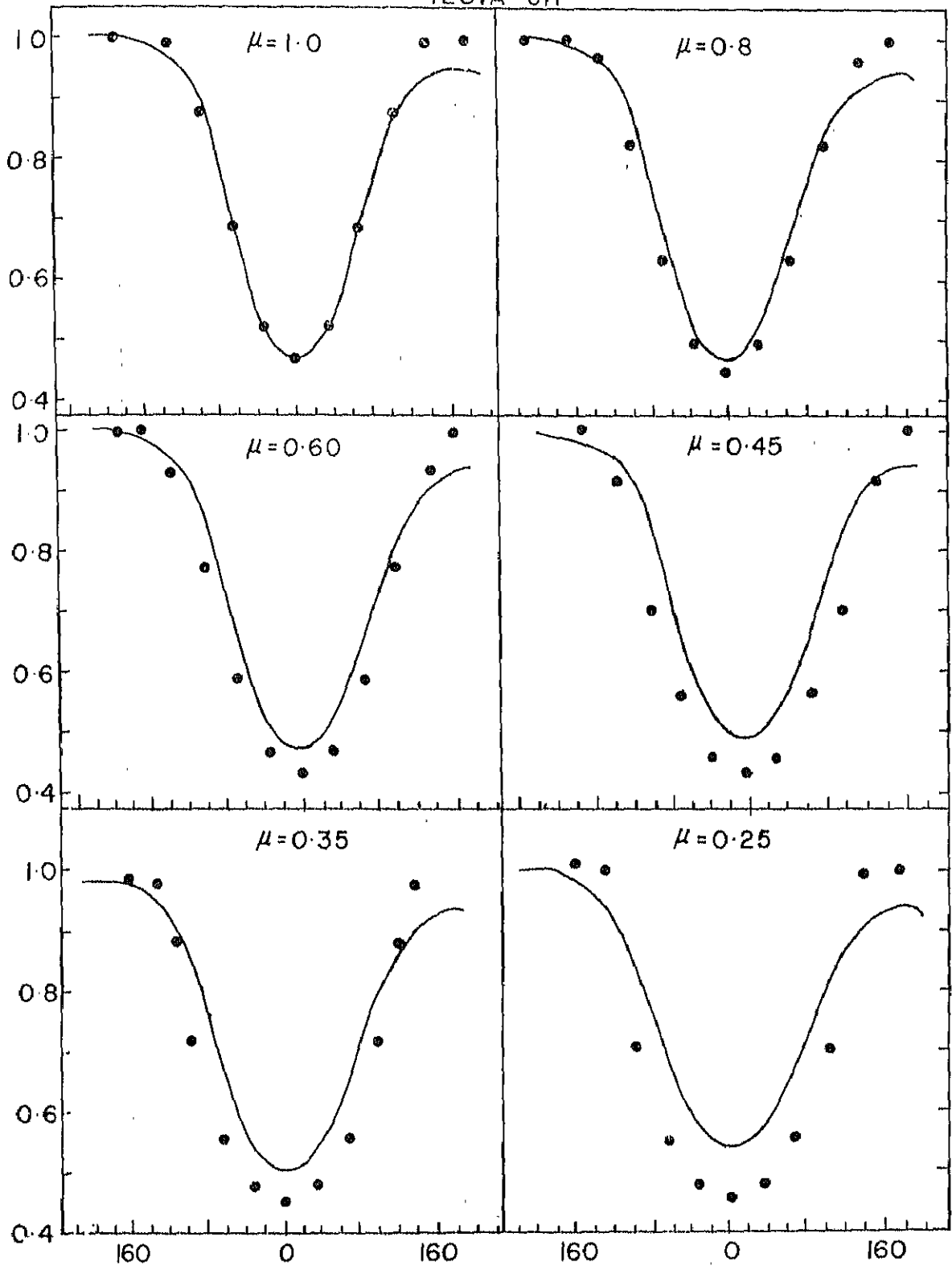


Fig. 5(a). Calculated and observed profiles on the singlet assumption.

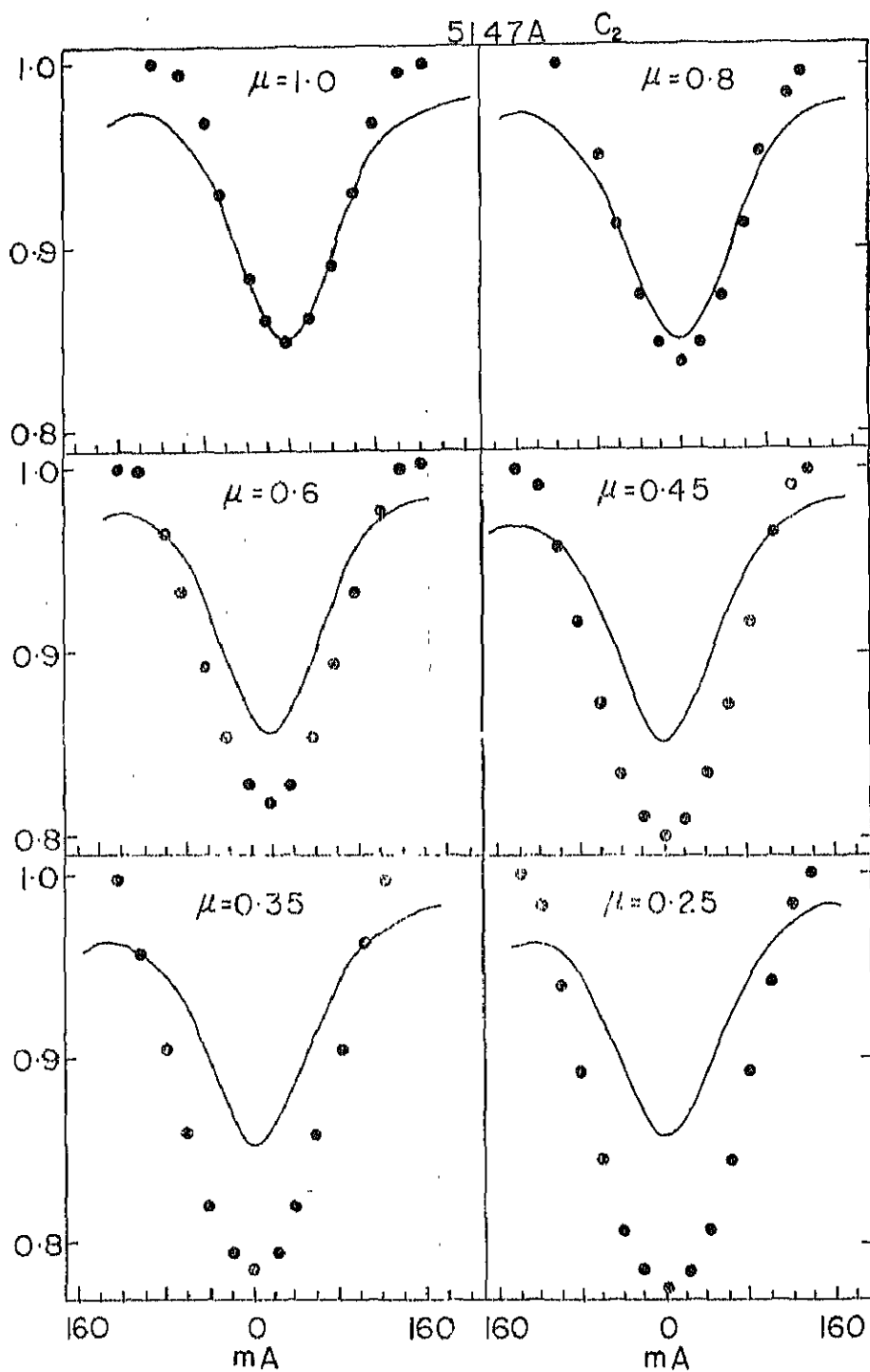


Fig. 5(b). Calculated and observed profiles on the singlet assumption.

The computed profiles for positions other than the centre are broader and deeper than observed ones. Although the trends of C-L variation of central intensities are similar, they are by no means identical (Fig. 6).

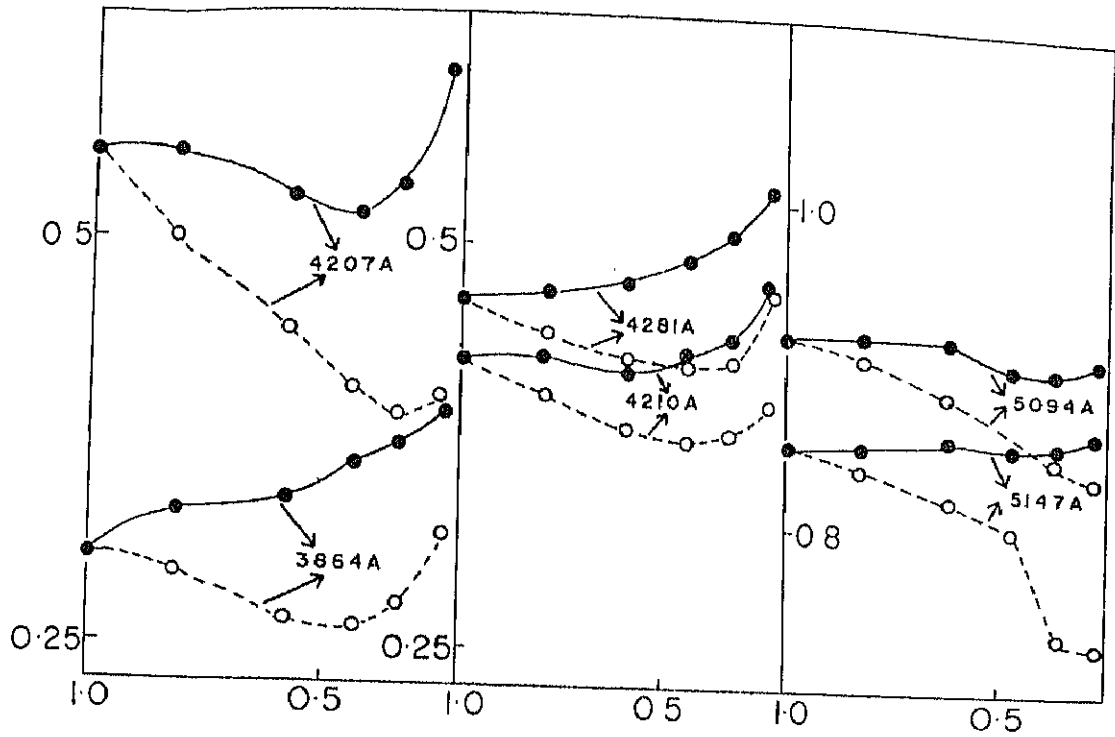


Fig. 6. Variation of central intensities with  $\mu$  observed—continuous curve; calculated—dashed curve.

Once again if  $F$  was changed to fit the central intensity at each  $\mu$  position, combination of  $\xi_{\text{tan}} = 5.1$  km/sec and  $\xi_{\text{rad}} = 4.0$  km/sec gives strikingly good profile fits. normalised variation of  $F\mu$  versus  $\mu$  has been plotted for each line in Fig 7.

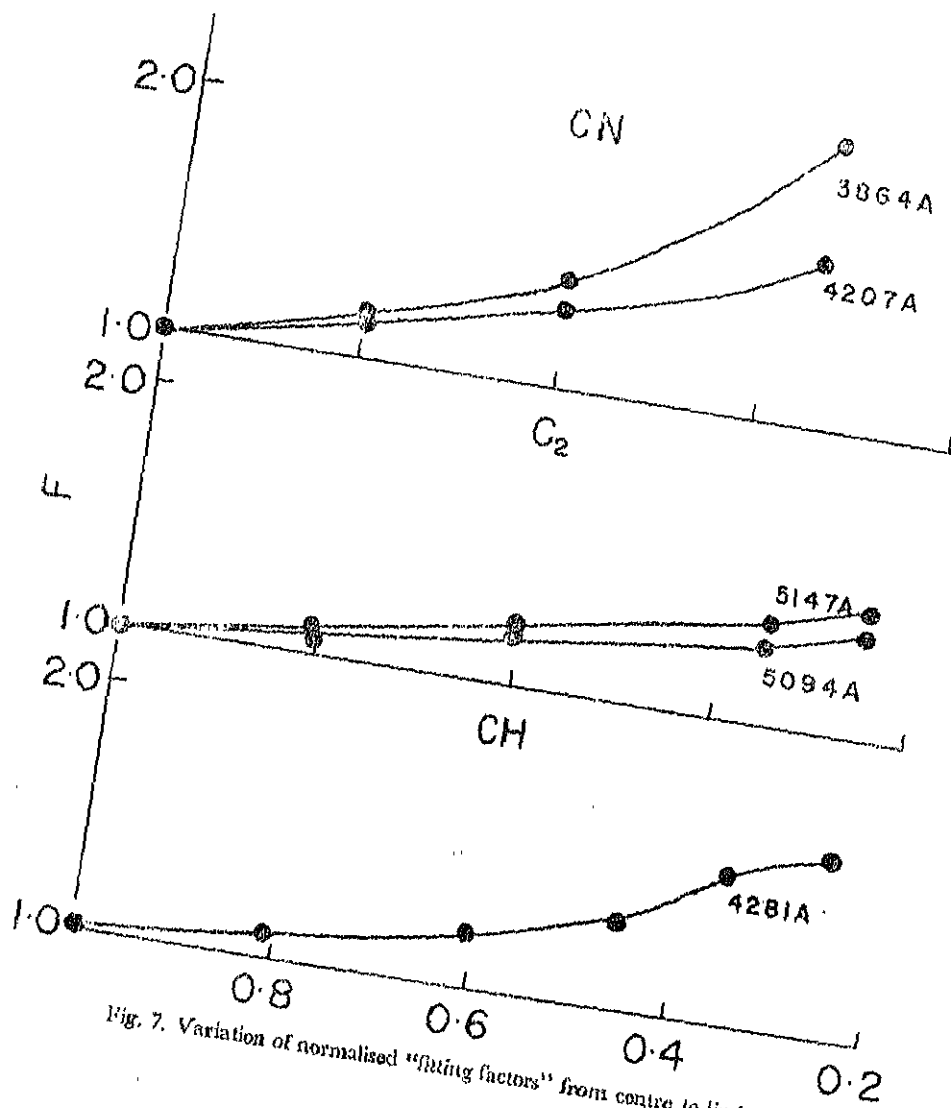


Fig. 7. Variation of normalised "fitting factors" from centre to limb.

## DISCUSSION

The results presented so far draw attention to three facts. First of all the calculations for lines  $3864\text{\AA}$  CN,  $4207\text{\AA}$  CN and  $5094\text{\AA}$  C<sub>2</sub> establish that  $\xi_{rad}=3$  km/sec. The value 3.6 km/sec for  $\xi_{tan}$  is less certain, although it represents the C-L variation of the profiles best.

The second result of interest is that, calculations based on the singlet assumption lead to higher values for  $\xi_i$ ; but the same value of 4 km/sec and 5.1 km/sec for  $\xi_{rad}$  and  $\xi_{tan}$  seems to fit all the observations uniformly well, in spite of the fact that the separations (which are not known) are certainly not the same. In order to understand this result, it is necessary to recall that although the value of  $\Delta\lambda_s$  is very critical in achieving an exact fit with the observed profile, for any given  $\Delta\lambda_s \pm 15$  mÅ of the true  $\Delta\lambda_s$ , one unique value of  $\xi_i$  gives the best over-all fit. This is borne out by the fact that both  $4207\text{\AA}$  CN ( $\Delta\lambda_s = 60$  mÅ) and  $5094\text{\AA}$  C<sub>2</sub> ( $\Delta\lambda_s = 93$  mÅ) give best fits for  $\xi_{rad} = 4.0$  km/sec and  $\xi_{tan} = 5.1$  km/sec. It must however be pointed out that these conclusions are strictly valid for doublet lines whose intensities are almost the same, as is true for molecular spin doublets of high J. These conclusions are not valid for atomic hyperfine structure where there is a wide range of intensities for the component lines.

The fact that a change in F for different  $\mu$  positions results in reproducing the observed profile almost exactly is striking. Of course changing F with  $\mu$  removes the one physical restriction imposed on comparing a set of theoretical profiles with the observed profile. But in fitting profile shapes rather than equivalent widths, changing F with  $\mu$ , does not make the matching calculations entirely arbitrary. On the other hand such a systematic variation of F with  $\mu$  may very well have some physical significance.

The only plausible factor that could cause the variation in F, must arise from variations in partial pressures of the molecules. Since all three molecules are similarly affected, the amount of free carbon available for the formation of C<sub>2</sub>, CN and CH must be a parameter affecting the C-L observations. This leads us to question the assumption that  $T_{dissociation} = T_c$ . Newkirk (1957) has reached the interesting conclusion that de Jager's (1952) model with hyper dissociation  $T_d \neq T_c$  explains the C-L variation of CO lines as well as do the Aller-Pierce or the Minnaert models. The explanation of the CO observations on the basis of  $T_d \neq T_c$  is important in as much as a similar treatment of C<sub>2</sub>, CN and CH might provide a unified explanation for all the four molecules. CO with its high dissociation potential and high concentration at the very highest layers of the Sun is capable of depleting the free carbon supply considerably and, therefore, affect the partial pressures of the other carbon constituent molecules very significantly. The variation of F with  $\mu$  has most probably a bearing on this question.

## SUMMARY AND CONCLUSIONS

By carrying out detailed line profile calculations for selected molecular lines of CN, CH and C<sub>2</sub> on the basis of LTE and an anisotropic model of turbulence the radial turbulence velocity is established to be 3.0 km/sec. A tangential turbulence velocity of 3.6 km/sec provides the best description of the C-L variation of the profiles. These values pertain to the region  $\tau_0 = .04$  to  $\tau_0 = 0.1$  of the solar atmosphere.

It has been shown that if the separation due to spin doubling is neglected the velocities derived are too high. This increase, however, is independent of the separation  $\Delta\lambda_s$  as long as the two blending lines are of comparable intensity and  $\Delta\lambda_s$  is of the order of  $\Delta\lambda_D$ , the doppler width. Singlet calculations of  $\xi_{rad}$  and  $\xi_{tan}$  based on this conclusion provide additional confirmation in the values 3.0 km/sec and 3.6 km/sec respectively.



A very interesting variation of the fitting factor  $F$  with  $\mu$  is observed. There is striking similarity of these variations from line to line. Although no quantitative confirmation is available, it is suggested that the explanation of this variation ought to be associated with the inequality  $T_{\text{dissociation}} \neq T_{\text{electronic}}$ .

Excellent matching obtained at the centre of the disc between observed and computed profiles prove that the assumption  $S_{\lambda} = B_{\lambda}$  for the molecular carbon lines is certainly adequate, a fact that is also borne out by consistent values of  $T_{\text{rotational}}$  obtained for these molecules. Regarding the treatment of dissociation equilibrium, however, the implicit assumption of LTE is questionable. Further work is planned for examining this question quantitatively. It is hoped that this would throw further light in explaining the C-L observations of the carbon molecules.

It is a pleasure to thank Dr. M. K. V. Bappu for his constant interest and encouragement. Extensive help rendered on many aspects of the problem by Dr. A. Bhatnagar is gratefully acknowledged. The research was carried out during the tenure of a Senior Research Scholarship of the Ministry of Education, Government of India, tenable at the Kodaikanal Observatory.

KODAIKANAL OBSERVATORY;  
September, 1968

#### REFERENCES

- Bracewell, R.N., 1955, J. Opt. Soc. Am. **45**, 873.  
 Cowley, C.R., 1964, Astrophys. J., **139**, 731.  
 Gingerich, O.J., 1961, Thesis, Harvard University.  
 Goldberg, L., Aller, L.H. and Müller, E.A., 1959, Astrophys. J. Suppl. **5**, 1.  
 Heurlinger, 1918, Lund Thesis.  
 Jager C.de., 1952, Rech. Astr. Obs. Utrecht. Vol. **13**, Part I.  
 Jager, C. de., and Neven, L., 1957, Mem. Soc. Roy. Sc. Liege, **18**, 357.  
 Laborde, G., 1961, Ann. Astrophys., **24**, 89.  
 Newkirk, G. A., 1957, Astrophys. J., **125**, 571.  
 Pecker, J. C. and Peyturaux, R., 1948, Ann. Astrophys. **11**, 90.  
 Pecker, J. C., 1949, Ann. Astrophys., **12**, 9.  
 Pecker J. C., 1957, Mem. Soc. Roy Sc. Liege, **18**, 332.  
 Pecker, J. C., 1960, Ann. Astrophys., **23**, 622.  
 Pierce, A. K. and Waddell, J. H., 1961 Mem. R. astr. Soc., **68**, 89.  
 Thomas, R. N. and Athay, R. G., 1961, Physics of the solar Chromosphere, Inter Science Publishers, New York.  
 Waddell, J. H., 1962, Astrophys. J., **136**, 223.  
 Waddell, J. H., 1963, Astrophys. J., **137**, 1210.  
 White, O. R., 1961, Thesis, University of Colorado.  
 Wilkinson, P. G., 1963, Astrophys. J., **138**, 779.

E R R A T A

KODAIKANAL OBSERVATORY BULLETIN NO. 187

<u>Location</u>	<u>Error</u>	<u>Read.</u>
Page A 149 First line of Abstract	Parts a Comet	Parts of a comet



# KODAIKANAL OBSERVATORY

## BULLETIN Number 187

Comet Ikeya-Seki (1965) and the nature of the interplanetary medium during its apparition

M. K. V. Bappu and K. R. Sivaraman

### Abstract

The effects of a solar wind on the different parts a comet are discussed in terms of the observations obtained of Comet Ikeya-Seki (1965f). The solar wind contribution to the formation of the scattering agencies in the cometary nucleus is shown to be negligible. Isophotes of the coma in the light of the CN (O,O) emission band and Na 5893 Å derived from slitless spectra are presented. The heliocentric distance of the termination point of Na emission is shown to be dependent on the varying nature of the interplanetary medium properties at different phases of the solar cycle.

It has been recognised from some time (Biermann 1951) that the plasma tails of comets are influenced by solar corpuscular radiation and that comets can be effective space probes for an evaluation of the properties of the interplanetary medium. Indeed, it has been the stimulation by such efforts that has led to the detection of the "solar wind" and its associated properties. That the differing aspects of cometary radiation are solar stimulated is obvious, though the agencies responsible may have different contributions to the emission and continuous spectra observed.

While nearly three hundred comets have been observed in the six and a half decades of the twentieth century, for very few among these have we reliable physical observations, that have contributed towards a better understanding of cometary physics. Observational difficulties are the prime cause and much of our information originates from the few bright comets that have perihelion passages that make them favourable for observation.

Comet Ikeya-Seki is one such object that has provided much new information. Its exceedingly short perihelion distance took it through the outer regions of the solar corona and the rather dramatic outcome of the close encounter made it one of the most spectacular comets ever seen. Its appearance at the minimum phase of the solar cycle provided a good opportunity for the assessment of the threshold characteristics of the interplanetary medium necessary for the well known features of cometary radiation.

\* We have, at Kodaikanal, observed the polarization of the emission bands and continuum (Bappu *et al.*, 1967a), measured the flux of the CN and C<sub>2</sub> emission bands (Bappu and Sivaraman 1967c) and obtained both slit and slitless spectra of the coma and tail (Bappu and Sivaraman 1967b). The energy distribution in the continuum has been determined by comparison with  $\theta$  Crt, HD 27836 and HD 28291, which have well determined energy curves. The coma of Comet Ikeya-Seki has an energy distribution that simulates the distribution of a typical G8V star. The polarization of the continuum measured at 5875 Å corresponds to a value of 17.9 per cent at a phase angle of 90°. The corresponding value for 4310 Å

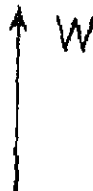
is 24.7 per cent. The value of polarization in the tail 3' away from the cometary nucleus is 13.6 per cent at  $5550\text{\AA}$ . The polarization values in the tail can be explained if we assume that Fe particles of diameter  $0.6\mu$  are the principal agencies for continuum scattering. We believe, that the continuous spectrum of the head is caused by single scattering predominantly by ice spheres and ice spheres with metallic particles imbedded in them. These particles cause the increase reddening that simulates a G8V spectrum energy distribution instead of that of a G2V star. Also, the magnitude and sign of polarization lead us to explain the scattering agencies as those described above.

An earlier measurement of polarization and reddening in the spectacular comets of 1957, comets Arend-Roland and Mrkos (Bappu and Sinhal 1960) and of polarization in the tail (Johnson 1960) of Comet Arend-Roland yielded values similar to those we have obtained for Comet Ikeya-Seki. It is interesting to note that despite the differences in the experiences of all three comets when they approached the solar vicinity, by and large the particle sizes that give rise to the continuum are more or less the same. It appears that the efflux of icy and metallic particles from the conglomerate that forms the nucleus is controlled more by the rate of evaporation and evaporation-stimulated fragmentation as a function of corpuscular radiation which may be essentially a second order effect.

A measure of the cometary flux in the emission bands would be useful in evaluating the role of the solar wind in producing the comet plasma. We have from the flux measures of the coma in the light of the  $C_2(1,0)$  and  $CN(0,0)$  bands, made an effort to calculate the number of molecules of each constituent that fluoresce by sunlight and which are contained in a cylinder of diameter 121300 km., centered on the cometary nucleus. These work out to  $1.554 \times 10^{29}$  molecules for  $CN$  and  $1.840 \times 10^{30}$  molecules for the  $C_2(1,0)$  bands. An "abundance" ratio for  $C_2/CN$  is thus 11.84 which may be compared with the value of 9.0 for Comet Ikeya (1964f) (Kovar and Kovar 1965). We have very little data of this kind to enable us to draw conclusions of real abundance differences between comets of different ages.

Abundance ratios of the kind derived above for cometary heliocentric distances of 1.0 A.U. would show up differences if solar wind contributions at different times are a strong controlling factor on the dissociation of parent molecules from which  $CN$  and  $C_2$  originate. We choose the value of  $r=1.0$  A.U. as a convenient heliocentric distance for cometary observations to be possible, and where excitation in the coma would be near optimum.

The apparent shape of the coma is one possible means of estimating the velocities of ejection of the molecules and their mean life times. These shapes can be derived from isophotes using the techniques of photographic photometry. We have in figures 1 and 2, indicated the isophote structure of the  $CN(0,0)$  coma and sodium coma of Comet Ikeya-Seki on October 29.9. These isophotes are derived from slitless spectrograms obtained at a dispersion of  $250\text{\AA}/\text{mm}$  in the yellow and  $125\text{\AA}/\text{mm}$  in the blue-violet regions. The image scale in the spectrograph camera focal plane was  $75''/\text{mm}$ . The exposures were of the order of a minute in order to keep fogging by moonlight to a minimum. While the isophotes do not extend to very large distances from the centre they nevertheless show up the nature of the equal intensity contours closer to the nucleus. In particular the isophotes of the Na-coma are of considerable interest, since we are not aware of any instance in the past where it has been possible to present such a system of

CN  $\lambda 3883$  

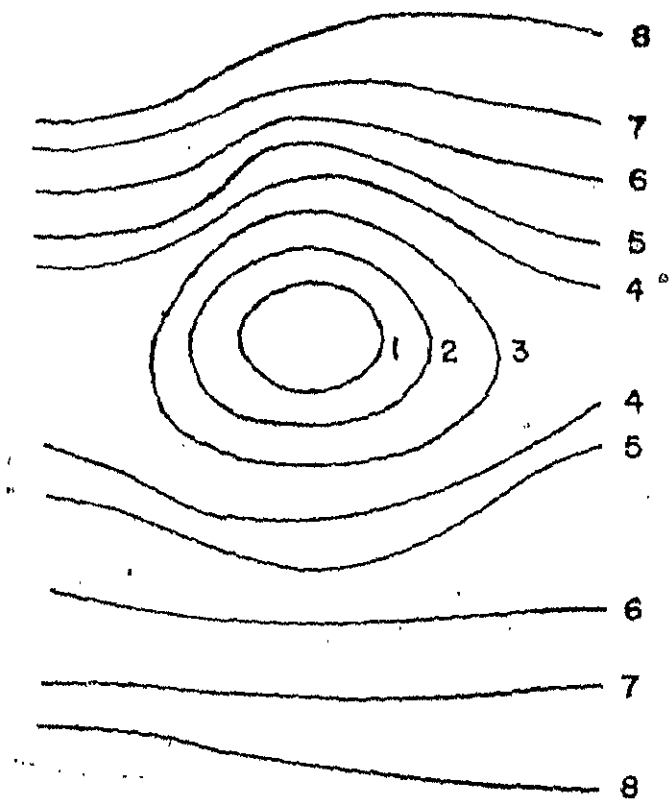


Fig. 1. Isophotes of the CN ( $\alpha, \alpha$ ) coma of Comet Ikeya-Seki (1965f). The tail is westward of the Sun.

10 mm  $\approx$  4.9 seconds of arc.

Number on Isophote	Intensity	Number on Isophote	Intensity
1	18.5	5	14.3
2	17.8	6	13.1
3	16.4	7	12.1
4	15.3	8	11.0

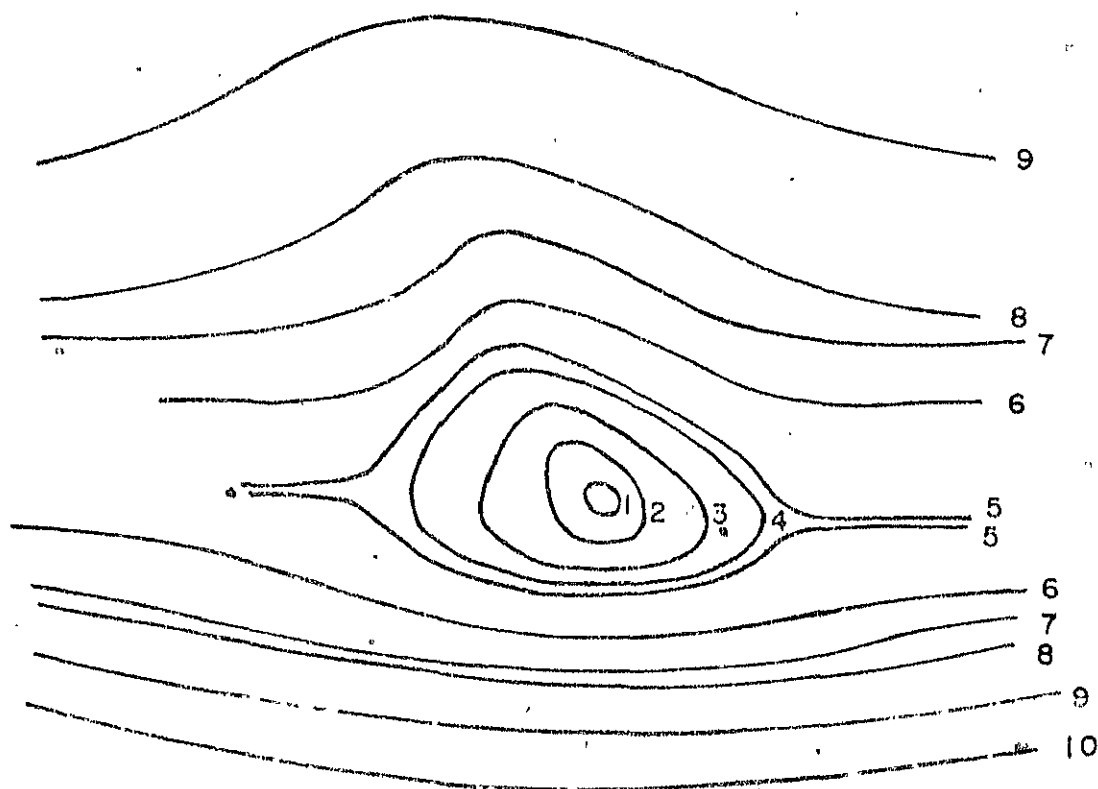
Na  $\lambda$  5893

Fig. 2. Isophotes of the Na-coma of Comet Ikeya-Seki (1965f). The tail is westward of the Sun.

10 mm = 5.2 seconds of arc.

Number on Isophoto	Intensity	Number on Isophoto	Intensity
1	38.0	6	18.6
2	34.4	7	16.0
3	28.1	8	14.9
4	24.8	9	12.6
5	22.3	10	11.6

isophotes. The most striking feature is the flattening of the contours in the direction of the sun, caused by the high  $f$ -value of the Na-atoms. These sunward contours are further affected by the differing radial velocity components for those Na-atoms ejected at an angle to the line of sight. This is so, since, the solar D-line absorption is wide and the velocity effects in the coma can, by virtue of the wide line-contour of the solar D-lines, simulate a varying excitation source.

On the tailward side the Na tail emanating from the coma is obvious. However, the contours indicate a slight bulge in the direction of the radius vector that points almost west, with a more intense portion of the tail twenty degrees away. A visual examination of the spectrum indicates that both "tails" are part of the same tail starting off in the direction of the radius vector. An apparent shadowing in the centre makes the single tail look double near its source. The effect, however, is marginal.

The CN coma, is very much more circular than Na. The contours on the sunward side are very slightly flattened. The contours follow the  $1/R$  trend of intensity variation along the radius vector. The isophotes are narrower on the tailward side which may be an indication of the existence of a dispersion in ejection velocities.

The behaviour of Na emission in coma and tail of Comet Ikeya-Seki has been specially noteworthy. We have slit spectra of the cometary head obtained on October 30.985 and November 3.975 when the heliocentric distances of the comet were 0.497 A.U. and 0.626 A.U. respectively. The D-line is the strongest feature in the spectrum of October 30.985 while it is non-existent in the spectrum of November 3.975. Prismatic camera exposures on November 2.967 and November 3.971 (Bappu and Sivaraman 1967b) fail to show the Na emission that was a striking characteristic of earlier days. Hence, the Na emission in the coma ceased to exist when the comet was at a heliocentric distance of only 0.593 A.U. Na emission in comets have commonly been observed in cometary spectra when their heliocentric distances were less than 0.8 A.U. In some cases, Comet Mrkos (1957d) for example, sodium emission was seen even at a heliocentric distance of 1.1 A.U. This difference in nature of sodium excitation can probably be accounted for in terms of the general effects of solar activity. A more energetic solar wind near solar maximum makes the Na display of a comet more striking than it can be at a minimum level of solar activity.

There are very few instances in the literature of systematic observations of Na emission in comets. However, about a dozen cases are available which indicate the validity of our conjecture, *viz.*, the Na emission display is seen to greater heliocentric distances near solar maximum than at solar minimum. This characteristic also seems to manifest itself in the excitation of the Na tail. Comet Mrkos (1957d) had a sodium tail of  $5^\circ$  extent (Bigay *et al.*, 1957) when the dust tail was about  $14^\circ$ . Comet Ikeya-Seki (1965f) had a dust tail of nearly  $20^\circ$  with only a  $2^\circ$  Na tail which we have observed on prismatic spectra of October 29, 30 and 31.

We believe that such a behaviour indicates the appreciable role of solar corpuscular radiation since polarization measures (Bappu and Sinvhal 1960) show convincingly that resonance fluorescence by sunlight causes the Na emission in the coma. The solar wind perhaps enables the release of the Na atoms from the parent molecules by the ionization processes effective in producing the cometary plasma.

KODAIKANAL OBSERVATORY

January 1969



## REFERENCES

- Bappu M. K. V. and Sinvhal S. D., 1960, Mon. Not. R. astr. Soc., **120**, 152
- Bappu M. K. V., Sivaraman K.R.,  
Bhatnagar A., and Natarajan V., 1967a, Mon. Not. R. astr. Soc., **136**, 19
- Bappu M.K.V. and Sivaraman K.R., 1967b, Kodaikanal Obs. Bull. Number 1
- Bappu M. K. V. and Sivaraman  
K. R., 1967c, Mon. Not. R. astr. Soc., **137**, 1
- Bierman L., 1951, Z. Astrophys., **29**, 274
- Bigay J., Doan N. H., and Dufay J., 1957, Comp. Rendus., **245**, 921
- Johnson H. M., 1960., Publ. astr. Soc. Pacific, **72**, 10
- Kovar N. A. and Kovar R.P., 1965, Astrophys. J., **142**, 1191

ERRATA  
KELLOGG OBSERVATORY BULLETIN NO. 188

Location	Error	Read.
Page A 155 - First line under "The Observational material."	Spectrogram	Spectrogram
-do- 4th line of same para	Spectrogram	Spectrogram
First line of Second para	Spectrogram	Spectrogram
Page A 158 - Equation under figure I	Curved bracket within square bracket incom- plete	The curved bracket should be closed.
Page A 160 - Last line of first para	amounts	amounts
Page A 162 - Seventh line of third para	$A_1 A_2 B_2 B$	$A_1 A_2 B_2 B$
Page A 163 - Second line of last para	$d' AB + EF$	$d' > AB + EF$



# KODAIKANAL OBSERVATORY

## BULLETIN Number 188

### Solar Limb Gradient from Eclipse Spectra of February 15, 1961

\*Aleksandar Kubicela

#### Abstract

On the occasion of the total solar eclipse of February 15, 1961 two spectrograms were obtained at the moments of second and third contact of the eclipse. The spectrograms contain a smooth transition of the photospheric spectrum into the chromospheric one and *vice versa*. Continual registration has been achieved by means of a moving plate combined with a slit spectrograph. The method adopted, and a description of the spectrograph and the chromospheric spectrophotometric results obtained have been published (Kubicela, 1968). In this study the 1961 eclipse data have been used to find the intensity of solar continuum radiation dependent on heliocentric heights within the last second of apparent solar radius.

#### The observational material

For this purpose the spectrogram of the second contact has been chosen which is photometrically superior as was estimated from the analysis of the chromospheric spectrum. Because of lower speed of the photoplate, this spectrogram covers better the low intensity domain about the sensitivity threshold of the photoemulsion.

The spectrogram contains a well defined, 300Å wide, region of the spectrum about the H $\gamma$  line. The dispersion of the original negative is 12Å/mm. The scale in the direction perpendicular to the dispersion is such that 1 mm on the plate corresponds to 313 km on the sun in the radial direction.

The photometric calibration enables one to obtain monochromatic intensities in arbitrary units. The transformation into intensity values expressed in terms of intensity of the center of the solar disc has been realised indirectly.

The measured continuum wavelengths have been chosen satisfying the following conditions: 1) Microphotometric measurements on the spectrogram have to be made without interference with neighbouring spectral lines. The used portion of the continuum also has to be as free of absorption lines as possible in a high resolution spectrum, (Minnaert et al 1940). This was done with the aid of the Utrecht Atlas. 2) The same wavelength intervals have to be free of chromospheric emission lines. The list of Mitchell (1947) aided such an examination.

In this way five wavelengths have been finally chosen. These are centered at  $\lambda_1=4215\text{\AA}$ ,  $\lambda_2=4316\text{\AA}$ ,  $\lambda_3=4336\text{\AA}$ ,  $\lambda_4=4413\text{\AA}$ , and  $\lambda_5=4477\text{\AA}$ .

Besides the already mentioned spectrograms there are 6 calibration spectra, obtained by a step slit fitted on after the eclipse to the same spectrograph and spectra taken in a similar way with different exposures, from 0<sup>s</sup>.05 to 1<sup>s</sup>.30. They were used in evaluating the calibration curve and the Schwarzschild exponent. In both cases previously obtained values (Kubicela 1968) have been confirmed.

\*On leave from Astronomical Observatory in Belgrade, Yugoslavia.

### Evaluation of the intensities

The second contact spectrogram and the calibration spectra were measured by the recording microphotometer of Kodaikanal Observatory. With a nearly square slit, 1 mm on each side, that corresponds to 0.5 Å in the spectrum and 12.5 km height in the solar atmosphere for each of five wavelengths, two photometric scans have been traced in a direction perpendicular to the dispersion.

Before reduction to intensities, the photometric scans were smoothed to avoid fluctuations caused by running shadows prior to second contact. Along these smoothed profiles about 30 points, at 25 km intervals on the sun, have been measured.

In spite of somewhat larger errors which could be expected in the process of numerical differentiation, small intervals between neighbouring measured points were used in order to obtain better coverage of the intensity curve at the extreme solar limb. We minimize the scatter in the measured intensity values by scanning two independent profiles at each wavelength and taking a mean value of five intensity curves from the different wavelengths.

According to the procedure described earlier (Kubicela 1968) application of the calibration curve to photometric profiles gives observed intensities in arbitrary units. Afterwards, they have to be multiplied by the following factor

$$\frac{s}{s^p} = s^{1-p} \quad \dots (1)$$

Here  $s$  is the length on the plate from the measured point to the point where the extrapolated photographic density vanishes. Schwarzschild's exponent,  $p$ , was 0.70. The quantity  $s$  is proportional to the exposure time of the observed point of the photoplate. Thus, the denominator at the left side of the equation (1) represents the Schwarzschild correction. In this way the observed intensities along any of the photometric profiles have been related to a unit of time. At the same time, the quantity  $s$  is proportional to the interval of heights in the solar atmosphere which, at the observed instant, had not yet been occulted by the moon. The corrected intensities can be considered as intensities related to a unit of length along the solar radius. Then, the numerator of the left member of (1) converts these intensities into the integrated ones within the corresponding interval of the solar radius.

At this stage of the photometric procedure, it was found that it would be useful to have an independent control quantity to check the photometric transformations and especially the application of Schwarzschild's law. The 1961 observation does not have any control of this kind. However, in Appendix I such a procedure has been briefly proposed.

Further, the integrated intensities obtained from two photometric profiles have been separately averaged at each wavelength. The transformation to intensity distribution along the apparent solar radius,  $i\lambda(h)$ , has been achieved by numerical differentiation. Due to small intervals between neighbouring measured points it was possible to use only the first differences of the integrated intensities.

In order to obtain a final mean value, the quantities  $i\lambda_1(h) \dots i\lambda_5(h)$  were multiplied with coefficients 3.155, 2.133, 1.560, 1.146 and 1.000 respectively. They were derived by satisfying the condition that all five curves  $i\lambda_i(h)$ , after some distance from the limb, have the same level in arbitrary intensity units.

In this way we normalize the five curves on to one system to eliminate variation caused by instrumental sensitivity at the different wavelengths.

### The results

These "normalized intensities",  $I\lambda$ , are presented in Table I. It contains,  $I\lambda$  (columns 2 to 6), their mean values  $I_m$  in the same arbitrary units (column 7), natural logarithms of intensities  $I_m$  (column 8),  $I_m$  expressed in per cent of the central intensity of the solar disc (column 9) and corresponding heights in the solar atmosphere in km (column 10).

Table I

No.	$I_{4215}$	$I_{4316}$	$I_{4336}$	$I_{4413}$	$I_{4417}$	$I_m$	$\ln I_m$	$I_m$ (%)	$h(\text{km})$
1	2	3	4	5	6	7	8	9	10
1	4.3	2.1	6.1	4.0	1.4	3.6	1.283	1.3	+250
2	6.1	3.3	8.2	4.9	2.6	5.0	1.611	1.8	+225
3	6.3	6.1	5.8	6.5	3.8	5.7	1.741	2.0	+200
4	12.1	6.7	9.2	8.2	4.2	8.1	2.094	2.8	+175
5	6.6	8.0	10.9	9.4	6.1	8.2	2.105	2.9	+150
6	12.9	9.5	13.4	11.3	6.7	10.8	2.380	3.8	+125
7	12.6	10.0	16.6	15.2	9.1	12.5	2.525	4.4	+100
8	14.8	14.0	19.8	16.5	13.2	15.7	2.753	5.6	+75
9	21.8	19.6	23.0	16.5	15.2	19.2	2.960	6.8	+50
10	22.7	19.9	22.8	23.3	12.8	20.3	3.015	7.2	+25
11	24.6	26.0	23.7	25.2	17.7	23.4	3.152	8.3	0
12	29.3	26.5	28.8	26.3	21.2	26.4	3.278	9.4	-25
13	32.5	35.8	34.0	30.9	22.8	31.2	3.443	11.1	-50
14	35.6	32.8	32.1	28.7	24.4	30.7	3.430	10.9	-75
15	38.5	35.8	34.2	32.1	27.7	33.7	3.518	12.0	-100
16	42.6	31.2	32.1	31.7	31.0	33.7	3.518	12.0	-125
17	34.7	39.0	44.8	29.8	30.4	35.7	3.578	12.7	-150
18	47.2	42.1	44.8	28.7	33.1	39.2	3.675	13.9	-175
19	47.0	46.8	44.8	32.1	36.9	41.5	3.729	14.7	-200
20	37.8	42.1	38.4	38.8	39.2	39.3	3.678	14.0	-225
21	41.0	35.8	53.3	42.2	38.4	42.1	3.743	15.0	-250
22	41.6	48.3	39.3	45.7	45.3	44.0	3.790	15.6	-275
23	41.0	49.9	41.3	51.5	44.6	45.7	3.826	16.2	-300
24	44.2	44.4	47.0	45.7	50.4	46.3	3.840	16.4	-325
25	47.2	48.3	51.5	45.9	43.7	47.3	3.860	16.8	-350
26	50.8	43.7	50.5	44.7	43.0	46.5	3.843	16.5	-375
27	47.2	48.0	44.2	48.1	40.2	45.5	3.822	16.2	-400
28	47.2	49.9	40.6		41.4	44.8	3.810	15.9	-425
29	59.8				45.5	52.6	3.968	18.6	-450
30	50.5				41.6	46.0	3.835	16.3	-475
31	47.6				45.4	46.5	3.843	16.5	-500
32	50.5					50.5	3.930	17.9	-525

The intensities  $I_m$  have also been shown in figure 1 by open circles, and the curve drawn through them as a heavy line. The abscissa contains the heights of column 10 of Table I, with the origin directly below the inflection point of the intensity curve. The intensity scale on the left of the diagram is expressed in arbitrary units, and the one on the right expresses the intensity in per cent of the central intensity of the solar disc. In a typical eclipse observation, it is very difficult to establish the relation between these two scales. An usual method is the extrapolation of observations outside an eclipse (usually on a reliable intensity scale) to a region as close to the solar limb as possible. The same procedure has been

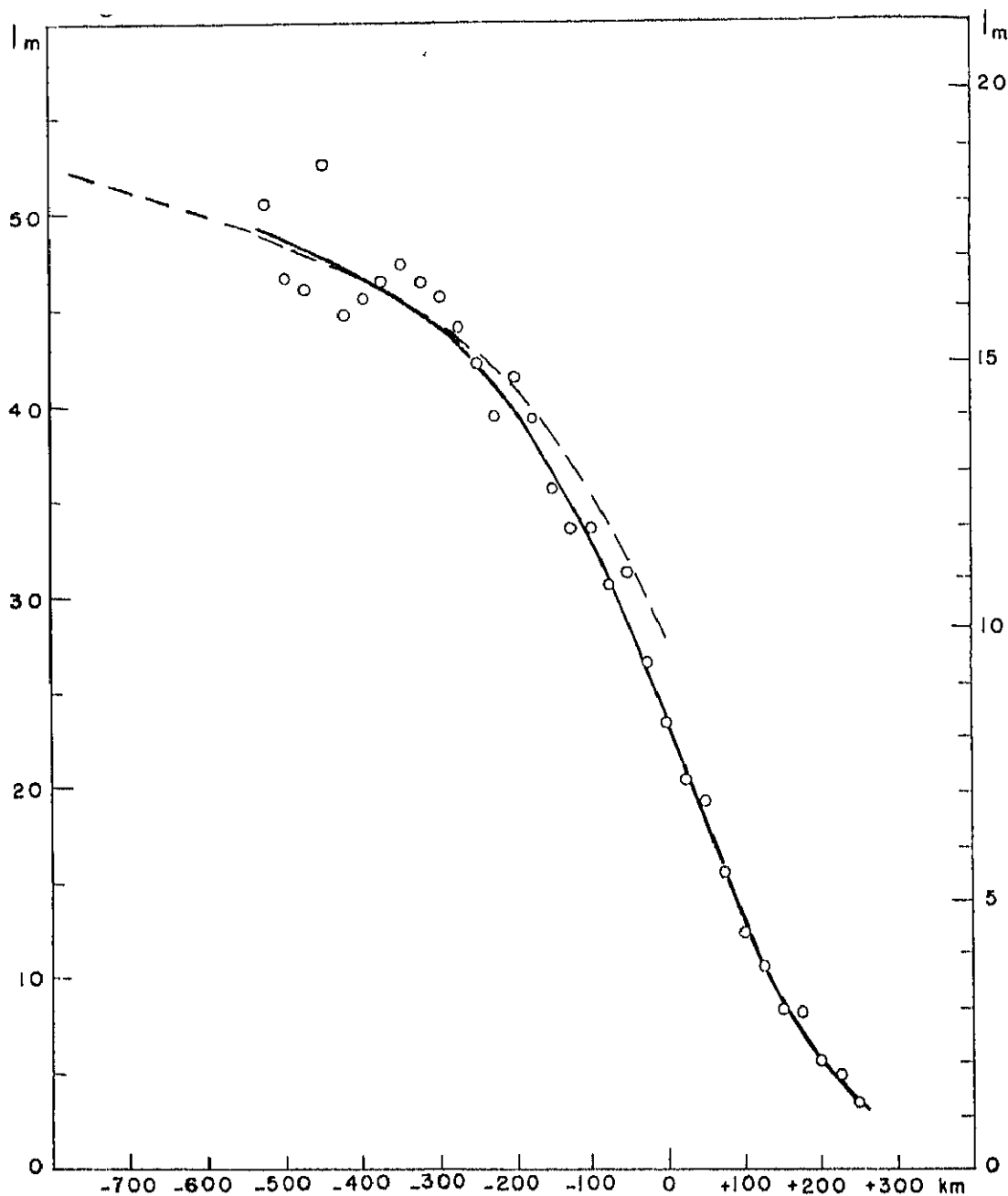


Figure 1

adopted here. The intensity curve (2) given by Pierce and Wadell (1961) was used. Hence

$$I(O, \theta) = a\lambda + b\lambda\mu + c\lambda [1 - \mu L_n(1 + \mu^{-1})] \dots (2)$$

Here  $\mu = \cos \theta$ , where  $\theta$  is the angle between the direction towards the observer and the radial direction at the observed point. The coefficients  $a\lambda$ ,  $b\lambda$ ,  $c\lambda$  are tabulated by Pierce and Wadell. We have in the present study interpolated these for value of  $\lambda = 4350\text{\AA}$ . Equation (2) satisfies the observations with high accuracy within the interval  $0.2 \leq \mu \leq 1.0$ . We have extrapolated it until  $\mu = 0.00$ . This extrapolated curve of Pierce and Wadell to small values of  $\mu$  is shown in Figure 1 by the dashed curve.

A comparison of the observed curve with the extrapolated Pierce-Wadell curve within the height interval  $-200$  to  $-500$  km expresses the unit of our arbitrary intensity scale in per cent of central intensity of the solar disc. We thus find that one unit of the arbitrary scale equals  $0.355$  per cent of the intensity of the centre of the solar disc. The maximum deviation between the two curves occurs at the very limb and amounts to  $1.4$  per cent. An almost ideal agreement of the curves could be achieved by the translation of one of them for about  $35$  km along the abscissa and by the use of a coefficient  $0.348$  instead of  $0.355$ .

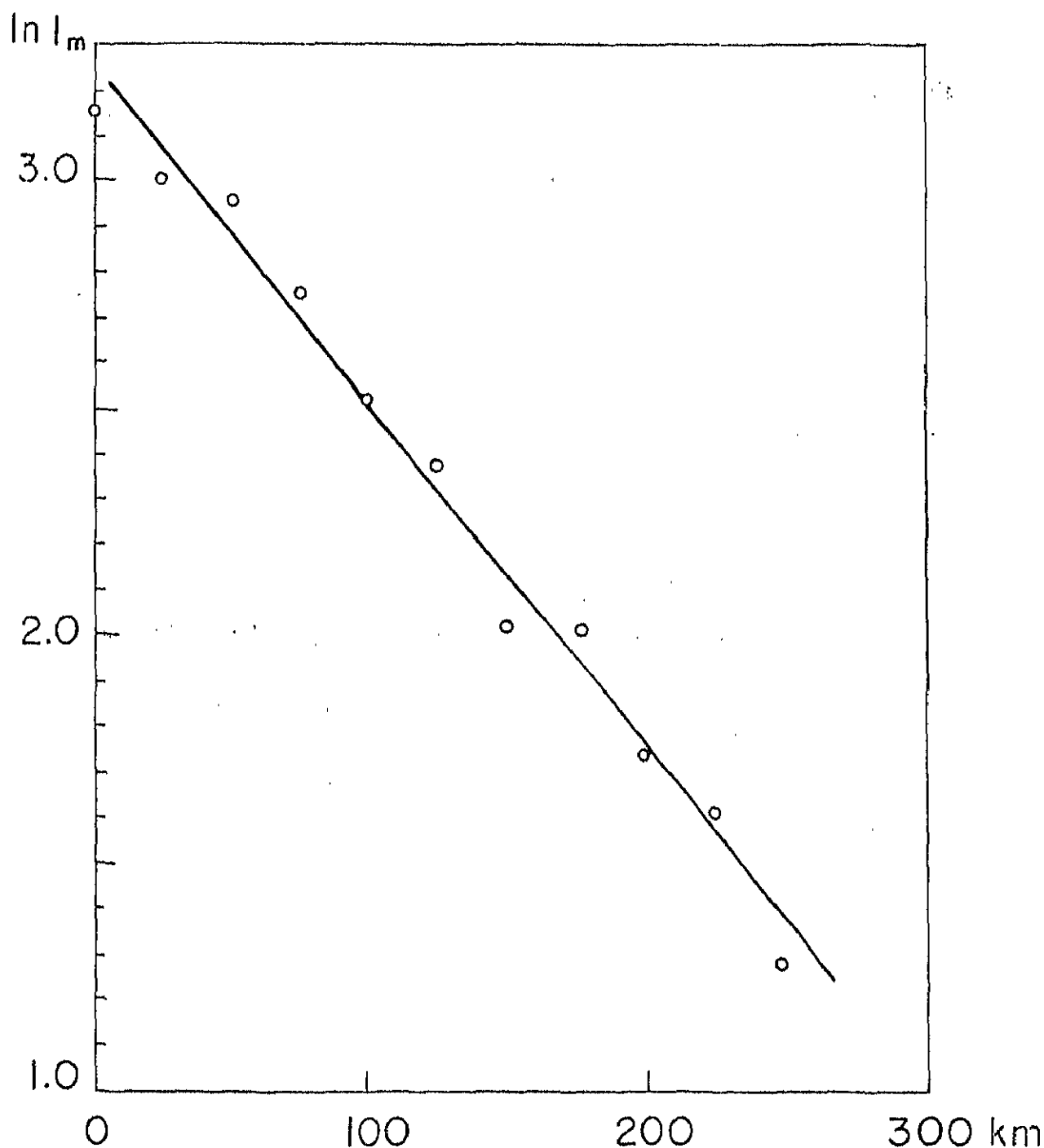


Figure 2



In figure 2, the natural logarithms of the intensity  $I_m$ , for  $h \geq 0$ , are shown. It can be seen that the curve, within the interval of positive heights, satisfies the exponential expression

$$I = I_0 e^{-\gamma h} \quad \dots(3)$$

where the gradient  $\gamma = 7.4 \times 10^{-6} \text{ cm}^{-1}$ . Its reciprocal, the scale height,  $H$  is 135 km. The limb intensity  $I_0$ , amounts to 8.4 per cent of the intensity at the center of the solar disc.

With a rather high value of the scale height this observation joins some other similar observations (e.g. Lindblad and Kristenson, 1953). On the other hand, the theoretical values of  $H$ , under the assumption of hydrostatic equilibrium and temperature of about  $4500^\circ$ , are systematically lower:  $H = 54 \text{ km}$  (Minnaert, 1953) and  $H = 84 \text{ km}$  (Pagel, 1967). This discrepancy is, so far, unexplained.

#### Acknowledgement

This work was completed at the Kodaikanal Observatory and I wish to express my thanks to the institution for this opportunity. I am also deeply indebted to the Director, Dr. M. K. Vainu Bappu for his valuable advice on several occasions during the progress of the work.

Kodaikanal Observatory  
May 1969

#### REFERENCES

- Kubicela A, 1968, *Publ. Astr. Obs. Beograd*, **15**
- Lindblad B., Kristenson H. 1953, *Convegno di Scienze Fisiche Matematiche E Naturali*, Roma, p. 61
- Minnaert M., Mulders G. P. W., Houtgast J., 1940, *Photometric Atlas of the Solar Spectrum*, Amsterdam.
- Minnaert M, 1953, *The Sun* (ed. Kuiper), Chicago, p. 88
- Mitchell S, 1947, *Astrophys J.* **105**, p. 1
- Pagel B. E. J. 1967, *Solar Physics* (ed. Xanthakis), London, p. 11
- Pierce A. K., Wadell J. H. 1961, *Mem. R. Ast. Soc.*, **68**, p. 89.

## APPENDIX I

## The Control Photometric Field on a Moving Plate

It is useful to have a good control of photometric reductions when a moving photographic plate is used as the radiation receiver in an eclipse observation. In order to secure such a control, the following procedure can be used.

The region ABCD of a moving photoplate, P, Figure 1, is illuminated by an artificial light source. The field ABCD does not move with the plate. The illumination is uniform, it lasts for some time during which time it is constant, but

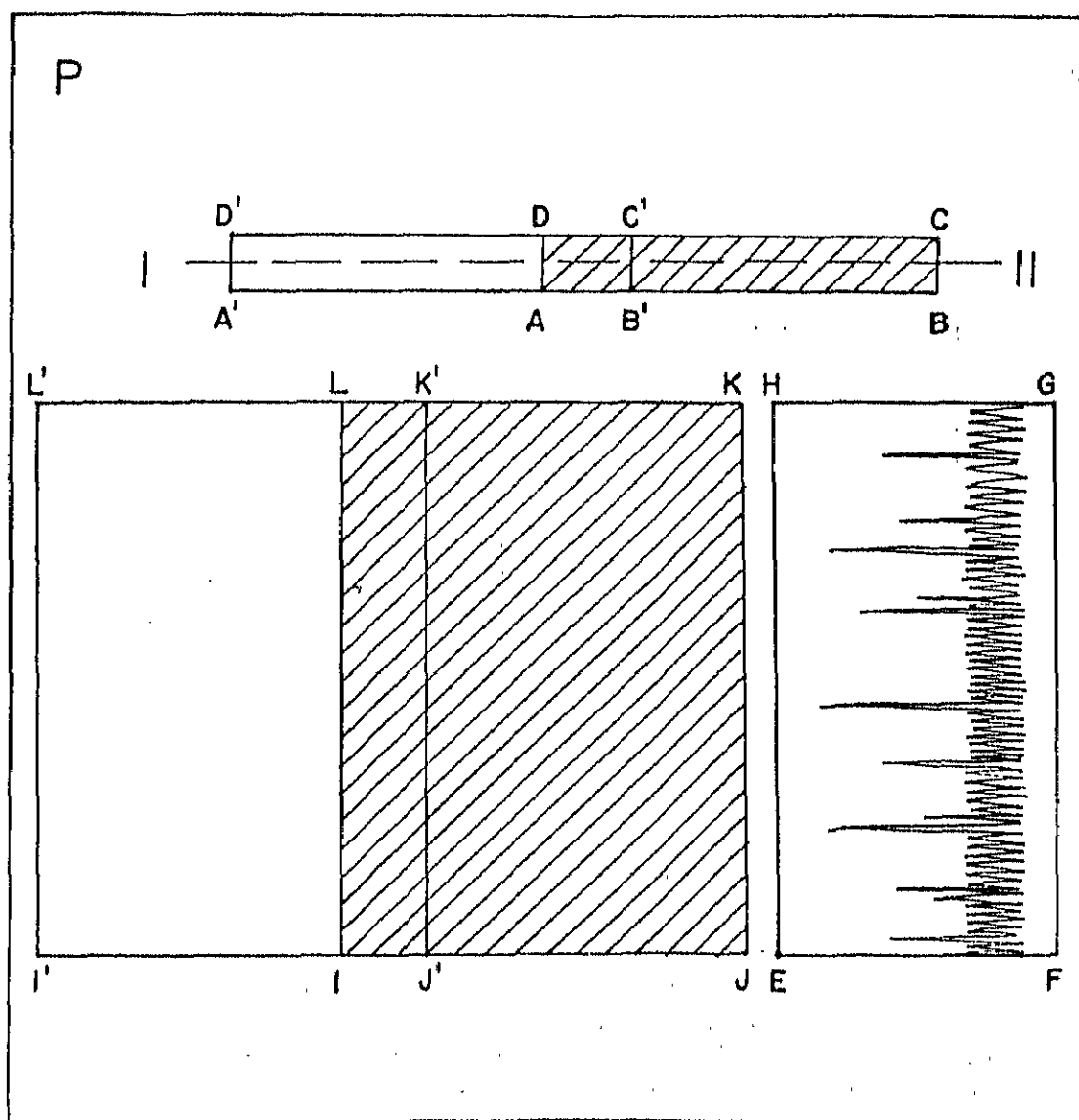


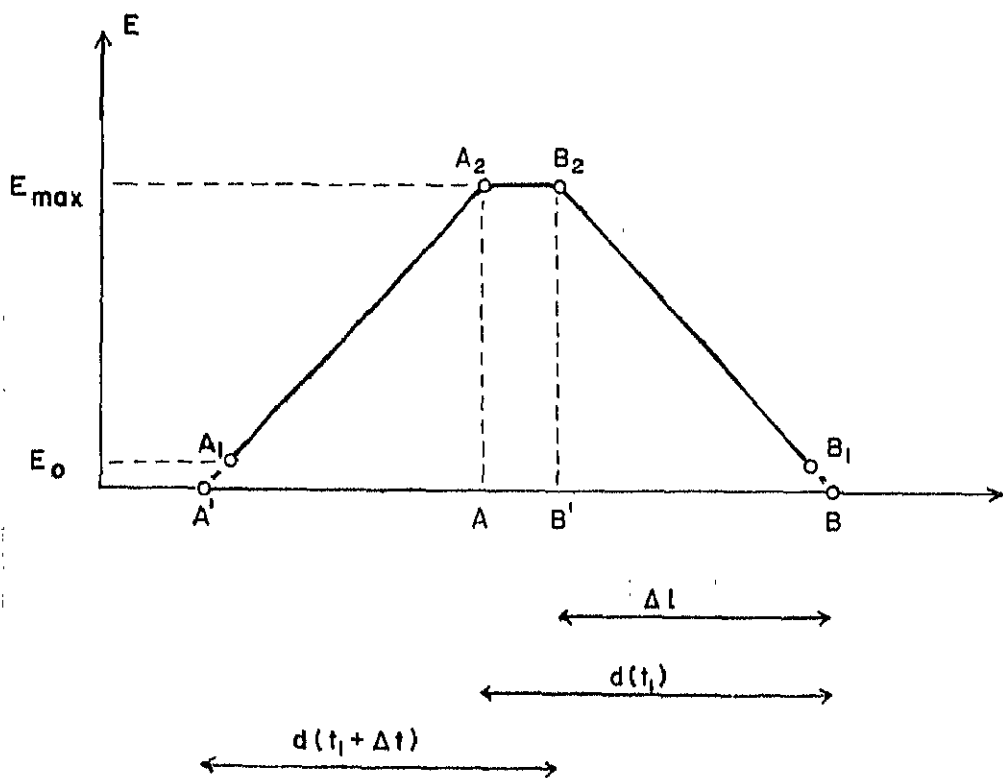
Figure 1.

starts and ends abruptly. The wavelengths of the radiation in the field are identical or similar to the wavelengths in the spectrum which are observed in the EFGH

regions of the plate. The length of the control field,  $d = \overline{AB}$ , is somewhat bigger than the total length,  $\overline{EF}$ , described by the plate during the movement. The intensity of light is such that the photographic density in the field ABCD nearly equals the expected density in the observed spectrum.

The desired illumination can be realized by a light source and an immovable mask with a window (of shape ABCD) immediately in front of the plate, or by a suitable projector inside the camera of the spectrograph.

The process is the following. The illumination of the filed ABCD begins at the instant  $t_1$  after the plate has started moving and ends at the instant  $t_1 + \Delta t$  before the plate stops. In this way the plate is exposed to the radiation from the control filed in the region  $A'BCD'$ . The distribution of the photographic density along the line I---II in Figure 1, is such that, after the correct application of the calibration curve and the Schwarzschild's law, the photometric profile must be like  $A_2B_2B$  shown in Figure 2. Here the abscissa contains the lengths,  $l$ , in the direc-



tion of the movement of the plate. The ordinate represents the total radiant energy,  $E$ , that a surface element of the plate receives during the exposure interval between  $t_1$  and  $t_1 + \Delta t$ .  $\Delta l$  is the distance covered by the plate within the interval  $\Delta t$ , and  $d(t_1)$  and  $d(t_1 + \Delta t)$  are the first and the last illuminated positions respectively of the field.

The energy  $E$  depends on the illumination,  $\epsilon$ , of the plate (the radiation energy received in a unit of time by a surface element of the plate in a given wavelength interval and of a given solid angle) according to

$$E = \int_{T_1}^{T_2} \epsilon dt. \quad \dots (1)$$

The limits of the integral (1),  $T_1$  and  $T_2$ , are the moments of the beginning and of the end of illumination of the observed element on the photographic plate. Because of constant illumination,  $E$  depends on time only through these limits.

Within the three sections of the profile in Figure 2, the limits of the integral (1) have the following values:

$$\text{On the section } \overline{A'A_2} : \begin{aligned} T_1 &= t \\ T_2 &= t_1 + t \end{aligned} \quad (2)$$

$$\text{On the section } \overline{A_2B_2} : \begin{aligned} T_1 &= t_1 \\ T_2 &= t_1 + t \end{aligned} \quad (3)$$

$$\text{On the section } \overline{B_2B} : \begin{aligned} T_1 &= t_1 \\ T_2 &= t. \end{aligned} \quad (4)$$

Here  $t$  is time connected with distances,  $l$ , on the plate by the equation of movement

$$l = v \cdot t + \text{const.} \quad (5)$$

where  $v$  is the constant speed of the plate with respect to the non-moving illuminated field.

From (1) and (2), and from (1) and (4), it can be seen that  $E$  is a linear function of time, and because of (5) it also depends linearly on  $l$ . The sections  $\overline{A'A_2}$  and  $\overline{B_2B}$  of the photometric profile are straight lines with the slope that reverses the sign when the variable moves from the lower to the upper limit of the integral (1). As both limits in (3) are constant, from (1) we find  $E = \text{const.} = E_{\max}$ ; the section  $\overline{A_2B_2}$  in figure 3 is a straight line parallel to the abscissa.

The photometric control consists in comparison of the observed profile I-II, Figure 1, with the shape in Figure 2. The degree of agreement of corresponding sections of the observed profile with straight lines from Figure 2 is the measure of the attained accuracy in photometric transformations.

In practice, the small sections  $\overline{A'A}$ , and  $\overline{BB_1}$  of the profile in Figure 2 will be lost. It is a necessary consequence of the existence of the sensitivity threshold of a photoemulsion, but it does not prevent the application of the described procedure.

In the case of a sufficiently long spectrograph slit, where the length of its projection,  $d'$ , in the plane of the photoplate satisfies the condition  $d' \gg AB + EF$ ; alternatively, the photometric field can be realized by uniform illumination of a section of the slit itself. At the first instant this radiation forms a spectrum in the IJKL region of the plate. During the movement of the plate, on the surface I'JKL' a picture with photometric profiles analogous with the profile I-II, is being built. It is evident that such a photometric field can be analysed in each wavelength separately.



E R R A T A

KODAIKANAL OBSERVATORY BULLETIN No. 189

tion	Error	Read.
A 164 - Second of abstract	displacements	displacements
A 164 - Sixth e (ibid)	comparator	comparator



# KODAIKANAL OBSERVATORY

## BULLETIN Number 189

### A Doppler Comparator for Solar Spectra

\*Aleksandar Kubicela and K. R. Sivaraman

#### Introduction

There are many programmes presently running at the Solar Tower of the Observatory to determine the local Doppler displacements using lines of different mean depths of formation. These studies also cover observations of velocity fields associated with super-granular cells as well as those of the quasi-periodic vertical oscillations in the photosphere. The necessity to evaluate these velocity fields from a huge mass of data of spectrograms lead us to design and construct a Doppler comparator. In this device the light flux from both the wings of a spectral line are directed to, two Light Dependent Resistances (LDR) through a system of two slits with their centres located at  $\pm \Delta$  on the line profile. Determination of Doppler displacement at any location on the line consists in equalising the D.C output signals of the two LDRs, by setting the two slits with a micrometer screw so that the line is centred on them and reading this displacement on the micrometer scale. The spectral line is scanned manually along its length and Doppler displacements are obtained at discrete points at the choice of the observer.

#### Optical Scheme

The Zeiss spectrum projector forms a sharp image of the spectrum S, magnified 18 times. This image is formed immediately behind the collimating lens C (Figure 1) in the plane of the system of two slits G. After passing through the slits and a field lens F, the beam is reflected by the two silvered faces of a right angle prism P and directed towards line shifters  $L_1$  and  $L_2$ , diffusers  $D_1$  and  $D_2$  and light dependent resistors  $LDR_1$  and  $LDR_2$ . The light-tight box B containing the optical elements beginning with double slit plate G, can be displaced in measurable amounts with a Hilger micrometer screw W, together with its nut N. The axis of the screw is parallel to the direction of dispersion of the magnified spectral image. The screw has a base support having no motion relative to the projector. Collimating lens C is fixed with respect to the projected beam and helps to secure constant directions of the two beams inside the box B, while the box is moved in the light field during measurements.

It is possible to rotate the line shifters  $L_1$  and  $L_2$  from outside the box about axes perpendicular to the plane of the figure. By means of this rotation positions of light spots on the diffusers  $D_1$  and  $D_2$  can be altered in small amounts in order to render illumination on the LDR's exactly equal. Such an adjustment is usually done with the spectrum removed from the beam and the slits uniformly illuminated with selected light intensity, before commencing a series of measurements. Necessary uniformity of the light beam has been obtained by means of an additional (fixed) diffuser D near the projector condensing lens.

The slits are rectangular apertures of suitable size and position on the slit plate G, which is made of glass with a non-transparent mask on it, or of metal. Slit plates can be easily made and are changed according to the width of the observed spectral line and the desired space resolution along the line.

---

\*On leave from Belgrade Astronomical Observatory, Yugoslavia.



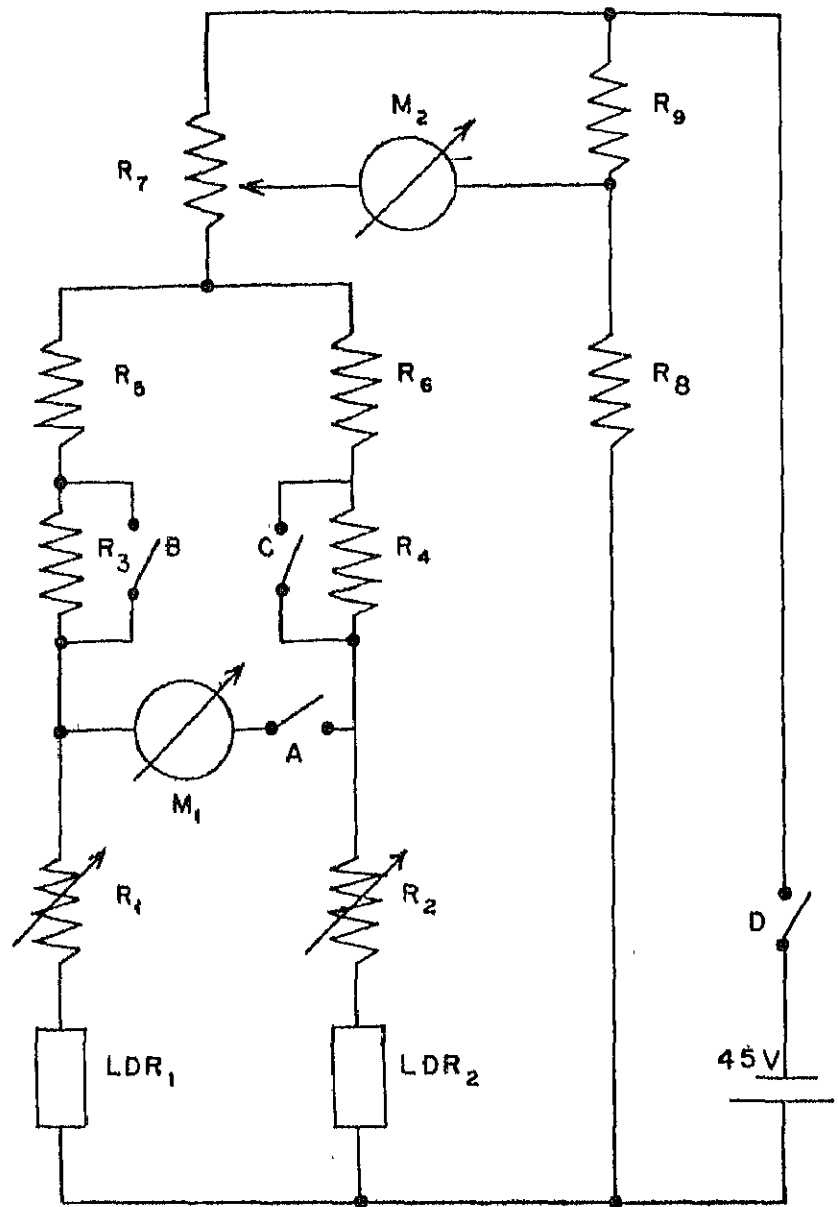


Fig. 2.  $R_1 = R_2 = 50 \text{ k}\Omega$   
 $R_3 = R_4 = 1 \text{ M}\Omega$  } Selected Pair.  
 $R_5 = R_6 = 272 \text{ k}\Omega$   
 $R_7 = 5 \text{ k}\Omega$   $R_8 = 320 \text{ k}\Omega$   $R_9 = 2 \text{ k}\Omega$   
 $\text{LDR}_1, \text{LDR}_2$  = Philips light dependent resistors.

Ten points along each line were measured and such a set of measurements was repeated 8 times. From ten r. m. s. errors  $\left(\sigma = \pm \sum \frac{\Delta_2}{\mu-1}\right)$  a mean value is derived and these results are shown in Table I. The errors are expressed in microns ( $\mu$ ) as well as in velocity units (m/s).

TABLE I

Slits	No. 1	No. 2	No. 6
Space resolution along the slit.	5".50	2".75	0".94
$\lambda = 4554\text{\AA}$ , R = 8	$\pm 1.0\mu$ $\pm 5.9 \text{ m/s}$	$\pm 1.6\mu$ $\pm 9.4 \text{ m/s}$	$\pm 2.7\mu$ $\pm 15.9 \text{ m/s}$
$\lambda = 4912\text{\AA}$ , R = 1	$\pm 2.5\mu$ $\pm 10.9 \text{ m/s}$	$\pm 5.3\mu$ $\pm 23.0 \text{ m/s}$	$\pm 7.6\mu$ $\pm 33.0 \text{ m/s}$

The strongest lines which can be accommodated in the field lens of the comparator are D<sub>1</sub> and D<sub>2</sub> lines of Na with a dispersion 11 mm/ $\lambda$ .

It was also found that after some practice, an observer working with the highest slit can measure about 150 points along 4554 B<sub>a</sub><sup>+</sup> line in one hour. This number would be less for higher space resolution or for a weaker line.

#### Acknowledgements

It is a pleasure to record our sincere thanks to Dr. M.K.V. Bappu for suggesting the construction of the Doppler comparator and to Mr. J.C. Bhattacharyya who helped us with circuit of LDRs and other components. One of us (A. K.) wishes to thank the Government of India for the award of a fellowship under the programme of exchange of scholars between India & Yugoslavia.

KODAIKANAL OBSERVATORY

August, 1969

#### REFERENCE

Evans J. W. & Michard R., 1962, *Astrophys. J.*, **135**, 812.



# KODAIKANAL OBSERVATORY

## BULLETIN Number 190

The Solar Corona of July 20, 1963

M. K. V. Bappu and A. Bhatnagar

### Abstract

The total solar eclipse of July 20, 1963 was observed at the AAVSO site near Wilton, Maine, U.S.A. where totality lasted for 58 seconds. Pictures of the corona were obtained with a camera of focal length 57 cm. on Kodak Plus X emulsion through a Wratten 15G filter. Photometric calibrations were impressed with a Hilger step wedge. Coronal isophotes have been derived by the Sabbattier procedure and intensities assigned to the equidensity contours by conventional microphotometry. Tables given contain the brightness distribution for different position angles to  $r=4.2$  solar radii. The coronal intensity gradients are presented over the range  $r=1.4$  to 2.8. The Ludendorff index of the corona's photometric form is 0.24.

### Introduction

At the total solar eclipse of July 20, 1963, the white light corona was photographed by one of us with the aim of coronal isophotometry to about four solar radii. The camera had a focal length of about 57 cm. providing a scale of 6 minutes of arc per mm. The corona was photographed on Kodak Plus-X 35 mm film through a Wratten 15G filter. The effective wavelength of our coronal pictures was, therefore,  $5300\text{\AA}$ . The exposure times were 0.5 seconds, 1.0 second and 2.0 seconds. The 2 second exposure was near mid-totality and forms the material for the present study. The equipment was located at the AAVSO site located 50 miles north-east of Wilton, Maine, U.S.A. and 12 miles from the central line. The duration of totality was 58 seconds.

### The Isophotes of the Corona

We have carried out our programme of isophotometry by two methods. The first was the tedious procedure of microphotometer scans in an arbitrary rectangular co-ordinate system. The scans were made at closely spaced intervals and intensities read off subsequently from the calibration curve. Contours of equal intensity were then drawn through the appropriate points. To ensure adequate repeatability, we have also scanned the corona radially in 10 degree intervals. The agreement in contour representation between the two types of microphotometer scans was quite satisfactory. The success of this technique rests largely on the close spacing of the scans and subsequent intensity evaluation. The advantage of simplicity and accuracy must nevertheless be considered along with the tedious and exceedingly time consuming aspect of the technique.

Our second approach was to determine the isophotes by the technique of equidensitometry employing the Sabattier effect. This is an exceedingly simple and accurate procedure that has probably not received the attention in astronomy that it certainly merits. Schroter (1958) has shown how line profile distortions can be easily evaluated by the use of this technique. Richter and his collaborators have demonstrated its efficiency in the study of extended nebulosities and galaxies. At this observatory Bappu and Sivaraman (1968) have shown its efficiency in the evaluation of the location of the centre of gravity of a diffuse feature on a spectrogram. We feel convinced of its great utility because equi-density contours can be determined most conveniently and speedily. It only remains then to evaluate the intensity levels for each density contour, a process which can be done by the microphotometer.

Hogner and Richter (1966) have described in detail the procedure to be used for determining equidensity contours. We have used exclusively ORWO FU 5 emulsion with its very high gamma and find this most satisfactory. Figure 1 shows these contours on the single coronal frame of two seconds exposure.

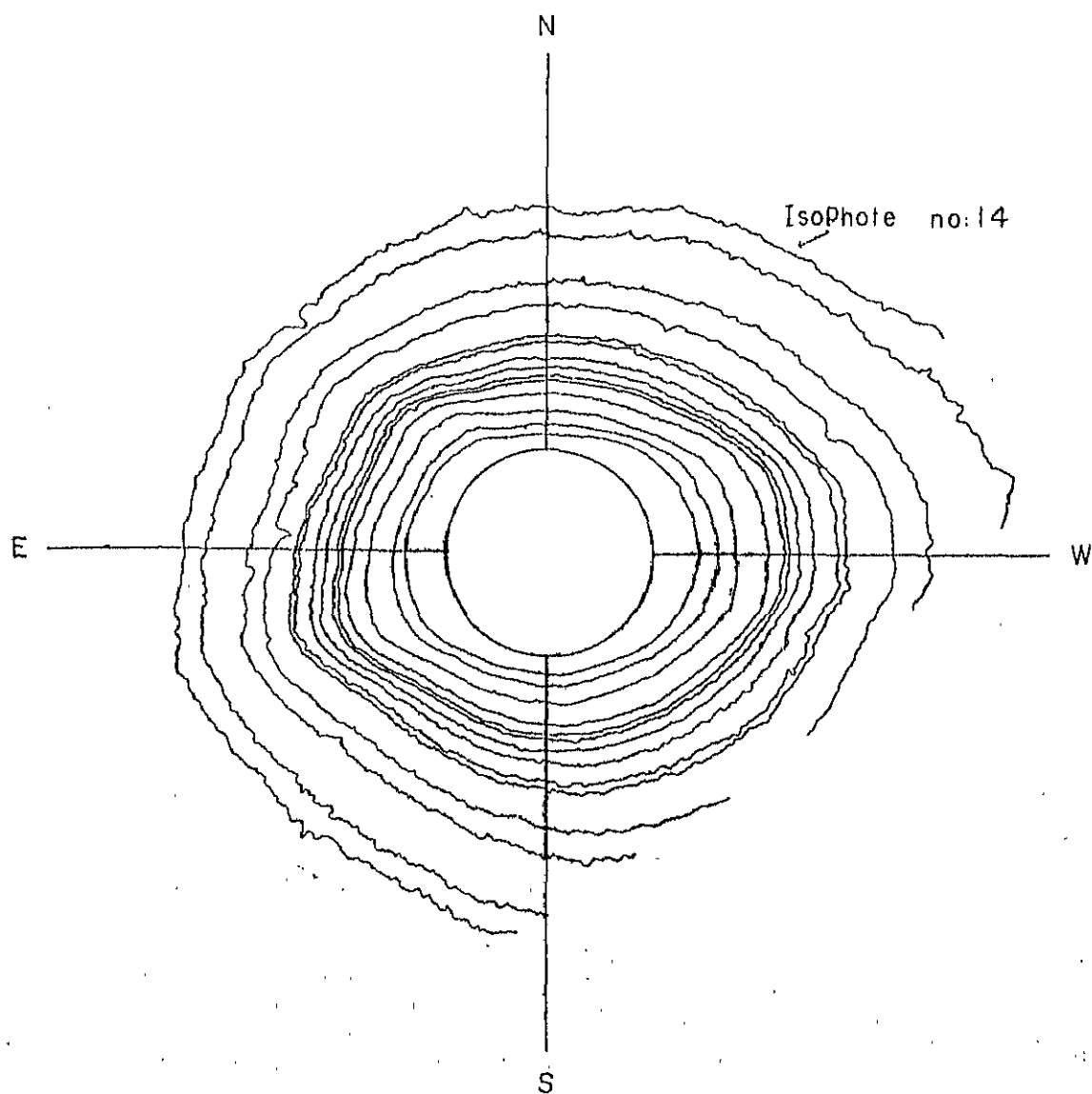


FIG. 1

The intensity marks utilized for deriving the calibration curves for conversion from density to intensity were impressed on the eclipse film a few hours after the event with the aid of a well calibrated Hilger step-wedge and a diffuse source of light of uniform intensity over the step-wedge. The intensity levels of these contours have been assigned from microphotometer scans along position angles  $0^\circ$ ,  $90^\circ$ ,  $180^\circ$  and  $270^\circ$ . The mean of these four values is chosen to indicate in Table 1, the value of intensity along each contour. We give here

TABLE 1

Isophote No.	Mean Log I
1	2.730
2	2.700
3	2.499
4	2.138
5	1.998
6	1.964
7	1.906
8	1.863
9	1.756
10	1.731
11	1.600
12	1.565
13	..
14	..

only those intensity levels for which the photometry can be considered to be secure. Such a consideration assigns a low weight to the intensity value of contour 1 and eliminates the use in subsequent discussion of contours 13 and 14, because of the inaccuracies in interpolation from the toe of the calibration curve. We, however, retain these equidensity contours in Figure 1 to show the general trend exhibited in the shape of the solar corona at these distances from the centre of the sun. It also shows up the efficacy of the Sabattier technique of equidensitometry in deriving a contour of equal density that has a level just detectable above that of the clear plate. Table 2 lists the values of  $r$  for the isophotes at different position angles.

TABLE 2

Iso- photo No.	Position Angle																	
	0°	10°	20°	30°	40°	50°	60°	70°	80°	90°	100°	110°	120°	130°	140°	150°	160°	170°
1	1.14	1.15	1.18	1.25	1.28	1.31	1.32	1.32	1.35	1.37	1.38	1.39	1.38	1.33	1.24	1.19	1.17	1.15
2	1.22	1.23	1.27	1.36	1.39	1.39	1.41	1.41	1.45	1.48	1.51	1.53	1.51	1.44	1.33	1.31	1.26	1.26
3	1.35	1.37	1.41	1.52	1.61	1.62	1.60	1.62	1.67	1.71	1.77	1.81	1.74	1.61	1.51	1.45	1.43	1.45
4	1.52	1.54	1.57	1.68	1.78	1.81	1.74	1.78	1.82	1.87	1.96	2.00	1.91	1.75	1.68	1.63	1.61	1.63
5	1.65	1.65	1.67	1.75	1.88	1.91	1.88	1.87	1.93	1.97	2.04	2.10	2.00	1.84	1.75	1.71	1.71	1.74
6	1.70	1.69	1.71	1.78	1.91	1.95	1.92	1.91	1.97	2.01	2.07	2.13	2.04	1.88	1.78	1.75	1.74	1.78
7	1.77	1.78	1.79	1.85	1.98	2.04	1.98	1.98	2.07	2.11	2.18	2.26	2.13	1.96	1.89	1.85	1.86	1.87
8	1.84	1.88	1.87	1.94	2.05	2.11	2.11	2.10	2.16	2.21	2.27	2.36	2.23	2.06	1.98	1.95	1.97	1.98
9	2.03	2.01	2.01	2.08	2.18	2.24	2.12	2.20	2.33	2.37	2.43	2.48	2.33	2.17	2.14	2.12	2.13	2.17
10	2.08	2.07	2.07	2.14	2.22	2.30	2.26	2.27	2.36	2.41	2.49	2.55	2.39	2.24	2.20	2.17	2.18	2.23
11	2.37	2.36	2.38	2.41	2.50	2.57	2.54	2.50	2.56	2.63	2.74	2.83	2.69	2.55	2.49	2.50	2.53	2.55
12	2.57	2.57	2.60	2.62	2.67	2.76	2.76	2.72	2.73	2.87	2.93	3.03	2.90	2.74	2.71	2.70	2.71	2.78
13	3.06	3.03	3.09	3.09	3.10	3.15	3.17	3.11	3.19	3.26	3.33	3.39	3.32	3.24	3.21	3.29	3.23	3.39
14	3.31	3.28	3.28	3.32	3.30	3.32	3.38	3.33	3.42	3.46	3.59	3.65	3.54	3.49	3.49	3.43	3.52	3.65

TABLE 2 --- *Contd.*

Iso- photo No.	Position Angle																	
	180°	190°	200°	210°	220°	230°	240°	250°	260°	270°	280°	290°	300°	310°	320°	330°	340°	350°
1	1.16	1.17	1.17	1.19	1.25	1.29	1.34	1.36	1.39	1.42	1.41	1.39	1.39	1.35	1.32	1.25	1.19	1.15
2	1.28	1.28	1.28	1.30	1.35	1.42	1.48	1.55	1.58	1.59	1.58	1.55	1.55	1.51	1.42	1.35	1.28	1.25
3	1.44	1.46	1.45	1.48	1.52	1.56	1.65	1.74	1.78	1.75	1.75	1.74	1.72	1.61	1.52	1.43	1.42	1.36
4	1.65	1.67	1.68	1.71	1.75	1.80	1.88	1.98	2.05	2.05	2.03	2.01	1.96	1.81	1.68	1.60	1.56	1.53
5	1.75	1.75	1.78	1.80	1.85	1.90	1.96	2.06	2.20	2.22	2.18	2.18	2.07	1.92	1.81	1.74	1.69	1.66
6	1.78	1.81	1.82	1.85	1.89	1.94	2.01	2.11	2.24	2.28	2.24	2.22	2.11	1.98	1.87	1.79	1.74	1.71
7	1.89	1.91	1.94	1.97	2.02	2.04	2.12	2.17	2.31	2.37	2.37	2.33	2.18	2.03	1.94	1.87	1.81	1.79
8	1.98	2.07	2.09	2.13	2.15	2.21	2.27	2.37	2.47	2.50	2.50	2.44	2.29	2.15	2.04	1.96	1.94	1.90
9	2.19	2.24	2.27	2.34	2.40	2.46	2.50	2.58	2.70	2.75	2.74	2.63	2.47	2.34	2.24	2.16	2.10	2.04
10	2.26	2.31	2.36	2.43	2.48	2.53	2.59	2.67	2.76	2.83	2.86	2.70	2.56	2.40	2.31	2.20	2.15	2.10
11	2.64	2.73	2.76	2.80	..	..	3.02	3.06	3.17	3.29	3.26	3.08	2.83	2.70	2.59	2.52	2.46	2.40
12	2.92	2.97	..	..	..	..	..	..	..	3.59	3.59	3.42	3.14	3.02	2.90	2.76	2.70	2.62
13	3.46	..	..	..	..	..	..	..	..	4.24	4.46	4.18	3.78	3.60	3.43	3.33	3.22	3.09
14	3.69	..	..	..	..	..	..	..	..	..	..	..	4.29	3.89	3.72	3.61	3.54	3.33



## The Radial Intensity Gradients

Several studies of coronal intensities have shown that over a restricted range of distances from the solar limb the distribution law of intensity can be represented by:

$$I = \frac{c}{d^n}$$

whence 
$$n = - \frac{\Delta \log I}{\Delta \log d}$$

where  $d$  is the distance from the solar limb. We have determined values of  $n$  over the range in intensity covered by isophotes 3 to 10 for every ten degree interval of position angle. These are given in Table 3.

TABLE 3  
Dependence of radial intensity gradients on  
position angle

Position Angle	n	Position Angle	n
0	1.50	180	1.63
10	1.60	190	1.60
20	1.89	200	1.63
30	2.25	210	1.55
40	2.62	220	1.61
50	2.35	230	1.66
60	2.05	240	1.86
70	2.22	250	2.05
80	2.13	260	2.10
90	2.40	270	1.97
100	2.51	280	1.92
110	2.72	290	2.08
120	2.79	300	2.26
130	2.42	310	2.08
140	1.82	320	1.77
150	1.74	330	1.64
160	1.60	340	1.61
170	1.65	350	1.62

The isophotes cover the range in  $r$  from 1.4 to 2.8 solar radii. Figure 2 contains a plot of  $\log(d+1)$  for the eight isophotes for different position angles. The

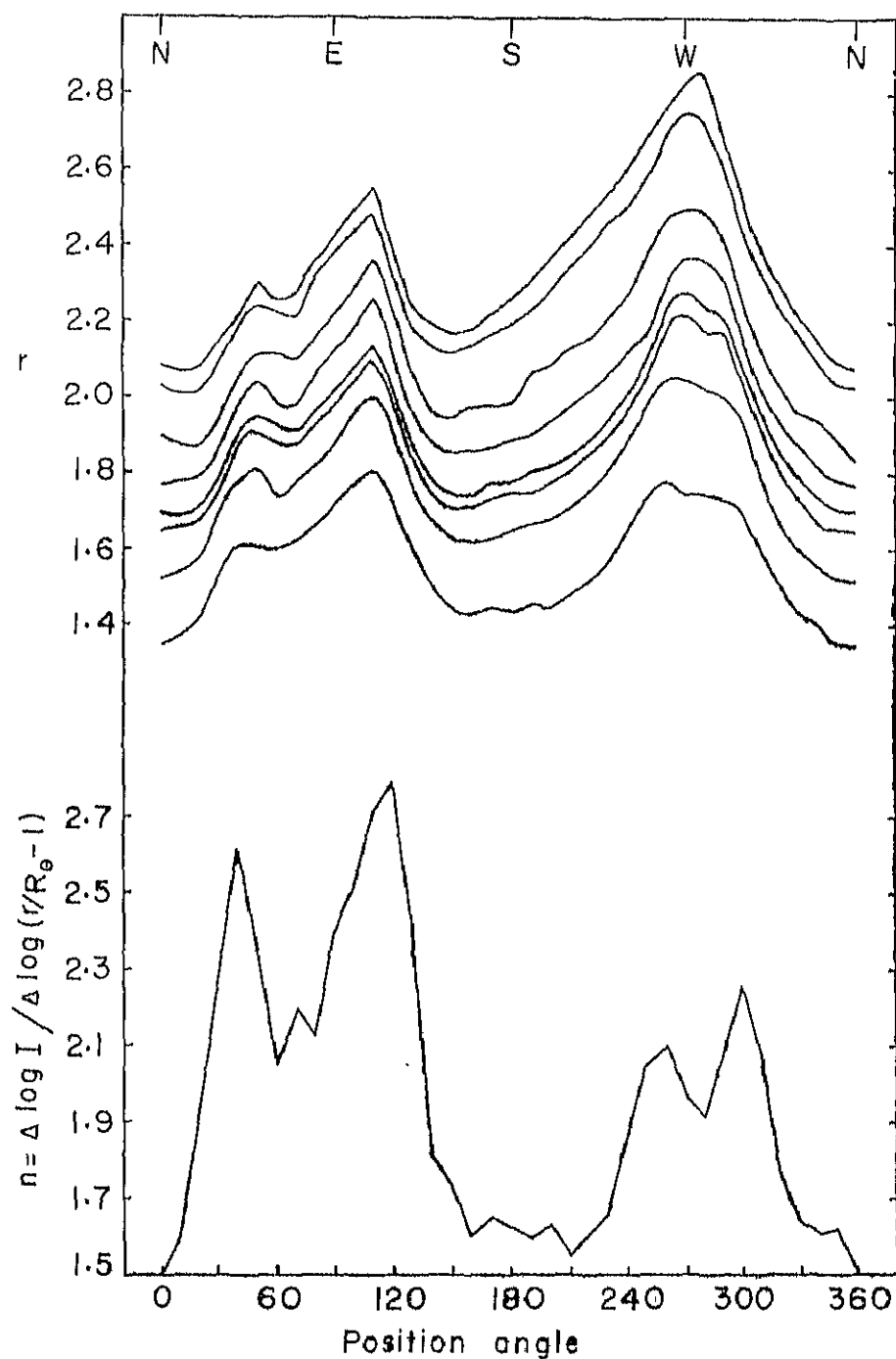


FIG. 2

lower portion of the diagram represents the variation in index  $n$  calculated by least squares from the eight intensity contours.

Ellipticity of the Corona

A measure of this parameter following Ludendorff (1928, 1934) needs measures of polar and equatorial diameters together with diameters inclined at 22.5° to each one of them. Hence  $\epsilon$ , the ellipticity is

$$\epsilon = \frac{3R}{D} - 1$$

where  $R$  is the mean of the equatorial diameter and those at position angles 67.5° and 112.5°, and  $D$  represents the sum of the three diameters at position angles 337.5°, 360° and 22.5°. Table 4 gives the Ludendorff ellipticity parameter for

TABLE 4  
Ludendorff ellipticity parameter  $\epsilon$  for the  
different isophotes

Isophote No.	R	$\epsilon$	Isophote No.	R	$\epsilon$
1	1.379	0.170	8	2.318	0.189
2	1.516	0.186	9	2.493	0.169
3	1.731	0.211	10	2.554	0.164
4	1.942	0.206	11	2.855	0.129
5	2.058	0.199	12	3.133	..
6	2.104	0.195	13	..	..
7	2.199	0.187	14	..	..

the different isophotes. Also shown in Fig. 3 is the ellipticity  $\epsilon'$  as defined by van de Hulst (1953) to be

$$\epsilon' = \frac{r_{\text{equator}}}{r_{\text{pole}}} - 1$$

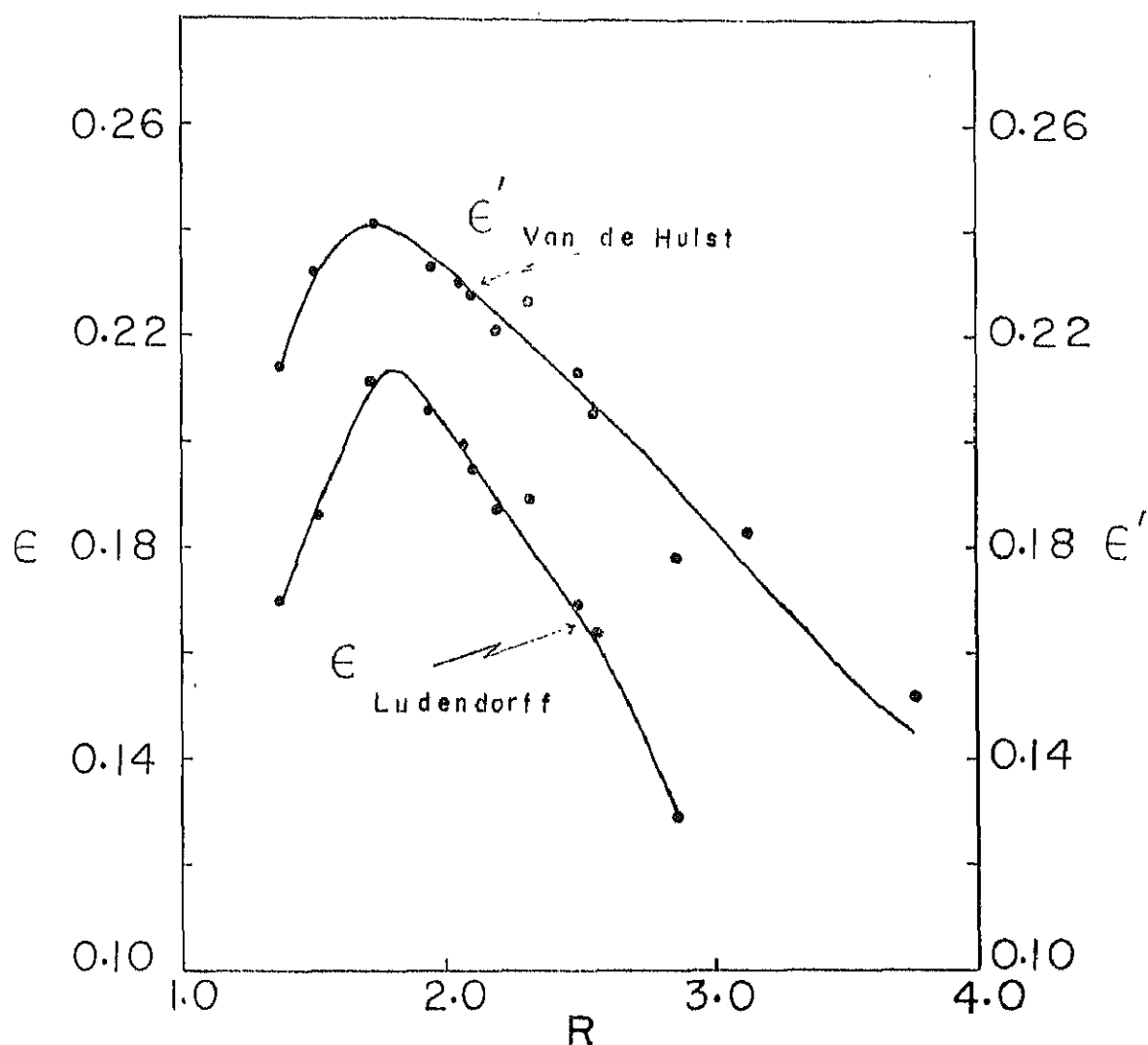


FIG. 3

In agreement with ellipticity values  $\epsilon$  as derived for previous eclipses near the minimum phase of the solar cycle we find that a maximum value of the Ludendorff parameter is at 1.8 solar radii. The solar eclipses of 1936, 1954 and 1955 all have maximum ellipticities near this value.

#### Acknowledgement

It is with great pleasure that we express our gratitude to the American Association of Variable Stars Observers, and in particular to its Director Mrs. Margaret W. Mayall, for providing all facilities for the observations at the eclipse site. Dark room facilities were generously provided by Prof. Harlan J. Smith at the Bethany station of Yale University Observatory. Prof. A. A. Wyller gave much needed help in covering the essential pre-requisites for successful photometric observation of the corona. The coronal photographs were obtained by one of us (MKVB) during a visit to the United States under the Foreign Visiting Professor's Programme of the American Astronomical Society.

KODAIKANAL OBSERVATORY  
July, 1969

## REFERENCES

- BAPPU, M. K. V. and SIVARAMAN, K.R., 1968 "Solar Active Regions" (I.A.U. Symposium No. 35, K.O. KIEPENHEUER editor), D. REIDEL, Dordrecht, P. 247.
- HOGNER, W. and RICHTER, N., 1966, Jena Review, **6**, 315.
- HULST, H.C. VAN DE, 1953, "The Sun" ed. by G.P. KUIPER, University of Chicago Press, P. 286.
- LUDENDORFF, H., 1928, Sitzungsber. der Preuss. Acad. d. Wiss., **185**, 1928.
- LUDENDORFF, H., 1928, Sitzungsber. der Preuss. Acad. d. Wiss., **200**, 1934.
- SCHROTER, E. H., (1958) Z. Astrophys., **45**, 68.

# KODAIKANAL OBSERVATORY

## BULLETIN Number 191

### Narrow Band Photometry of Rho Puppis

A. Thulasi Doss

#### Abstract

Monochromatic flux values of the dwarf Cepheid Rho Puppis have been evaluated over the cycle from observations made in the 1967 season through four narrow band filters centred at 3858 Å, 4310 Å, 4720 Å and 5875 Å. The amplitudes at the above wavelengths are 0.17, 0.14, 0.12 and 0.09 magnitudes respectively. The effective temperature variation over a cycle is 320°K. Photoelectric light curves have also been obtained in Blue and Yellow colours and amplitude of light variations are 0<sup>m</sup>.15 and 0<sup>m</sup>.09 respectively. The period is further improved as 0.14088067 day.

#### Introduction

Simultaneous spectrophotometric and spectral observations of the short period pulsating star Rho Puppis have been reported recently by Danziger and Kuhi (1967) and Bessel (1967). Earlier works on this star have been summarised by Danziger and Kuhi who have obtained at minimum light an effective temperature of  $T_e = 6071^\circ\text{K}$  ( $\theta_e = \frac{5040}{T_e} = 0.83$ ) and a low mass of 0.2 solar masses. They suggest that the star may be pulsating in a higher harmonic. This result has been criticized by Bessel who obtains values of  $\theta_e$  and mass to be 0.74 and 2.0 respectively and hence concludes that the star may be pulsating in the first overtone.

Ponsen (1962) has determined the mean light curve of Rho Puppis through a blue filter and improved the period combining all the observed epochs of maximum since the discovery by Eggen (1956), as well as from the radial velocity data.

The present study is undertaken to determine  $\theta_e$  for different phases from both (B-V) colour curves using interference filters. It was also of interest to investigate the constancy of the value of period derived by Ponsen.

#### Observations

The star was observed photoelectrically at Kodaikanal during January and February 1967, with a photometer attached to the 20cm Cooke refractor. An unrefrigerated RCA 1P21 photomultiplier tube was used and the amplified output

was recorded on a Brown recording potentiometer. The star was observed on 5 nights during January 1967 with the aid of standard B, V filters. The comparison stars were  $\xi$  Puppis and 11 Puppis. On one night in February Rho Puppis was observed through four narrow band interference filters with  $\xi$  Puppis and 11 Puppis as comparison stars. These two stars were later tied in with  $\alpha$  Tau,  $\xi$  Ori,  $\pi^3$  Ori and Leo for absolute flux determinations on Oke's (1961) system of standards.

Characteristics of the four narrow band filters used are given below:

Peak transmission wavelength	Width at half intensity
3858Å	94Å
4310Å	75Å
4720Å	46Å
5875Å	66Å

#### The light curves

The observations of Rho Puppis through B and V filters on 18, 21, 22, 23 and 24 January 1967 have been reduced to magnitudes outside the atmosphere by applying extinction corrections. The difference in magnitude between  $\xi$  Puppis and the variable have been computed. It was seen that the maximum light occurred about 20 minutes later than the computed epoch with Eggen's ephemeris (JD 2435555.911 + 0.141 E) and 16 minutes earlier than the computed epoch with Ponsen's ephemeris (JD 2437330.425 + 14088141E). The latter period is preferred as it has taken into account all the photometric and radial velocity measurements over a large interval from 1897 to 1963. Combining with the present epoch the period has been further improved as 0.14088067 days.

Hence the present ephemeris can be given as Max. J.D. (Hel) 2439512.244 + 0.14088067E.

It is with this present ephemeris that all the phases (heliocentric) in terms of period were computed. The  $\Delta m$  against phase for blue and yellow are given in tables I and II. The instrumental (B-V) colours that are determined are converted to standard (B-V) colours using linear transformations. The values are given in Table III and plotted in Figure 1 along with the blue light curve.

TABLE I

#### Blue observations of Rho Puppis

J. D. Helio-centric	Phase	$\Delta m$	J. D. Helio-centric	Phase	$\Delta m$
2439512.1377	0.2448	1.255	2439513.2523	0.1568	1.303
1474	0.3138	1.251	2571	0.1909	1.283
1502	0.3336	1.239	2578	0.1959	1.271
1543	0.3627	1.224	2641	0.2406	1.265
1620	0.4173	1.213	3057	0.5359	1.208
1648	0.4372	1.221	3113	0.5758	1.213
1689	0.4664	1.214	3182	0.6246	1.218

TABLE I—*Contd.*

J.D. Helio- centric	Phase	$\Delta m$	J.D. Helio- centric	Phase	$\Delta m$
2439512.1724	0.4912	1.201	2439513.3238	0.6643	1.233
1779	0.5302	1.219	3293	0.7035	1.237
1814	0.5551	1.203	3289	0.7005	1.261
1849	0.5799	1.211	3418	0.7923	1.277
1877	0.5997	1.211	3474	0.8333	1.303
1946	0.6487	1.201	3661	0.9646	1.338
1974	0.6684	1.211	3752	0.0399	1.340
2029	0.7077	1.218	3807	0.0688	1.338
2071	0.7375	1.245	3870	0.1136	1.317
2085	0.7474	1.252	4161	0.3207	1.238
2113	0.7673	1.263	4210	0.3549	1.215
2161	0.8013	1.273	4252	0.3847	1.211
2175	0.8115	1.288	4266	0.3945	1.208
2203	0.8311	1.290	4300	0.4188	1.203
2238	0.8564	1.304	4342	0.5906	1.192
2259	0.8709	1.313			
2300	0.9001	1.307	2439514.2759	0.4231	1.238
2321	0.9149	1.335	3309	0.8120	1.302
2384	0.9596	1.341	3349	0.8416	1.314
2411	0.9788	1.353	3543	0.9817	1.359
2425	0.9887	1.329	3564	0.9945	1.364
2453	0.0092	1.354	3585	0.0094	1.364
2481	0.0241	1.347	3606	0.0241	1.359
2495	0.0391	1.341	3627	0.2390	1.357
2550	0.0781	1.333	3641	0.0489	1.349
2564	0.0811	1.322	3661	0.0632	1.350
2585	0.1029	1.320	3682	0.0799	1.348
2627	0.1327	1.314	3710	0.0979	1.346
3071	0.4478	1.222	3724	0.1078	1.343
3127	0.4877	1.226	3745	0.1227	1.335
3141	0.4975	1.220	3752	0.1279	1.325
3161	0.5118	1.221	3773	0.1426	1.329
3411	0.6892	1.239	3786	0.1519	1.322
3439	0.6452	1.252	3800	0.1619	1.315
3479	0.7325	1.257	3825	0.1767	1.319
3495	0.7417	1.259	3835	0.1881	1.317
3814	0.9752	1.356	3842	0.1916	1.315
3849	0.0000	1.347	3856	0.2015	1.310
2439514.3863	0.2065	1.307	2439515.1842	0.8702	1.310
3891	0.2264	1.299	1856	0.8800	1.313
3898	0.2314	1.295	1870	0.8972	1.318
3911	0.2406	1.287	1884	0.9000	1.322
3918	0.2455	1.280	1898	0.9099	1.329
3922	0.2484	1.281	1911	0.9192	1.333
3946	0.2654	1.276	1925	0.9291	1.338
3953	0.2704	1.276	1940	0.9398	1.335
3974	0.2853	1.264	1953	0.9490	1.339
3995	0.3082	1.267	1967	0.9589	1.333



TABLE I—*contd.*

J.D. Helio- centric	Phase	$\Delta m$	J.D. Helio- centric	Phase	$\Delta m$
2439514.4009	0.3101	1.255	2439515.1995	0.9788	1.340
4036	0.3294	1.264	2009	0.9887	1.352
4057	0.3442	1.255	2023	0.9994	1.345
4092	0.3691	1.235	2036	0.0079	1.345
4113	0.3840	1.213	2050	0.0177	1.344
4141	0.4039	1.228	2064	0.0276	1.344
4154	0.4131	1.229	2092	0.0475	1.340
4175	0.4280	1.203	2120	0.0675	1.338
4189	0.4379	1.200	2141	0.0839	1.335
4307	0.5217	1.200	2161	0.0965	1.334
4321	0.5316	1.205	2189	0.1164	1.329
4356	0.5564	1.219	2203	0.1263	1.325
4377	0.5714	1.218	2217	0.1362	1.325
4398	0.5863	1.294	2231	0.1462	1.316
4439	0.6154	1.197	2245	0.1561	1.314
			2259	0.1660	1.309
2439515.1516	0.6388	1.196	2256	0.1710	1.305
1529	0.6480	1.194	2693	0.1902	1.303
1550	0.6700	1.205	2300	0.1952	1.297
1564	0.6729	1.210	2314	0.2051	1.296
1578	0.6829	1.212	2328	0.2150	1.290
1585	0.6879	1.216	2349	0.2300	1.287
1620	0.7127	1.224	2370	0.2449	1.282
1634	0.7226	1.231	2391	0.2597	1.278
1648	0.7325	1.238	2401	0.2569	1.282
1675	0.7516	1.254	2543	0.3676	1.232
1689	0.7616	1.256	2578	0.3925	1.225
1703	0.7715	1.259	3029	0.7126	1.272
1720	0.7832	1.266	3043	0.7225	1.267
1731	0.7913	1.274	3113	0.7722	1.275
1759	0.8113	1.282	3134	0.7871	1.281
1773	0.8205	1.282	3148	0.7971	1.278
1786	0.8304	1.293	3168	0.8113	1.291
1800	0.8404	1.292			
1814	0.8503	1.299			
1828	0.8603	1.304			

TABLE II  
Yellow Observations of Rho Puppis

J. D. Helio- centric	Phase	$\Delta m$	J. D. Helio- centric	Phase	$\Delta m$
2439509.1953	0.3598	0.522	2439513.2543	0.1711	0.561
2016	0.4045	0.516	2606	0.2157	0.566
2085	0.4536	0.507	2654	0.2498	0.547

TABLE II—*Contd.*

J.D. Helio- centric	Phase	$\Delta m$	J.D. Helio- centric	Phase	$\Delta m$
2439509.2210	0.5423	0.508	2439513.3148	0.6005	0.516
2266	0.5870	0.503	3210	0.6445	0.519
3161	0.2172	0.571	3266	0.6842	0.526
3196	0.2420	0.547	3321	0.7233	0.534
3314	0.3088	0.534	3370	0.7580	0.542
3370	0.3655	0.527	3346	0.7411	0.562
3426	0.4046	0.519	3710	0.9999	0.600
3467	0.4344	0.519	3779	0.0488	0.597
3509	0.4642	0.512	3828	0.0837	0.592
3557	0.4981	0.508	3904	0.1377	0.578
3620	0.6139	0.508	4182	0.3350	0.525
3789	0.6629	0.506	4238	0.3745	0.532
3946	0.7034	0.543	4279	0.3747	0.523
3995	0.8092	0.557	4286	0.4088	0.505
4036	0.8382	0.563	4326	0.4372	0.514
4085	0.8731	0.579	4370	0.4684	0.516
4134	0.9078	0.590	4441	0.5188	0.501
4175	0.9367	0.594	4425	0.5075	0.503
4231	0.9768	0.589			
2439512.1307	0.1959	0.546	2439515.1439	0.5841	0.501
1668	0.4521	0.517	2335	0.2200	0.543
2002	0.6892	0.515	2356	0.2399	0.541
2279	0.8858	0.588	2384	0.2548	0.540
2599	0.1128	0.590	2411	0.2739	0.543
3092	0.4060	0.511	2564	0.3825	0.513
3279	0.5955	0.504	3036	0.7176	0.568
3460	0.7311	0.543	3127	0.7822	0.546
			3154	0.8013	0.547
			3411	0.8418	0.594
			3627	0.1369	0.562

TABLE III  
(B-V) colour and  $\theta_e$  values of Rho Puppis

J.D. Heliocentric	Phase	(B-V)	$\theta_e$
2439509.1946	0.3549	+0.358	0.743
2002	0.3946	+0.360	0.745
2078	0.4486	+0.364	0.748
2189	0.5272	+0.378	0.755
2252	0.5721	+0.370	0.752
2293	0.6012	+0.375	0.754

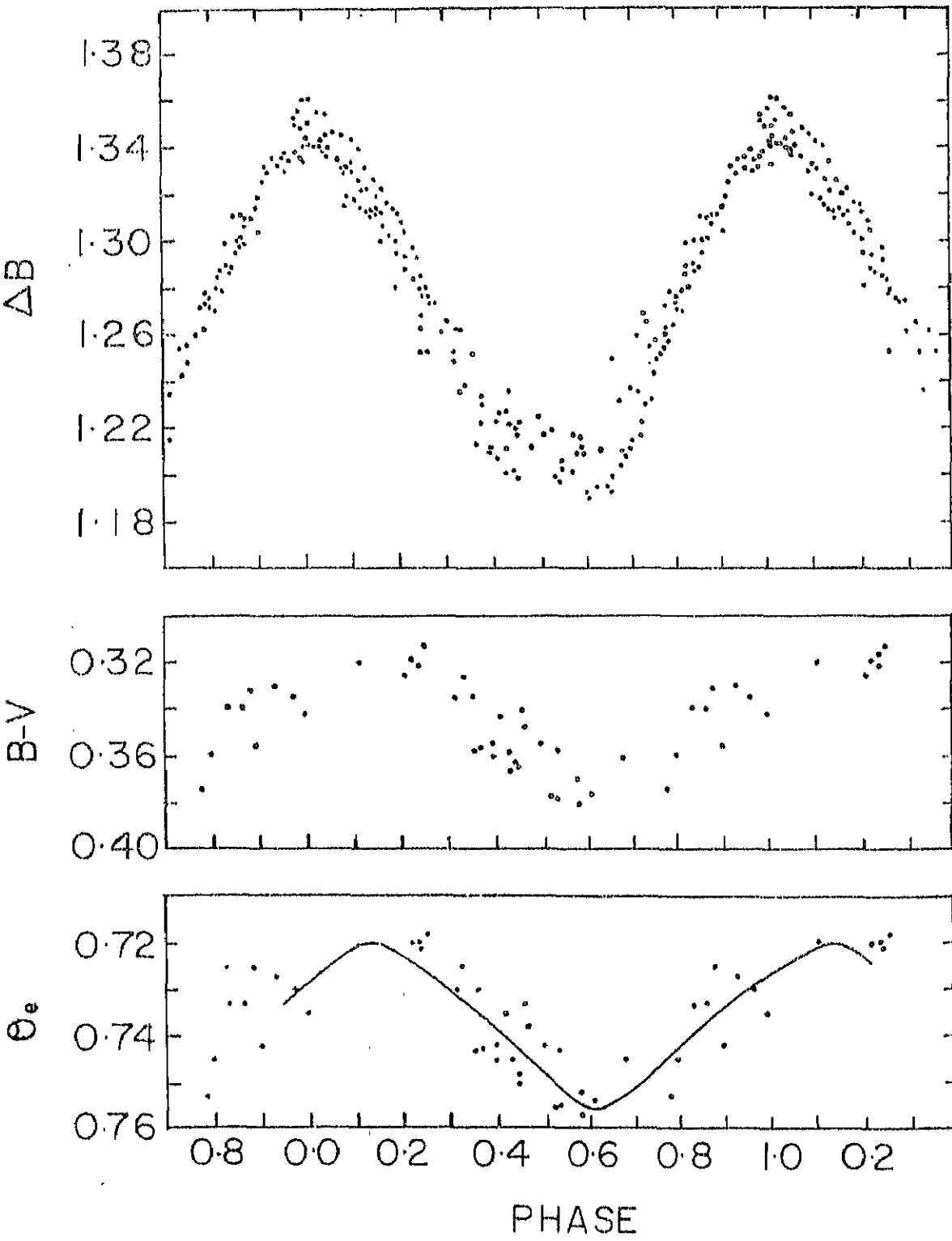


Figure 1—Light, colour and temperature curves of Rho Puppis.

TABLE III—*Contd.*

J.D. Heliocentric	Phase	(B-V)	$\theta_e$
2439509.3154	0.2212	+0.319	0.720
3189	0.2370	+0.321	0.721
3300	0.3158	+0.335	0.730
3356	0.3556	+0.334	0.730
3460	0.4294	+0.359	0.745
3502	0.4592	+0.348	0.738
3550	0.4933	+0.355	0.742
3599	0.5281	+0.358	0.743
3932	0.7786	+0.374	0.753
3981	0.7992	+0.359	0.745
4029	0.8333	+0.339	0.733
4071	0.8631	+0.339	0.733
4120	0.8979	+0.355	0.742
4168	0.9319	+0.330	0.727
4217	0.9667	+0.334	0.730
2439512.1654	0.4422	+0.363	0.748
1759	0.5167	+0.377	0.755
1988	0.6792	+0.361	0.745
2273	0.8815	+0.331	0.725
2432	0.9944	+0.342	0.735
2592	0.1078	+0.320	0.720
3085	0.4578	+0.340	0.733
2439513.2597	0.2058	+0.325	0.724
4175	0.3301	+0.326	0.725
4224	0.3648	+0.357	0.743
4273	0.3996	+0.355	0.742
4293	0.4138	+0.343	0.735
4326	0.4372	+0.366	0.750
2439515.1432	0.5792	+0.380	0.757
2356	0.2349	+0.316	0.720
2377	0.2497	+0.313	0.718

The shape of the light curve agrees with that of Ponsen with a sharper maximum than minimum and with equally steep rising and descending branches. It is noted that a scatter of about  $0^m.01$  was seen in the light curves. The mean amplitude in blue and yellow are  $0^m.15$  and  $0^m.09$  respectively.

#### Temperatures

The B-V colour variation with phase is utilised to derive the changes in effective temperature over a cycle. The values of effective temperatures against (B-V) obtained by Oke and Conti (1965) for the Hyades stars were utilised and  $\theta_e$  with phase were computed for Rho Puppis. The values are given in Table III and also plotted in Figure 1. It can be seen from figure 1 that  $\theta_e = .755$  at minimum and the variation is .035 over a cycle. The value of  $\theta$  at minimum compares well with that obtained by Bessel ( $\theta_e = .74$ ).

The effective temperature variation over a cycle was also studied by the observations taken through four interference filters.

The flux values with the filter 3859Å were not given a high weight in the slope determination due to the large blanketing corrections involved.

The monochromatic fluxes given by Oke for  $\alpha$  Leo and  $\epsilon$  Ori were utilised to derive that for  $\Pi$  Puppis and  $\xi$  Puppis. The method given by Oke (1965) has been followed for determining absolute fluxes AB and effective temperatures  $\theta_e$ . The absolute energy fluxes of  $\xi$  Puppis,  $\Pi$  Puppis and Rho Puppis are given in Table IV. Figure 2 is a plot of the flux values of Rho Puppis for the different phases. It can be seen that the light amplitude decreases with increasing wavelength. The ranges are 0.17, 0.14, 0.12 and 0.09 magnitudes for 3859Å, 4310Å, 4720Å and 5875Å respectively.

TABLE IV  
Monochromatic flux AB\* and  $\theta_e$  values of Rho Puppis

Time U.T	3858Å	4310Å	4720°	5875Å	Phase	$\theta_e$
February 7, 1967						
1621	3.649	3.108	2.870	2.733	0.1959	0.726
1632	3.699	3.112	2.887	2.744	0.2499	0.712
1640	3.739	3.134	2.885	2.739	0.2889	0.734
1648	3.733	3.132	2.900	2.782	0.3286	0.715
1655	3.753	3.159	2.911	2.783	0.3634	0.725
1710	3.787	3.177	2.931	2.792	0.4372	0.726
1734	3.782	3.181	2.916	2.779	0.5551	0.732
1742	3.783	3.179	2.921	2.765	0.5948	—
1758	3.766	3.131	2.883	2.765	0.6736	—
1812	3.745	3.113	2.873	2.737	0.7425	0.723
1819	3.735	3.101	2.853	—	0.7773	0.706
1827	3.736	3.074	—	—	0.8170	—
1856	3.614	3.039	2.807	2.714	0.9597	0.704
1912	—	3.042	2.808	2.693	0.0383	0.715
1917	3.612	3.036	2.808	2.716	0.0632	0.700
1934	3.650	3.065	2.834	2.720	0.1469	0.708
1940	3.610	3.070	2.838	2.751	0.1760	0.697
1947	3.632	3.107	2.857	2.748	0.2108	0.702
1954	3.649	3.104	2.868	2.762	0.2456	0.710
2001	3.643	3.125	—	2.762	0.2797	0.719
$\xi$ Puppis	6.108	4.641	3.804	3.072		
$\Pi$ Puppis	5.642	4.900	4.460	4.079		

\*Flux AB =  $[-2.5 \log F_\nu + \text{Const}]$  normalised to  $m_v$  at 5556Å.

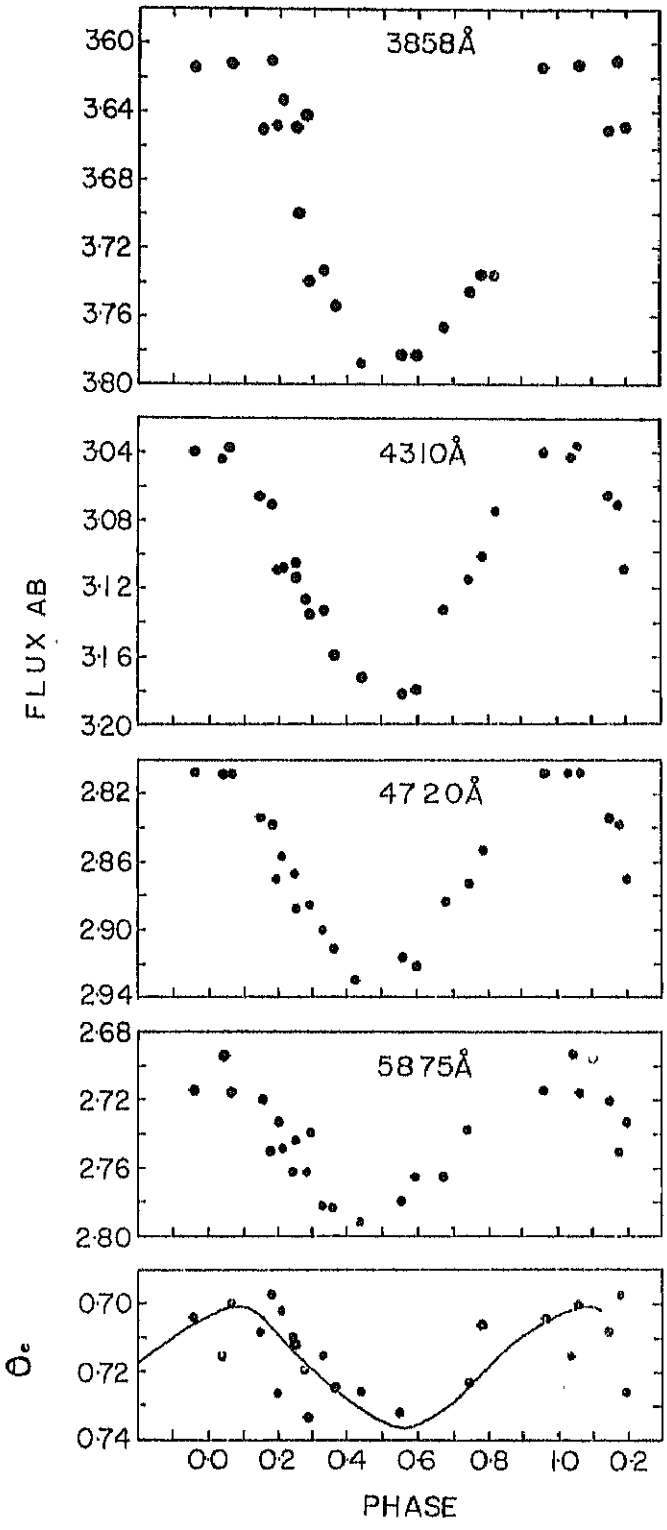


Figure 2—Light curves of Rho Puppis with four narrow band filters and the temperature variation over a cycle.

Assuming  $\log g = 0.34$  and the blanketing corrections given by Bessel, the  $\theta_e$  variation over the cycle for Rho Puppis is derived and plotted in Figure 2.

It is seen that both  $\theta_e$  curves in Figures 1 and 2 agree with each other in the amplitude, though there is a slight shift of .02 in  $\theta_e$  scale. It is also seen that the minimum temperature occurs about 0.1P in phase after the minimum light. Even though the differential variations agree in amplitude and phase, the effective temperatures derived by Danziger and Kuhl are systematically lower by about 700°K. Our value of  $\theta_e$  minimum for Rho Puppis confirms the results obtained by Bessel ( $\theta_e = .74$ ) and not that of  $\theta_e = .83$  obtained by Danziger and Kuhl.

The amplitude of  $\theta_e$  from Figures 1 and 2 is .035 and hence the effective temperature variation over a cycle is 320°K. The earlier values reported were 300°K by Bappu (1959) and 280°K by Danziger and Kuhl.

#### Acknowledgements

The author is indebted to Dr. M.K.V. Bappu for suggesting this programme and for his continued guidance. I wish to thank Mr. C.V. Ramakrishna Rao and Mr. K.K. Kunju Kunju Kutty for their help during observations and computations.

Kodaikanal Observatory

July, 1969

#### REFERENCES

- Bappu, M.K.V., 1959, Mon. Not. R. astr. Soc. **119**, 400  
 Bessel, M.S., 1967, Astrophys. J (Letters), **149**, L 67  
 Danziger, I. J., and Kuhl, L.V., 1967, Astrophys. J., **146**, 743  
 Eggen, O.J., 1956, Publ. astr. Soc. Pacific, **68**, 238  
 Oke, J. B., 1964, Astrophys. J., **140**, 689  
 Oke, J. B., 1965, A Rev. Astr. Astrophys., **3**, 23  
 Oke, J. B., and Conti, P. S., 1966, Astrophys. J., **143**, 134  
 Ponsen, J., 1963, Bull. astr. Inst. Netherl., **17**, 44.

KODAIKANAL OBSERVATORY  
BULLETIN Number 204

On the Polar Coronal Rays of the Sun

A. Bhatnagar and K.C.A. Raheem

**Abstract**

A study of the polar coronal rays made on two eclipse photographs is presented. From the frequency distribution of polar rays, it is shown that the maximum distribution of polar rays occurs in an annular zone around  $10^\circ$  from the poles and a minimum at the poles. From the orientation of the polar rays the length of the hypothetical bar magnet has been determined. A variation in the length of the hypothetical bar magnet with the phase of solar activity cycle is confirmed.

**1. Introduction**

Campbell, Moore and Bell (1923) were the first to point out the similarity between the polar coronal rays and a bar magnet. They showed that the distribution and orientation of polar rays matches fairly well with the magnetic lines of force due to a bar magnet, situated inside the sun and whose poles are separated by two thirds of the sun's diameter. In recent years, Waldmeier (1961), Bachmann (1957), Saito (1958, 1965), Stoddard, Carson and Saito (1966) and Suda (1966) have studied the geometry of the polar rays and tried to correlate with the magnetic lines of force due to a bar magnet. Saito (1965) has shown from a study of several eclipse-photographs that the length of the hypothetical bar magnet is a function of the solar activity cycle.

For further verification of the hypothetical bar magnet, it is necessary to analyse as many large scale eclipse photographs as possible. In the plate collection of the Kodaikanal Observatory, we had two large scale eclipse photographs, obtained during the total eclipse of 1898 and 1922. In this paper we have presented a study of the orientation and the frequency distribution of the polar rays, made on these two eclipse plates.

**2. Observational data**

*The eclipse of 1898 January 21.* This photograph obtained by Michie Smith at Sahdol, Central India (Lat. =  $23^\circ 16'N$ , long. =  $81^\circ 21'E$ ), using a camera of 15cm aperture and 12 metres focal length, giving an image scale of



16".5/mm. The polar rays could be traced out to distances of the order of 1.2 solar radii as measured from the sun's centre. A high contrast copy of the original negative was enlarged and projected on a screen to obtain an image scale of 3".9/mm. The outlines of individual polar rays were drawn independently by the two authors. A comparison of the two drawings showed no significant difference. A copy of the eclipse photograph obtained by the Lick 1898 eclipse expedition with a similar focal length camera, was generously made available by Director, Lick Observatory, and a comparison of the two pictures showed that almost all polar rays were common on both pictures. Another small scale plate (1".5/mm), made available from the Lick collection showed polar rays, extending upto 1.6 R. The small scale plate was enlarged to yield an image scale of 3".9/mm and both small and large scale plates were combined to give a composite drawing of the polar rays, as shown in Figure 1. The polar rays were extended from the limb of the moon to meet the solar limb.

At the time of the eclipse the apparent semidiameter of the sun was  $16'.14''.8$  and that of the moon was  $16'.24''.3$ . The position angle  $P$  of the sun's axis was  $-7^\circ$  and the heliographic latitude of the sun's centre,  $B_0$  was  $-5^\circ$ . The north-south orientation on the plate was determined, using the position angle of the prominences seen on the plate. According to the Lundendorff definition the phase of the solar cycle at the time of eclipse was  $-0.46$ . On this photograph 20 north polar rays (N.P.R.), and 30 south polar rays (S.P.R.) were distinctly seen. The number of the polar rays in 5 degree intervals of the polar angle is given in Table I and a histogram in Figure 2. A distinct peak in the histogram is seen at  $10^\circ-15^\circ$  zone of the polar angle.

*The eclipse of 1922 September 21.* This plate was obtained by John Evershed (1922) at Wallal, Western Australia, (Lat.  $=19^\circ.46'S$ , Long.  $=120^\circ.41'E$ ), using a 30cm aperture and 6.3 meter focal length Cooke triplet lens, in conjunction with a coelostat. The image scale on this plate was 33".4/mm. The plate was partly fogged, but for our purpose of determining the geometry of the polar rays the plate was usable. As in the case of the 1898 eclipse plates, this plate was enlarged and projected to yield an image scale of 4"/mm. The outlines of the individual coronal polar rays were drawn and are shown in Figure 1.

At the time of totality the apparent semidiameter of the sun was  $15'.56''.0$  and that of the moon was  $16'.43''.6$ . The position angle  $P$  of the sun's axis was  $+25.3^\circ$  and  $B_0$  was  $+7^\circ$ . The north-south orientation was determined from the symmetry of the polar rays. The assumption is made here that the magnetic poles and the rotation axis of the sun are in good coincidence (Campbell *et al* 1923). At the time of eclipse the phase of the solar activity cycle was  $-0.14$ . 18 polar rays in the north and 17 in the south were identified on the plate. The polar rays in the south were not as clearly seen as in the north, probably because the sun's south pole was tipped away from the observer ( $B_0 = +7^\circ$ ). We give in Table I the number of rays in each of the  $5^\circ$  intervals of the polar angle. A histogram showing the distribution of the polar rays is given in Figure 2. This shows a peak at  $(5^\circ-10^\circ)$  zone of polar angle and a minimum at the pole.

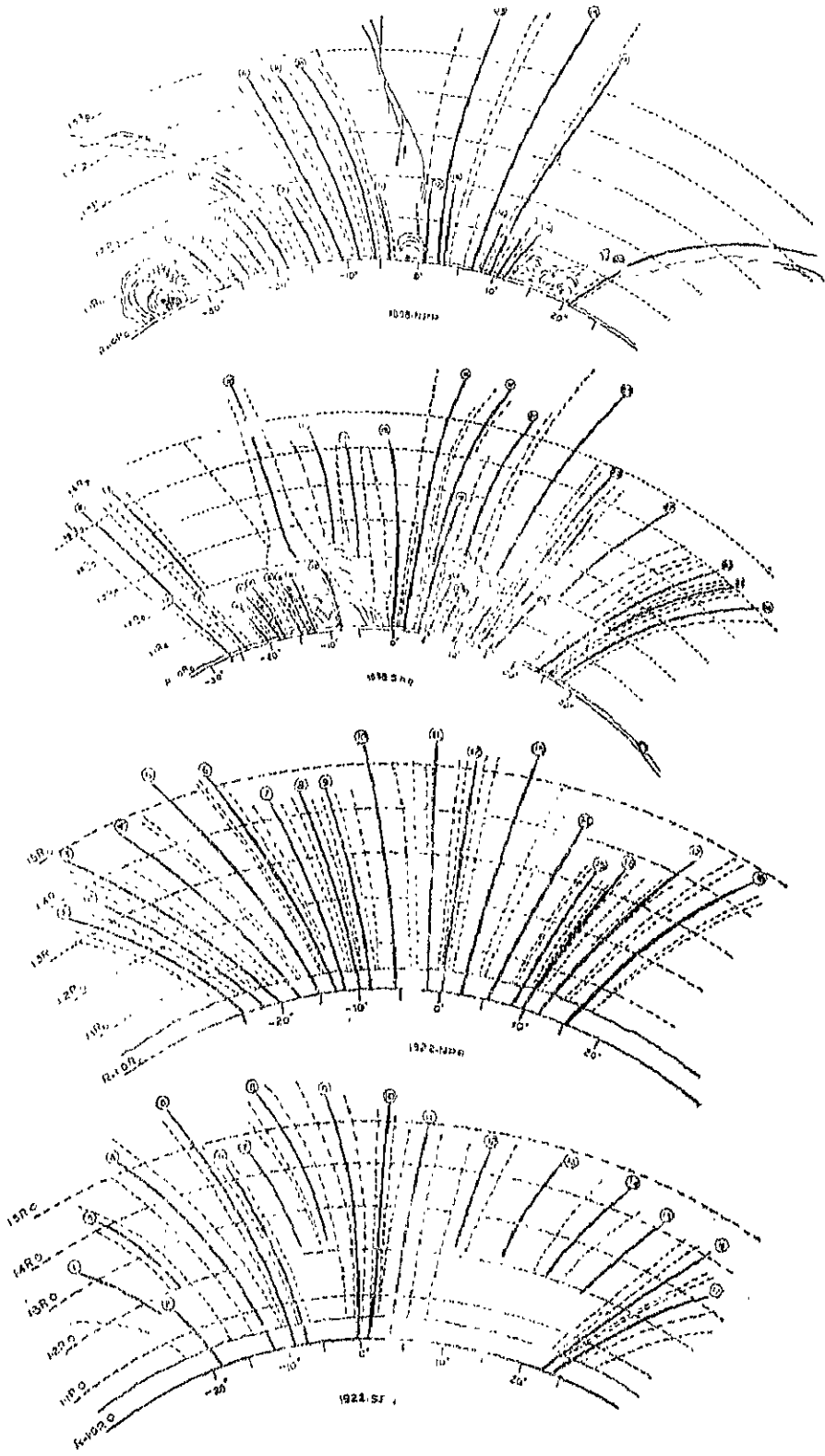


Fig. 1

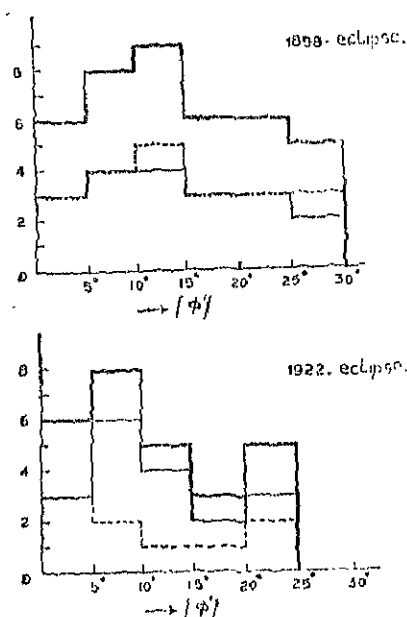


Fig. 2

From Saito's (1958, 1965), data for 6 eclipses and from these two eclipses, we conclude that there is no apparent relation between the position of the polar angle of the peak in the histogram and the solar activity cycle. But during all phases of the solar cycle, the polar rays are consistently seen to avoid the poles of the sun. On the contrary Tsubakia *et al* (1964) have shown in the case of the 1962 eclipse, that the distribution of the polar rays is a maximum at the poles and a minimum near the  $(12^\circ - 15^\circ)$  zone, while for the same eclipse of 1962, Saito (1965) has obtained a maximum at the  $10^\circ$  zone and a minimum at the pole. Saito has explained this discordance in the two results as due to the statistical error introduced by Tsubaki *et al*, because they had chosen smaller intervals of the polar angle. From these observations it appears that polar rays are distributed in an annular zone  $10^\circ$  away from the pole. In this connection it is interesting to note that, on examining the prominence data from the Kodaikanal Observatory Bulletins for several solar cycles, there is a tendency for prominences to persist around  $\pm 80^\circ$  latitude and to avoid the poles. However, recently Harvey (1965) from study of the 1963 eclipse photographs, has found a correlation between the polar rays and surface features observed in  $K_3$  spectroheliograms and has taken this correlation to establish the close association between polar rays and surface magnetic fields.

### 3. Apparent orientation of the polar rays

*1898 eclipse:* The apparent angle of obliquity  $\Psi$  and the polar angle  $\varnothing$  were measured at the limb of the sun and also at distances of  $1.1 R_\odot$ ,  $1.2 R_\odot$ ,  $1.3 R_\odot$ ,  $1.4 R_\odot$ ,  $1.5 R_\odot$ ,  $1.6 R_\odot$ , from the sun's centre.  $\Psi$  denotes the apparent angle between the tangent drawn at a point  $P$  on polar ray and the radius vector, and  $\varnothing$  is the apparent polar angle of the point  $P$  as measured from the N-S axis. It has been shown by several authors, on the basis of observations, that a linear relation of the form  $\Psi = k \varnothing$  exists between  $\Psi$  and  $\varnothing$  and that the parameter  $k$  depends on the phase of the polar activity cycle.

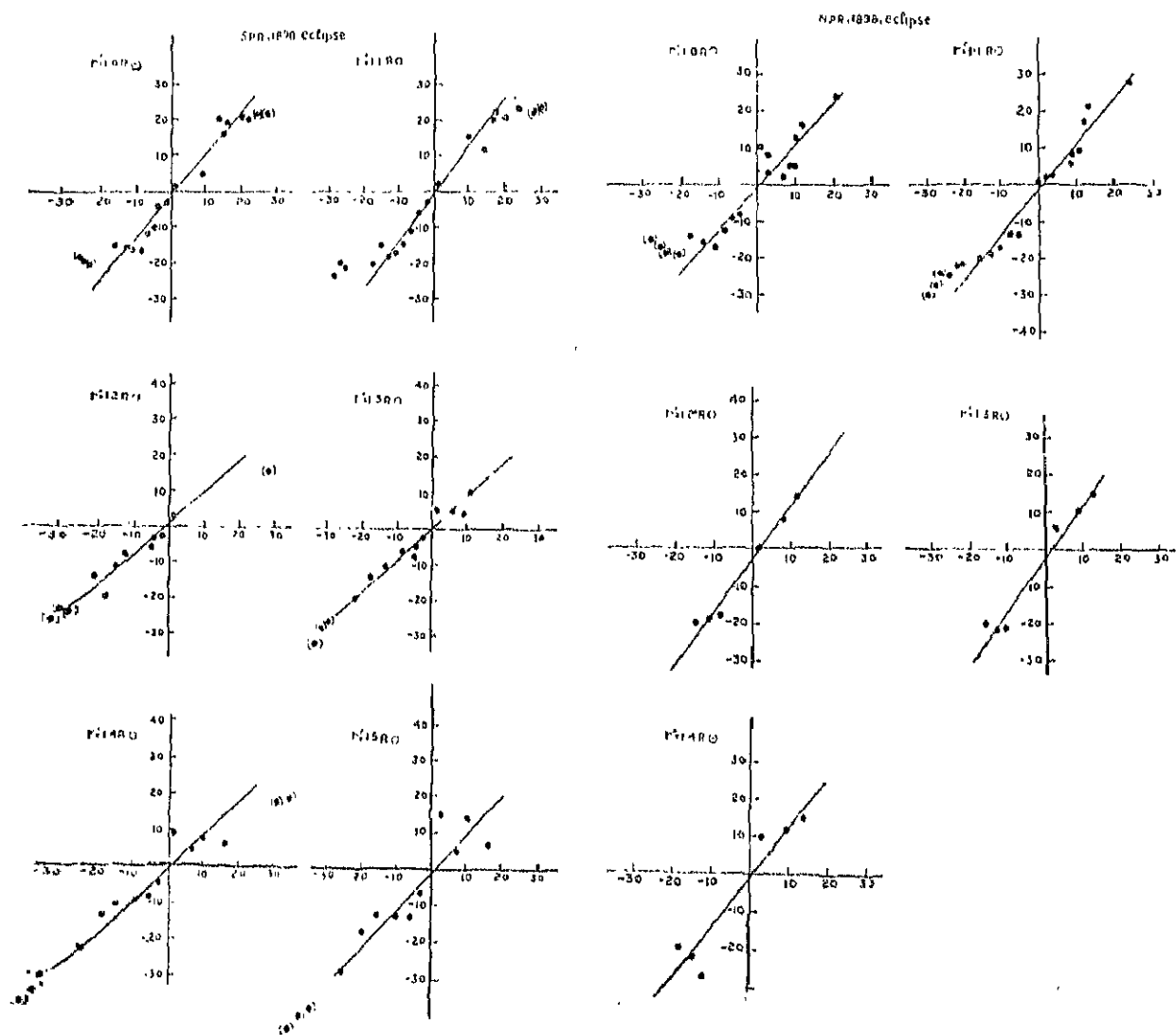


Fig. 3 (i)

HPR, 1922, Eclipse

SPR, 1922, Eclipse

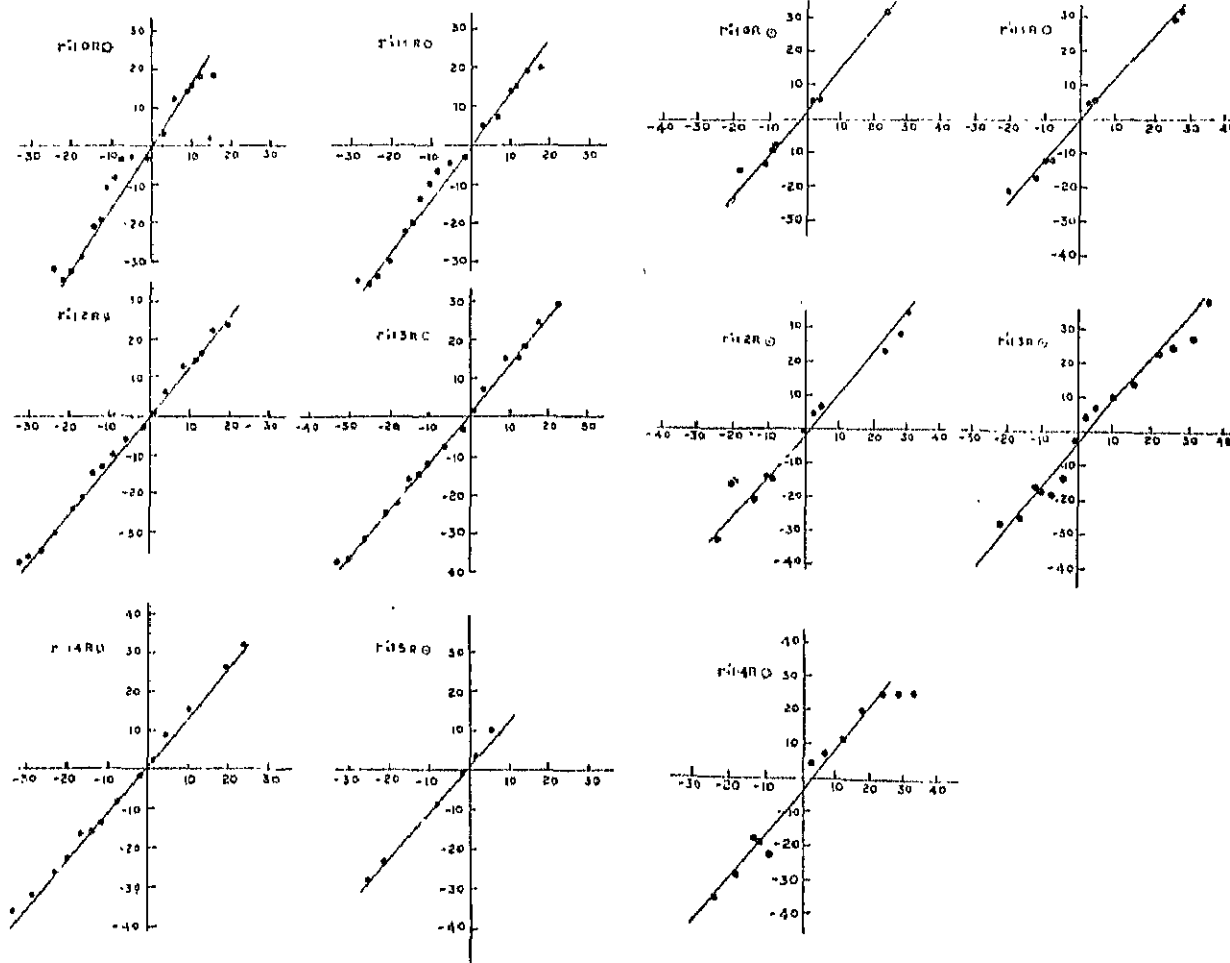


Fig. 3 (ii)

In Table 2a and 2b we give the apparent obliquity and polar angle for each of the polar rays and at several distances from the sun's centre, for both north and south solar polar regions. These are plotted in Figure 3. A few polar rays seem to have been influenced by the local prominence activity and the points are enclosed in parentheses. In Figure 4 is shown the variation of parameter  $k$  with the radial distance from the sun's centre. In the north polar region,  $k$  shows an increasing tendency with distances upto  $1.2 R_{\odot}$  while in the south side,  $k$  shows a peak at  $1.1 R_{\odot}$  and then a steep decline till  $1.2 R_{\odot}$  after which it remains constant.

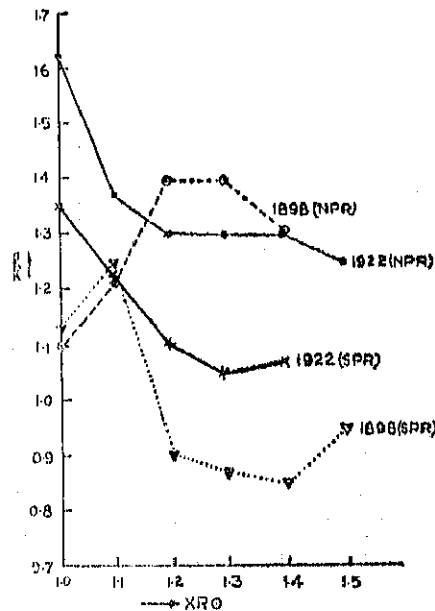


Fig. 4

Saito (1958) has obtained a relation between the parameter  $k$  and the length of a hypothetical bar magnet, situated inside the sun. Using Saito's relation, we obtain the half length of the bar magnet as  $0.43 R_{\odot}$  for the north polar rays and  $0.46 R_{\odot}$  for the south polar rays. We have measured the parameter  $\bar{q}$ , which is the distance between the point of intersection of the tangents drawn on the polar rays at the limb of the sun and the centre of the solar disc. The mean  $\bar{q}$ , is found to be  $0.50 R_{\odot}$  for the system of N.P.Rs and  $0.48 R_{\odot}$  for the S.P.Rs. The two values are in close agreement and we can consider that the two poles of the hypothetical magnet are equally separated apart from the sun's centre. The half-length of the bar magnet according to Saito is in fair agreement with the parameter  $\bar{q}$ .

**1922 eclipse :** The apparent angle of obliquity  $\Psi$  and the polar angle  $\varnothing$  were measured on the drawings of the polar rays. The values of  $\Psi$  and  $\varnothing$  are tabulated in Table 3a and 3b, and are plotted in Figure 3. The variation of parameter  $k$ , with the radial distance from the sun's centre is given in figure 4. In the case of 1922 eclipse the parameter  $k$ , decreases with increasing distance from the sun's disc up to  $1.2 R_{\odot}$  and then remains nearly constant.

Using Saito's relation, the half length of the hypothetical bar magnet obtained from the N.P.R. system is  $0.61 R_{\odot}$  and for the S.P.R. system is  $0.55 R_{\odot}$ . The parameter  $\bar{q}$  for the N.P.R. was  $0.69 R_{\odot}$  ( $\bar{q}_N$ ) and for the S.P.R. was  $0.61 R_{\odot}$  ( $\bar{q}_S$ ). In the case of 1922 eclipse the hypothetical north

magnetic pole seems to be nearer to the sun's surface compared to the south magnetic pole. A similar result for the asymmetric location of the hypothetical magnet in the sun, has been obtained by Nesmyanvich (1963), from a study of 38 eclipse photographs.

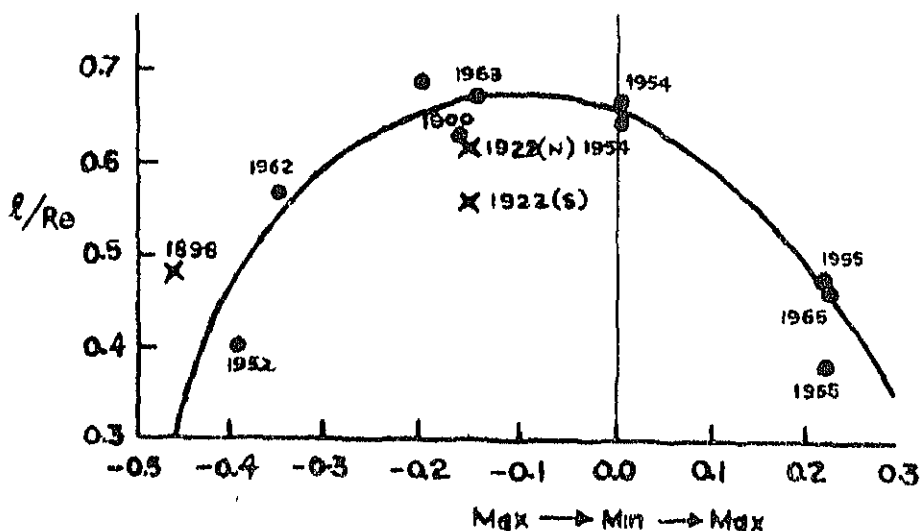


Fig 5.

The length of the hypothetical bar magnet as obtained in the case of the 1898 and 1922 eclipses show variation with the phase of the solar active cycle. We have plotted in Figure 5, the corresponding length of the magnet for these eclipses on Saito's curve showing the variation of length of the hypothetical magnet with the phase of the solar cycle.

#### Variation of parameter $k$ with distance from the solar limb

Several authors have made detailed study of the variation of parameter  $k$  with distance from the sun. Waldmeier (1965) has shown for the 1962 eclipse that  $k$  is independent of  $r$ , while Bachman (1957) and Ivancuk (1964) have observed that  $k$  decreases with increasing distance  $r$ , for 1954 eclipse. Kopecky and Suda (1966) have made a detailed study of the variation of  $k$  with  $r$  for several eclipses and could not arrive at any definite conclusion on the dependence of  $k$  on  $r$ .

Our results obtained from the two eclipses show a variation of  $k$  with  $r$  near the sun's limb but at large distances  $k$  becomes nearly constant with  $r$ .

The authors are indebted to Dr M. K. V. Bappu for his helpful suggestions and to the Director of the Lick Observatory for generously making available the Lick Observatory eclipse photographs. Thanks are due to Mr. V. Natarajan for his help during the investigation.

Kodaikanal Observatory,  
October 1970.

## REFERENCES

- Bachmann H., 1957, *Zs. f. Ap.*, **44**, 56, 1957.
- Campbell W. W., Moore J. H. and Bell R. H., 1923, *P. A. S. P.*, **35**, 163.
- Evershed J., 1922, *Kodaikanal Obs. Bull.*
- Harvey J. W., 1965, *Astrophys. J.*, 141, 832.
- Ivancuk V. J., 1964, *Materials of IGY, Infor. Bull. No. 6*, Kijev, p. 46.
- Kopecky M., Suda J., 1966, *B. A. G.*, **17**, 144.
- Nesmyanovich A. T., 1963, *Soviet Astron. A. J.*, **6**, 774.
- Saito K., 1958, *Publ. A. S. Japan*, **10**, 49.
- Saito K., 1965, *ibid*, **17**, 1.
- Stoddard L. G., Carson D. G., and Saito K., 1966, *Astrophys. J.*, **145**, 796.
- Tsubaki T., Tominaga S., Kubata J., and Kawaguchi I., 1964, *Publ. A. S. Japan*, **16**, 13.
- Waldmeier M., 1961., *Zs. f. Ap.* **51**, 286.
- Waldmeier M., 1965, *Zs. f. Ap.* **61**, 186.



TABLE 1

*Frequency distribution of Polar rays*

Eclipse of	Distance from the centre	0°—5°	5°—10°	10°—15°	15°—20°	20°—25°	25°—30°
1898	$r = 1.0 R_0$	NPR	3	4	3	3	2
		SPR	3	4	3	3	3
		Total	6	8	6	6	3
1922	$r = 1.0 R_0$	NPR	3	6	4	2	3
		SPR	3	2	1	1	1
		Total	6	8	5	3	5

TABLE 2 a

*Apparent angle of obliquity  $\psi$  and polar angle  $\phi$  for the north polar region in 1898 eclipse plate.*

No. of P. R.	$r=1.0R_0$		$r=1.1R_0$		$r=1.2R_0$		$r=1.3R_0$		$r=1.4R_0$		$r=1.5R_0$	
	$\psi$	$\phi$	$\psi$	$\phi$	$\psi$	$\phi$	$\psi$	$\phi$	$\psi$	$\phi$	$\psi$	$\phi$
1	-15.0	-28.0	-30.0	-30.0								
2	-17.0	-25.5	-27.0	-28.0								
3	-18.5	-24.0	-24.0	-26.5								
4	-19.0	-20.5	-24.5	-24.0								
5	-18.0	-20.0	-22.0	-22.0								
6	-14.0	-18.0	-21.5	-20.5	-34.0	-22.5						
7	-15.5	-14.0	-20.5	-16.0								
8	-17.0	-11.0	-19.0	-13.0	-20.0	-15.0	-20.0	-16.5	-20.0	-18.0		
9	-12.5	-8.5	-17.0	-10.5	-19.0	-11.5	-21.5	-13.0	-22.0	-15.0		
10	-9.0	-6.5	-13.5	-7.5	-18.0	-8.5	-21.0	-10.5	-27.5	-12.0		
11	-8.0	-4.5	-14.0	-5.5								
12	10.0	1.0	1.0	0.0								
13	8.0	3.0	2.0	2.0	0.0	2.0	6.0	3.0	10.0	3.0	11.5	4.0
14	3.0	3.0	2.5	3.0								
15	2.5	7.0	6.0	8.0	8.0	8.5	10.5	9.0	12.0	9.5	13.0	10.5
16	5.0	8.5	8.5	9.0								
17	5.0	9.5	9.5	10.5	14.0	11.5	15.0	12.5	15.0	14.0	14.0	15.0
18	12.0	10.5	17.0	12.0								
19	16.0	12.0	21.0	13.5								
20	24.0	21.0	28.0	24.0								

TABLE 2b

*Apparent angle of obliquity  $\Psi$  and polar angle  $\phi$  for South polar region on 1898 eclipse plate*

No. of P.R.	$r=1.0 R_0$		$r=1.1 R_0$		$r=1.2 R_0$		$r=1.3 R_0$		$r=1.4 R_0$		$r=1.5 R_0$		$r=1.6 R_0$	
	$\Psi$	$\phi$	$\Psi$	$\phi$	$\Psi$	$\phi$	$\Psi$	$\phi$	$\Psi$	$\phi$	$\Psi$	$\phi$	$\Psi$	$\phi$
1	21.5	27.5	23.5	30.0										
2														
3	21.5	24.5	22.0	27.5			18.5	33.0	19.0	34.6	22.0	36.0		
4					15.0	28.5	17.0	30.0	18.0	31.2	20.0	32.5		
5	20.0	21.5	23.0	24.0										
6	20.5	20.0	26.0	22.0										
7			20.0	20.0										
8	19.0	15.5	22.5	17.0										
9	16.0	15.0	20.0	17.0			10.0	11.0	6.0	16.5	6.5	17.0	10.0	17.5
10														
11	20.0	13.5	11.5	15.0										
12	5.0	9.0	15.0	10.0										
13							4.0	9.5	8.0	10.0	14.0	11.0		
14	1.0	1.0	2.0	1.0	3.0	1.5	5.0	6.2	4.5	7.0	5.0	7.5		
15							5.0	1.5	9.0	2.0	15.0	3.0		
16	3.0	1.5	3.0	2.0	3.0	2.0	2.5	2.5	5.0	2.5	7.0	3.0	10.0	3.0
17	4.0	4.0	6.0	4.5	3.5	4.5	5.0	4.5	9.0	5.5	13.5	6.0	18.0	7.0
18	10.0	5.0	11.0	6.5	6.0	5.0	8.0	5.1						
19							6.5	8.5	9.5	9.0	13.0	10.0	25.0	11.0
20														
21	12.0	7.0	14.5	8.5										
22	16.5	9.0	17.0	11.0										
23					8.0	12.5	10.5	13.5	11.0	14.5	13.0	15.5	16.5	16.0
24	16.0	11.5	18.0	13.0										
25	16.0	13.0	15.0	15.0	15.0	16.5	13.5	17.5	14.0	18.5	17.5	19.5		
26	15.0	16.0	20.0	17.0										
27					14.0	21.0	19.5	22.0	23.0	24.0	28.5	26.0		
28	20.0	23.5	21.0	25.5	24.0	27.5	26.5	29.5	30.5	32.0	39.0	34.5		
29	19.5	24.5	20.0	27.0	23.5	29.0	28.0	31.5	35.0	34.0	41.0	37.5		
30	18.0	26.0	23.5	29.0	26.5	31.0	32.0	33.5	38.0	37.0	49.0	41.0		

TABLE 5a

*Apparent polar angle  $\zeta$  and angle of obliquity  $\psi$  of polar rays on 1922 eclipse plate (North polar rays)*

Ray No.	$r = 1.0 R$		$r = 1.1 R$		$r = 1.2 R$		$r = 1.3 R$		$r = 1.4 R$		$r = 1.5 R$	
	$\psi$	$\zeta$	$\psi$	$\zeta$	$\psi$	$\zeta$	$\psi$	$\zeta$	$\psi$	$\zeta$	$\psi$	$\zeta$
1	-32.0	-24.6	-35.0	-28.4	-38.0	-32.0	-41.0	-35.7				
2	-35.0	-22.2	-36.0	-26.2	-36.5	-29.7	-37.5	-33.0				
3	-32.5	-20.2	-34.0	-23.7	-35.0	-27.0	-36.5	-30.5	-36.5	-33.5		
4	-29.0	-17.5	-30.0	-20.5	-30.5	-23.4	-31.5	-26.0	-32.5	-28.5	-20.0	-25.4
5	-21.0	-14.5	-22.5	-16.7	-24.0	-18.8	-25.0	-21.0	-27.0	-23.2	-24.0	-21.7
6	-19.5	-12.6	-20.0	-14.7	-21.0	-16.6	-22.0	-13.2	-23.0	-20.0		
7	-11.0	-11.5	-14.0	-12.8	-15.0	-14.2	-16.0	-15.5	-17.0	-16.8		
8	-8.5	-9.6	-10.0	-10.5	-13.0	-11.6	-14.5	-12.7	-16.0	-14.0		
9	-3.5	-8.0	-6.0	-8.8	-10.0	-9.0	-12.0	-10.6	-14.0	-11.6		
10	-3.0	-5.2	-4.5	-5.5	-6.0	-6.0	-7.5	-6.5	-8.5	-7.3	-9.0	-9.0
11	-3.5	-1.4	-3.0	-1.7	-2.8	-1.7	-3.0	1.7	-2.0	-2.0	-1.5	-1.5
12	-0.0	0.5	0.5	0.7	1.0	1.0	1.5	1.0	2.0	1.1	3.0	3.0
13	3.0	2.6	5.0	3.0	6.5	3.5	7.0	4.0	8.5	4.5	10.0	10.0
14	12.0	5.7	12.5	6.7	13.0	8.0	15.0	9.2	15.0	10.0		
15	14.0	8.8	14.0	10.1	14.5	11.2	15.5	12.5				
16	15.5	10.0	15.0	11.5	16.2	12.6	18.0	14.2				
17	18.0	12.0	19.0	14.0	22.0	15.6	24.0	17.6	25.5	19.5		
18	18.0	15.6	20.0	17.5	23.5	19.5	29.0	21.5	31.5	24.2		

TABLE 3b

*Apparent polar angle  $\varpi$  and angle of obliquity  $\psi$  of polar rays on 1922 eclipse plate (South polar rays)*

Ray No.	$r = 1.0 R_0$		$r = 1.1 R_0$		$r = 1.2 R_0$		$r = 1.3 R_0$		$r = 1.4 R_0$		$r = 1.5 R_0$	
	$\varpi$	$\phi$	$\varpi$	$\phi$	$\varpi$	$\phi$	$\varpi$	$\phi$	$\varpi$	$\phi$	$\varpi$	$\phi$
1					-33.0	-24.5	-40.0	-27.5				
2	-15.5	-18.5	-21.0	-20.5								
3					-16.5	-20.4	-28.0	-21.8	-36.0	-24.6		
4	-13.0	-11.5	-17.5	-12.8	-21.0	-14.6	-26.0	-16.4	-29.0	-18.7	-32.5	-21.0
5	-8.0	-8.5	-12.0	-9.6	-14.0	-10.8	-16.5	-12.0	-18.0	-13.5	-22.0	-15.0
6	-8.0	-7.2	-12.0	-8.0	-15.0	-9.3	-18.0	-10.5	-19.0	-12.0		
7												
8					-19.0	-7.5	-23.0	-9.4	-23.0	-9.4	-26.0	-7.5
9	0.0	0.3	0.0	-0.3	-0.5	-0.5	-14.0	-4.5	-20.0	-5.5	-17.0	-2.0
10	5.0	1.5	4.5	1.7	4.5	2.0	-3.0	-1.0	-10.0	-1.2	4.0	2.6
11	5.5	3.4	5.5	4.2	6.5	4.6	4.0	2.2	4.0	2.3	5.7	
12							6.5	5.0	7.0	5.7		
13							10.0	10.3	11.5	11.2		
14							14.0	15.5	20.0	17.0		
15							22.5	22.2	25.0	23.0		
16	31.5	22.5	29.5	25.5	23.0	23.5	24.5	25.5	25.0	27.6		
17	31.0	24.2	32.0	27.4	28.0	28.4	27.0	30.6	25.5	32.5		
					34.5	30.5	38.0	34.0				

# KODAIKANAL OBSERVATORY

## BULLETIN Number 205

### The Solar Magnetometer of Kodaikanal Observatory

J. C. Bhattacharyya

#### Abstract

An instrument capable of measurement of weak longitudinal component of magnetic fields on the sun has been designed and constructed for operation with the horizontal solar telescope and high dispersion spectrograph of Kodaikanal Observatory. Detailed features of the optical and electronic design have been discussed. The instrument uses the principle of the Babcock magnetograph and has additional facilities of simultaneous measurements of Doppler velocities and line core intensities. A photo-electric guiding attachment for the solar image has also been described. The performance of the instrument and reliability of the measurements have been discussed.

#### 1. Horizontal Solar Telescope

The new horizontal solar telescope was installed in 1960 in Kodaikanal Observatory to facilitate detailed studies of the sun. The complete optical and electronic drive system was supplied by Grubb Parsons and consists of a three mirror coelostat arrangement feeding a 38cm,  $f/90$  two element objective lens. A 35cm solar image is produced by the telescope which is followed in the optical train by a high dispersion spectrograph, that provides high resolution spectra for further refined measurements. The horizontal telescope is housed in a long underground tunnel to minimise the effects of temperature variation. The first two mirrors of the coelostat system are mounted on a tower 10 meters above ground level to avoid seeing fluctuations that originate near the ground.

#### 2. The Coelostat System

The first mirror of the coelostat, an optical flat of fused quartz of aluminised surface 61cm in diameter, is mounted in a cell with equatorial mounting arrangement and is driven by a synchronous motor geared down in such a way as to follow the sun with high accuracy. The supply frequency of the synchronous motor is 47.333 cycles nominally, which is generated by a Wein bridge oscillator with its elements in a thermostatically controlled oven. A separate tuning unit provides small adjustments needed to cope with the variations in the sun's apparent motion. The oscillator output is phase split and amplified by three power amplifiers to produce a 3 phase 440V supply with a very stable frequency.

The second coelostat mirror, identical to the first is also equatorially mounted and has independent remote controlled slow and fast movements around two perpendicular axes, that enable the observer to move and centre any part of the solar image on to the spectrograph slit.

The third mirror located at the bottom of the tower is again a 61cm optical fused quartz flat, but fixed at an angle of  $45^\circ$  to the vertical so as to render the beam from the tower coelostat mirrors horizontal along the axis of the 60 metre long underground tunnel.

### 3. The Imaging System

The horizontal solar beam falls on a 38 cm diameter, two element achrom objective lens with a focal length of 36 meters. Anti-reflection coating of a thin film of magnesium fluoride is provided on the lens to reduce light loss by reflection at the two surfaces. The lens is mounted on a remote controlled traction carriage to enable carrying out small changes in focussing when working at extreme edges of the spectrum. To facilitate visual inspection, the solar image is focussed on a white metal screen, which forms the end plate of the 18 metre diffraction spectrograph.

### 4. The Spectrograph

The high dispersion spectrograph consists of a large plane reflection Babcock grating in a Littrow arrangement. The grating has an area of 153 mm  $\times$  203 mm which gives 600 lines to the millimetre and is blazed in the fifth order at 5000  $\text{\AA}$ . The Littrow lens is a 20 cm, f/90 two element achromat with a focal length of 1800 cm, and is mounted on a remote controlled traction carriage. The dispersion and spectral resolution are extremely high; in the fifth order green, where it is blazed, a dispersion of 9 mm/ $\text{\AA}$  is obtained with a resolving power of 600,000.

### 5. Theory of Measurement

The longitudinal component of solar magnetic field is measured from the Zeeman splitting of certain Fraunhofer lines. In the direction of the magnetic field, most of the spectral lines split up into two components, both circularly polarised, but in opposite sense. The shift in wavelength of each component is related to the magnetic field strength by the following relation :

$$\Delta\lambda = 4.67 \cdot 10^{-5} g \lambda^2 H \quad \dots (1)$$

where  $\Delta\lambda$ ,  $\lambda$  are in cms,  $H$  is in gauss and  $g$  is in the Landé splitting factor for particular line. The shift, as may be seen, is extremely small for small magnetic fields and cannot be detected photographically or even by the usual photoelectric arrangements. The two components remain unresolved even for moderately strong fields; in that case, the line appears a trifle broadened. If, however, by introducing a quarter wave plate and a polariser, one of the circularly polarised components is removed, the other component will be seen and the line will appear shifted.

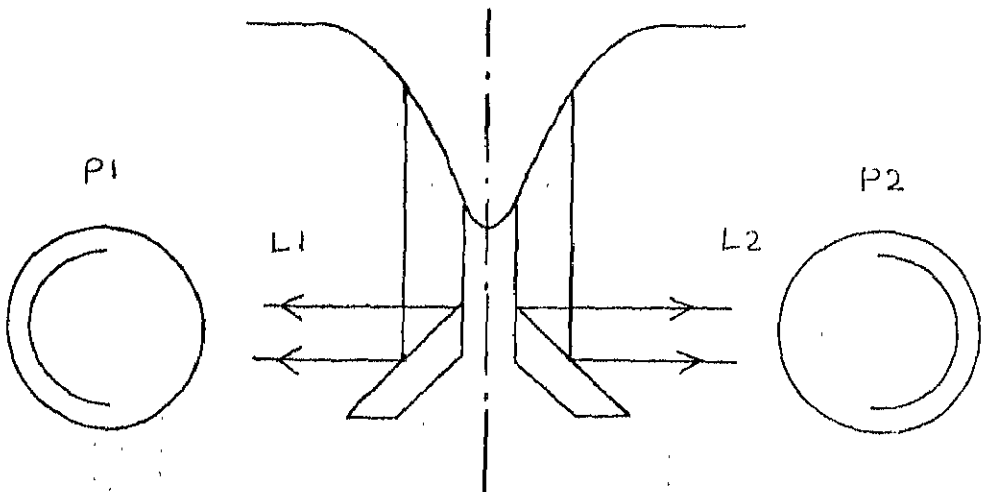


Fig. 1

If one sets up an arrangement as shown in Figure 1, which separates the light from the two wings of a line into components  $L_1$  and  $L_2$ , the difference  $\Delta L = L_1 - L_2$  will be zero if the line is properly centred, but introduction of a circular polarisation analyser will result in a fractional change,

$$\frac{\Delta L}{L} = 4.67 \cdot 10^{-5} \frac{1-R}{1+R} \frac{2}{B} g \lambda^2 H \quad \dots \quad (2)$$

in a Zeeman affected line,  $R$  being the residual intensity at the centre of the line and  $B$  the half width of the line, assuming a straight triangular profile. If the light is received on two photomultiplier tubes of identical and linear response characteristics, then a small change in photomultiplier output current  $\Delta i$  should result with the introduction of a circular polarization analyser given by :

$$\frac{\Delta i}{i} = 4.67 \times 10^{-5} \frac{1-R}{1+R} \frac{2}{B} g \lambda^2 H \quad \dots \quad (3)$$

where  $i$  is the mean current delivered by the photomultipliers receiving light from the wings of the spectral line under investigation.

The difference current  $\Delta i$  is extremely small for low values of magnetic field and cannot be unambiguously determined with the normal d.c. amplification techniques. Connecting two photomultipliers receiving light from the two wings in a differential arrangement doubles the difference, but even then the signal current is very small and completely submerged in the noisy photomultiplier output currents. To amplify the signal out of the noise background, a selective amplification technique is employed. To achieve this, an electro-optic modulation arrangement is used. A mounted crystal of ammonium di-hydrogen-phosphate (ADP) has the property of becoming birefringent when an electrical potential gradient is applied across it. When an appropriate voltage is used, the crystal behaves as a quarter wave plate. Used in conjunction with a polariser, it serves as a circular polarisation analyser. By reversing the polarity of the voltage, the combination changes from a right to left circular polarisation detector or vice-versa. If an alternating voltage of appropriate magnitude is applied across the ADP, the combination behaves as an oscillating circular polarisation analyser. When such a system is introduced in the beam the right and left circularly polarised light are cut off in alternate half cycles. The differential output of the two photomultipliers thus contains a single frequency signal whose amplitude is proportional to the longitudinal magnetic field. This when channelled through narrow band selective amplifiers, rises above the noise level and makes it possible for being recorded after suitable further amplification, filtering and synchronous detection.

## 6. The Magnetometer Detector Head

For measurement of weak solar magnetic fields, therefore, it is necessary to measure the wings of a Zeeman sensitive spectral line with a precise photoelectric set up. The high dispersion and spectral resolution required for this purpose is provided by the spectrograph. The photoelectric detector head consists of a combination of two adjustable slits  $S_1$  and  $S_2$ , so that if a spectral line of proper width is allowed to fall on them, the wings will be reflected to two photomultipliers  $P_1$  and  $P_2$  while the core will pass through to the third photomultiplier  $P_3$  as in Figure 2. The slit  $S_1$  is a standard Hilger bilateral slit of length 18 mm and adjustable upto a maximum width of 1800 microns. The slit  $S_2$  is a bilateral arrangement of two optically worked reflecting jaws of speculum, coated with Aluminium in a vacuum deposition chamber at a precisely controlled rate. This is adjustable upto a maximum width of 1500 microns.  $S_2$  is mounted on a table controlled by a precision screw which allows accurate alignment of the two slits in respect of the beam coming from the spectrograph.



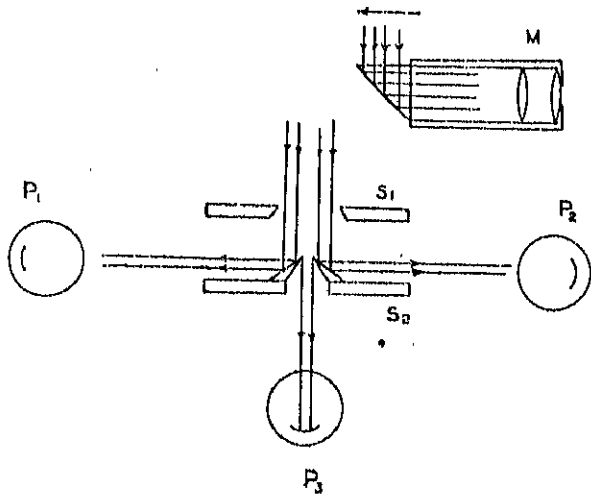


Fig. 2

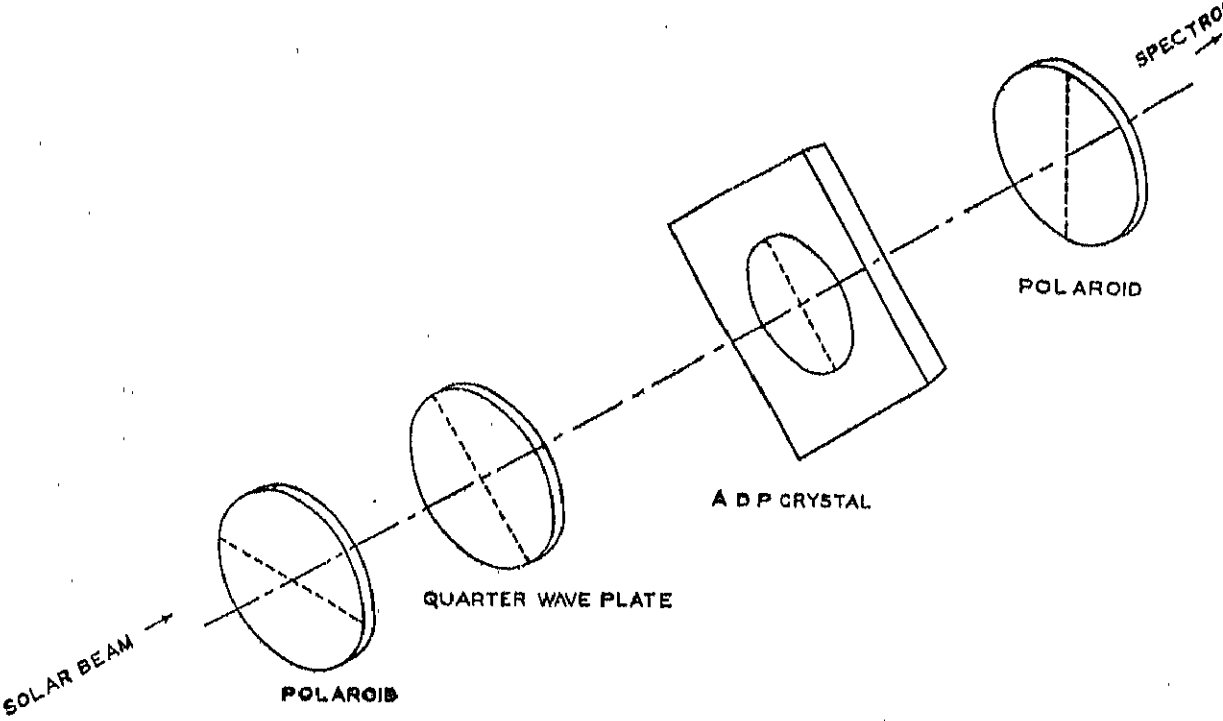


Fig. 3

The three photomultipliers  $P_1$ ,  $P_2$  and  $P_3$  are RCA 1P21 photo tubes with S-4 cathode surfaces. The photomultipliers  $P_1$  and  $P_2$  form a matched pair selected from about 2 dozen tubes and show almost identical characteristics. To improve their signal to noise ratio characteristics, they are operated with double the normal stage voltages across the cathode and the first dynode and slightly reduced voltage between the ninth dynode and anode. The photomultiplier  $P_3$  is provided with equal voltages at all stages, the potential divider chain being located at the base of the tube. But the supplies to tubes  $P_1$  and  $P_2$  are independently given to individual electrodes by means of multicore cables, voltage division being controlled by elaborate networks on the main instruments rack. The outputs of the two "wing" photomultipliers  $P_1$  and  $P_2$  are taken out by a pair of shielded cables for feeding into the difference amplifier. A small monitor viewer M, consisting of a total reflecting prism and an eye-piece, is mounted on a draw tube which can be brought in or out of the beam by manual operation. The monitor helps identification of the spectral region and approximate centering of the line on the slit combination.

### 7. The Electro-optic Modulator

The heart of the electro-optic modulator is a Baird Atomic mounted ADP crystal type AM-2 with optically transparent NESA electrodes. The mounted crystal is fixed on an adjustable stand and introduced in the solar beam just before the spectrograph entrance slit. A polaroid is also fixed on a rotatable frame following the ADP. The stand has facilities for accommodating a fixed circular polariser for converting the equipment for velocity recording and for calibrating the scale of the instrument as explained later. Two separate heavily insulated conductors supply the 2500 volt A.C needed for the crystal to switch  $\pm \lambda/4$  retardation between the two polarised components of the light beam.

The emergent light is completely polarised in the direction of the polaroid axis; for the sake of optical efficiency it should be parallel to the grating ruling, which is vertical in our set up. The orientation of the polaroid is hence fixed, and the ADP crystal orientation adjusted with respect to this so that the direction of the optic axis of the crystal remains at angle of  $45^\circ$  to the polaroid axis. As the direction of the optic axis of the crystal is known from the manufacturers specification as being parallel to one of the sides, the crystal is mounted with its sides at one angle of  $45^\circ$  to the vertical. A schematic arrangement of the different elements of the modulator is shown in Figure 3.

### 8. The Electronic Design

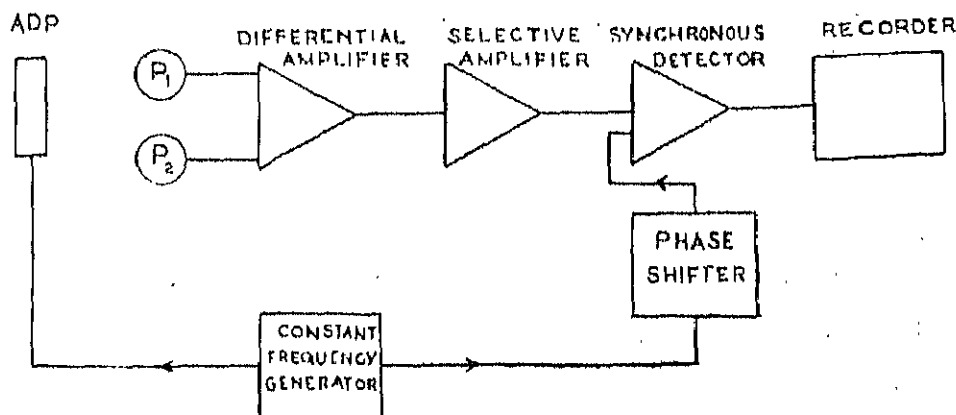


Fig. 4

The electrical arrangement for modulation, selective amplification and detection is shown schematically in Figure 4. The modulating frequency employed in this instrument is 125 Hz, obtained from a crystal controlled oscillator and a scaler chain. The

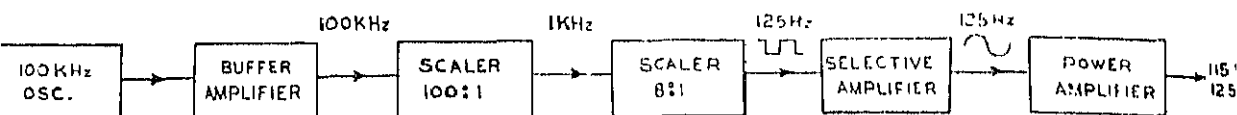


Fig. 5

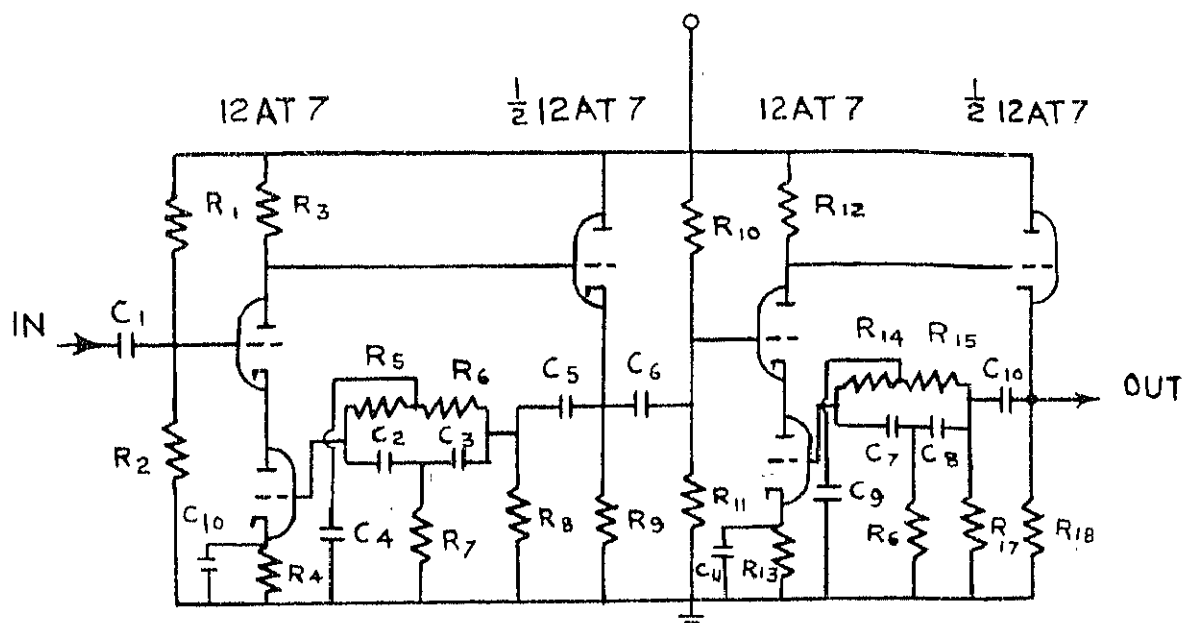
constant frequency generator unit consists of a 100 KHz quartz oscillator, a buffer amplifier, two scaler units providing a scale of 800 and giving a square wave of frequency 125 Hz, an active filter comprising of a selective amplifier at 125 Hz and finally a push-pull Class AB power amplifier delivering 40 Watts at 115 volts. The whole set up is shown schematically in Figure 5. The output of this constant frequency generator feeds two transformers, the first one supplying 2500 V to the optical modulator and the second, chopper vibrator through the phase shifter unit.

The difference amplifier used is a DA-102 low level differential amplifier manufactured by EPSCO Inc. U.S.A. This accepts two inputs and amplifies the difference by means of a Wheatstone bridge network and a cascode input stage. For obtaining a flat response from DC to 200 KHz, it divides the DC and very low frequency signals from others and amplifies by a separate chopper stabilised amplification system. In the final output the two channels are combined together. Common mode rejection is high, the rejection ratio at 125 Hz being 50,000 to 1. Differential gain is adjustable from 100 to 2000 in five steps. The bandwidth is inversely proportional to gain, the gain band width product being equal to 20 MHz. The equivalent noise input being less than 3 microvolts r.m.s., the amplifier is ideally suitable for amplification of low photomultiplier signals. Simultaneous amplification of the DC with the 125 Hz signal frequency permits D.C. to be separated at the output and is used for operating a servo system that keeps the line continuously centred on the double slit of the photomultiplier detector head.

The selective amplifier consists of two stages. The individual units are of a cascode input stage with a twin-T rejection network in its feed back loop. Figure 6 shows the circuit diagram of this stage. Use of a cathode follower in the feed back path improves the frequency response characteristics, the half power points being less than 5 Hz away from the centre frequency of 125 Hz. Use of high precision, high stability components in its construction has made the amplifier intrinsically very stable.

The phase sensitive synchronous detector employs an electro-mechanical single pole 2-way chopper driven at the synchronous frequency of 125 Hz. The circuit arrangements are shown diagrammatically in Figure 7. The four-pole, six-way switch can select 6 different R.C. combinations to vary the time constant of the synchronous detector. The values of the time constant which can be chosen this way are 0.3, 1.1, 2.8, 6.8 and 11 seconds. Feeding into the detector is done through a cathode follower stage with D.C. coupling and the output is obtained from a pair of balanced cathode followers in differential arrangement. The balance point is adjustable by a precision ten-turn helical potentiometer connected between the two cathode points and the ground.

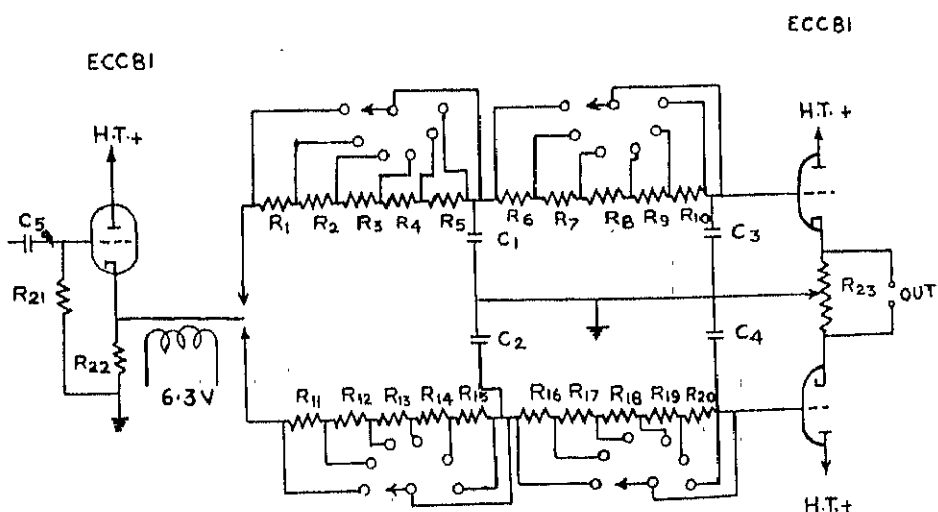
For proper adjustment of the phase sensitive detector a phase shifting arrangement for the driving voltage has been provided. The network is shown in Figure 8. The resistances are chosen in such a way that each step in the eleven point switch shifts the phase by  $18^\circ$ . The output impedance of the network is kept low, so that the connection of the chopper that draws about 100 MA at 6.3 volts does not affect the operation of the network.



$R_1, R_{10} = 2M$   
 $R_2, R_{11} = 820K$   
 $R_3, R_{12} = 150K$   
 $R_4, R_{13} = 1K$   
 $R_5, R_6, R_{13}, R_{14}, R_{15} = 10K + 2K \text{ Variable}$   
 $R_7, R_{16} = 5K + 1K \text{ Variable}$

$C_1, C_5, C_6, C_{10} = 0.11\mu F$   
 $C_2, C_3, C_7, C_8 = 0.11\mu F$   
 $C_4, C_9 = 0.22\mu F$   
 $C_{10}, C_{11} = 100\mu F, 12V.$

Fig. 6



$R_1, R_6, R_{11}, R_{16} = 85K\Omega$   
 $R_2, R_7, R_{12}, R_{17} = 240K\Omega$   
 $R_3, R_8, R_{13}, R_{18} = 470K\Omega$   
 $R_4, R_9, R_{14}, R_{19} = 1M\Omega$   
 $R_5, R_{10}, R_{15}, R_{20} = 1M\Omega$   
 $R_{21} = 1M\Omega$   
 $R_{22} = 5K\Omega$   
 $R_{23} = 10K \text{ turn helipot}$

$C_1, C_2, C_3, C_4 = 4\mu F$   
 $C_5 = 0.1\mu F$

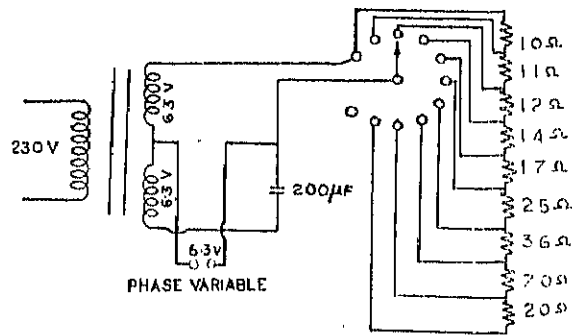


Fig. 8

9. Auxiliary Electronic Equipment

The recorder used is a Honeywell Brown potentiometric strip chart recorder with a standard resistance box connected across its input terminals. The recorder has a full scale sensitivity of 10mV with a response time for full scale deflection of 1 sec. The chart used is of standard 10 inch width being drawn at the rate of either 0.5 inch/min. or 2 inches/min. depending on the requirement. The output stage of the synchronous detector is kept slightly off-balance, so that the zero can be located at the centre of the chart.

The output of the central photomultiplier tube is amplified directly by a D.C. electrometer amplifier\* and recorded on a second strip-chart recorder. To smooth out the noise fluctuations of the photoelectric output current, an R.C. network of time constant 1 sec. is introduced at the input of the amplifier.

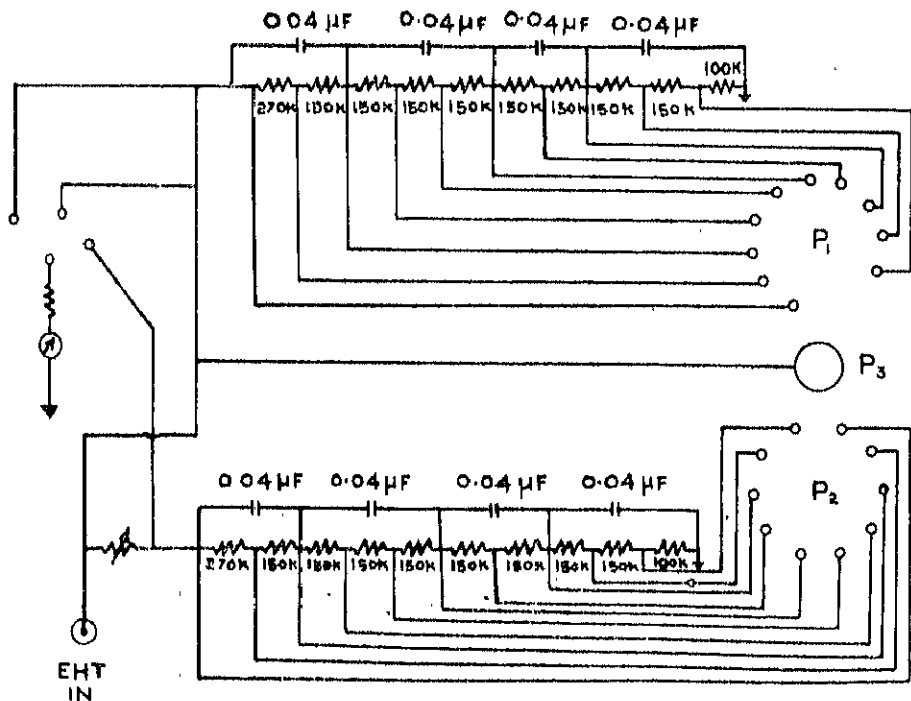


Fig. 9

\*Electrometer D. C. Amplifier and voltmeter type 1230A manufactured by Messrs. General Radio Co., U.S.A.



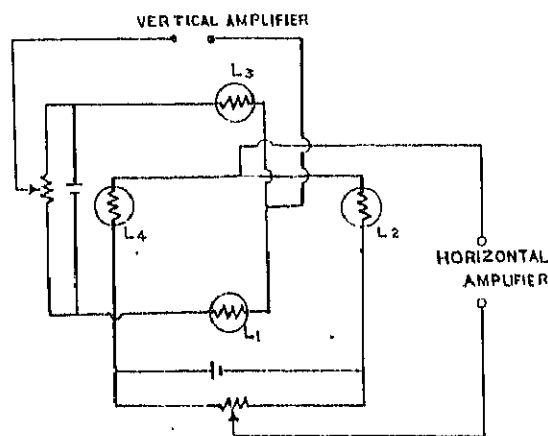


Fig. 11

### 10. The Photoelectric Guiding Attachment

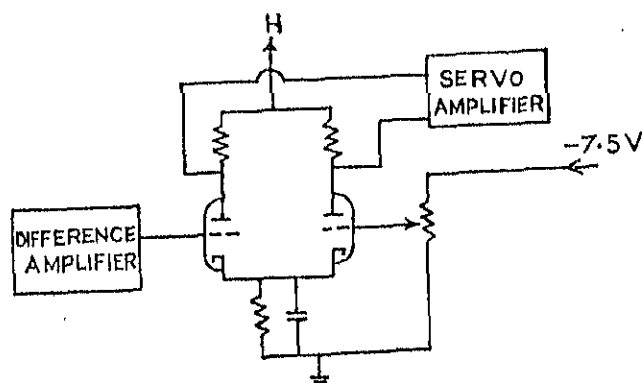
To facilitate accurate guiding of the solar image a photoelectric guiding unit is incorporated in the set up. The property of limb darkening gradient has been utilised for this purpose. Four light dependent resistors Philips type LDR are mounted behind a screen in such positions as to receive light from two perpendicular pair of diametrically opposite points near the sun's limb. Each pair of LDR is connected in a Wheatstone bridge arrangement as shown in Figure 11. After visual initial centering of the solar image, the two bridges can be balanced by using the respective potentiometers. The unbalance voltages are detected by the vertical and horizontal deflection amplifiers of the Dumount D.C. oscilloscope which deflects the cathode ray spot on the screen according to the unbalance voltages in corresponding directions. Because of strong gradients of solar limb intensities, any small shift of the solar image result in appreciable unbalance voltages, which can be corrected by recentering the image by operating the guide buttons of the coelostat arrangement.

The arrangement is useful in cases where observations are made not too close to the solar limb. The frame holding the LDRs do not permit the light from the limb to enter the spectrograph. The frame is capable of movement in two perpendicular directions controlled by two fine precision screws. Two calibrated sensitive dial gauges are used to determine the positions and movements of the frame, where such movements become necessary in cases of long continuous observations at a point, to compensate for solar rotation during the period of observation.

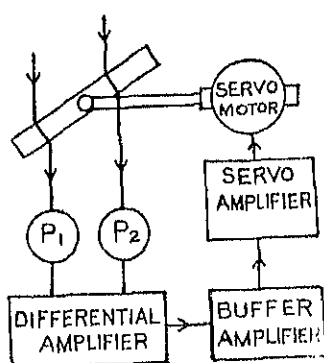
### 11. Automatic Doppler Compensator Unit

For measurement of longitudinal magnetic fields, it is necessary that the spectral line should remain properly centred on the double slit during observations extending over different parts of the solar surface and time. There exists considerable amounts of Doppler shifts of all spectral lines originating from different parts of the solar disc as a result of solar rotation and a variety of large and small scale motions. The quasi-periodic variations in Doppler shifts of lines originating from a fixed area is also well known. If not properly compensated, the spectral line is apt to get shifted from the central position during the observation, thereby introducing errors in the determined values. An automatic Doppler compensating arrangement is hence absolutely essential for operation and is provided in this equipment.

The basic component of the Doppler compensator is a plane parallel quartz line shifter mounted just before the focal plane of the spectrograph. The plate is optically worked to an accuracy of  $\lambda/2$  and has a thickness of 3.085 mm. It is mounted on a rotatable axis which extends below through the metal frame meant for holding various attachments at the spectrograph focal plane and is connected to a two phase servo-motor.



(a)



(b)

Fig. 12

The servo-system driving the line shifter to compensate for any Doppler shift works in the following manner. Whenever the spectral line gets shifted a differential D.C. voltage is developed across the  $P_1$ ,  $P_2$  photomultiplier outputs. The EPSCO differential amplifier amplifies this difference along with any 125 Hz modulation present in the signal. At the output of the differential amplifier this amplified D.C. signal is separated, and fed into a servo amplifier through a D.C. buffer stage. The output of the servo amplifier drives the servo-motor controlling the line shifter. The arrangement is diagrammatically shown in Figure 12.

The servo amplifier used is a commercial unit employed in Honeywell continuous balance units in their strip chart recorders. The buffer stage is a simple D.C. differential amplifier whose balance can be adjusted arbitrarily. This has been found necessary while centering certain asymmetric lines of the solar spectrum and to compensate for small characteristic variation between the two parts of the double-triode used.



## 12. The Doppler Recorder

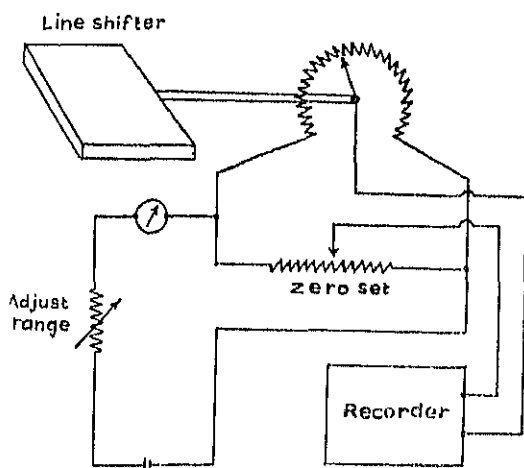


Fig. 13

A small attachment to the automatic Doppler compensator unit makes the simultaneous recording of the Doppler motion of the region possible. While the main unit determines the Zeeman splitting of the line, the automatic Doppler compensating unit keeps the line properly centred, by sensing the error voltage due to Doppler displacement and correcting the shift through a servo loop. A continuous record of this error voltage directly gives the Doppler velocity information.

The attachment basically consists of a good quality potentiometer rigidly fixed to the shaft carrying the line shifter plate. A precisely controlled current flows through the potentiometer, so that any minute movements of the slider results in small changes of the potential of the slider contact. These changes, which are proportional to the line shifter movement are recorded on a second potentiometric recorder. The electrical arrangement is illustrated in Figure 13.

It is obvious from the electrical arrangement that the scale of deflection is directly proportional to the current flowing through the potentiometer. This is of great advantage as extra amplification of the deflections can be easily achieved when recording velocity variations of small amplitudes. A simple R.C. filter is used at the recorder input to smooth out the fluctuations originating mainly from the seeing defects.

## 13. Reimaging Attachment

The solar tower equipment at Kodaikanal consisting of the horizontal telescope and the spectrograph is used on several different research projects on the sun. As such it would be difficult if the complex and heavy magnetograph head is designed to fit permanently in the standard focal plane of the spectrograph. This difficulty has been overcome by locating the magnetograph detector head at one side of the spectrograph and reimaging the spectrum on the analysing slit of the magnetograph. Changing over from the magnetographic mode of operation to the conventional photographic mode of operation requires removal of this reimaging attachment, and can be accomplished in a matter of seconds. A total reflecting prism placed just ahead of the focal plane of the spectrograph bends the beam at right angles and is reimaged by a lens of 20 cm focal length, without magnification. The lens position is adjustable for accurate focus, which can be monitored at the detector head on which the spectra are reimaged. A light tight mount for 5 cm x 5 cm is provided in this unit to enable working in the higher order spectra by interposing suitable filter combinations to cut out the unwanted overlapping orders.

#### 14. Instrument Characteristics

For proper evaluation of the readings obtained by the instrument described above, a thorough controlled calibration and checking of various key units as well as the instrument as a whole is essential. The method and results of such operations are now described in the following paragraphs.

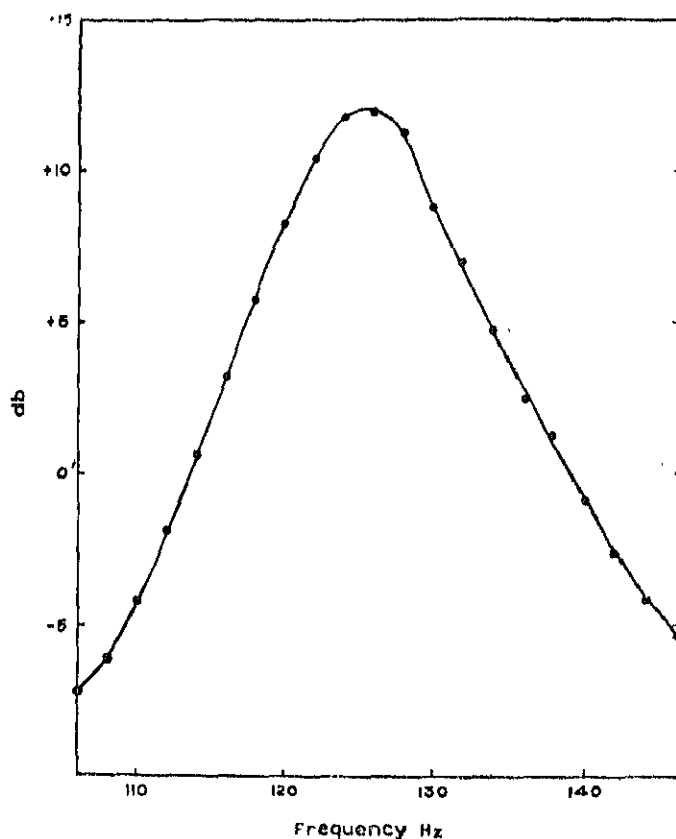


Fig. 14

The gain-frequency characteristics of the selective amplifier is a factor which determines the minimum signal detectable by the instrument. For the sake of proper maintenance of the instrument, it is preferable to have this checked periodically. Facilities are provided in the equipment for doing this. Output of a laboratory standard oscillator is fed through a calibrated attenuator to the input of the selective amplifier, the input from the differential amplifier being removed and the output measured directly on the cathode ray oscilloscope screen. An alternate path by-passing the amplifier is made for measuring the input on the same scope. The output/input ratios are measured at frequencies around the operating frequency. Figure 14 shows the gain-frequency characteristics of the selective amplifier used in our equipment.

The linearity characteristics of the entire amplifier-detector chain is extremely important, as variations in this may introduce large errors in our measurement. This is checked by the following arrangement. The input to the differential amplifier is removed and a small fraction of the generator voltage fed instead, through the calibrated attenuator. The output is directly measured on the recorder, taking care to keep the phase of the synchronous detector reference voltage properly adjusted. Measurements are

done at various input levels and the input vs output characteristics determined. Reversing the input connections permits obtaining the points on the negative side. Any non-linearity, if obtained has to be corrected by adjusting the biases of the different amplifier and cathode follower tubes. This has been done by a trial and error method in the first instance, and use of high stability components has reduced the probability of shifts later. In any case the original linearity characteristics are kept as a reference and subsequent periodic measurements compared with the same. Figure 15 shows the linearity characteristics of the equipment.

Differential Amplifier  
Gain setting: 1000

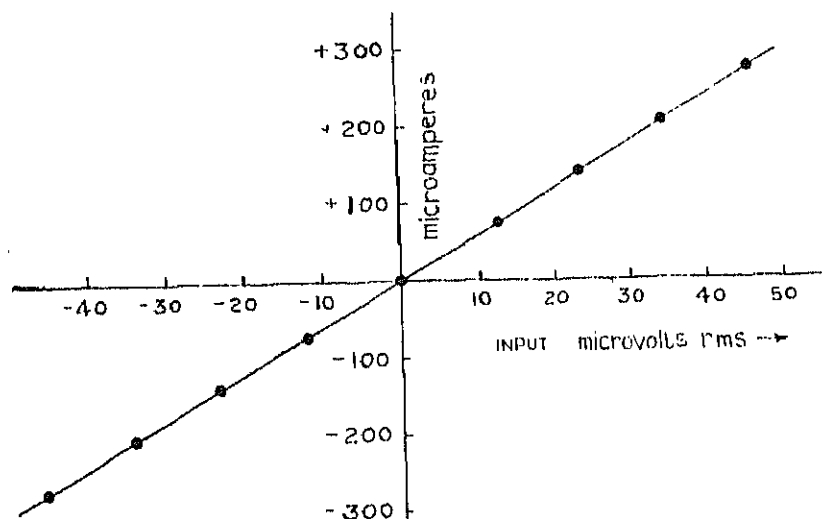


Fig. 15

The light passing through the ADP polaroid assembly is completely polarised and the final output has large variations for different orientations of the grating ruling and photo-cathodes. Since the orientation of the grating ruling is fixed with respect to the photomultiplier cathodes in our set up, it is necessary to know the variation of the photo-electric output for different orientations of the ADP-polaroid assembly, to enable one to adjust the instrument for optimum response. This has been done by noting the third photomultiplier response for different orientations of the assembly. Figure 16 shows the transmission characteristic for different orientations of the assembly; angles are measured from the vertical, and the response is symmetrical about this axis. The variation is quite large and is of the order of 40 per cent of maximum response between two extreme orientations at right angles. It may be noticed that the ADP-polaroid assembly blocks a major part of the incident light. The loss is inherent in the arrangement: the maximum transmission is only 44 per cent in the present set up.

For accurate measurements, it is essential that the linear drift of the output should be a minimum. From systematic studies it has been seen that the equipment almost completely stabilises after half-an-hour's warm up time. During observations, care is taken not to record data before such stabilisation is achieved.

Stabilisation of the photomultipliers, however, is much more difficult to obtain. There is a tendency for large differential drifts to occur after the EHT is switched on,

which may require hours to come down to a reasonable value. To avoid such drifts the photomultiplier voltages are kept on during the observing period lasting over days. The photomultiplier pair is balanced at the beginning of each observation by focussing a portion of the continuum on the slit pair, and the balance checked at the end of observation.

Adjustment of the reference voltage phase can be done without ambiguity by looking at the G.R.O. waveforms at the electromechanical chopper outputs. The phase once adjusted does not require frequent changes. The phase need be checked at the beginning of a day's observation or when optical adjustments are altered.

### 15. Doppler Mode Operation

The electronic amplification and detection arrangement is extremely sensitive to even a trace of the signal modulated at the operating frequency. By a simple optical arrangement it is possible to introduce signal frequency modulation to any spectral line, irrespective of whether Zeeman polarisation of the wings is present or not. When a fixed circular polariser is placed in front of the ADP-polaroid assembly, the light falling on the electro optic modulator is totally circular polarised, and the effect of the oscillating detector is to modulate the total light falling on the spectrograph. When a symmetrical spectral line is properly centred the differential output of the two wing photomultipliers is zero. A slight shift of the line produces a non-zero output, as explained earlier. When the total light is modulated at the signal frequency, as a result of putting a fixed circular polariser ahead of the ADP-polaroid assembly, the differential output is also modulated. This is amplified by the selective amplifier and detected by the synchronous detector, with extreme high sensitivity. The equipment, under these conditions, is said to operate in the "Doppler mode". Even a minute shift of the line is detected and recorded by this arrangement.

The shift of any spectral line results in a differential output of the two photomultipliers that receive light from the wings. The proportionate change in the differential photomultiplier output is given by:

$$\frac{\Delta i}{i} = \frac{v\lambda}{c} \frac{1-R}{1+R} \frac{2}{B} \quad \dots \quad (4)$$

where  $v$  is the line of sight component of velocity of source and  $c$  is the velocity of light expressed in the same units; the other symbols representing the same parameters as in Equation (3).

### 16. Calibration

The possibility of operating the instrument in the Doppler mode provides a convenient way of calibrating the records. The sun's disc as imaged by the telescope can be used for this purpose. It is known that the axial rotation of the sun on its equator results in a linear velocity of 2 Km/sec. On the east limb this results in a blue-shift of the lines of equivalent amount and on the west limb it results in a red-shift and of equal magnitude. If any spectral line is centred on the double slit illuminated by the light from the centre of disc, and the instrument is operated in the velocity mode, the output would be zero, nominally. If, now the image is moved so that a point on the east limb illuminates the spectrograph slit, some non-zero detector output will be obtained. By moving the image similarly in the other direction, an output of equal magnitude, but of opposite sign should result. On the recording chart the pen will deflect from one side to another for such movements of the image and the difference between the two deflections will be equivalent to a Doppler shift of 4 Km/sec. This can be used as the calibration standard provided certain other difficulties are properly taken care of.

The first difficulty one encounters is the random shifts of the spectral lines, resulting in an unsteady output. The effect is most pronounced at the centre of the solar disc, but very much less at the limbs, at least for some lines. For such lines one can get reasonably steady deflections for the two limb positions. For others it is necessary to take a large number of readings at the two positions to work out a mean value.

The fall in light intensity near the limbs also require correction. The electrical signal as per equation (4) is proportional to the product of the Doppler shift and the mean intensity. To compensate for this it is also necessary to know the proportionate reduction of intensity in the nearby continuum at the calibration points on East and West limb positions. In the present equipment, facilities already exist for measuring the line core intensity simultaneously and this can be utilised for applying this correction. The centre to limb variation of the line profile can be neglected without much loss in accuracy for most of the Fraunhofer lines.

With the above two corrections, it is possible to determine the scale coefficients of the instrument for individual lines. The deflection 'd' obtained in our instrument can be represented by a general equation :

$$d = K \cdot v \cdot I \quad \dots (5)$$

where v is the line of sight velocity, say in meters/sec., I is the intensity of the adjacent continuum and K is the instrument constant working under certain conditions. Suppose D is the difference of the two deflections at the calibration points which are taken close to the limb on the solar equator, and whose theoretical Doppler velocities differ by M meters/sec. (which is close to 4000 meters/sec.) and I' is the intensity of the adjacent continuum at those points, then

$$D = K \cdot M \cdot I' \quad \dots (6)$$

Eliminating K, between equations (5) and (6) one gets,

$$v = M \cdot \frac{I'}{I} \cdot \frac{d}{D} \text{ meters/sec.} \quad \dots (7)$$

The value of M can be calculated from the geometry of the calibration positions and the previously determined values of solar rotation. The ratios I'/I and d/D can be directly measured and thus the value of v for different deflections calculated.

The direction of the velocity vector component can be determined by noting that the velocity of a point on the east limb is approaching the observer on earth and may be taken as negative and that of the point on west limb as positive. The deflections on the chart can thus unambiguously indicate the direction of the velocity component.

The same value of calibration constant can be used for magnetic field measurements. Only it is necessary to know the equivalence of the Doppler and Zeeman shifts of particular lines. Also, because in the Doppler mode an additional fixed circular polariser is introduced in the beam, its transmission properties are also to be taken into account.

The line generally used for the magnetic field measurements is the FeI line of  $\lambda = 5250.218\text{\AA}$  with a Lande' factor of 3. Substituting these values in equation (1) the separation of the two longitudinal Zeeman components becomes :

$$\begin{aligned} \Delta\lambda_H &= 2 (4.67 \cdot 10^{-6} g \lambda^2 H) \\ &= 7.72 \times 10^{-6} H \end{aligned} \quad \dots (8)$$

where  $\Delta\lambda_H$  is expressed in  $\text{\AA}$  and H in gauss.

The Doppler shift of the same line is related to the line of sight velocity by the relation,

$$\begin{aligned}\Delta\lambda_v &= \frac{\lambda}{c} v \\ &= 1.75 \cdot 10^{-5} v\end{aligned}\quad (9)$$

where  $\Delta\lambda_v$  in  $\text{\AA}$  and  $v$  is in meters/sec. So other things remaining equal, the equivalence between the Doppler and longitudinal Zeeman shifts is given by,

$$\begin{aligned}1.75 \cdot 10^{-5} v &= 7.72 \times 10^{-5} H \\ \text{or, } H &= 0.225 v\end{aligned}\quad (10)$$

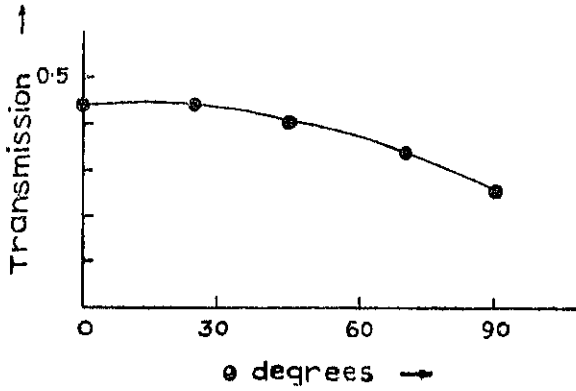


Fig. 16

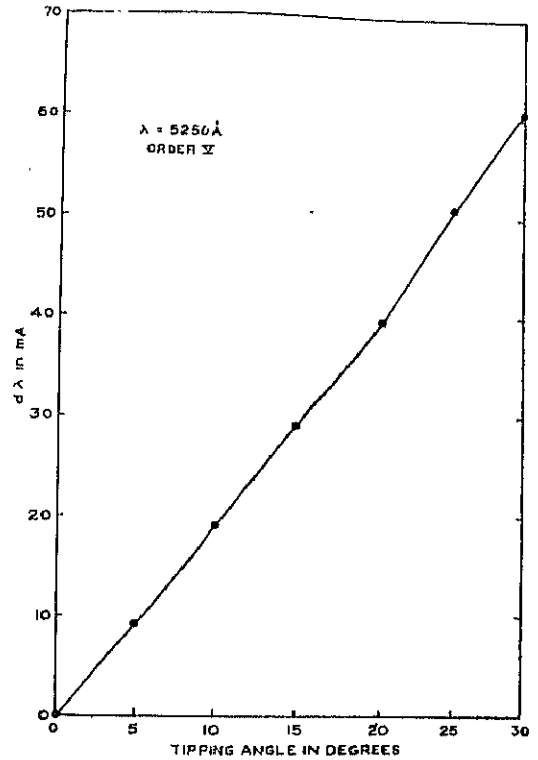


Fig. 17

But as we have to introduce a fixed circular polariser in front of the electro-optic modulator, the light transmitted in the Doppler mode is usually a fraction of that in the magnetic mode. If we designate this fraction as  $p$  the final relation between the two quantities will be given by :

$$H = 0.225 p.v. \quad (11)$$

$H$  being obtained in gauss when  $v$  is in meters per sec.

It may be mentioned that the value of this fraction  $p$  is highly dependent on the relative orientation of the two polaroid axes. To avoid any error due to this, the value of the transmission fraction is determined separately for every magnetic record by noting the third photomultiplier readings with and without the circular polariser and actual orientation of the two elements in the optical modulator.

An alternative method of calibration is by the use of the parallel plate line shifter employed in the automatic Doppler compensator unit. The lateral shift  $\delta$  of an image by a tipped parallel plate is given by the expression :

$$\delta = t \sin i \left[ 1 - \left( \frac{1 - \sin^2 i}{\mu^2 \sin^2 i} \right)^{\frac{1}{2}} \right] \quad \dots \quad (12)$$

where  $t$  is the thickness of the parallel plate,  $\mu$  its refractive index and  $i$  the angle between the normal to the parallel plate and the direction of light beam. The thickness and the refractive index of the parallel plate is known, and the tipping angle can be accurately measured on the scale provided. Thus it is possible to produce known shifts of any spectral line by manipulating the line shifter. Since the linear dispersion of the spectrograph is known with high precision, the lateral shifts can be converted into equivalent wavelength shifts of any particular line. A plot of the wavelength shifts for different tipping angles for the line FeI 5250.218A is shown in Figure 17.

The procedure for calibration is as follows:

By using an auxiliary lens the solar image is defocussed so that the light entering the spectrograph does not exhibit the granulation stimulated periodic component of Doppler motions. The equipment is run on the Doppler mode with automatic Doppler compensation unit disabled and the spectral line in question is centred on the double slit as judged from the null output on the recorder. The line shifter is then tipped by a known angle and the resulting deflection on the chart noted. The third photomultiplier reading is also noted for the purpose of the computation. The process is repeated for several tipping angles, and results plotted. The plot indicates the scale of deflection for different wavelength shifts which can be converted into equivalent Doppler velocities. From these values the instrument constant  $K$  can be directly calculated, enabling one to estimate values of Doppler velocity directly from the chart readings.

### 17. Sensitivity

The sensitivity or the minimum signal detectable by the instrument is basically noise limited. But apart from the noise, there are certain factors limiting the maximum value of amplification. The photomultiplier stage voltages are decided mainly from the noise considerations. The gain of the differential amplifier is adjusted on the basis of signal available. At a gain setting of 1000, for example, non-linearity sets in beyond an input 50 microvolts. The input resistance to the potentiometric recorder is adjusted to give full scale utilisation with available signal strength. It is, however, useful to have an idea of the sensitivity of the instrument under typical condition. Substituting the following typical values in equation (7)  $M=4000$ ,  $P/I=0.5$ ,  $D=90$ , the minimum detectable signal for  $d=1$  works out to be 22 meters/sec. With an equivalent noise input over the instrument pass band as 0.5 microvolt r.m.s., the root mean square fluctuation due to noise in the output is 3 microamperes, giving a deflection of less than one division on the chart. Under these conditions, a 2.8 second time-constant in the output circuit produces smooth records.

The above figures are, however, for favourable working conditions and in actual practice several other disturbing factors limits the accuracy of measurement. These are discussed in the next section.

Under favourable conditions it is theoretically possible to increase the sensitivity by as much as a factor of 10. With the differential amplifier gain setting of 100, it is possible to get a full scale deflection for some strong spectral lines, between the East-West calibration positions. After that the instrument gain can be increased to 1000 and

a sensitivity of 2.2 meters/sec per division on the chart can be obtained. The noise is somewhat higher, but can be smoothed out by 6.8 seconds network combination to an r.m.s. fluctuation of the order of one division.

For records on low magnetic fields, it is the latter combination which is usually used in this equipment. The typical value of  $p$  in equation (11) is about 0.4 so that in the most favourable conditions, an accuracy of 0.2 gauss per division can be obtained with noise fluctuations of the order of 1 division. It may be noticed that under these working conditions the instrument is capable of measuring upto  $\pm 25$  gauss before non-linearity sets in and the measurements become unreliable.

### 18. Accuracy and Limitations

The noise introduced by our amplified-detector chain is extremely small. By proper choice of tubes and voltages dividing network the two photomultipliers also introduce very little dark noise, the individual dark currents at the operating voltage of 900 V being about  $2 \cdot 10^{-9}$  A. But it is the random nature of the photo-electron cascades which limits the ultimate accuracy of the measurements. The scale of the solar image in the optical set up is  $5''.6$  per mm. and a standard spectrograph slit of width 250 microns and 1 mm length is normally used. The angular dimension of the solar disc covered by the slit is thus  $1''.4 \times 5''.6$ . At the detector head slit pair, the spectrum is reimaged without magnification and to quote a typical dimension, the wing photomultipliers view a portion of spectrum  $1\text{mm} \times 350$  microns each. In the fifth order, where it is mostly used, the dispersion is extremely high and the level of illumination at the photomultiplier cathodes is low indeed. In the Doppler mode with the fixed circular polariser introduced in the beam, a typical order of photomultiplier output current is  $10^{-8}$  A. At this level of illumination, the random nature of the photo-electron pulses dictates the limits of gain and resolution that can be achieved in the present set up.

A good spatial resolution, which is a major objective of the instrument is thus limited by the availability of the light flux. In the  $f/90$  system used the standard slit size of  $1''.4 \times 5''.6$  has been chosen after several series of experiments as the optimum dimensions seeking a compromise between spatial and time resolution and the noise error which can be tolerated. For measurement on certain weak spectral lines, it is necessary to widen and increase the slit size at the cost of resolution.

Another limiting factor encountered at Kodaikanal is the seeing at the observation site. Owing to its location on a high peak surrounded by uneven terrain, the period of good seeing at Kodaikanal is limited to only an hour or so after sunrise. For long continuous records, observations have to be carried out when the seeing was no better than 2-3 seconds of arc. Lowering the slit dimension under such conditions is obviously useless.

For experiments requiring scanning over an extended area, the rate of scan has to be chosen consistent with the time constant of the detector. Higher time constants have to be employed with higher amplifier gain, which may be necessary for weak signals, thus requiring slower rates of scan. The spatial nature of certain time varying features of weak intensity can thus be studied with limited accuracy.

### Acknowledgements

For the design and construction of this equipment valuable help and co-operation from several members of the Kodaikanal Observatory staff are gratefully acknowledged. First and foremost, grateful thanks are due to Dr. M.K.V. Bappu, Director,



for not only his constant advice and guidance during the various phases of the design and construction but also for his active participations in various experiments during the construction of the equipment. Extremely valuable help of Sarvashri A.P. Jayarajan, K.C. Abdur Raheem and K. S. Muthu in fabrication of the optical components; of M. Iqbal Ali, L. Peter, M. Paranjothi, V Germanappan and Alfred Charles in mechanical constructions and of Sistla Gopal, Satya Prakash and M. Mohd. Abbas in design and construction of electronic accessories is gratefully acknowledged. It is a pleasure to record my heartfelt thanks to Dr. V.E. Stepanov of Sayan Observatory, U.S.S.R. and to Dr. W.A. Baum of Lowell Observatory, U.S.A. for their valuable advices during their respective visits to this observatory, which have helped me to a great extent in arriving at the present design of the equipment.

Kodaikanal Observatory,

October 1970

# KODAIKANAL OBSERVATORY

## BULLETIN Number 208

### Apsidal motion in the binary Delta Orionis

V. Natarajan and R. Rajamohan

#### ABSTRACT

A velocity curve of the spectroscopic binary 'Delta Orionis' has been obtained from the spectrograms taken at Kodaikanal during the years 1968-70. The orbital elements derived are in good agreement with earlier values except for the longitude of periastron ' $\omega$ '. The period of rotation of the line of apsides is found to be 208 years.

*Key Words:* Spectroscopic binary—Delta Orionis—Apsidal motion

#### INTRODUCTION

The star Delta Orionis is a well known spectroscopic binary, which has drawn the attention of several investigators [J. Hartmann, (1904), F. C. Jordan (1914), R. H. Curtiss (1914), A. Hnatek (1920), W. J. Luyten, O. Struve and W. W. Morgan (1939), P. Pismis, G. Haro and O. Struve (1950), G. R. Miczaika (1951)]. The values of P, e and K found by all these investigators are in good agreement except that Miczaika finds a lower value for K and e. There is some evidence for apsidal rotation, but there is too large a scatter in the values of the longitude of periastron  $\omega$ , to reach any conclusion. Since the last investigation of this system was that of Miczaika in 1950, the star was placed on the regular binary star programme of the Kodaikanal Observatory.

#### OBSERVATIONS

The spectrograms were taken on Eastman Kodak IIa-O emulsion, during the period 1968-70 with the grating spectrograph attached to the 50cm Cassegrain reflector. The projected slit width was 20 microns and the spectra had a dispersion of  $47\text{\AA}/\text{mm}$  at  $\lambda 4340\text{\AA}$ . All the spectra were measured by one observer (VN). The wavelengths used for radial velocity determination are listed in Table 1. The observations are given in Table 2. The phases were computed from

$$T_0 = \text{JD } 2428382.263 + 5^d.732357$$

following Pismis, Haro and Struve. The observations were then combined into eleven normal places of equal weight and are listed in Table 3.

TABLE 1

*Wavelengths used for radial velocity determination*

Wavelength $\text{\AA}$	Line
4471.48	HeI
4340.47	H $\gamma$
4101.74	H $\delta$

Wavelength Å	Line
4026.36	HeI
3970.07	He
3889.05	H8

TABLE 2

*Radial Velocity measures of Delta Orionis*

Plate No.	Julian Day of Observation	Phase from Node (Period)	Radial Velocity Km/Sec.	No. of lines measured
	2440000 +			
847	216.616	0.413	— 71	5
53	218.326	781	+ 49	6
57	222.422	496	— 77	5
59	223.228	636	— 35	6
66	226.099	137	+ 98	6
884	230.385	0.885	+ 92	4
93	232.153	193	+ 60	6
904	234.142	543	— 76	5
10	239.131	411	— 88	5
11	239.153	415	— 59	4
915	240.126	0.584	— 52	3
26	243.133	109	+105	6
38	247.334	842	+ 81	6
50	250.286	357	— 69	4
53	256.226	393	— 75	6
958	264.181	0.781	+ 35	6
68	268.142	472	— 81	6
76	271.276	018	+104	6
79	272.097	162	+ 64	6
88	273.228	359	— 63	5

Plate No.	Julian Day of Observation	Phase from Node (Period)	Radial Velocity Km/Sec.	No. of lines measured
	2440000 +			
995	274.214	0.531	— 91	6
1005	279.229	406	— 41	4
15	282.161	917	+106	6
21	283.169	093	+ 95	6
27	284.181	270	— 05	6
1030	288.164	0.964	+ 97	6
45	293.152	835	+ 44	6
1119	590.104	637	— 36	5
27	591.097	810	+ 40	5
31	591.319	849	+ 55	5
1136	592.163	0.996	+142	4
39	592.364	031	+103	5
40	593.194	176	+ 59	5
43	594.146	342	— 17	4
51	597.308	894	+ 87	4
1159	598.262	0.060	+ 89	6
85	614.292	857	+ 90	5
89	618.242	546	— 94	6
94	624.260	596	— 52	4
98	630.251	641	— 42	5
1199	631.143	0.796	+ 65	4
1202	632.214	983	+ 87	4
05	633.215	158	+ 72	5
08	643.226	904	+ 68	5
11	644.206	075	+112	5
1217	648.221	0.776	+ 19	5
23	650.235	127	+ 90	4
26	651.228	300	— 39	4
29	655.163	987	+115	5

TABLE 3

*Normal points*

Phase from node	Radial Velocity (Observed) Km/Sec.	Radial Velocity (Calculated) Km/Sec.	O—C Km/Sec
0.00	+108	+109	— 1
10	+ 98	+ 95	+ 3
17	+ 94	+ 64	0
30	— 20	— 22	+ 2
39	— 67	— 69	+ 2
51	— 82	— 81	— 1
58	— 66	— 63	— 3
64	— 38	— 37	— 1
79	+ 41	+ 41	0
85	+ 68	+ 70	— 2
90	+ 88	+ 89	— 1

## ORBITAL ELEMENTS

The preliminary orbital elements were obtained by the Lehman-Filhes method and the elements were corrected by a least square solution following Sterne (1941). The preliminary and final elements with their probable errors are given below:

Elements	Preliminary	Final
$\gamma$	+ 15 Km/Sec.	+ 14.8 $\pm$ .5 Km/Sec
K	97.0 Km/Sec.	96.5 $\pm$ .7 Km/Sec
e	0.000	0.066 $\pm$ .005
$\omega$	—	106°58' $\pm$ 14°30'
To	JD 2440437.41	JD 2440437.41 $\pm$ .01

The computed velocity curve along with the normal points is shown in Figure 1.

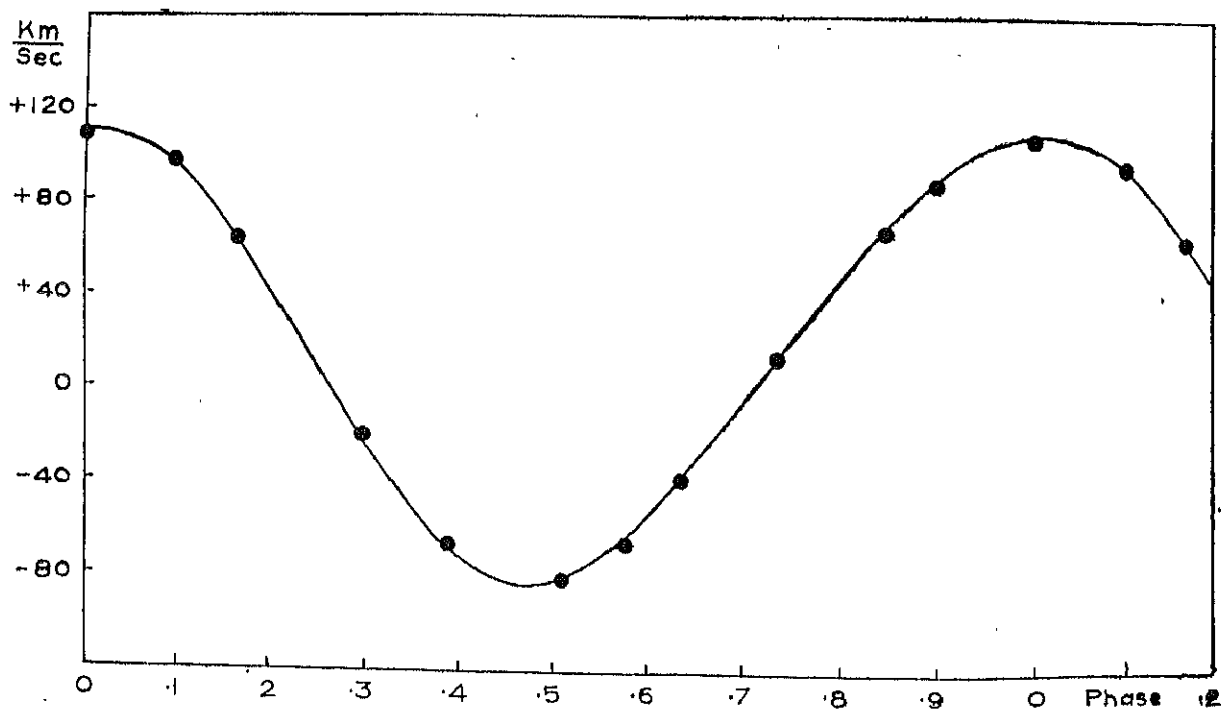


Fig.1 RADIAL VELOCITY CURVE OF DELTA ORIONIS

Luyten, Struve and Morgan have discussed the earlier observations and tabulated the elements obtained by various investigators. The subsequent investigations together with the present one have been added to the above table and are given in Table 4 for ready comparison.

TABLE 4

Observatory	Epoch (Year)	No. of Observations	$\omega$ (Degrees)	$\gamma$ Km/Sec.	K Km/Sec.	e	To Julian Day.
POTSDAM	1902-14	24	355	+22	100.5	0.080	2415799.43
POTSDAM	03-05	13	352	21	102.0	0.136	16131.96
ALLEGHENY	10-84	36	0	15	100.0	0.090	18981.02
MICHIGAN	13-10	74	359	20	101.0	0.097	19806.39
VIENNA	20-19	17	351	19	99.5	0.130	22391.82
YERKES	36-52	140	38	12	101.0	0.079	28382.26
MCDONALD	47-95	48	71	12	99.7	0.085	32509.47
HEIDELBERG	51-00	73	352	13	88.6	0.047	33656.11
KODAIKANAL	69-58	49	107	15	96.5	0.066	40437.41

Figure 2 is a plot of the longitude of periastron  $\omega$  and the year of its determination. Excepting the values of  $\omega$  determined at Vienna and Heidelberg (by A. Hnatek and G. R. Miczaika respectively), the rest fall on a straight line with the slope  $1^{\circ}.73/\text{year}$ . We derive from this value a period of apsidal rotation of 208 years.

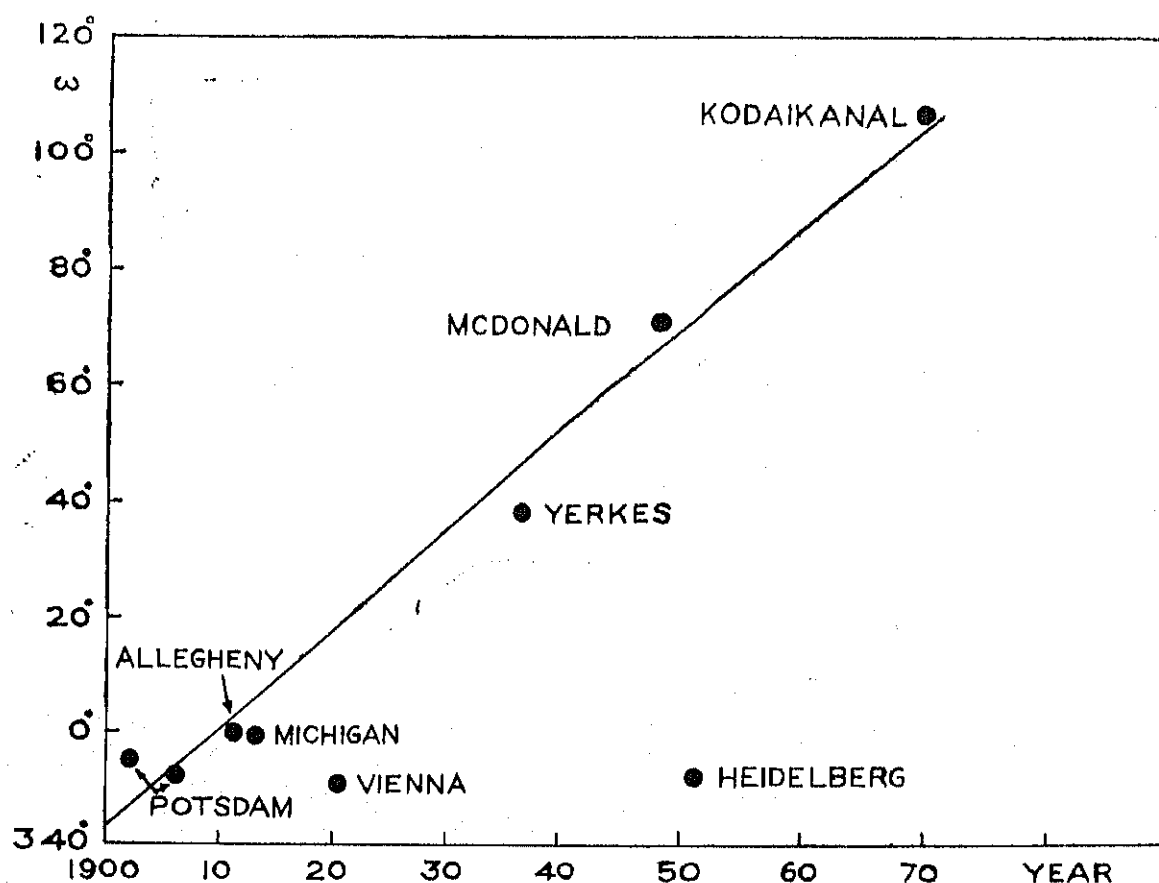


Fig. 2 change in  $\omega$  with Time

#### ACKNOWLEDGEMENT

The authors are thankful to Dr. M.K.V. Bappu, Director, Astrophysical Observatory, Kodaikanal for his encouragement during the course of this study.

#### REFERENCES

- Curtiss, R. H., 1914, Publ. Obs. Univ. Michigan, **1**, 118.  
 Hartmann, J., 1904, Astrophys. J., **19**, 268  
 Hnatek, A., 1920, Astr. Nachr., **213**, 17  
 Jordan, F. C., 1914, Publ. Allegheny Obs., **3**, 125  
 Luyten, W. J., Struve, O and Morgan W. W., 1939, Publ. Yerkes Obs., 7—pt. IV, 256  
 Miczaika, G. R., 1951, Z. Astrophys., **30**, 299  
 Pismis P., Haro G and Struve O., 1950, Astrophys. J. **111**, 509  
 Sterne T., 1941, Proc. Nat. Acad. Sci., **27**, 175  
 MGIPCBE-S4-3 DAOK/71-16-2-72-365,





# KODAIKANAL OBSERVATORY

## BULLETIN Number 209

### Photoelectric and Spectrographic Studies of Nova Delphini (1967)

A. Thulasi Doss, A. Bhatnagar and V. Natarajan  
Kodaikanal Observatory  
India

#### Abstract

The measurement and analysis of the spectra of Nova Delphini (1967) obtained at Kodaikanal is presented. An estimate of the photospheric temperature of the nuclear star of the nova is also made.

Key words : Nova Delphini—Radial velocities and line  
profiles—Ionisation temperature

#### Introduction

Nova Delphini was discovered on July 8, 1967, by Alcock (1967) at a visual magnitude of 5.6. From the predisccovery magnitude records published in later IAU circulars, it appears that the star took nearly 35 days to attain this brightness from an initial value of 12<sup>m</sup>.0. The nova reached a maximum brightness of 3.7 magnitude on 14th December 1967. In this paper we present a detailed study of photoelectric and spectrographic observations of Nova Delphini obtained at Kodaikanal during the period September 12, 1967 to December 13, 1968. This bright slow type nova gave us an unique opportunity to record spectra at different stages of nova development viz. premaximum, principal and early nebular stages.

#### Photoelectric observations

The first Kodaikanal photoelectric observations on Nova Delphini were made on September 12, 1967, with the photometer on the 20 cm. Cooke refractor. The nova was observed through standard B, V filters. The comparison star was BD + 19°4484 with  $V = 6.29$  and  $(B-V) = +0.64$ . The V magnitudes and the colours obtained by us for the nova are given in Table I. The plotted light curve contains data obtained from the IAU circulars and Onderlicka

and Vetesnick (1968) as well as Grygar *et al.* (1968). Figure 1 shows this plot which includes the Kodaikanal observations. During September 1967 the V and (B-V) values were around 4.6 and +0.37 respectively with a fluctuation of only 0.1 magnitude. After the discovery there

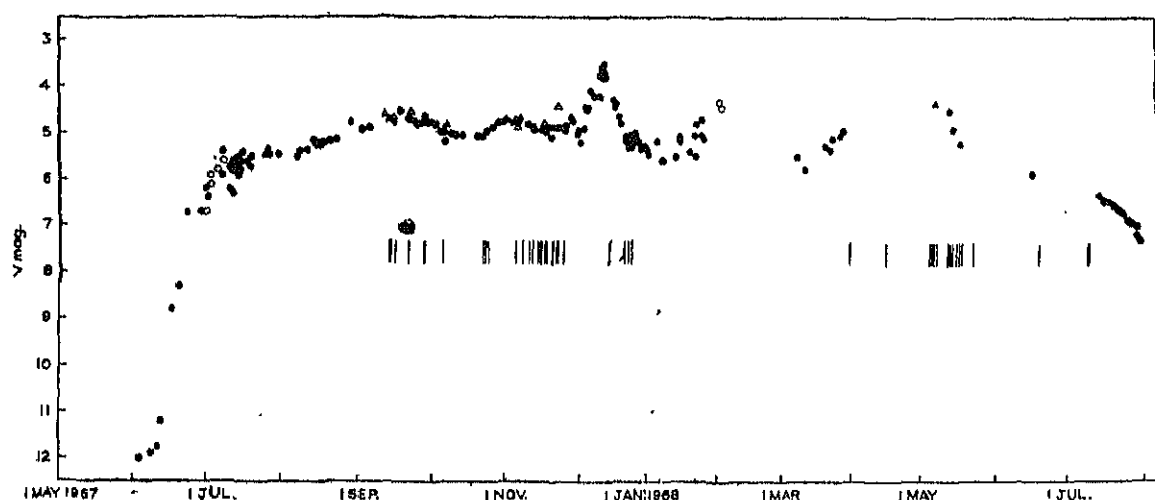


Figure 1 : Light curve of Nova Delphini (1967)

Published photoelectric values

Visual observations

Kodaikanal photoelectric values

Line to indicate the epoch of Kodaikanal spectrograms.

were many conspicuous bursts of  $0^m.5$  to  $0^m.9$  but the major outburst was reported on December 14, 1967, when the Nova reached the maximum brightness of 3.4 magnitude. The brightness variation of Nova Delphini resembles that of a typical very slow nova.

### The Spectroscopic Observations

Our first spectrographic observations of the nova were made on September 15, 1967. The absorption spectrum with faint emission lines recorded on September 15, refer to the pre-maximum stage of the nova's spectral development. The spectra were obtained during the period September 15, 1967 to December 13, 1968.

TABLE I  
Nova Delphini 1967—Photoelectric measurements

Date U.T.				V	(B-V)
1967	September	..	12.71	4.60	+0.27
			14.64	4.70	+0.36
			15.69	4.68	+0.38
			23.62	4.52	—
			29.76	4.62	—
	October	..	7.73	4.84	+0.42
	November	..	6.70	4.85	+0.46
			7.63	4.67	+0.34
			18.62	4.84	+0.37
			23.59	4.42	+0.34
	December	..	19.60	4.30	+0.33
1968	May	..	7.94	4.34	—

The spectrograms, discussed in this paper, were obtained with the Cassegrain spectrograph of the 50cm. telescope. The dispersion in the second order is 45 Å/mm with the 5-inch camera. During the faint stages of the nova apparition, a 2-inch camera was utilized with the spectrograph for slitless spectroscopy. Details of the spectrograms obtained are given in Table II. The spectral region indicated as photographic, covers from 3800Å-4600Å. The visual range covers from 4860-6570Å. The spectrograms were calibrated for spectro-photometry by a Hilger step wedge filter, attached to an auxiliary spectrograph. Radial velocity measures and line identifications have been carried out with the aid of an Abbe Comparator. Tables III and IV cover identifications made on spectra obtained on September 15 and October 7, 1967, respectively.

TABLE II  
*Details of Spectrograms of Nova Delphini (1967)*

Plate No.	Date of mid-exposure U.T.		Exposure time Minutes	Spectral region (*)	Type of emulsion
1	2		3	4	5
492	1967 September	..	15.74	P	H $\alpha$ -O
495			17.77	P	103a-F
496			23.72	P	H $\alpha$ -O
499			29.71	P	H $\alpha$ -O
500			30.73	V	103a-F
503	October	..	7.74	V	103a-F
508			24.63	P	H $\alpha$ -O
514			25.65	V	103a-F
518			26.69	P	H $\alpha$ -O
522	November	..	6.71	V	103a-F
524			9.65	P	H $\alpha$ -O
530			12.68	V	103a-F
533			14.67	P	H $\alpha$ -O
536			15.64	V	103a-F
537			16.65	P	H $\alpha$ -O
538			17.68	V	103a-F
539	December	..	18.65	P	H $\alpha$ -O
540			19.64	V	103a-F
541			22.64	P	H $\alpha$ -O
542			23.64	V	103a-F
544			24.64	P	H $\alpha$ -O
545			26.62	V	103a-F
548			27.64	P	H $\alpha$ -O
551			16.60	V	103a-F
552			23.62	P	H $\alpha$ -O
553			24.58	V	103a-F
555	1968 April	..	26.58	V	103a-F
731			1.99	V	103a-F
743			17.94	P	H $\alpha$ -O
746			6.00	V	103a-F
750	May	..	7.00	V	103a-F
751			7.00	P	H $\alpha$ -O
753			7.94	P	H $\alpha$ -O
754			7.96	P	H $\alpha$ -O
756			8.98	V	103a-F
764			13.96	V	103a-F
769			15.00	P	H $\alpha$ -O
770			15.83	I	I-N+H <sub>2</sub> O
772			15.95	V	103a-F
774			15.98	P	H $\alpha$ -O

\* P = Photographic, V = Visual, I = Infrared.

TABLE II—(Contd.)  
*Details of Spectrograms of Nova Delphini (1967)*

Plate No.	Date of mid-exposure U.T.			Exposure time Minutes	Spectral region (*)	Type of emulsion	
1	2			3	4	5	
777				17.93	8	V	103a-F
778				17.96	10	P	11a-O
780				18.98	20	P	11a-O
782				19.97	10	P	11a-O
784				20.93	9	V	103a-F
785				23.86	20	P	11a-O
788				28.95	12	V	103a-F
789				29.86	20	P	11a-O
797	June	..	..	19.82	18	V	103a-F
799				19.97	60	V	103a-F
802	July	..	..	10.75	15	V	103a-F
812	September	..	..	25.00	5	V	103a-F
813	October	..	..	4.75	100	V	103a-F
814				4.81	10	P	103a-F
815				14.68	10	V	103a-F
817				21.69	20	V	103a-F
823	November	..	..	15.60	30	V	103a-F
831	December			13.62	20	V	103a-F

\* P = Photographic, V = Visual, I = Infrared

TABLE III  
*Identification of absorption lines in photographic region on September 15, 1967*

Measured $\lambda$ Å	Reduced with factor 0.00075 Å	$\lambda$ lab. Å	Element and Multiplet No.	$\lambda$ lab.— $\lambda$ rel Å
3886.1	3889.0	3889.1	He I (1)	+0.1
3897.9	3900.8	3900.6	Ti II (34)	-0.2
3911.3	3914.2	3913.5	Ti II (34)	-0.7
3929.9	3932.8	3933.7	Ca II (1)	+0.9
3964.5	3967.4	3968.5	Ca II (1)	+1.1
4009.2	4012.2	4012.4	Ti II (11)	+0.2
4021.3	4024.3	4025.1	Ti II (11)	+0.8
4026.1	4028.0	4028.3	Ti II (87)	+0.3
		4029.6	Ti II (87)	+1.6
4042.8	4045.8	4046.8	Fe II (126)	+1.0
4050.9	4053.9	4053.8	Ti II (87)	-0.1
4074.9	4077.9	4077.7	Sr II (1)	-0.2
4098.9	4102.0	4101.7	Hg I (1)	-0.3
4160.8	4163.9	4163.6	Ti II (105)	-0.3
4169.7	4172.8	4173.5	Fe II (27)	+0.7
4176.6	4179.7	4178.8	Fe II (28)	-0.9
4212.6	4215.8	4215.5	Sr II (1)	-0.3
4223.4	4226.6	4226.7	Ca I (2)	+0.1
4230.2	4233.3	4233.2	Fe II (27)	-0.1
4243.8	4246.9	4246.8	Sc II (7)	-0.1
4286.6	4289.8	4290.2	Ti II (41)	+0.4
4292.0	4295.3	4296.6	Fe II (28)	+1.3
		4294.8	Sc II (15)	-0.5
4298.0	4301.2	4300.0	Ti II (41)	-1.2
		4300.2	Mn II (6)	-1.0
		4301.9	Ti II (41)	+0.7
4305.1	4308.4	4307.9	Ti II (41)	-0.5
4311.1	4314.3	4314.1	Sc II (15)	-0.2
		4315.0	Ti II (41)	+0.7

TABLE III—(Contd.)

*Identification of absorption lines in photographic region on September 15, 1967*

Measured $\lambda$ A	Reduced with factor 0.00075 A	$\lambda$ lab. A	Element and Multiplet No.	$\lambda$ lab.— $\lambda$ red A
4318.0	4321.3	4320.9 4320.7	Ti II (41) Sc II (14)	—0.4 —0.4
4322.6	4325.8	4325.0 4325.1	Sc II (15) Mn II (6)	—0.8 —0.7
4336.5	4339.8	4340.5	H $\delta$ I (1)	+0.7
4348.7	4351.9	4351.8	Fe II (27)	—0.1
4365.0	4368.2	4369.4	Fe II (28)	+1.2
4372.0	4375.3	4374.5 4374.8	Sc II (14) Ti II (93)	—0.8 —0.5
4382.1	4385.4	4385.4 4384.8	Fe II (27) Sc II (14)	0.0 —0.6
4391.9	4395.2	4395.0	Ti II (19)	—0.2
4397.7	4400.9	4400.4 4400.6	Sc II (14) Ti II (93)	—0.5 —0.3
4413.8	4417.1	4416.8 4415.6 4417.7	Fe II (27) Sc II (14) Ti II (40)	—0.3 —1.5 +0.6
4440.7	4444.0	4443.8 4444.6	Ti II (19) Ti II (31)	—0.2 +0.6
4447.4	4450.7	4450.5	Ti II (19)	—0.2
4465.9	4469.2	4468.5 4469.2 4470.8	Ti II (31) Ti II (18) Ti II (40)	—0.7 0.0 +1.6
4477.8	4481.2	4481.3 4481.1	Mg II (4) Mg II (4)	+0.1 —0.1
4485.9	4489.3	4489.2	Fe II (37)	—0.1
4498.2	4501.5	4500.3 4501.3	Ti II (18) Ti II (31)	—1.2 —0.2
4505.5	4508.9	4508.3	Fe II (38)	—0.6
4511.9	4515.3	4515.3	Fe II (37)	0.0
4518.6	4522.0	4520.2 4522.6	Fe II (37) Fe II (38)	—1.8 +0.6
4531.0	4534.4	4534.0 4534.2	Ti II (50) Fe II (37)	—0.4 —0.2
4546.6	4550.0	4549.6 4549.5	Ti II (82) Fe II (38)	—0.4 —0.5
4553.2	4556.6	4555.9	Fe II (37)	—0.7
4561.0	4564.5	4563.8	Ti II (50)	—0.7
4569.0	4572.4	4572.0	Ti II (82)	—0.4
4580.0	4583.5	4582.8 4583.8	Fe II (37) Fe II (38)	—0.7 +0.3
4586.3	4589.8	4590.0	Ti II (50)	+0.2

TABLE IV

*Identification of Absorption lines on Plate No. 503 taken on October 7, 1967*

Measured $\lambda$	Reduced with a factor 0.00076	$\lambda$ Lab.	Element and Multiplet No.	$\lambda$ lab.— $\lambda$ red.
6557.5	6562.5	6562.8	H $\gamma$ (1)	+0.3
6513.1	6518.1	6516.1	Fe II (40)	-2.0
		6519.4	Mn I (39)	+1.3
6450.4	6455.3	6456.4	Fe II (74)	+1.1
6377.9	6382.7	6383.7	Fe II ( )	+1.0
		6382.2	Mn I (39)	-0.5
		6384.7	Mn I (39)	+2.0
6341.4	6346.2	6347.1	Si II (2)	+0.9
6243.5	6248.2	6247.6	Fe II (74)	-0.6
6154.4	6159.1	6158.2	OI (10)	-0.9
		6156.8	OI (10)	-2.3
		6156.0	OI (10)	-3.1
5892.0	5896.5	5895.9	Na I (1)	-0.6
5886.3	5890.8	5889.9	Na I (1)	-0.9
5532.1	5536.3	5534.9	Fe II (55)	-1.4
5312.2	5316.2	5316.6	Fe II (49)	-0.4
		5316.8	Fe II (48)	-0.6
5279.9	5283.9	5284.1	Fe II (41)	+0.2
5271.1	5275.1	5276.0	Fe II (49)	+0.9
5231.1	5235.1	5234.6	Fe II (49)	-0.5
5193.4	5197.4	5197.6	Fe II (49)	+0.2
5165.0	5168.9	5169.0	Fe II (42)	+0.1
5012.4	5016.2	5018.4	Fe II (42)	+2.2
4916.5	4920.2	4923.9	Fe II (42)	+3.7
4853.7	4857.4	4861.3	H $\beta$ (1)	+3.9

### General discussion of the development of the nova spectrum

The main features of the spectra in September, October and November 1967 were the strong violet displaced absorption lines of H, CaII, FeII, TiII, SrII, ScII, CaI, OI and NaI. Almost all absorption lines are accompanied by faint emission features on the longward side. These absorption lines did not show any companion absorption system.

The radial velocity measures show that all absorption lines were systematically displaced towards the shortward side indicating velocity of approach. The hydrogen absorption lines did not show the same velocity. This may be explained as due to the interaction of absorption profile with emission line on the longer wavelength side and as the emission associated with the hydrogen lines increases with decreasing member of the Balmer series, a spurious violet shift may be introduced in the velocity measurements from the hydrogen lines. Tables V and VI give the radial velocity measures made on the blue and red spectra respectively.

The expanding envelopes showed uniform constant velocity of ejection around 250 km/sec. from September 1967 until the burst that enabled peak brightness to be attained on December 14, 1967. The premaximum spectra during September, October and November 1967 showed very few changes other than a gradual increase in the intensity of the emission lines. This stage was characterised by strong absorption lines due to hydrogen and ionized calcium and also those of TiII and FeII. All the strong absorption lines were associated with faint emission on the longward side.

The spectrum in the visual region obtained on December 16, 1967, two days after the major outburst, is of particular interest. This showed tremendous changes as compared to the earlier spectra which were rather steady for nearly three months. Remarkable changes had taken

TABLE V

*Velocities in km/sec of absorption lines (Photographic region)*

A	Plate No. Date Identification	492 1967 Sept. 15	496 1967 Sept. 23	499 1967 Sept. 29	539 1967 Nov. 18	548 1967 Nov. 27	743 1968 Apr. 18	753 1968 May 7	769 1968 May 15	785 1968 May 23
1	2	3	4	5	6	7	8	9	10	11
3889.1	Mg	232			239		1128			
3900.6	Ti II	203		230						
3913.5	Ti II	167		185	219					
3933.7	Ca II (K)	288		308	358		383		494	
							1100		1220	
3968.5	Ca II (H) }	303		277	280				529	
3970.1	He }								1246	
4012.4	Ti II	237		188	241					
4025.1	Ti II	230		241						
4029.0	Ti II	164	241							
4046.8	Fe II	298	208	293	283					
4053.8	Ti II	216			164					
4077.7	Sr II	164		159	212					
4101.7	H $\delta$	203	174	150	159	139	332	998	426	1118
									1256	1518
4163.6	Ti II	204		237	218					
4173.5	Fe II	271		227						
4178.8	Fe II	164	290							
4215.5	Sr II	205		181	202					
4226.7	Ca I	236	199	212	183					
4233.2	Fe II	213	184	198	271					
4246.8	Sc I	215	165	166	179					
4290.2	Ti II	258	207	207	201					
4294.8	Sc II }									
4296.6	Fe II }	191	244	292	165					
4300.0	Ti II }									
4300.2	Mn II }	145	135	107						
4301.9	Ti II }									
4307.9	Tn II	192	155	152	125					
4314.1	Sc II }									
4315.0	Ti II }	210	195	191	216					
4320.7 }	Sc II	204	212	171	188					
4320.9 }										
4325.0	Sc II }									
4325.1	Mn II }	167	132	128	120					
4340.5	H $\gamma$	272		288	269	216	237	1006	426	1116
							1116		1221	1534
4351.8	Fe II	213		177	154					
4374.5	Sc II }									
4374.8	Ti II }	169	150	169						
4384.8	Sc II }	225	217	203	219		397			
4385.8	Fe II }						983			
4395.0	Ti II	210	180	204	209					
4400.4	Sc II }									
4400.6	Ti II }	184	196	198	193					
4415.6	Sc II }									
4416.8	Fe II }	204	168	161	162					
4417.7	Ti II }									
4443.8	Ti II }									
4444.6	Ti II }	212	198		197					



TABLE V—(Contd.)

*Velocities in km/sec of absorption lines (Photographic region)*

A	Plate No. Date Identification	492 1967 Sept. 15	496 1967 Sept. 23	499 1967 Sept. 29	539 1967 Nov. 18	548 1967 Nov. 27	743 1968 Apr. 18	753 1968 May 7	769 1968 May 15	785 1968 May 23
1	2	3	4	5	6	7	8	9	10	11
4450.5	Ti I	208	187	202	152					
4468.5	Ti II	175	140	144	152					
4469.2	Ti II									
4470.8	Ti II									
4481.1	Mg II	234		145	182					
4481.3	Mg II									
4489.2	Fe II	218	169	233						
4500.3	Ti II	144	169		104					
4501.3	Ti II									
4508.3	Fe II	186	123	197	182					
4515.3	Fe II	215	209	177	182					
4520.2	Fe II	190	142	126						
4522.6	Fe II									
4534.0	Ti II	198	125	177	154					
4534.2	Fe II									
4549.5	Fe II	196	185	200	188					
4549.6	Ti II									
4555.9	Fe II	176		129	157					
4563.8	Ti II	179	188	157	159					
4572.0	Ti II	195	200	198	186					
4582.8	Fe II	183	155	136	116					
4583.8	Fe II									
4590.0	Ti II	237		240	221					

place in the continuum as well as absorption and emission lines. Continuum and emission were considerably increased in intensity whereas absorption lines had become narrower with secondary absorption system appearing on violet side. Emission was found spilled over the first absorption system on to its violet side. The new absorption system was identified as the principal absorption spectrum with associated strong and wide emission bands.

All these and the foregoing features can be noticed from the mosaic of nova spectra presented in Plates I and II. It can be clearly seen how the intensity of the emission lines have increased and reached maximum after the December outburst. The premaximum absorption lines could be traced even after a few days of this major outburst, but with narrowed lines. Most of the metallic lines especially in the photographic region had disappeared. The gradual decrease in the earlier absorption system would mean that the premaximum shell responsible for this absorption was being dissipated slowly. The new shell ejected due to 14th December outburst could be identified on 16th December itself by the doubling of FeII lines in the green region. A faint suggestion of this secondary absorption for H-alpha could be seen on 24th December. This became a conspicuous shallow broad absorption on 26th December 1967. The measured velocity of  $-1350$  km/sec is the highest velocity recorded at Kodaikanal for this Nova.

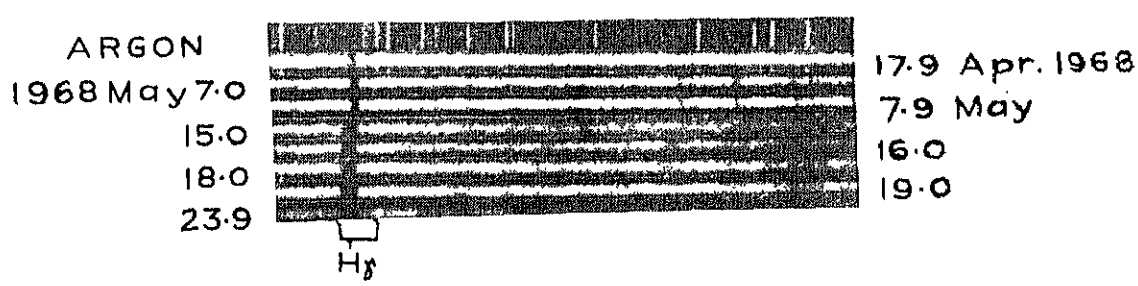
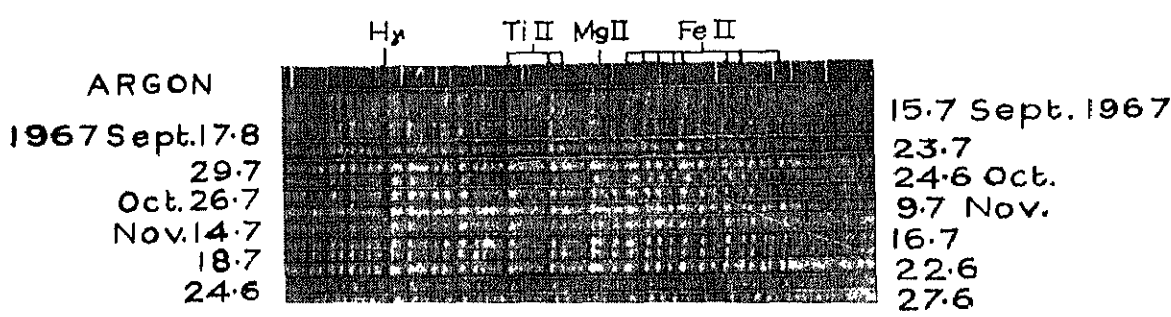
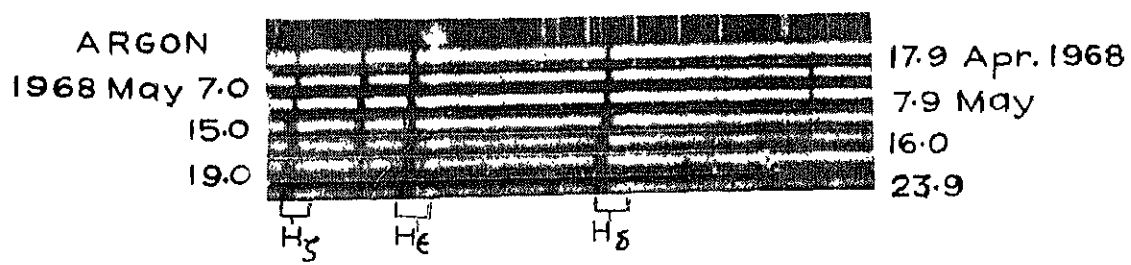
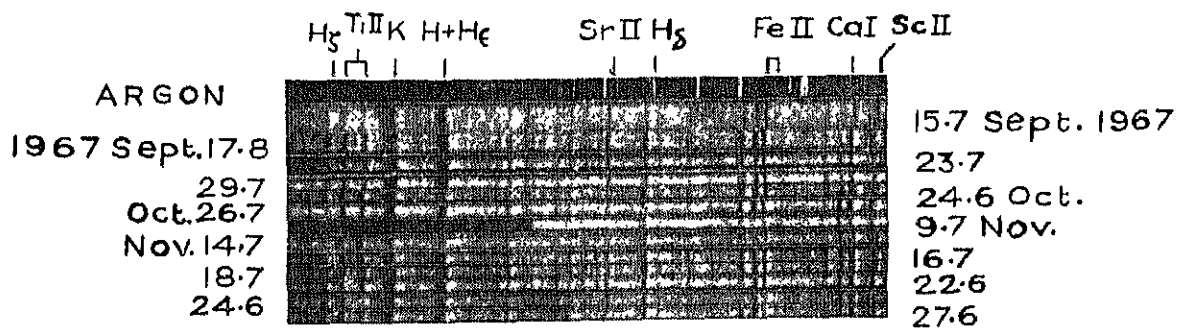


Plate I: Mosaic of blue spectrograms of Nova-Delphini (1967)—Dates are in U.T.

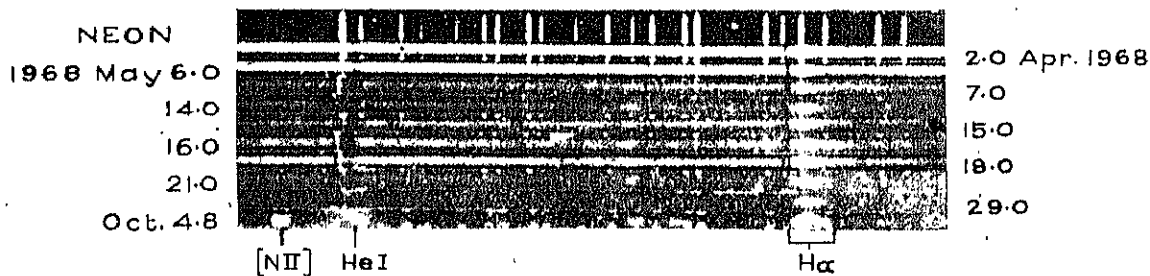
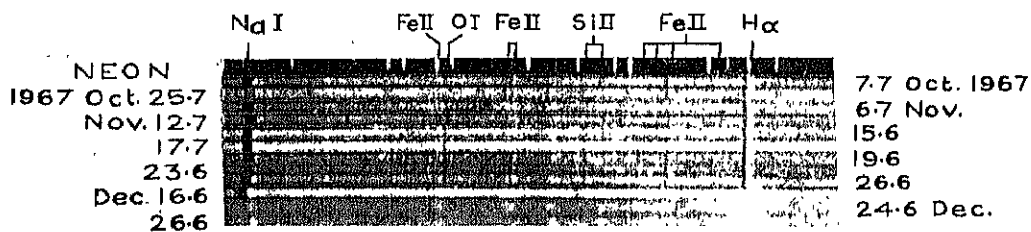
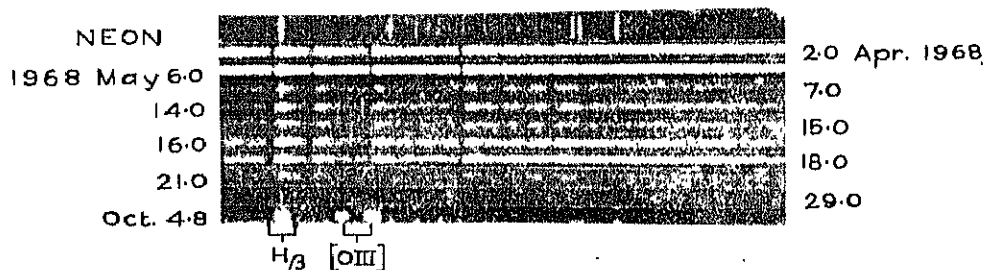
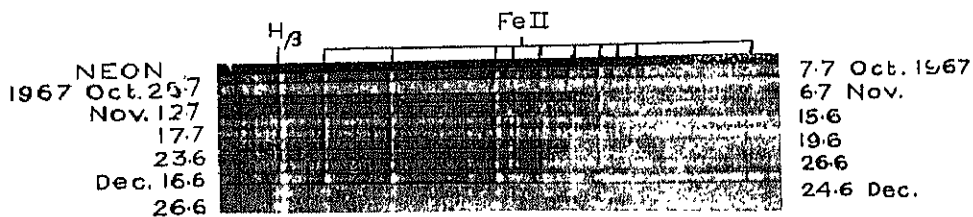


Plate II: Mosaic of red spectrograms of Nova-Delphini (1967) Dates are in U.T.

TABLE VI  
Velocities in km/sec of absorption lines (Visual region)

A	1	2	3	4	5	6	7	8	9	10	11	12	13	14	15	16	17
		Plate No. Date Identification	503 1967 Oct. 7	514 1967 Oct. 25	522 1967 Nov. 6	530 1967 Nov. 12	536 1967 Nov. 15	538 1967 Nov. 17	542 1967 Nov. 23	551 1967 Dec. 16	553 1967 Dec. 24	555 1967 Dec. 26	731 1968 Apr. 1	746 1968 May 6	750 1968 May 7	772 1968 May 15	777 1968 May 17
6562.8		H $\gamma$	240	270	264	225	234	225	220	191	181	207 1350	848 1115	401 946	420 968	414 1227	411 977 1382
6516.1		Fe II } Mn I }	137														
6456.4		Fe II	279	249	105	108	219	186					957				
6383.8		Fe II } Mn I }	275														
6437.1		Si II	247					129									
6247.6		Fe II	194	177	138	63	153	153									
6157.0		O I	185		609								846 1199	964			
5895.9		Na I	202		258	249	255	228	231	225				435			
5890.0		Na I	188	144	225	240	225	225		215		1078	489 1026	1062	450 1262		
5534.9		Fe II	148														
5316.8		Fe II	261							283			1017				
5276.0		Fe II	233			381							1021				
5234.6		Fe II	203			333				212			939				
5197.6		Fe II	333			345											
5169.0		Fe II	232						232	293 667		646 1060				1282	1259
5018.4		Fe II				339			223	356 766		587 1131	877	1064	445 1258	420	
4923.9		Fe II		314	321	267	354	342	222	362 774		627 1170	910	1074	387 1227	445 1188	
4861.3		H $\beta$		371	345	258	297	351	286	326	302	315	648 1180	605 1045	462 1008	434 1213	569 1351

No spectrographic observations were possible between January 1968 to March 1968 because of the proximity of the nova to the Sun. Spectra obtained during April 1968 showed two distinct absorption systems one narrow and the other broad. On May 17, 1968, the broad absorption line of H-alpha appeared to have split into two, conveying the emergence of another shell. The velocities of these 3 shells as on 17th May, 1968, were 1382 km/sec, 977 km/sec, and 411 km/sec.

In the development of the principal spectrum, the OI flash at 6300A was recorded earlier than OI at 6364A. Both these lines could be seen conspicuously on the spectrum of 17th May 1968. The NII flash at 5755A was first recorded on 10th July 1968 on a slitless spectrum. The next slitless spectrum obtained on 25th September, 1968, showed the emergence of the nebular stage with the characteristic emission blobs of OIII at 4959A and 5007A. The line OIII 5007A was more intense than H $\beta$ . Also the 4640A band of NIII appeared on a slitless spectrum taken on 4th October 1968 along with the emission band 4363A OIII. An infra-red spectrum obtained on 15th May 1968 on hypersensitized I-N film showed apart from intense 6563A, emission lines of OI at 7774A and 8446A.

### Spectrophotometric measurements and study of line profiles

As mentioned earlier, all spectrograms were calibrated using a step wedge filter attached to an auxiliary spectrograph. The density traces of the spectra were obtained with the recording microphotometer with a magnification of 108. The intensity measurements are in terms of the intensity of the continuum.

TABLE VII

*Measured intensity of emission and absorption lines in terms of equivalent km/sec. (Photographic region)*

Plate No.	Date		Emission						Absorption					
			H $\gamma$	H $\delta$	H+H $\epsilon$	K	H $\zeta$	H $\eta$	H $\gamma$	H $\delta$	H+H $\epsilon$	K	H $\zeta$	H $\eta$
	1967													
492	September	15.74	750	100	140	80			200	190			130	50
548	November	27.64	440	400	500	480	230						170	
	1968													
753	May	7.94	2680	1810	1850	680		440	410	390				330
769	May	15.00	1840	1150	700	210	320	190	510					410
785	May	23.86	620	810	330		300	200	610	400	310			

TABLE VIII

*Measured intensity of emission and absorption lines in terms of equivalent km/sec. (Visual region)*

Plate No.	Date U.T.		Emission			Absorption		
			H $\zeta$	H $\beta$	D $_1$ & D $_2$	H $\zeta$	H $\beta$	D $_1$ & D $_2$
	1967							
503	October	7.74		960	180		120	460
514	October	25.65	1990	900	60	80	230	
522	November	6.71	960	410	370	110	270	
530	November	12.68	1280	570	130	100	250	
536	November	15.64	1150	380	400	150	190	170
538	November	17.68	1430	720	210	230	230	
542	November	23.64	1300	980	180	250	250	290
551	December	16.60	1680	1320	1250	260	260	
553	December	24.58	14500		760			190
	1968							
750	May	7.0	3330	1550	350	250	260	340
772	May	15.95	12790	2380	360	450	380	430
777	May	17.93	33740	6740	480	340		440

Intensity profiles of 6563A and 4861A of hydrogen and 5890A, 5896A of neutral sodium are given in Figure 2. The profiles of H $\gamma$ , H $\delta$  and the region between 3820A and 3970A are shown in Figure 4. In Tables VII and VIII, we give the total observed intensity of the hydrogen lines H $\alpha$  to H $\epsilon$ , H and K, D $_1$  and D $_2$ , all expressed in terms of equivalent Kms/sec for both absorption and emission. The striking increase in intensity and width of the hydrogen lines after the maximum phase can be seen clearly. The earlier absorption system is present like a sharp central absorption in the H $\alpha$  and H $\beta$  emission bands nearly at its normal position. This gives a saddle type structure to the line profiles. Such structures were recorded for earlier novae by Larson Leander (1954). Figures 2 and 3 bring out structural changes experienced by the emission and absorption bands of different lines with time. The emission lines are asymmetrical due to absorptions on the violet side. Hence a good approximation to the true total emission intensity of any line can be obtained by computing twice the area of emission on the longward half of the profile. Similarly the true total absorption band intensity can be computed by adding the difference between the longward half and the shortward half of the emission band to the intensity of the observed absorption band. In Tables VII and VIII are given the intensity of some of the emission and absorption bands. If  $E_L$  and  $E_S$  are the intensity of the longward and shortward half of the emission band and A is the intensity of the absorption band, we take the true emission band intensity as equal to  $2 E_L$  and true absorption band intensity to be  $A + (E_L - E_S)$ . These are given in Table IX.

TABLE IX

*Computation of corrected intensity of emission and absorption lines in terms of equivalent km/sec.*

Date		Line	$E_L$	$E_S$	A	$E_L + E_S$	$2E_L$	$A + E_L - E_S$	$E_p$
1967									
November	23.6	H $\alpha$	700	600	250	1300	1400	350	0047
		H $\beta$	590	390	250	980	1180	450	0039
November	27.6	H $\gamma$	270	170		440	540		0018
		H $\delta$	265	135		400	530		0018
1968									
May	7.0	H $\alpha$	1870	1460	250	3330	3740	660	0125
		H $\beta$	990	560	260	1550	1980	690	0066
May	7.9	H $\gamma$	1860	820	410	2680	3720	1450	0124
		H $\delta$	1200	610	390	1810	2400	980	0080
May	15.0	H $\gamma$	1300	540	510	1840	2600	1270	0087
		H $\delta$	670	480		1340	1150		0045
May	16.0	H $\alpha$	7540	5250	450	12790	15080	2740	0503
		H $\beta$	1370	1010	380	2380	2740	740	0091

### Zanstra Ionisation temperature

It will be of interest to determine the photospheric temperature of the nuclear star at different phases of the nova development. An attempt has been made here to derive Zanstra ionisation temperatures using the intensities of hydrogen emission lines. The theory is based on the assumption that the radiation of the emission lines of expanding envelope are due to the photoionisation of atoms by the ultra-violet radiation of the central star followed by recombination. In the case of hydrogen the number of ultraviolet quanta emitted by the central star

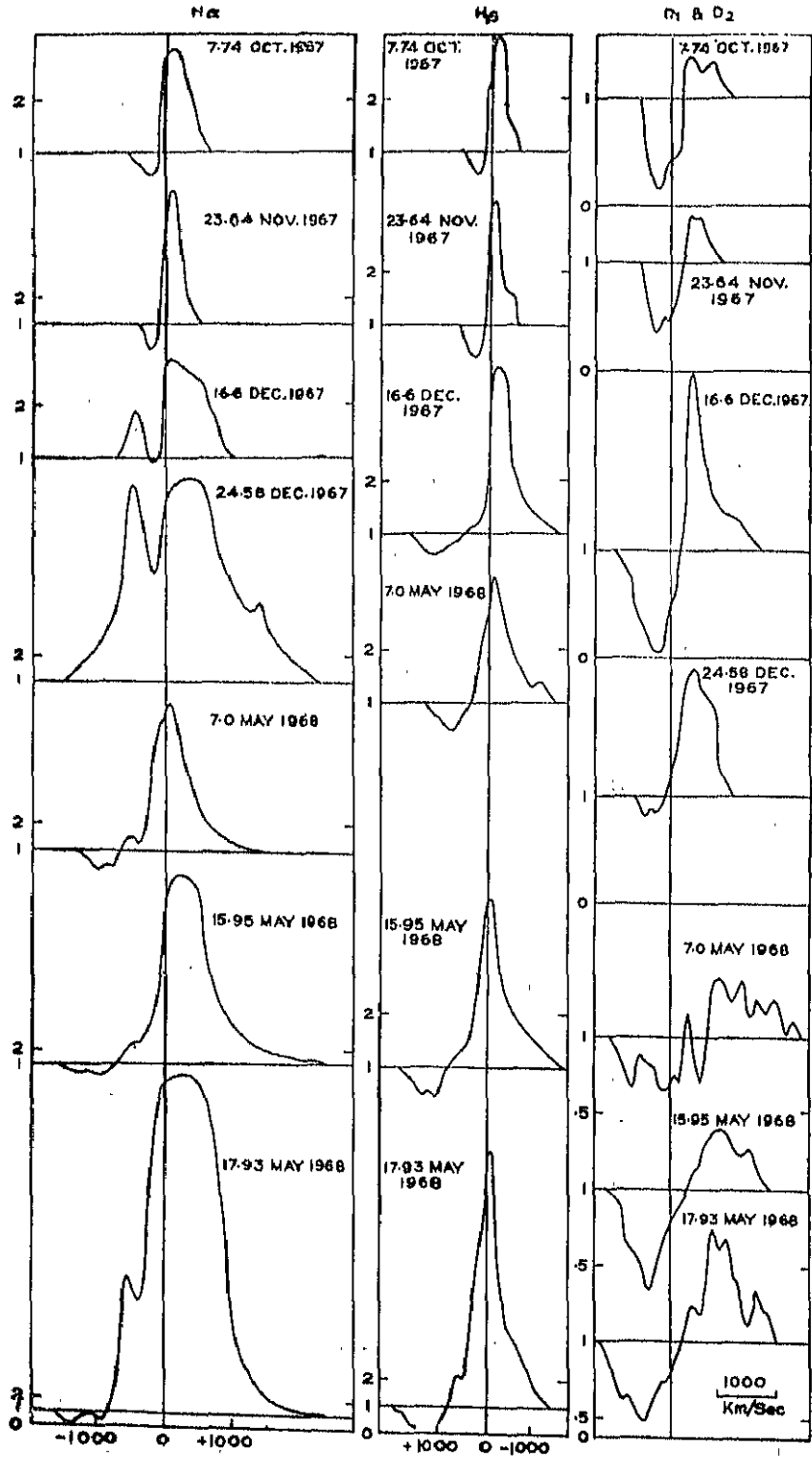


Figure 2 : Intensity profiles of  $H\alpha$ ,  $H\beta$ ,  $D_1$  &  $D_2$   
Abcissa is in km/sec.

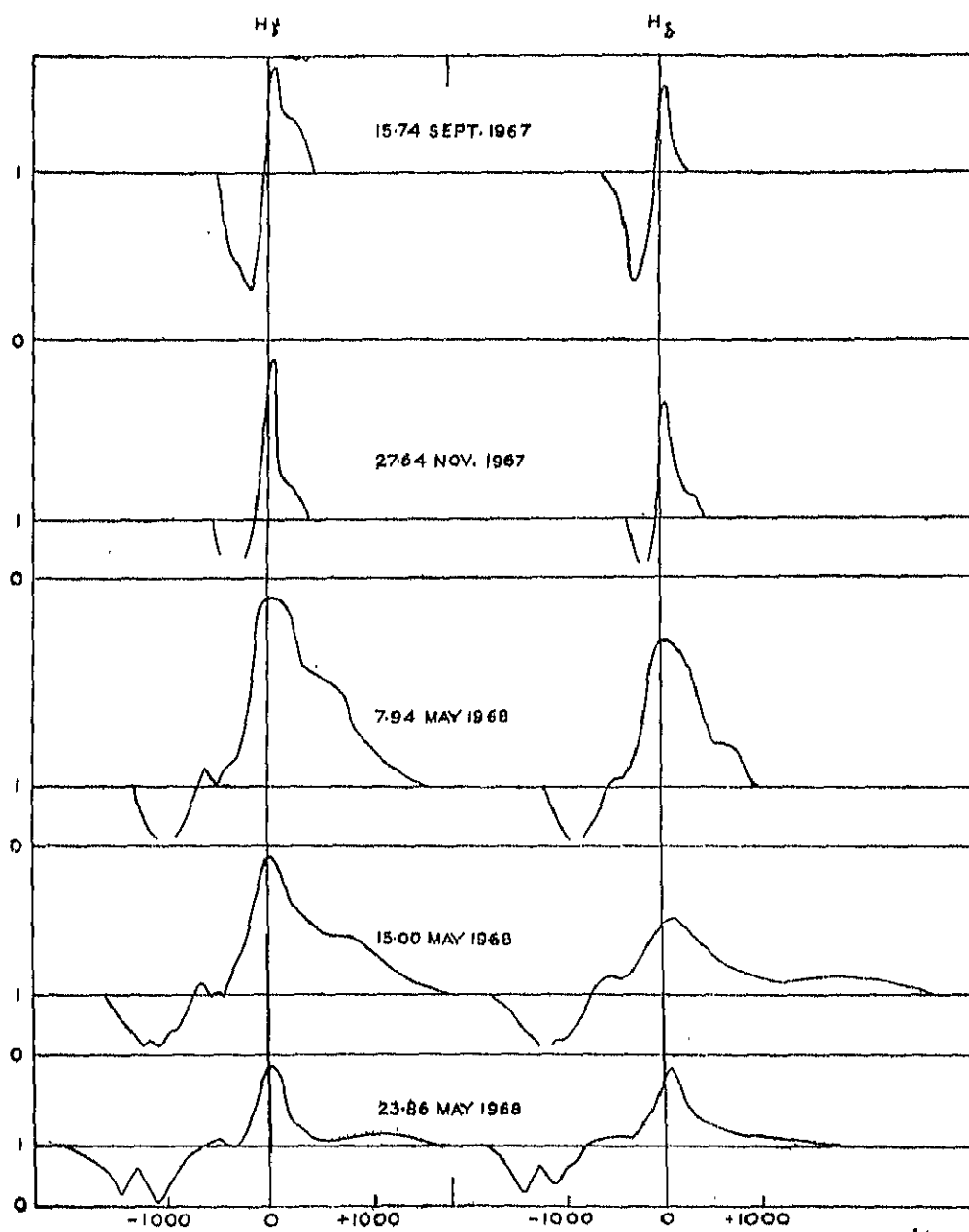


Figure 3 : Intensity profiles of  $H$  and  $H\delta$   
 Abscissa is in km/sec.  $\gamma$





shortward of Lyman limit is equal to the number of quanta emitted by the expanding envelope in the Balmer lines and the adjoining continuum. Then the equation will be of the form

$$\int_{x_0}^{\infty} \frac{x^2}{e^x - 1} dx = \sum \frac{x^3}{e^x - 1} E_\nu \quad (1)$$

$$\text{where } x = \frac{h\nu}{kT}, \quad x_0 = \frac{h\nu_0}{kT}$$

$\nu_0$  = minimum ionising frequency i.e., the Lyman limit = 912A

$T$  = temperature of the nuclear star

$h$  = Planck's constant

$k$  = Boltzmann constant

$E_\nu$  is a quantity such that  $\nu E_\nu$  is the total intensity of the emission band expressed in frequency units of the continuous spectrum.

Following Larson-Leander (1950)  $E_\nu$  was obtained from the equation

$$E_\nu = \frac{2E_L}{c}$$

where 'c' is the velocity of light. The value of  $2E_L$  was obtained from Table IX which we consider to be the total intensity in equivalent km/sec of the emission band. The values of  $E_\nu$  of H $\gamma$ , H $\beta$ , H $\gamma$  and H $\delta$  on different dates are also listed in Table IX. The higher members of the Balmer lines and the adjoining continuum are not taken into account as they are relatively insignificant. But in practice extrapolations may be made from a limited number of observed bands.

In equation (1) let  $J$  represent the integral term and  $S$  the summation term. Then the equation can be written as

$$J - S = \Delta = 0$$

In practice the difference is computed for various assumed values of temperature  $T$ , using Zanstra's (1931) tabulated values for the integral. The temperature  $T$  for which  $\Delta = 0$  is obtained by interpolating between two temperatures giving  $\Delta$  values of positive and negative signs. The computed results are given in Table VI. We should point out that the intensities of the emission lines have been measured on plates obtained in a short interval of time within three to four days. Since Nova Delphini (1967) happens to be a very slow nova, the assumption that there are no large spectral variations on these spectrograms is, therefore, reasonable.

The summation term as obtained directly from the observed bands H $\gamma$ , H $\beta$ , H $\gamma$  and H $\delta$  are given in the columns headed (S). The final value of this term including the extrapolated values for the higher members of the Balmer series is in the column headed  $S_{\text{corr}}$ .

The ionisation temperature values are in the last column of Table X.

TABLE X  
Ionisation temperatures

Date		T	$x_0$	J	S	$S_{\text{corr}}$	$J - S_{\text{corr}}$	Ionisation temperature
1967		$^{\circ}\text{K}$						$^{\circ}\text{K}$
November	25.6	17400	9.0	0.012	0.012	0.015	- 0.003	
		19600	8.0	0.028	0.011	0.013	+ 0.015	17800
1968								
May	7.5	19600	8.0	0.028	0.037	0.047	- 0.019	
		22400	7.0	0.059	0.033	0.041	+ 0.018	21000
1968								
May	15.5	19600	8.0	0.028	0.057	0.063	- 0.035	
		22400	7.0	0.059	0.048	0.054	+ 0.005	22100

## Acknowledgement

The authors are greatly indebted to Dr. M. K. V. Bappu, Director, Indian Institute of Astrophysics, Kodaikanal, for his valuable guidance and interest in the project.

KODAIKANAL OBSERVATORY,  
July, 1972.

## REFERENCES

1. ALCOCK, G. E. D., I.A.U. Circular No. 2022 (1967).
  2. GRYGAR, J., KOHOUTEK, L., AND HARMANEC, P. *Bull. Astr. Inst. Czech.* 19: 101, (1968).
  3. LARSON-LEANDER, G., *Ann. Stockholm Obs.* 17: 46 (1950).
  4. ———— *Ibid.*, 18: 4, (1954).
  5. ONDERLICKA, B., AND VETESNICK, M., *Bull. Astr. Inst. Czech.* 19: 99 (1968).
  6. ZANSTRA, H., *Publ. Dom. Astrophys. Obs.* 4: 209 (1931).
-

